

# Measurements of prompt charm production cross-sections in $pp$ collisions at $\sqrt{s} = 5 \text{ TeV}$

C. Burr<sup>1</sup>, M. Gersabeck<sup>1</sup>, V. V. Gligorov<sup>2</sup>, D. Müller<sup>1</sup>, A. Pearce<sup>1,3</sup>, P. Spradlin<sup>4</sup>

<sup>1</sup>*School of Physics and Astronomy, University of Manchester, Manchester, United Kingdom*

<sup>2</sup>*LPNHE, CNRS/IN2P3, Paris, France*

<sup>3</sup>*STFC Rutherford Appleton Laboratory, Didcot, United Kingdom*

<sup>4</sup>*School of Physics and Astronomy, University of Glasgow, Glasgow, United Kingdom*

## Abstract

Production cross-sections of prompt charm mesons are measured with data from  $pp$  collisions at the LHC at a centre-of-mass energy of  $\sqrt{s} = 5 \text{ TeV}$ . The data sample corresponds to an integrated luminosity of  $(8.60 \pm 0.33) \text{ pb}^{-1}$  collected by the LHCb experiment. The production cross-sections of  $D^0$ ,  $D^+$ ,  $D_s^+$ , and  $D^{*+}$  mesons are measured in bins of charm meson transverse momentum,  $p_T$ , and rapidity,  $y$ , and cover the range  $0 < p_T < 8 \text{ GeV}$  and  $2 < y < 4.5$ . The inclusive cross-sections for the four mesons, including charge conjugation, within the range of  $1 < p_T < 8 \text{ GeV}$  are found to be

$$\begin{aligned}\sigma(pp \rightarrow D^0 X) &= 1190 \pm 3 \pm 64 \mu\text{b} \\ \sigma(pp \rightarrow D^+ X) &= 456 \pm 3 \pm 34 \mu\text{b} \\ \sigma(pp \rightarrow D_s^+ X) &= 195 \pm 4 \pm 19 \mu\text{b} \\ \sigma(pp \rightarrow D^{*+} X) &= 467 \pm 6 \pm 40 \mu\text{b}\end{aligned}$$

where the uncertainties are due to statistical and systematic uncertainties, respectively.



# Contents

<b>1</b>	<b>Introduction</b>	<b>1</b>
1.1	Analysis overview . . . . .	1
1.2	Theory . . . . .	2
1.3	Propagation of uncertainties . . . . .	2
<b>2</b>	<b>Data</b>	<b>5</b>
2.1	Trigger strategy . . . . .	5
2.2	Data flow . . . . .	6
2.3	Simulation . . . . .	7
2.3.1	Truth matching . . . . .	8
2.3.2	Generator MC with no acceptance requirements . . . . .	9
2.4	Crossing angle correction . . . . .	9
<b>3</b>	<b>Selection</b>	<b>11</b>
3.1	Discriminating variables . . . . .	11
3.2	Trigger . . . . .	12
3.2.1	HLT1 reconstruction and selection . . . . .	12
3.2.2	HLT2 reconstruction and selection . . . . .	13
3.3	Offline processing . . . . .	13
<b>4</b>	<b>Efficiencies</b>	<b>18</b>
4.1	LHCb acceptance . . . . .	18
4.2	Reconstruction . . . . .	20
4.2.1	Tracking efficiency correction . . . . .	20
4.2.2	Monte Carlo truth matching inefficiency . . . . .	22
4.3	Trigger . . . . .	23
4.4	Offline selection . . . . .	24
4.5	Combination of efficiencies . . . . .	24
4.6	Propagation of uncertainties . . . . .	25
4.7	Particle identification . . . . .	25
4.7.1	Overview . . . . .	26
4.7.2	Binning of the calibration sample . . . . .	27
4.7.3	Results . . . . .	28
4.8	Signal window efficiency . . . . .	31

<b>5 Yield extraction</b>	<b>33</b>
5.1 Definition of species . . . . .	33
5.2 Overview . . . . .	33
5.3 Mass fit . . . . .	34
5.4 $\ln \chi^2_{\text{IP}}$ fit . . . . .	34
5.5 Mode-specific details . . . . .	36
5.6 Fit results . . . . .	42
<b>6 Results</b>	<b>57</b>
6.1 Integrated cross-sections . . . . .	57
6.2 Total $c\bar{c}$ cross-section . . . . .	57
6.3 Relative cross-sections . . . . .	59
6.3.1 Relative to 13 TeV measurements . . . . .	59
6.3.2 Relative between charm mesons . . . . .	61
<b>7 Systematic uncertainties</b>	<b>83</b>
7.1 Finite Monte Carlo sample size . . . . .	83
7.2 Monte Carlo modelling . . . . .	84
7.3 Monte Carlo truth matching . . . . .	85
7.4 PID calibration . . . . .	86
7.5 Luminosity . . . . .	87
7.6 Tracking efficiency correction . . . . .	88
7.7 Branching fractions . . . . .	89
7.8 Fit model . . . . .	90
7.9 Signal window . . . . .	90
7.10 Correlations and summary . . . . .	91
7.11 Correlations between $\sqrt{s} = 5$ TeV and 13 TeV measurements . . . . .	92
<b>8 Conclusion</b>	<b>94</b>
<b>A Comparison of upper and lower sidebands</b>	<b>95</b>
<b>B Per-bin <math>\ln \chi^2_{\text{IP}}</math> fits</b>	<b>97</b>
B.1 $D^0 \rightarrow K^- \pi^+$ . . . . .	97
B.2 $D^+ \rightarrow K^- \pi^+ \pi^+$ . . . . .	108
B.3 $D_s^+ \rightarrow \phi \pi^+$ . . . . .	118
B.4 $D^{*+} \rightarrow D^0 \pi^+$ with $D^0 \rightarrow K^- \pi^+$ . . . . .	128
<b>C Efficiency tables</b>	<b>137</b>

<b>D Systematics tables</b>	<b>147</b>
D.1 Statistical uncertainty . . . . .	147
D.2 Finite Monte Carlo sample size . . . . .	149
D.3 PID calibration . . . . .	151
D.4 Tracking efficiency correction . . . . .	155
D.5 Fit model . . . . .	157
<b>E MC and data comparison after full selection</b>	<b>159</b>
<b>References</b>	<b>164</b>

# List of Figures

1.1	Illustration posterior distribution . . . . .	3
3.1	$K^-K^-$ window used in the CLEO $D_s^+ \rightarrow \phi\pi^+$ branching fraction . . . . .	17
4.1	Tracking correction table . . . . .	21
4.2	$D^0 \rightarrow K^-\pi^+$ mass distributions for different background categories . . . . .	23
4.3	Example of PID per bin fit . . . . .	29
4.4	Stat. correlation between $K^\pm$ and $\pi^\pm$ calib. tables . . . . .	30
5.1	Signal window and sideband definitions for $D^0 \rightarrow K^-\pi^+$ . . . . .	37
5.2	Signal window and sideband definitions for $D^+ \rightarrow K^-\pi^+\pi^+$ . . . . .	38
5.3	Signal window and sideband definitions for $D_s^+ \rightarrow \phi\pi^+$ . . . . .	39
5.4	Signal window and sideband definitions for $D^{*+} \rightarrow D^0\pi^+$ with $D^0 \rightarrow K^-\pi^+$ . . . . .	40
5.5	Integrated $\ln \chi_{\text{IP}}^2$ prefits for $D^0 \rightarrow K^-\pi^+$ . . . . .	43
5.6	Integrated $\ln \chi_{\text{IP}}^2$ prefits for $D^+ \rightarrow K^-\pi^+\pi^+$ . . . . .	43
5.7	Integrated $\ln \chi_{\text{IP}}^2$ prefits for $D_s^+ \rightarrow \phi\pi^+$ . . . . .	44
5.8	Integrated $\ln \chi_{\text{IP}}^2$ prefits for $D^{*+} \rightarrow D^0\pi^+$ with $D^0 \rightarrow K^-\pi^+$ . . . . .	44
5.9	Integrated mass fit for $D^0 \rightarrow K^-\pi^+$ . . . . .	45
5.10	Integrated $\ln \chi_{\text{IP}}^2$ fit for $D^0 \rightarrow K^-\pi^+$ . . . . .	46
5.11	Integrated mass fit for $D^+ \rightarrow K^-\pi^+\pi^+$ . . . . .	47
5.12	Integrated $\ln \chi_{\text{IP}}^2$ fit for $D^+ \rightarrow K^-\pi^+\pi^+$ . . . . .	48
5.13	Integrated mass fit for $D_s^+ \rightarrow \phi\pi^+$ . . . . .	49
5.14	Integrated $\ln \chi_{\text{IP}}^2$ fit for $D_s^+ \rightarrow \phi\pi^+$ . . . . .	50
5.15	Integrated fit to $D^0$ mass for $D^{*+} \rightarrow D^0\pi^+$ with $D^0 \rightarrow K^-\pi^+$ . . . . .	51
5.16	Integrated $\delta m$ fit for $D^{*+} \rightarrow D^0\pi^+$ with $D^0 \rightarrow K^-\pi^+$ . . . . .	52
5.17	Integrated $\ln \chi_{\text{IP}}^2$ fit for $D^{*+} \rightarrow D^0\pi^+$ with $D^0 \rightarrow K^-\pi^+$ . . . . .	53
6.1	Integrated cross-section measurements (black diamonds) as well as their average (black circle and blue band) shown (left) based on the $D^0$ and $D^+$ cross-sections and theory predictions (red squares) [1, 2] for $0 < p_T < 8 \text{ GeV}/c$ and (right) for all four mesons for $1 < p_T < 8 \text{ GeV}/c$ . The “absolute” predictions are based on calculations of the 13 TeV cross-section, while the “scaled” predictions are based on calculations of the 13 to 7 TeV ratio multiplied with the LHCb measurement. . . . .	60
6.2	Differential cross-sections for $D^0$ . . . . .	66
6.3	Differential cross-sections for $D^+$ . . . . .	66
6.4	Differential cross-sections for $D_s^+$ . . . . .	67
6.5	Differential cross-sections for $D^{*+}$ . . . . .	67
6.6	Cross-sections relative between 13 TeV and 5 TeV for $D^0$ . . . . .	68

6.7	Cross-sections relative between 13 TeV and 5 TeV for $D^+$	69
6.8	Cross-sections relative between 13 TeV and 5 TeV for $D_s^+$	70
6.9	Cross-sections relative between 13 TeV and 5 TeV for $D^{*+}$	71
6.10	Ratios of cross-section measurements of (top) $D^+$ , (middle) $D_s^+$ , and (bottom) $D^{*+}$ mesons with respect to the $D^0$ cross-sections. The blue bands indicate the corresponding ratios of fragmentation fractions. The ratios are given as a function of $p_T$ and different symbols indicate different ranges in $y$ .	75
6.11	Ratios of cross-section measurements of (top) $D^{*+}$ , and (middle) $D_s^+$ mesons with respect to $D^+$ cross-sections, and (bottom) $D_s^+$ over $D^{*+}$ mesons. The blue bands indicate the corresponding ratios of fragmentation fractions. The ratios are given as a function of $p_T$ and different symbols indicate different ranges in $y$ .	76
A.1	Sideband comparison $D^0 \rightarrow K^- \pi^+$	95
A.2	Sideband comparison $D^+ \rightarrow K^- \pi^+ \pi^+$	96
A.3	Sideband comparison $D_s^+ \rightarrow \phi \pi^+$ and $D^{*+} \rightarrow D^0 \pi^+$ with $D^0 \rightarrow K^- \pi^+$	96
B.1	$\ln \chi_{\text{IP}}^2$ fits in $0 \leq p_T < 1 \text{ GeV}$ for $D^0 \rightarrow K^- \pi^+$	98
B.2	$\ln \chi_{\text{IP}}^2$ fits in $1 \leq p_T < 2 \text{ GeV}$ for $D^0 \rightarrow K^- \pi^+$	99
B.3	$\ln \chi_{\text{IP}}^2$ fits in $2 \leq p_T < 3 \text{ GeV}$ for $D^0 \rightarrow K^- \pi^+$	100
B.4	$\ln \chi_{\text{IP}}^2$ fits in $3 \leq p_T < 4 \text{ GeV}$ for $D^0 \rightarrow K^- \pi^+$	101
B.5	$\ln \chi_{\text{IP}}^2$ fits in $4 \leq p_T < 5 \text{ GeV}$ for $D^0 \rightarrow K^- \pi^+$	102
B.6	$\ln \chi_{\text{IP}}^2$ fits in $5 \leq p_T < 6 \text{ GeV}$ for $D^0 \rightarrow K^- \pi^+$	103
B.7	$\ln \chi_{\text{IP}}^2$ fits in $6 \leq p_T < 7 \text{ GeV}$ for $D^0 \rightarrow K^- \pi^+$	104
B.8	$\ln \chi_{\text{IP}}^2$ fits in $7 \leq p_T < 8 \text{ GeV}$ for $D^0 \rightarrow K^- \pi^+$	105
B.9	$\ln \chi_{\text{IP}}^2$ fits in $8 \leq p_T < 9 \text{ GeV}$ for $D^0 \rightarrow K^- \pi^+$	106
B.10	$\ln \chi_{\text{IP}}^2$ fits in $9 \leq p_T < 10 \text{ GeV}$ for $D^0 \rightarrow K^- \pi^+$	107
B.11	$\ln \chi_{\text{IP}}^2$ fits in $0 \leq p_T < 1 \text{ GeV}$ for $D^+ \rightarrow K^- \pi^+ \pi^+$	108
B.12	$\ln \chi_{\text{IP}}^2$ fits in $1 \leq p_T < 2 \text{ GeV}$ for $D^+ \rightarrow K^- \pi^+ \pi^+$	109
B.13	$\ln \chi_{\text{IP}}^2$ fits in $2 \leq p_T < 3 \text{ GeV}$ for $D^+ \rightarrow K^- \pi^+ \pi^+$	110
B.14	$\ln \chi_{\text{IP}}^2$ fits in $3 \leq p_T < 4 \text{ GeV}$ for $D^+ \rightarrow K^- \pi^+ \pi^+$	111
B.15	$\ln \chi_{\text{IP}}^2$ fits in $4 \leq p_T < 5 \text{ GeV}$ for $D^+ \rightarrow K^- \pi^+ \pi^+$	112
B.16	$\ln \chi_{\text{IP}}^2$ fits in $5 \leq p_T < 6 \text{ GeV}$ for $D^+ \rightarrow K^- \pi^+ \pi^+$	113
B.17	$\ln \chi_{\text{IP}}^2$ fits in $6 \leq p_T < 7 \text{ GeV}$ for $D^+ \rightarrow K^- \pi^+ \pi^+$	114
B.18	$\ln \chi_{\text{IP}}^2$ fits in $7 \leq p_T < 8 \text{ GeV}$ for $D^+ \rightarrow K^- \pi^+ \pi^+$	115
B.19	$\ln \chi_{\text{IP}}^2$ fits in $8 \leq p_T < 9 \text{ GeV}$ for $D^+ \rightarrow K^- \pi^+ \pi^+$	116
B.20	$\ln \chi_{\text{IP}}^2$ fits in $9 \leq p_T < 10 \text{ GeV}$ for $D^+ \rightarrow K^- \pi^+ \pi^+$	117
B.21	$\ln \chi_{\text{IP}}^2$ fits in $1 \leq p_T < 2 \text{ GeV}$ for $D_s^+ \rightarrow \phi \pi^+$	119
B.22	$\ln \chi_{\text{IP}}^2$ fits in $2 \leq p_T < 3 \text{ GeV}$ for $D_s^+ \rightarrow \phi \pi^+$	120

B.23	$\ln \chi^2_{\text{IP}}$ fits in $3 \leq p_T < 4 \text{ GeV}$ for $D_s^+ \rightarrow \phi\pi^+$	121
B.24	$\ln \chi^2_{\text{IP}}$ fits in $4 \leq p_T < 5 \text{ GeV}$ for $D_s^+ \rightarrow \phi\pi^+$	122
B.25	$\ln \chi^2_{\text{IP}}$ fits in $5 \leq p_T < 6 \text{ GeV}$ for $D_s^+ \rightarrow \phi\pi^+$	123
B.26	$\ln \chi^2_{\text{IP}}$ fits in $6 \leq p_T < 7 \text{ GeV}$ for $D_s^+ \rightarrow \phi\pi^+$	124
B.27	$\ln \chi^2_{\text{IP}}$ fits in $7 \leq p_T < 8 \text{ GeV}$ for $D_s^+ \rightarrow \phi\pi^+$	125
B.28	$\ln \chi^2_{\text{IP}}$ fits in $8 \leq p_T < 9 \text{ GeV}$ for $D_s^+ \rightarrow \phi\pi^+$	126
B.29	$\ln \chi^2_{\text{IP}}$ fits in $9 \leq p_T < 10 \text{ GeV}$ for $D_s^+ \rightarrow \phi\pi^+$	127
B.30	$\ln \chi^2_{\text{IP}}$ fits in $1 \leq p_T < 2 \text{ GeV}$ for $D^{*+} \rightarrow D^0\pi^+$ with $D^0 \rightarrow K^-\pi^+$	128
B.31	$\ln \chi^2_{\text{IP}}$ fits in $2 \leq p_T < 3 \text{ GeV}$ for $D^{*+} \rightarrow D^0\pi^+$ with $D^0 \rightarrow K^-\pi^+$	129
B.32	$\ln \chi^2_{\text{IP}}$ fits in $3 \leq p_T < 4 \text{ GeV}$ for $D^{*+} \rightarrow D^0\pi^+$ with $D^0 \rightarrow K^-\pi^+$	130
B.33	$\ln \chi^2_{\text{IP}}$ fits in $4 \leq p_T < 5 \text{ GeV}$ for $D^{*+} \rightarrow D^0\pi^+$ with $D^0 \rightarrow K^-\pi^+$	131
B.34	$\ln \chi^2_{\text{IP}}$ fits in $5 \leq p_T < 6 \text{ GeV}$ for $D^{*+} \rightarrow D^0\pi^+$ with $D^0 \rightarrow K^-\pi^+$	132
B.35	$\ln \chi^2_{\text{IP}}$ fits in $6 \leq p_T < 7 \text{ GeV}$ for $D^{*+} \rightarrow D^0\pi^+$ with $D^0 \rightarrow K^-\pi^+$	133
B.36	$\ln \chi^2_{\text{IP}}$ fits in $7 \leq p_T < 8 \text{ GeV}$ for $D^{*+} \rightarrow D^0\pi^+$ with $D^0 \rightarrow K^-\pi^+$	134
B.37	$\ln \chi^2_{\text{IP}}$ fits in $8 \leq p_T < 9 \text{ GeV}$ for $D^{*+} \rightarrow D^0\pi^+$ with $D^0 \rightarrow K^-\pi^+$	135
B.38	$\ln \chi^2_{\text{IP}}$ fits in $9 \leq p_T < 10 \text{ GeV}$ for $D^{*+} \rightarrow D^0\pi^+$ with $D^0 \rightarrow K^-\pi^+$	136
C.1	$D^+ \rightarrow K^-\pi^+\pi^+$ mass distributions for different background categories	140
C.2	$D^{*+} \rightarrow D^0\pi^+$ mass distributions for different background categories	141
E.1	MC-data comparison $D^0 \rightarrow K^-\pi^+$	160
E.2	MC-data comparison $D^+ \rightarrow K^-\pi^+\pi^+$	161
E.3	MC-data comparison $D_s^+ \rightarrow \phi\pi^+$	162
E.4	MC-data comparison $D^{*+} \rightarrow D^0\pi^+$ with $D^0 \rightarrow K^-\pi^+$	163

# List of Tables

2.1	List of fills and L0 rates.	6
2.2	List of event types simulated for each decay mode	8
3.1	HLT1 1Track selection	13
3.2	$D^0 \rightarrow K^-\pi^+$ HLT2 selection	14
3.3	$D^{*+}$ HLT2 selection	14
3.4	$D^+ \rightarrow h^-h^+h^+$ HLT2 selection	15
4.1	Acceptance efficiency $D^0 \rightarrow K^-\pi^+$	19
4.2	Tracking efficiency correction for $D^0 \rightarrow K^-\pi^+$ . Shown uncertainties are due to the size of the simulated sample.	22
4.3	Truth matching efficiencies	24
4.4	MC selection efficiency $D^0 \rightarrow K^-\pi^+$	25
4.5	Total PID selection efficiency for $D^0 \rightarrow K^-\pi^+$ in bins of $D^0 p_T$ and $y$ . Shown uncertainties are due to the size of the calibration sample, estimated by bootstrapping the calibration sample.	31
4.6	Signal window requirement efficiencies for $D^0 \rightarrow K^-\pi^+$	32
5.1	Prompt signal yields for $D^0 \rightarrow K^-\pi^+$	54
5.2	Prompt signal yields for $D^+ \rightarrow K^-\pi^+\pi^+$	55
5.3	Prompt signal yields for $D_s^+ \rightarrow \phi\pi^+$	55
5.4	Prompt signal yields for $D^{*+} \rightarrow D^0\pi^+$ with $D^0 \rightarrow K^-\pi^+$	56
6.1	Integrated charm hadron cross-sections	58
6.2	Charm hadron fragmentation fractions	58
6.3	Differential cross-sections for $D^0$	62
6.4	Differential cross-sections for $D^+$	63
6.5	Differential cross-sections for $D_s^+$	64
6.6	Differential cross-sections for $D^{*+}$	65
6.7	Relative cross-sections for $D^0 \rightarrow K^-\pi^+$	72
6.8	Relative cross-sections for $D^+ \rightarrow K^-\pi^+\pi^+$	73
6.9	Relative cross-sections for $D_s^+ \rightarrow \phi\pi^+$	74
6.10	Relative cross-sections for $D^{*+} \rightarrow D^0\pi^+$ with $D^0 \rightarrow K^-\pi^+$	74
6.11	The ratios of differential production cross-sections in $10^{-2}$ for prompt $D^+$ and $D^0$ mesons in bins of $(y, p_T)$ . The first uncertainty is statistical, and the second is the total systematic.	77
6.12	The ratios of differential production cross-sections in $10^{-2}$ for prompt $D_s^+$ and $D^0$ mesons in bins of $(y, p_T)$ . The first uncertainty is statistical, and the second is the total systematic.	78

6.13	The ratios of differential production cross-sections in $10^{-2}$ for prompt $D^{*+}$ and $D^0$ mesons in bins of $(y, p_T)$ . The first uncertainty is statistical, and the second is the total systematic. . . . .	79
6.14	The ratios of differential production cross-sections in $10^{-2}$ for prompt $D_s^+$ and $D^+$ mesons in bins of $(y, p_T)$ . The first uncertainty is statistical, and the second is the total systematic. . . . .	80
6.15	The ratios of differential production cross-sections in $10^{-2}$ for prompt $D^{*+}$ and $D^+$ mesons in bins of $(y, p_T)$ . The first uncertainty is statistical, and the second is the total systematic. . . . .	81
6.16	The ratios of differential production cross-sections in $10^{-2}$ for prompt $D_s^+$ and $D^{*+}$ mesons in bins of $(y, p_T)$ . The first uncertainty is statistical, and the second is the total systematic. . . . .	82
7.1	Relative statistical uncertainty for $D^0 \rightarrow K^- \pi^+$ . . . . .	83
7.2	Finite Monte Carlo sample size systematic for $D^0 \rightarrow K^- \pi^+$ . . . . .	84
7.3	Monte Carlo modelling systematic results . . . . .	85
7.4	Truth matching systematic for $D^0 \rightarrow K^- \pi^+$ . . . . .	86
7.5	Finite PID calibration sample size systematic for $D^0 \rightarrow K^- \pi^+$ . . . . .	87
7.6	PID binning scheme systematic for $D^0 \rightarrow K^- \pi^+$ . . . . .	88
7.7	Tracking efficiency correction systematic for $D^0 \rightarrow K^- \pi^+$ . . . . .	89
7.8	Branching ratios . . . . .	90
7.9	Fit model systematic for $D^0 \rightarrow K^- \pi^+$ . . . . .	91
7.10	Systematic uncertainties summary . . . . .	92
C.1	Acceptance efficiency $D^+ \rightarrow K^- \pi^+ \pi^+$ . . . . .	137
C.2	Acceptance efficiency $D_s^+ \rightarrow \phi \pi^+$ . . . . .	138
C.3	Acceptance efficiency $D^{*+} \rightarrow D^0 \pi^+, D^0 \rightarrow K^- \pi^+$ . . . . .	138
C.4	Tracking efficiency correction for $D^+ \rightarrow K^- \pi^+ \pi^+$ . Shown uncertainties are due to the size of the simulated sample. . . . .	139
C.5	Tracking efficiency correction for $D_s^+ \rightarrow \phi \pi^+$ . Shown uncertainties are due to the size of the simulated sample. . . . .	139
C.6	Tracking efficiency correction for $D^{*+} \rightarrow D^0 \pi^+$ with $D^0 \rightarrow K^- \pi^+$ . Shown uncertainties are due to the size of the simulated sample. . . . .	140
C.7	Total MC selection efficiency $D^+ \rightarrow K^- \pi^+ \pi^+$ . . . . .	142
C.8	Total MC selection efficiency $D_s^+ \rightarrow \phi \pi^+$ . . . . .	142
C.9	Total MC selection efficiency $D^{*+} \rightarrow D^0 \pi^+, D^0 \rightarrow K^- \pi^+$ . . . . .	143
C.10	Total PID selection efficiency for $D^+ \rightarrow K^- \pi^+ \pi^+$ in bins of $D^+ p_T$ and $y$ . Shown uncertainties are due to the size of the calibration sample, estimated by bootstrapping the calibration sample. . . . .	143

C.11 Total PID selection efficiency for $D_s^+ \rightarrow \phi\pi^+$ in bins of $D_s^+ p_T$ and $y$ . Shown uncertainties are due to the size of the calibration sample, estimated by bootstrapping the calibration sample. . . . .	144
C.12 Total PID selection efficiency for $D^{*+} \rightarrow D^0\pi^+$ , $D^0 \rightarrow K^-\pi^+$ in bins of $D^{*+} p_T$ and $y$ . Shown uncertainties are due to the size of the calibration sample, estimated by bootstrapping the calibration sample. . . . .	144
C.13 Signal window requirement efficiencies for $D^+ \rightarrow K^-\pi^+\pi^+$ . . . . .	145
C.14 Signal window requirement efficiencies for $D_s^+ \rightarrow \phi\pi^+$ . . . . .	145
C.15 Signal window requirement efficiencies for $D^{*+} \rightarrow D^0\pi^+$ with $D^0 \rightarrow K^-\pi^+$ . . . . .	146
D.1 Relative statistical uncertainty for $D^+ \rightarrow K^-\pi^+\pi^+$ . . . . .	147
D.2 Relative statistical uncertainty for $D_s^+ \rightarrow \phi\pi^+$ . . . . .	148
D.3 Relative statistical uncertainty for $D^{*+} \rightarrow D^0\pi^+$ with $D^0 \rightarrow K^-\pi^+$ . .	148
D.4 Finite Monte Carlo sample size systematic for $D^+ \rightarrow K^-\pi^+\pi^+$ . . . . .	149
D.5 Finite Monte Carlo sample size systematic for $D_s^+ \rightarrow \phi\pi^+$ . . . . .	150
D.6 Finite Monte Carlo sample size systematic for $D^{*+} \rightarrow D^0\pi^+$ with $D^0 \rightarrow K^-\pi^+$ . . . . .	150
D.7 Finite PID calibration sample size systematic for $D^+ \rightarrow K^-\pi^+\pi^+$ . .	151
D.8 Finite PID calibration sample size systematic for $D_s^+ \rightarrow \phi\pi^+$ . . . . .	152
D.9 Finite PID calibration sample size systematic for $D^{*+} \rightarrow D^0\pi^+$ with $D^0 \rightarrow K^-\pi^+$ . . . . .	152
D.10 PID binning scheme systematic for $D^+ \rightarrow K^-\pi^+\pi^+$ . . . . .	153
D.11 PID binning scheme systematic for $D_s^+ \rightarrow \phi\pi^+$ . . . . .	153
D.12 PID binning scheme systematic for $D^{*+} \rightarrow D^0\pi^+$ with $D^0 \rightarrow K^-\pi^+$ .	154
D.13 Tracking efficiency correction systematic for $D^+ \rightarrow K^-\pi^+\pi^+$ . . . . .	155
D.14 Tracking efficiency correction systematic for $D_s^+ \rightarrow \phi\pi^+$ . . . . .	156
D.15 Tracking efficiency correction systematic for $D^{*+} \rightarrow D^0\pi^+$ with $D^0 \rightarrow K^-\pi^+$ . . . . .	156
D.16 Fit model systematic for $D^+ \rightarrow K^-\pi^+\pi^+$ . . . . .	157
D.17 Fit model systematic for $D_s^+ \rightarrow \phi\pi^+$ . . . . .	158
D.18 Fit model systematic for $D^{*+} \rightarrow D^0\pi^+$ with $D^0 \rightarrow K^-\pi^+$ . . . . .	158

# 1 Introduction

Measurements of  $c\bar{c}$  and  $b\bar{b}$  cross sections test the predictions of quantum chromodynamics, and as the rapidity range available to LHCb is unique at the LHC, such measurements are complementary to those made by other experiments. In addition, charm cross section measurements are used as inputs to background estimations in atmospheric neutrino experiments [3], and to determine the parton distribution functions [4].

This analysis note documents the efforts to measure the double differential cross sections of various promptly produced open charm hadrons at a centre-of-mass energy of  $\sqrt{s} = 5 \text{ TeV}$ . The cross section is measured in bins of charm hadron transverse momentum  $p_T = \sqrt{p_x^2 + p_y^2}$  and rapidity  $y = 1/2 \ln(E + p_z)/(E - p_z)$ , as computed in the rest frame of the proton-proton collision.

A measurement of prompt open charm cross sections has been made using a dataset corresponding to an integrated luminosity of  $(15.0 \pm 0.5) \text{ nb}^{-1}$  collected in 2010 at a centre-of-mass energy of  $\sqrt{s} = 7 \text{ TeV}$  [5], and also at 13 TeV with  $(4.98 \pm 0.19) \text{ pb}^{-1}$  of integrated luminosity collected in 2015 [6]. This analysis follows a near-identical methodology to the latter, which is thoroughly documented in the corresponding analysis note [7].

The open charm hadrons used for this measurement are  $D^0$ ,  $D^+$ ,  $D_s^+$ , and  $D^{*+}$ . These are reconstructed in the following final states:  $D^0 \rightarrow K^-\pi^+$ ,  $D^+ \rightarrow K^-\pi^+\pi^+$ ,  $D_s^+ \rightarrow \phi\pi^+$ , and  $D^{*+} \rightarrow D^0\pi^+$  with  $D^0 \rightarrow K^-\pi^+$ . Unless otherwise stated, the addition of the charge conjugate process is implied throughout this note.

As charm hadrons can be produced both promptly from the  $pp$  collision and in the decays of  $B$  hadrons, we statistically separate the two contributions through extended maximum likelihood fits to the charm hadron  $\chi^2_{\text{IP}}$  distribution in order to measure the prompt yields. Aside from the explicit measurement of the  $D^{*+}$  production cross-section, no attempt is made to distinguish prompt hadrons produced from prompt excited charm resonances from those produced directly in the  $pp$  collision.

## 1.1 Analysis overview

The analysis will reconstruct and select the various charm decays, measure the size of the prompt signal component  $N$ , and then compute the efficiency  $\epsilon$  of each step, from the geometrical limitations imposed by the LHCb detector acceptance, to the selection cuts. Combined with a measurement of the collected integrated luminosity  $\mathcal{L}$  and the branching fraction  $\mathcal{B}$  of the decay mode  $f$  in question, the cross section for

35 a single charm hadron  $H_c$  in a given  $p_T$ - $y$  bin  $i$  can be computed as

$$\sigma_i(H_c) = \frac{N_i(H_c \rightarrow f)}{\epsilon_i(H_c \rightarrow f) \cdot \mathcal{B}(H_c \rightarrow f) \cdot \mathcal{L}}. \quad (1.1)$$

36 Double differential cross sections can then be determined using the width of the bin  
37 in  $p_T$ ,  $\Delta p_T$ , and the width of the bin in rapidity,  $\Delta y$ , in which the yield and efficiency  
38 measurements were made

$$\left. \frac{d^2\sigma(H_c)}{dp_T dy} \right|_i = \frac{\sigma_i(H_c)}{\Delta p_T \Delta y}. \quad (1.2)$$

39 Throughout this note, bin boundaries are given using the ISO 31-11 standard, where,  
40 for example, the half-open interval  $a \leq x < b$  is denoted  $[a, b[$  [8].

41 We intend to measure the absolute cross sections of  $D^0$ ,  $D^+$ ,  $D_s^+$ , and  $D_s^+$  hadrons  
42 in bins of width 1 GeV in transverse momentum, for  $p_T \in [0, 8]$  GeV, and in bins of  
43 width 0.5 in rapidity, for  $y \in [2.0, 4.5[$ .

44 In addition, we intend to measure the  $\sqrt{s} = 5$  TeV cross-sections relative between  
45 modes, such as  $\sigma(D^0)/\sigma(D^+)$ , and relative between bins, where every measurement  
46 is normalised to a single ‘central’ bin. The motivation for making these additional  
47 measurements also comes from the theory community.

## 48 1.2 Theory

49 In the course of this analysis, we have been in contact with three groups of theorists  
50 who provided predictions for the production cross-sections that we measure: Cacciari  
51 et al. (FONLL)[2], Gauld et al. (POWHEG+NNPDF3.0L)[1], and Spiesberger et  
52 al. (GMVFNS)[9]. (In parentheses are nicknames by which we will refer to the  
53 sets of predictions in the following discussion.) Two of these groups, Cacciari et  
54 al. and Spiesberger et al., previously provided the predictions used in the 7 TeV  
55 measurements [5, 10], and predictions from all three groups were used for comparison  
56 with the 13 TeV measurements [6, 7]. The same set of predictions has been provided  
57 for the 5 TeV measurement as well, using the same calculations, and a description  
58 can be found in the 13 TeV analysis note.

## 59 1.3 Propagation of uncertainties

60 When computing the uncertainty on a function  $f(a)$ , the assumptions of linear error  
61 propagation may not hold. In this analysis, the uncertainties on the quantities in the  
62 denominator of Equation 1.1 can be large in some  $p_T$ - $y$  bins, thereby making a linear  
63 approximation of  $\sigma_i$  insufficient.

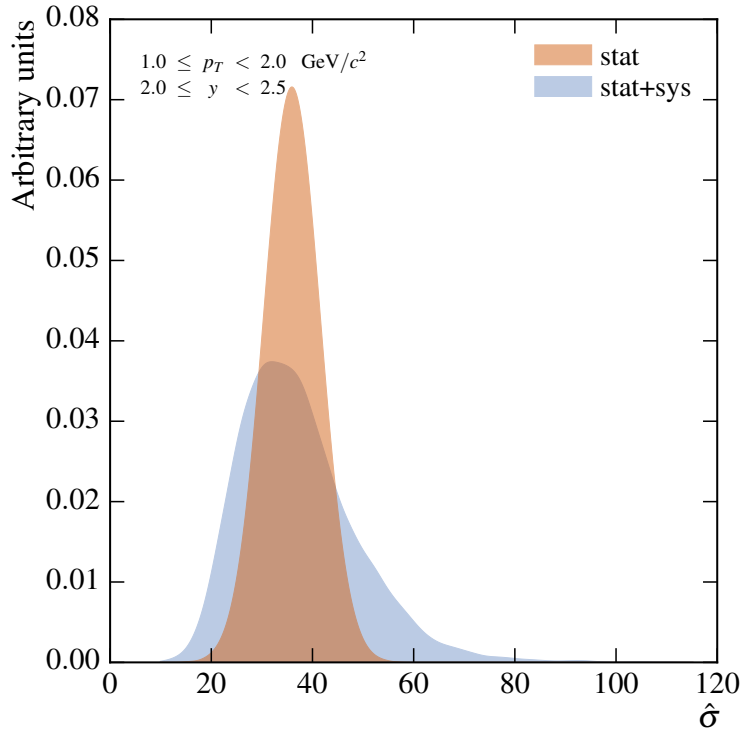


*Figure 1.1: Distribution of the posterior probability for one  $p_T$ - $y$  bin in the differential  $D_s^+ \rightarrow \phi\pi^+$  measurement, illustrating the asymmetric distribution due to large uncertainties in the denominator.*

Instead of using this analytical approach, we instead use a Monte Carlo error propagation technique. With this, a large set of numbers  $S$  is sampled from a chosen model  $M$ , and operations are performed directly on the ensemble by mapping the operation on to the elements on  $S$ . Statistics such as the mean and standard deviation can then be computed on the resulting set.

Unless stated otherwise, each quantity to which an uncertainty is assigned is modelled as a normal distribution,  $N(\mu, \sigma)$ , whose mean  $\mu$  is the value found by the appropriate procedure, and whose standard deviation  $\sigma$  is taken as the uncertainty on that value. In the case of the prompt signal yield, for example, the mean of the normal distribution will be the fitted value, and the width will be the uncertainty returned by the fitter. We generate ten thousand numbers from each model  $M$  per ensemble. An illustration for the obtained posterior distributions is given in Figure 1.1.

Having outlined the general analysis, Section 1.2 shall describe the theoretical models available for comparison with the data. The data itself will then be discussed in

78 Section 2, including details on the running conditions of the LHC, the trigger strategy,  
79 and which simulated samples are used. The selection applied to the candidates will  
80 follow in Section 3, including a brief description of how the charm hadron candidates  
81 are reconstructed. In Section 4 the efficiencies of each reconstruction and selection  
82 stage will be described and given, and the fitting framework that counts the yields of  
83 the various signal and background components after the full selection will be shown  
84 in Section 5. The sources of systematic uncertainty in the analysis will be enumerated  
85 and evaluated in Section 7. Finally, the results of the measurement will be given in  
86 Section 6.

## 87 2 Data

88 The dataset used for the analysis corresponds to an integrated luminosity of  $(8.60 \pm 0.33) \text{ pb}^{-1}$   
89 of proton-proton collisions at a centre of mass energy of  $\sqrt{s} = 5 \text{ TeV}$ , collected in  
90 November 2015 with the magnet in the ‘down’ polarity. This analysis uses fills 4640,  
91 4643, and 4647.

### 92 2.1 Trigger strategy

93 The trigger chain is nearly identical to that used in the 13 TeV analysis, of which a de-  
94 scription follows. The only difference is that, for this dataset, the `Hlt1TrackAllL0Decision`  
95 HLT1 line also allowed decisions from `L0Muon`, whereas for the 13 TeV measurement  
96 only the `LONoBias` decision was required at L0. Events where only the `L0Muon` fired  
97 are filtered out for this analysis, as they mostly contain signal decays that originate  
98 from  $B$  hadrons.

99 The LHCb Run 2 trigger consists of three stages: a hardware (L0) trigger which can  
100 use information from the calorimeter, muon, and pile-up systems; a software (HLT1)  
101 trigger which can use information from all sub-detectors and processes all events  
102 selected by L0 in real-time; and a software (HLT2) trigger which runs asynchronously  
103 on events selected by HLT1 and performs a final selection using the full offline-quality  
104 alignment, calibration, and detector reconstruction. The L0 trigger is also able to  
105 deliver a fixed rate of randomly selected events, a fact this analysis will exploit.

106 The trigger strategy for this analysis is defined within these three stages:

- 107 1. L0: A ‘NOBIAS’ trigger which fires at a determined rate on beam-beam bunch  
108 crossings;
- 109 2. HLT1: A single-track trigger which selects L0 events based on track transverse  
110 momentum; displacement from the primary proton-proton interaction region,  
111 and track quality; and
- 112 3. HLT2: A set of exclusive trigger lines which fully reconstruct each type of signal  
113 process being analyzed.

114 Each level of the trigger requires the previous one to have fired: the HLT1 single-track  
115 line only runs on events selected by the NOBIAS L0 trigger; and the HLT2 lines require  
116 that the single track which caused HLT1 to fire is part of the signal candidate which  
117 causes HLT2 to fire.

118 The specific selection criteria for the HLT lines are described in [3.2](#). For the L0  
119 trigger, the event rate was set to 300 kHz to minimize dead-time, which depends on

*Table 2.1: List of fills used in analysis, the HLT TCK used in the fill, the integrated luminosity (“lumi.”) collected in the fill, the number of colliding bunches at LHCb  $N_{\text{Coll. bunches}}$  during the fill, the L0 NOBIAS rate during the fill, and the corresponding effective L0 efficiency (“eff.”). (As of 14<sup>th</sup> June 2016, the luminosity calibration for this dataset is not available, and so the luminosity reported in this note is incorrect.)*

Fill	Runs	HLT TCK	Lumi. collected	$N_{\text{Coll. bunches}}$	L0 NOBIAS rate	L0 NOBIAS eff.
4640	168171–168196	0x0115014E	(1.80 ± 0.07) pb <sup>-1</sup>	1248	300 kHz	2.138 %
4643	168233–168261	0x0115014E	(4.49 ± 0.17) pb <sup>-1</sup>	1486	300 kHz	1.795 %
4647	168325–168350	0x0115014E	(2.31 ± 0.09) pb <sup>-1</sup>	1486	300 kHz	1.795 %

120 the LHC fill structure. The known LHC fill structure determines the total number of  
 121 beam-beam crossings (the number of colliding bunches)  $N_{\text{Coll. bunches}}$ , which is then  
 122 combined with the NOBIAS rate  $R_{\text{NOBIAS}}$  to give the effective efficiency of the L0 trigger  
 123  $\epsilon_{\text{L0}}$  for a given fill

$$\epsilon_{\text{L0}} = \frac{R_{\text{NOBIAS}}}{N_{\text{Coll. bunches}} \nu_{LHC}}, \quad (2.1)$$

124 where  $\nu_{LHC}$  is the bunch revolution frequency, taken to be 11.246 kHz. The overall  
 125 efficiency of the L0 trigger is then determined as the luminosity-weighted average of  
 126 the efficiencies for the individual fills

$$\bar{\epsilon}_{\text{L0}} = \frac{\sum_{\text{Fills}} \epsilon_{\text{L0},i} \mathcal{L}_i}{\sum_{\text{Fills}} \mathcal{L}_i}. \quad (2.2)$$

127 This information is summarised in Table 2.1, which can be used to compute the  
 128 effective L0 efficiency as  $\bar{\epsilon}_{\text{L0}} = 1.86\%$ , given the total collected luminosity of  
 129  $\sum_{\text{Fills}} \mathcal{L}_i = (8.60 \pm 0.33) \text{ pb}^{-1}$ . The effective luminosity used in this measurement is  
 130 then

$$\mathcal{L}_{\text{eff.}} = \bar{\epsilon}_{\text{L0}} \cdot \sum_{\text{Fills}} \mathcal{L}_i = (161 \pm 6) \text{ nb}^{-1}. \quad (2.3)$$

## 131 2.2 Data flow

132 Events containing candidates selected by any of the exclusive HLT2 lines are saved to  
 133 the ‘Turbo’ stream, along with the selection reports of the HLT2 candidates that fired  
 134 the lines. The raw files are processed with DAVINCI v38r0 and TESLA v2r0, which  
 135 recreates the HLT2 candidates from the selection reports as objects consumable by  
 136 the DecayTreeTuple algorithm. Using TESLA is considerably quicker than running

137 BRUNEL, as no further reconstruction is needed, and is simpler to analyse as any  
138 differences between the HLT2 and offline reconstruction are irrelevant (although no  
139 such differences are expected to exist in Run 2). This analysis uses candidates from  
140 the Turbo stream exclusively, using HLT-level information rather than quantities  
141 computed by Brunel.

142 The HLT2 candidates from the Turbo stream are then made into ROOT ntuples  
143 with DAVINCI v38r0.

## 144 2.3 Simulation

145 Monte Carlo (MC) events are generated for each decay mode used in the analysis.  
146 The event types used for each mode, the corresponding decay file nicknames, and the  
147 number of generated events saved to disk are given in Table 2.2.

148 The events are generated with PYTHIA 8 and GAUSS v49r1, with the conditions  
149 set to mimic the 25 ns bunch spacing used during the data taking, with an average  
150 number of  $pp$  interactions per bunch crossing  $\nu$  of 0.8, corresponding to average number  
151 of *visible*  $pp$  interactions per bunch crossing  $\mu$  of 0.53. Spillover, detector signals  
152 caused by particles from the previous or subsequent beam crossings, is simulated.  
153 Unstable particles are decayed by EVTGEN, and all particles are transported through  
154 a simulation of the detector geometry by GEANT4 and the detector response is  
155 recorded. The responses are converted into the format produced by the real detectors  
156 by BOOLE v30r1. The trigger software MOORE v24r3 is then run using the trigger  
157 configuration key (TCK) 0x4115014E, TESLA v2r0 is run to resurrect the HLT2  
158 candidates into a format readable by DAVINCI, and then the reconstruction is run  
159 using BRUNEL v48r2. The simulation version is Sim09a and the reconstruction version  
160 is Reco15a.

161 For all samples, one signal decay in each event is required to pass the DaughtersInLHCb  
162 generator-level cut. This requires that the polar angle  $\theta$  of all charged, stable decay  
163 products is within  $10 < \theta < 400$  mrad, and that all of these decay products are  
164 travelling in the same direction along the  $z$ -axis. These requirements are made on  
165 the true MC particles.

166 The output of the simulation is DSTs. These are processed with DAVINCI v41r0,  
167 where for each decay mode three ROOT ntuples are produced: one containing the  
168 decay tree of the generated signal particles; one containing the decay tree of the  
169 generated signal particles whose final state particles are fully reconstructed as long  
170 tracks, which can be matched with true signal MC particles of the correct identity,  
171 and that originate from the signal charm parent; and one containing the candidates  
172 passing the relevant HLT2 line. The second, truth-matched ntuple should contain a

*Table 2.2: List of event types simulated for each decay mode with number of generated events saved to disk. The  $D^{*+}$  samples are used for both the  $D^{*+}$  studies and the untagged  $D^0$  studies.*

Decay mode	Event type	Nickname	Number ( $\times 10^6$ )
$D^{*+} \rightarrow (D^0 \rightarrow K^-\pi^+)\pi^+$	27163003	Dst_D0pi,Kpi=DecProdCut	2.0
$D^+ \rightarrow K^-\pi^+\pi^+$	21263010	D+_K-pi+pi+=res,DecProdCut	2.0
$D_s^+ \rightarrow \phi\pi^+$	23263020	Ds+_K-K+pi+=res,DecProdCut	2.0

173 subset of the latter, but the ntuple containing HLT2 candidates may not necessarily  
174 contain a subset of the truth-matched.

175 The TCK used in the MC productions, 0x4115014E, is nearly identical to the  
176 one used during data-taking, and in particular contains the same particle identifi-  
177 cation (PID) requirements. This is problematic, as the PID variables are known to  
178 be poorly modelled in the MC, and so efficiency determinations are not possible.<sup>1</sup>  
179 To circumvent this problem, we use the truth-matched BRUNEL output, as the par-  
180 itiy between offline and online reconstruction should make the HLT2 reconstruction  
181 equivalent to that in BRUNEL.

### 182 2.3.1 Truth matching

183 Each charm hadron candidate, in all ntuples, is flagged as either secondary or prompt,  
184 based on whether the charm hadron was produced in a decay chain containing a  
185 heavier long-lived hadron. This check is done by `MCTupleToolPrompt`, which traverses  
186 up the full MC ancestry tree, marking the charm hadron as secondary if an ancestor  
187 has a lifetime greater than 0.1 fs.

188 The truth-matching is performed using the `mcMatch LOKI` functor, which compares  
189 the reconstructed candidate with an ASCII decay descriptor, and defines a positive  
190 match as one where the selected stable tracks are associated to true MC particles,  
191 where those particles originate from a common parent, and where the particle identities  
192 have been correctly assigned. An arbitrary number of additional photons originating  
193 from the signal particle are allowed to be missing in the truth-matched final state.  
194 This allows us to filter candidates based on their true identity.

195 The background category tool (`IBackgroundCategory`) is used to classify the  
196 output of the trigger, which is not required to pass an `mcMatch` requirement. We

---

<sup>1</sup>One could perform relative PID efficiency studies, rather than the absolute measurements described in Section 4.7, but this would require PID calibration MC, which is not available at the time of this writing.

197 define a ‘true signal decay’ as one with a background category value of either zero or  
198 ten. These values correspond to:

- 199 **0** All final state Particle objects in the signal candidate decay chain are associated  
200 to an **MCParticle** with the same particle ID, all associated **MCParticles** have  
201 the same top-level (excluding quarks) **MCParticle** parent, and the top-level  
202 **MCParticle** parent has same particle ID as signal candidate **Particle**; and
- 203 **10** Same as 0 but one or more intermediate resonances (*e.g.* the  $\phi$  in  $D_s^+ \rightarrow \phi\pi^+$ )  
204 are present in the **MCParticle** chain but not present in the signal candidate  
205 **Particle** chain, or vice-versa.

206 Photons generated from **PHOTOS** are ignored when computing the background  
207 category value.

208 **2.3.2 Generator MC with no acceptance requirements**

209 In addition to the previously described MC samples, additional samples are also  
210 created that do not have any requirements imposed on them at the generator level  
211 (the **DaughtersInLHCb** cut described earlier). They are used to evaluate the efficiency  
212 of the generator requirements in  $p_T$ - $y$  bins, and are required as the information  
213 used to compute such efficiencies is not available in the standard samples (simulated  
214 samples that do not pass the generator requirements are discarded). These samples  
215 are not simulated through the detector; only the MC truth information is saved.

216 The samples are generated using the same configuration of Gauss as is used for  
217 the fully simulated samples, described above. Around 1.5 million events are simulated  
218 per decay mode.

219 **2.4 Crossing angle correction**

220 Due to the non-zero crossing angles of the two proton beams provided by the LHC,  
221 the  $pp$  collision frame is boosted with respect to the laboratory frame. As this  
222 measurement is made in bins of charm hadron transverse momentum and rapidity  
223 measured in the  $pp$  collision rest frame, a correction must be applied to the  $p_T$  and  $y$   
224 measured in the laboratory frame.

225 Two crossing angles are defined per beam:  $\theta_h$  is the angle made with the  $z$  axis in  
226 the horizontal  $xz$  plane, and  $\theta_v$  is the angle made with the  $z$  axis in the vertical  $yz$

227 plane. With  $\theta_h = 0$  and  $\theta_v = 0$  we have

$$p_{z+}^\mu = \begin{pmatrix} E_{\text{Beam}} \\ 0 \\ 0 \\ p_{\text{Beam}} \end{pmatrix} \quad \text{and} \quad p_{z-}^\mu = \begin{pmatrix} E_{\text{Beam}} \\ 0 \\ 0 \\ -p_{\text{Beam}} \end{pmatrix}, \quad (2.4)$$

228 where  $z\pm$  indicates the beam moves to increasing or decreasing  $z$ ,  $E_{\text{Beam}}$  is the  
229 nominal beam energy of  $\sqrt{s}/2 = 2.51 \text{ TeV}$ , and  $p_{\text{Beam}}$  is the beam momentum as  
230  $p_{\text{Beam}}^2 = E_{\text{Beam}}^2 - m_{\text{Proton}}^2$ . With non-zero crossing angles, the beam four-vectors  
231 become

$$\begin{aligned} p_{z+}^\mu &= \begin{pmatrix} E_{\text{Beam}} \\ p_{\text{Beam}} \sin \theta_{h,+} \\ p_{\text{Beam}} \sin \theta_{v,+} \\ p_{\text{Beam}} \sqrt{1 - \sin^2 \theta_{h,+} - \sin^2 \theta_{v,+}} \end{pmatrix} \quad \text{and} \\ p_{z-}^\mu &= \begin{pmatrix} E_{\text{Beam}} \\ -p_{\text{Beam}} \sin \theta_{h,-} \\ -p_{\text{Beam}} \sin \theta_{v,-} \\ -p_{\text{Beam}} \sqrt{1 - \sin^2 \theta_{h,-} - \sin^2 \theta_{v,-}} \end{pmatrix}, \end{aligned} \quad (2.5)$$

232 where  $\theta_{h,\pm}$  and  $\theta_{v,\pm}$  are defined to allow for asymmetrical crossing angles between the  
233 two beams. The centre-of-mass four vector  $p_{\text{CoM}}^\mu$  is then the sum of  $p_{z+}^\mu$  and  $p_{z-}^\mu$ .

234 Charm hadron candidates are boosted into the centre-of-mass rest frame, and the  
235 system is then rotated to make the boosted beam axes coincide with the laboratory  $z$   
236 axis. The transverse momentum and rapidity are then recomputed. Whenever charm  
237 hadron  $p_T$  or  $y$  are mentioned, it is the  $pp$  rest frame quantities that are used.

238 In the data sample used, the only non-zero crossing angle was in the  $xz$  plane  
239 and this was symmetric between the two beams. The crossing angle values were  
240  $\theta_{h,+} = \theta_{h,-} = 790 \mu\text{rad}$  and  $\theta_{v,+} = \theta_{v,-} = 0$ .

241 **3 Selection**

242 Most of the selection criteria in the analysis are applied the exclusive charm HLT2  
243 lines, with only a minimal number of additional criteria applied offline. This section  
244 shall begin by listing the variables used in the selection, and shall then describe the  
245 online trigger and offline selections.

246 **3.1 Discriminating variables**

247 We consider there to be three major differences between the different charm hadron  
248 decays we wish to select: the invariant mass of the charm hadron; its lifetime; and  
249 the topology of the decay (that is, how many particles are in the final state and if  
250 there is any decay substructure). These three properties broadly drive the selection  
251 differences between the modes.

252 For charm hadrons with higher masses, the search window in the invariant mass  
253 distribution will be centred on a higher value, and the transverse momentum available  
254 to the decay products will be higher for a given topology. A longer lifetime means a  
255 larger mean separation of the decay vertex from the production vertex, and larger  
256 child impact parameters with respect to the production vertex. Higher multiplicity  
257 decays, *i.e.* those with more particles in the final state, will have lower average child  
258 momenta and more combinatorial background.

259 Additional variables with power to discriminate between signal and background  
260 include the direction angle (or ‘DIRA’, the angle between the vector connecting the  
261 production and decay vertex and the charm hadron momentum vector), the distance  
262 of closest approach of the child tracks, and the quality of vertex fit. The impact  
263 parameter of the charm hadron is not used in the selection as its distribution is used  
264 to extract the prompt and secondary components of the signal yield, as described in  
265 Section 5.

266 The selections are first taken from the  $\sqrt{s} = 7 \text{ TeV}$  stripping selections, and are  
267 then tightened to reduce the trigger rate, using experience gained from selecting  
268 charm decays in Run 1 to tune the cut values. The selection for this  $\sqrt{s} = 5 \text{ TeV}$   
269 analysis are identical to those used for the 13 TeV analysis, which were tuned by hand  
270 before any 13 TeV data were available. The selections worked well, with the exception  
271 of a cut in the  $D_{(s)}^+$  lines that required that there was at least one track with a  $p_T$   
272 greater than 1000 MeV. This cut is very inefficient for  $D_{(s)}^+$  in the  $0 < p_T < 1000 \text{ MeV}$   
273 bin, but was not changed for this analysis due to trigger rate considerations (the  
274 lowest  $p_T$  bin has the highest fraction of combinatorial background, which this tight  
275 cut helps to suppress).

276 **3.2 Trigger**

277 As discussed in Section 2.1, the L0 trigger selects beam-beam crossings randomly,  
278 and so its efficiency for each fill is a function of the selection rate and the LHC filling  
279 scheme. Events selected by the L0 trigger are further selected by the HLT based on  
280 reconstructed information from the tracking and RICH sub-detectors.

281 The HLT selection is split into two parts. The first, HLT1, selects events containing  
282 a single, high transverse momentum, good quality track which is displaced from the  
283 primary proton-proton interaction vertex. The second, HLT2, reconstructs and fully  
284 selects the relevant signal candidate. In addition to documenting the selection criteria  
285 used by these triggers, this section will also briefly recap the detector reconstruction  
286 strategy used in the HLT. The efficiencies of these selections are documented in  
287 Section 4.3.

288 **3.2.1 HLT1 reconstruction and selection**

289 The HLT1 trigger stage has to process the full output rate of the L0 trigger and so  
290 does not have time to perform the full offline event reconstruction. The performed  
291 reconstruction relevant to this analysis is:

- 292 1. The full offline charged particle (track) reconstruction inside the VELO sub-  
293 detector, including the Kalman fitting of reconstructed track trajectories (which  
294 assumes a track  $p_T$  of 400 MeV);
- 295 2. The full offline reconstruction of proton-proton collision vertices (primary  
296 vertices) based exclusively on the reconstructed VELO tracks, regardless of  
297 whether they are later promoted to long tracks; and
- 298 3. The reconstruction and Kalman fit of all VELO tracks in the TT and downstream  
299 (IT, OT) tracking detectors. VELO tracks are first extrapolated to the TT, and  
300 if at least two matching hits are found they are further extrapolated through  
301 the magnetic field within a search window restricted to a minimum transverse  
302 momentum of 800 MeV.

303 Because only tracks with a transverse momentum above 800 MeV are fully recon-  
304 structed, it would be inefficient to try and fully reconstruct the signal decays at  
305 this stage. Instead, a single track is searched for which meets the criteria given in  
306 Table 3.1. The presence of such a track is sufficient to identify the presence of a  
307 heavy flavour (charm or beauty) hadron decay in the event, and to reduce the rate of  
308 NOBIAS L0 triggers by approximately a factor of 6.5. A further efficient selection of

*Table 3.1: Requirements made on the track that fires the HLT1 `1Track` trigger line.*

Particle	Variable	Cut value	LoKI functor
Any track	$p_T$	$> 800 \text{ MeV}$	<code>PT</code>
	$p$	$> 3 \text{ GeV}$	<code>P</code>
	Track $\chi^2$	$< 3$	<code>N/A</code>
	$\chi^2_{\text{IP}}$	$> 10$	<code>BPVIPCHI2</code>
	VELO hits	$> 9$	<code>TrIDC('isVelo')</code>

309 those charm hadron decays which are of interest to this analysis, however, requires a  
310 more complete detector reconstruction.

### 311 3.2.2 HLT2 reconstruction and selection

312 The HLT2 trigger stage processes events selected by HLT1. It runs asynchronously,  
313 processing events not only during LHC fills but also during the inter-fill gaps, by  
314 using hard disks located in the HLT computing cluster nodes to buffer events. This  
315 leads to an increase in the effective processing power available to HLT2 of roughly a  
316 factor of two to three, and allows it to perform the full offline detector reconstruction.  
317 In addition, the asynchronous nature of HLT2 processing allows the detector to be  
318 aligned and calibrated in real-time before HLT2 runs. Thanks to these factors, the  
319 reconstruction in HLT2 should be identical to that offline.

320 The following trigger lines are used in the analysis:

- 321 A trigger line which selects  $D^0 \rightarrow K^-\pi^+$  decay candidates;
- 322 A trigger line which adds a charged pion to the  $D^0 \rightarrow K^-\pi^+$  candidates to  
323 select  $D^{*+} \rightarrow D^0\pi^+$  candidates; and
- 324 A set of trigger lines which select the charged, three-body  $D^+ \rightarrow K^-\pi^+\pi^+$  and  
325  $D_s^+ \rightarrow K^-K^+\pi^+$  decay candidates, one line per mode.

326 The specific selection criteria are given in Tables 3.2, 3.3, and 3.4.

## 327 3.3 Offline processing

328 Further offline requirements are imposed on the candidates passing the respective  
329 HLT2 lines. All final state particles which have PID cuts applied to them are required  
330 to be within  $3 \leq p < 100 \text{ GeV}$  and  $2 \leq \eta < 5$ , due to the constraints of the PID

Table 3.2: Selection requirements made in the  $D^0 \rightarrow K^-\pi^+$  HLT2 trigger line. The track  $\chi^2$  criterion is applied in the reconstruction and listed here for completeness. The DIRA requirement,  $\cos \theta > 0.99985$ , is approximately equivalent to a cut of  $\theta < 17.32$  mrad.

Particle	Variable	Cut value	LoKI functor
$\pi^\pm, K^\pm$	$p_T$	$> 250$ MeV	PT
	$p$	$p > 2$ GeV	P
	Track $\chi^2$	$< 3$	N/A
	$\chi_{\text{IP}}^2$	$> 16$	BPVIPCHI2
$\pi^\pm$	$\text{DLL}_{K-\pi}$	$< 5$	PIDK - PIDpi
$K^\pm$	$\text{DLL}_{K-\pi}$	$> 5$	PIDK - PIDpi
$D^0$	$m(K^-\pi^+)$	$1784 \text{ MeV} < m < 1944 \text{ MeV}$	<code>in_range(m1,m,m2)</code>
	$K^\pm$ to $\pi^\pm$ DOCA	$< 0.1$ mm	AMINDOCA
	Vertex fit $\chi^2$	$< 10$	VFASPF(VCHI2/VDOF)
	Direction angle	$> 0.99985$	BPVDIRA
	Vertex displacement	$VD\chi^2 > 49$	BPVVDCHI2

Table 3.3: Selection requirements made on HLT2  $D^{*+}$  candidates.

Particle	Variable	Cut value	LoKI functor
$\pi^\pm$	$p_T$	$> 100$ MeV	PT
	Track $\chi^2$	$< 3$	N/A
$D^{*+}$	$m(D^{*+}) - m(D^0)$	$130 \text{ MeV} < m < 160 \text{ MeV}$	<code>in_range(m1,m,m2)</code>
	Vertex fit $\chi^2$	$< 25$	VFASPF(VCHI2/VDOF)

*Table 3.4: Selection requirements made in the three-body HLT2 lines. The lines are split into  $D^+$  ( $D^+ \rightarrow K^-\pi^+\pi^+$ ,  $D^+ \rightarrow K^-K^+\pi^+$ ) and  $D_s^+$  ( $D_s^+ \rightarrow K^-K^+\pi^+$ ) decays according to the mass window. Cuts of the form  $x > x_1, x_2, x_3$  require that all particles satisfy  $x > x_1$ , at least two satisfy  $x > x_2$ , and at least one satisfies  $x > x_3$ . The DIRA requirement,  $\cos\theta > 0.9994$ , is approximately equivalent to a cut of  $\theta < 34.64$  mrad.*

Particle	Variable	Cut value	LoKI functor
$\pi^\pm, K^\pm$	$p_T$	$> 200, 400, 1000$ MeV	PT
	$p$	$p > 2$ GeV	P
	Track $\chi^2$	$< 3$	N/A
	$\chi_{\text{IP}}^2$	$> 4, 10, 50$	BPVIPCHI2
$\pi^\pm$	$\text{DLL}_{K-\pi}$	$< 5$	PIDK - PIDpi
$K^\pm$	$\text{DLL}_{K-\pi}$	$> 5$	PIDK - PIDpi
$D^+$	$m(h^-h^+h^+)$	$1789 \text{ MeV} < m < 1949 \text{ MeV}$	in_range(m1,m,m2)
$D_s^+$	$m(h^-h^+h^+)$	$1889 \text{ MeV} < m < 2049 \text{ MeV}$	in_range(m1,m,m2)
$D^+/D_s^+$	Vertex fit $\chi^2$	$< 25$	VFASPF(VCHI2/VDOF)
	Direction angle	$> 0.9994$	BPVDIRA
	Vertex displacement	$VD\chi^2 > 16$ AND $\tau > 0.150$ ps	BPVVDCHI2 & BPVLTIME()

331 calibration procedure described in Section 4.7. The PID cut on pions (excluding  
332 the slow pion in  $D^{*+}$  decays) is tightened to  $\text{DLL}_{K-\pi} < 3$ . Additionally, the ghost  
333 probability of all tracks, specifically the `TRACK_GhostProb` variable, is required to be  
334 less than 0.3 to reduce combinatorial background.

335 As the  $D_{(s)}^+$  candidates still contain a large combinatorial background component  
336 even after these requirements, especially in the low charm hadron  $p_T$  region, the  
337 vertex fit  $\chi^2$  is required to be less than 6, and the cosine of the direction angle is  
338 required to be greater than 0.9999 (approximately equivalent to requiring that the  
339 direction angle itself is less than 14.1 mrad).

340 To isolate the  $\phi\pi^+$  component of the reconstructed  $D_s^+ \rightarrow K^-K^+\pi^+$  system, the  
341  $K^-K^+$  mass is required to be within a window 40 MeV wide centred on the nominal  
342  $\phi(1020)$  mass (referred to here for brevity as just ‘ $\phi$ ’). The set of remaining candidates  
343 will also contain non-resonant  $D_s^+ \rightarrow K^-K^+\pi^+$  decays, but for notational simplicity  
344 the candidates will be referred to as ‘ $D_s^+ \rightarrow \phi\pi^+$ ’. That is to say: throughout this  
345 document, the notation ‘ $D_s^+ \rightarrow \phi\pi^+$ ’ should be interpreted as ‘ $D_s^+ \rightarrow K^-K^+\pi^+$  where  
346 the  $K^-K^+$  mass is within  $\pm 20$  MeV of the nominal  $\phi$  mass’. The  $K^-K^+$  mass window  
347 requirement does not have an associated efficiency as it is part of the definition of the  
348 decay. The original number of  $D_s^+$  candidates is obtained by using a measurement  
349 of the  $D_s^+ \rightarrow \phi\pi^+$  branching fraction made by the CLEO collaboration, discussed  
350 in Section 7.7, where the same  $K^-K^+$  mass window definition is used [11]. The  
351  $K^-K^+$  mass spectrum from the CLEO measurement is shown in Figure 3.1, along  
352 with the various mass windows with which they make several ‘ $D_s^+ \rightarrow \phi\pi^+$ ’ branching  
353 fraction measurements, where the window corresponding to the measurement we use  
354 is delimited by solid red lines.

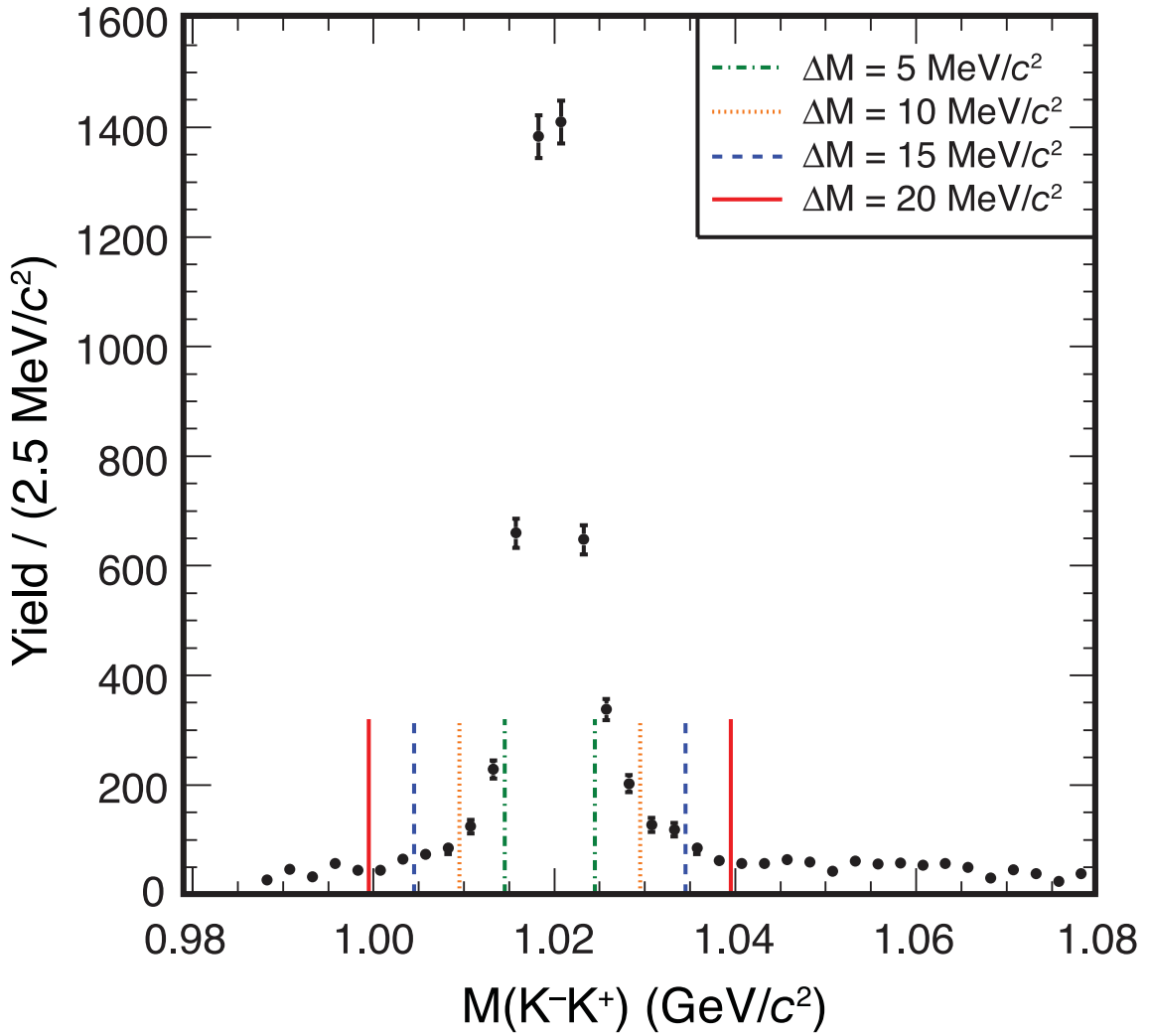


Figure 3.1: Definition of the  $K^-K^+$  mass windows used by the CLEO collaboration to measure the  $D_s^+ \rightarrow \phi\pi^+$  branching fraction [11]. The  $K^-K^+$  mass window used in the analysis described in this document corresponds to the window delimited by the solid red lines in the figure. Figure from [11].

## 355 4 Efficiencies

356 The efficiency chain defines the fraction of prompt signal candidates that pass each  
357 stage of the selection. The chain is defined in steps grouped by physical requirements  
358 and those imposed by software, and each step is relative to the previous one.

359 This starts with the efficiency of a signal hadron to decay within the LHCb  
360 acceptance,  $\epsilon_{\text{Acceptance}}$ , having been produced in a  $pp$  collision. The efficiency of  
361 such a decay to be fully reconstructed is the reconstruction efficiency  $\epsilon_{\text{Reconstruction}}$ ,  
362 corrected for data-MC differences with  $\rho_{\text{Tracking}}$  and the inefficiency of the Monte  
363 Carlo truth matching with  $\rho_{\text{Truth}}$ , and then the efficiency of the reconstructed decay  
364 to be triggered through L0, HLT1, and HLT2 is the trigger efficiency  $\epsilon_{\text{Trigger}}$ . Finally,  
365 there is the efficiency of triggered candidates to pass through the offline selection,  
366 and the requirements imposed on PID variables, which we split as  $\epsilon_{\text{Offline}}$  and  $\epsilon_{\text{PID}}$ .

367 The total efficiency in a  $p_{\text{T}}\text{-}y$  bin  $\epsilon_i(H_c \rightarrow f)$ , used in the total cross section  
368 formula in Equation 1.1, is the product of the individual efficiencies

$$\epsilon_i(H_c \rightarrow f) = \epsilon_{\text{Acceptance}} \times \epsilon_{\text{Reconstruction}} \times \rho_{\text{Tracking}} \times \rho_{\text{Truth}} \\ \times \epsilon_{\text{Trigger}} \times \epsilon_{\text{Offline}} \times \epsilon_{\text{PID}}. \quad (4.1)$$

369 where each efficiency  $\epsilon$  is dependent on the charm hadron  $H_c$  and the final state  $f$ ,  
370 and is conditional on the previous step. The correction factors  $\rho$  also depend on  $H_c$   
371 and  $f$ , and their computation is described in Sections 4.2.1 and 4.2.2.

372 As the full distributions of the selection variables are not available once a selection  
373 has been made on them, and we only have access to hadron candidates after HLT2,  
374 we must rely on Monte Carlo simulations, described in Section 2.3, to evaluate most of  
375 the efficiencies. The validity of the computed efficiencies relies on the MC accurately  
376 modelling the selection variables. The quantification of the mis-modelling will be  
377 discussed in the context of systematic uncertainties in Section 7.2.

378 In this section we shall detail how the efficiency of each selection step is computed,  
379 and give  $p_{\text{T}}\text{-}y$  efficiency tables for each open charm hadron and final state. The  
380 notation for conditional yields will be used throughout, where  $N_{A|B}$  denotes the  
381 prompt signal yields after process  $A$  given that process  $B$  preceded  $A$ .

### 382 4.1 LHCb acceptance

383 An acceptance efficiency arises due to the finite spatial acceptance of the LHCb  
384 detector. By instrumenting the forward region in the pseudorapidity range  $2 < \eta < 5$ ,  
385 any particles flying outside this region are not detected. As there is no way to access  
386 these particles in data, simulated data must be used. The acceptance is modelled

Table 4.1: Acceptance efficiency for  $D^0 \rightarrow K^-\pi^+$  in bins of  $D^0$   $p_T$  and  $y$ .

$p_T$ [MeV/c]	$y$				
	[2, 2.5]	[2.5, 3]	[3, 3.5]	[3.5, 4]	[4, 4.5]
[9000, 10000]	$98.69^{+0.33}_{-0.43}$	$100.00^{+0.00}_{-0.17}$	$99.78^{+0.16}_{-0.38}$	$99.56^{+0.32}_{-0.75}$	$100.00^{+0.00}_{-1.47}$
[8000, 9000]	$99.05^{+0.22}_{-0.28}$	$100.00^{+0.00}_{-0.10}$	$99.87^{+0.09}_{-0.22}$	$99.54^{+0.25}_{-0.47}$	$100.00^{+0.00}_{-0.70}$
[7000, 8000]	$98.16^{+0.24}_{-0.28}$	$99.95^{+0.03}_{-0.08}$	$99.93^{+0.05}_{-0.12}$	$99.76^{+0.13}_{-0.25}$	$98.71^{+0.47}_{-0.72}$
[6000, 7000]	$97.08^{+0.23}_{-0.25}$	$99.92^{+0.04}_{-0.06}$	$99.93^{+0.04}_{-0.08}$	$99.75^{+0.10}_{-0.16}$	$98.48^{+0.38}_{-0.50}$
[5000, 6000]	$95.73^{+0.21}_{-0.22}$	$99.82^{+0.04}_{-0.06}$	$99.87^{+0.04}_{-0.06}$	$99.34^{+0.13}_{-0.16}$	$98.31^{+0.28}_{-0.33}$
[4000, 5000]	$93.97^{+0.18}_{-0.18}$	$99.49^{+0.06}_{-0.06}$	$99.76^{+0.04}_{-0.05}$	$99.06^{+0.11}_{-0.12}$	$96.52^{+0.28}_{-0.30}$
[3000, 4000]	$90.59^{+0.15}_{-0.16}$	$98.39^{+0.07}_{-0.08}$	$99.19^{+0.06}_{-0.06}$	$97.62^{+0.12}_{-0.12}$	$92.67^{+0.26}_{-0.27}$
[2000, 3000]	$85.72^{+0.13}_{-0.13}$	$96.66^{+0.07}_{-0.07}$	$98.35^{+0.06}_{-0.06}$	$95.83^{+0.10}_{-0.11}$	$87.87^{+0.21}_{-0.21}$
[1000, 2000]	$79.53^{+0.11}_{-0.11}$	$93.86^{+0.07}_{-0.07}$	$96.97^{+0.05}_{-0.06}$	$93.68^{+0.09}_{-0.09}$	$82.61^{+0.16}_{-0.16}$
[0, 1000]	$75.78^{+0.12}_{-0.12}$	$91.70^{+0.08}_{-0.09}$	$95.06^{+0.07}_{-0.07}$	$91.19^{+0.10}_{-0.10}$	$77.85^{+0.17}_{-0.17}$

by the `DaughtersInLHCb` generator-level cut, which requires that all stable charged  $H_c$  child particles have  $10 < \theta < 400$  mrad, where  $\theta$  is the polar angle of the particle momentum vector, and that they all point in same  $z$  direction. This is applied to all generated signal samples, and any decays failing this cut are rejected. By counting the number of charm hadrons passing and failing the cut, the acceptance efficiency is defined as

$$\epsilon_{\text{Acceptance}} = \frac{N_{\text{DaughtersInLHCb}|\text{Generated}}}{N_{\text{Generated}}}. \quad (4.2)$$

As the nominal MC samples already have the generator-level cut applied, the dedicated MC samples described in Section 2.3.2 are used for computing this efficiency.

The  $D^0$  acceptance efficiency is computed using the  $D^{*+}$ -tagged MC samples, and these same samples are used for subsequent  $D^0$  efficiency evaluations, such as the reconstruction efficiency described in Section 4.2. The  $D^{*+}$ -tagged samples include the requirement that the soft pion, in the  $D^{*+} \rightarrow D^0\pi^+$  decay, passes the `DaughtersInLHCb` cut, as well as the requirement that each  $D^0$  child also passes the same cut. The  $D^0$  efficiency chain evaluated with this sample would then be the  $D^0$  efficiency assuming a tagging soft pion is within the LHCb acceptance, and hence would be incorrect for our  $D^0$  measurement as we do not make this requirement in the data. Therefore, the effect of the soft pion acceptance requirement must be corrected

404 for in the  $D^0$  efficiency chain.

405 The  $D^{*+}$  acceptance efficiency can be described in two ways: firstly as in Equation 4.2, and secondly as the product of the  $D^0$  acceptance efficiency and the acceptance efficiency of the soft pion given that the  $D^0$  has passed the acceptance requirements

$$\epsilon_{\text{Acceptance}}(D^{*+}) = \frac{N_{\text{DaughtersInLHCb}|\text{Generated}}(D^{*+})}{N_{\text{Generated}}(D^{*+})} \\ = \epsilon_{\text{Acceptance}}(D^0)\epsilon_{\text{Acceptance}}(\pi_{\text{Soft}}|D^0). \quad (4.3)$$

409 To remove the effect of the soft pion requirement that occurs when using the  $D^{*+}$   
410 sample to evaluate the  $D^0$  efficiency chain, we divide the  $D^{*+}$  acceptance efficiency  
411 by the reciprocal of  $\epsilon_{\text{Acceptance}}(\pi_{\text{Soft}}|D^0)$ , that is

$$\epsilon_{\text{Acceptance}}(D^0) = \frac{\epsilon_{\text{Acceptance}}(D^{*+})}{\epsilon_{\text{Acceptance}}(\pi_{\text{Soft}}|D^0)}. \quad (4.4)$$

412 This factor is computed separately in each  $p_{\text{T}}\text{-}y$  bin.

413 Tables 4.1 and C.1–C.3 give the obtained acceptance efficiencies for the different  
414 modes.

## 415 4.2 Reconstruction

416 Given a set of child tracks within the LHCb acceptance, the fraction of final states  
417 that are fully reconstructed is the reconstruction efficiency. This includes the physical  
418 creation of ‘hits’ in the various tracking detectors, as well as the construction of tracks  
419 in software.

420 We compute the reconstruction efficiency by counting the number of truth-matched  
421 reconstructed decays, and comparing this with the number of decays passing the  
422 acceptance cuts defined in Section 4.1

$$\epsilon_{\text{Reconstruction}} = \frac{N_{\text{Reconstructed}|\text{DaughtersInLHCb}}}{N_{\text{DaughtersInLHCb}|\text{Generated}}}. \quad (4.5)$$

423 The truth-matching is described in Section 2.3.

### 424 4.2.1 Tracking efficiency correction

425 It is known that the tracking, or track reconstruction, efficiency is not correctly  
426 modelled in simulated data, and so the LHCb tracking group produces correction

427 tables that analysts can apply to their efficiencies [12]. These tables are produced by  
 428 measuring the tracking efficiency in data with  $J/\psi \rightarrow \mu^-\mu^+$  decays, and comparing  
 429 how the same quantity in the MC.

430 Figure 4.1 shows the corrections in bins of track momentum  $p$  and pseudorapidity  
 431  $\eta$  for each track individually. The actual correction factor  $\rho_{\text{Tracking}}$ , which is used in  
 432 Equation (4.1) to compute the total efficiency, depends on the actual decay as it is  
 433 dependent on the track kinematics and the number of final state particles. Hence, a  
 434 calibration procedure is performed, in which every track in the reconstructed Monte  
 435 Carlo sample is assigned its individual correction factor. In each event, the factors  
 436 of all final state tracks are multiplied to obtain the total correction factor, which is  
 437 then averaged over all events to obtain  $\rho_{\text{Tracking}}$ . When computing this average, event  
 438 weights are assigned which reweight the distribution in the number of hits in the SPD  
 439 detector to match the distribution seen in data.

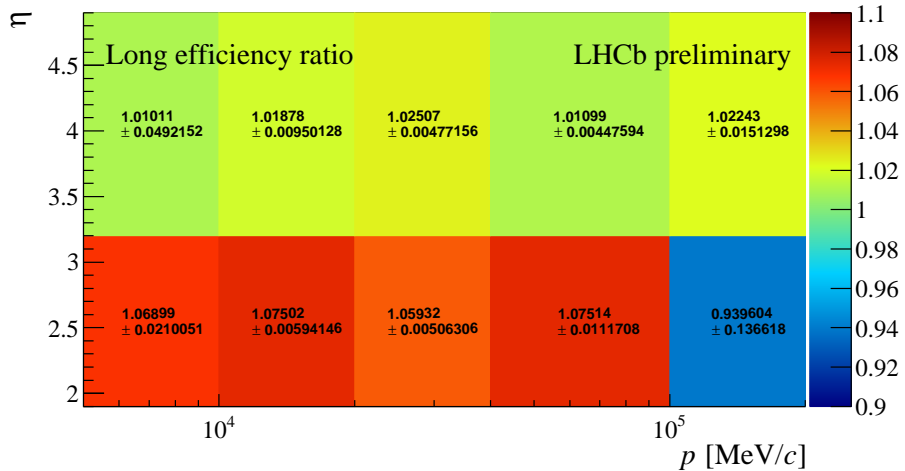


Figure 4.1: Per track correction factors obtained from 2015 data processed with *Reco15em* and including  $a < 0.3$  cut on the ghost probability (*TRACK\_GhostProb*). Quoted uncertainties are due statistical uncertainties due to the size of the calibration mode.

440 The actual procedure, including the evaluation of the statistical uncertainty due  
 441 to the limited size of the MC calibration sample, is identical to the PID calibration  
 442 procedure described in Section 4.7.

443 The obtained tracking correction factors are given in Table 4.2 for  $D^0 \rightarrow K^-\pi^+$ ,  
 444 Table C.4 for  $D^+ \rightarrow K^-\pi^+\pi^+$ , Table C.5 for  $D_s^+ \rightarrow \phi\pi^+$ , and Table C.6 for  $D^{*+} \rightarrow$   
 445  $D^0\pi^+$  with  $D^0 \rightarrow K^-\pi^+$ .

*Table 4.2: Tracking efficiency correction for  $D^0 \rightarrow K^-\pi^+$ . Shown uncertainties are due to the size of the simulated sample.*

$p_T$ [MeV/c]	[2, 2.5]	[2.5, 3]	$y$ [3, 3.5]	[3.5, 4]	[4, 4.5]
[9000, 10000]	$113.72 \pm 0.06$	$114.12 \pm 0.09$	$108.01 \pm 0.29$	$103.72 \pm 0.11$	$103.95 \pm 0.09$
[8000, 9000]	$113.69 \pm 0.05$	$113.67 \pm 0.09$	$107.71 \pm 0.20$	$103.71 \pm 0.13$	$103.87 \pm 0.06$
[7000, 8000]	$113.69 \pm 0.07$	$113.49 \pm 0.07$	$107.87 \pm 0.15$	$103.69 \pm 0.09$	$103.96 \pm 0.05$
[6000, 7000]	$113.85 \pm 0.04$	$113.02 \pm 0.06$	$107.79 \pm 0.12$	$103.59 \pm 0.05$	$103.77 \pm 0.04$
[5000, 6000]	$114.19 \pm 0.04$	$112.58 \pm 0.04$	$107.65 \pm 0.07$	$103.54 \pm 0.04$	$103.66 \pm 0.04$
[4000, 5000]	$114.25 \pm 0.04$	$112.27 \pm 0.04$	$107.71 \pm 0.04$	$103.66 \pm 0.03$	$103.57 \pm 0.03$
[3000, 4000]	$113.97 \pm 0.03$	$112.02 \pm 0.03$	$107.93 \pm 0.03$	$104.00 \pm 0.02$	$103.45 \pm 0.02$
[2000, 3000]	$113.21 \pm 0.03$	$111.82 \pm 0.02$	$108.33 \pm 0.02$	$104.58 \pm 0.02$	$103.36 \pm 0.01$
[1000, 2000]	$113.17 \pm 0.02$	$111.64 \pm 0.02$	$108.31 \pm 0.02$	$105.10 \pm 0.02$	$103.49 \pm 0.01$
[0, 1000]	$113.84 \pm 0.02$	$111.81 \pm 0.02$	$108.10 \pm 0.02$	$105.25 \pm 0.02$	$103.90 \pm 0.02$

446 A set of systematic uncertainties is also provided by the tracking group and are  
447 discussed in Section 7.6.

#### 448 4.2.2 Monte Carlo truth matching inefficiency

449 The LHCb Monte Carlo truth matching deems a reconstructed particle matched  
450 to an MC particle if there is an overlap of at least 70 % between the hits created  
451 by the reconstructed particle and those created by the MC particle. This 70% is  
452 somewhat arbitrary, and leads to an inefficiency in the truth matching, *i.e.* some  
453 reconstructed particles are not marked as ‘matched’ despite truly belonging to MC  
454 particles, and hence to an underestimation to the efficiency and an inflation of the  
455 final measurement.

456 The size of the inefficiency can be determined by counting the number of signal  
457 yields that fail the truth matching requirement. Figure 4.2 shows the  $D^0$  mass  
458 distributions for the various background category values, of which we only consider  
459 values of 0 and 10 as signal. The only background category above 10 to show a  
460 signal-like structure is 60, which means the truth-matching tool classified the decays  
461 as ‘ghosts’, *i.e.* containing at least one track that was determined to be a ghost track.

462 Figures C.1 and C.2, show the same information as Figure 4.2 but for  $D^+ \rightarrow$   
463  $K^-\pi^+\pi^+$  and  $D^{*+} \rightarrow D^0\pi^+$ , with  $D^0 \rightarrow K^-\pi^+$ . These plots demonstrate that the  
464 truth matching efficiency is mode-dependent, and so is evaluated per-mode. Due to  
465 the limited Monte Carlo statistics, the inefficiency is assumed to be constant across

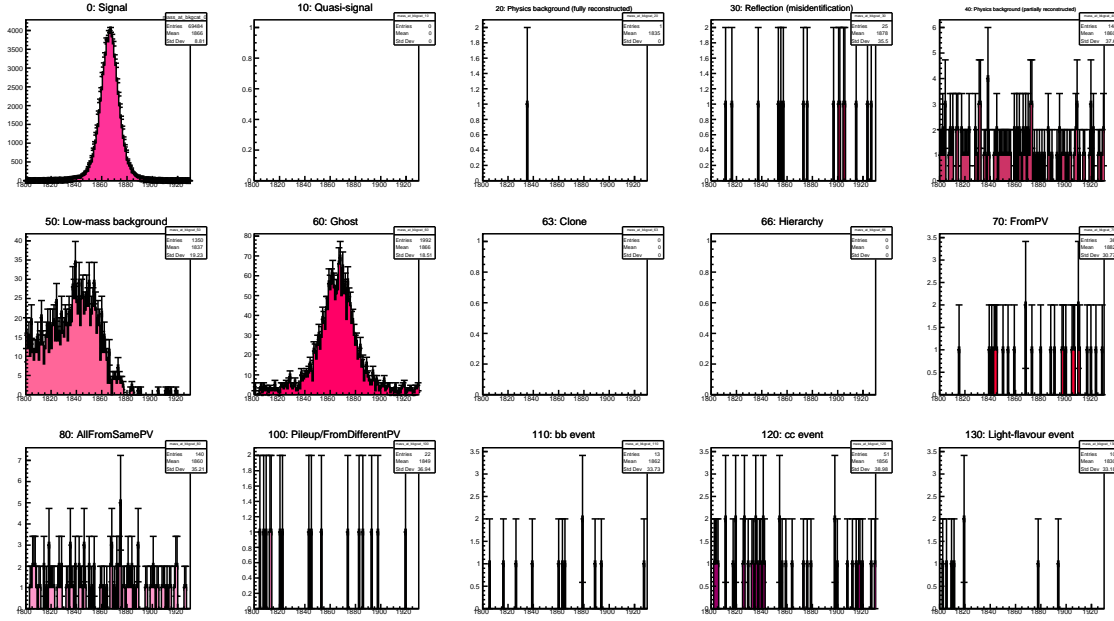


*Figure 4.2:*  $D^0 \rightarrow K^- \pi^+$  mass distributions for all the possible background categories values. Any signal-like peaking structures in background categories other than 0 or 10 indicate an inefficiency in the truth matching.

466 the charm hadron  $p_T$ - $y$  bins.

467 Labelling the number of correctly matched signal decays as  $N$ , and the number of  
468 incorrectly labelled signal decays as  $U$ , the selection efficiency defined in Equation 4.5  
469 is incorrect by a factor  $\rho_{\text{Truth}} = (U + N)/N$ . We compute  $U$  for each mode by a  
470 fitting the charm hadron mass spectrum of the Monte Carlo which fails the truth  
471 matching. Table 4.3 lists the obtained efficiencies.

### 472 4.3 Trigger

473 The three stages of the trigger, L0, HLT1, and HLT2, each carry a related efficiency.  
474 The L0 efficiency  $\epsilon_{L0}$  is discussed and given in Section 3.2. As it is a function of  
475 the known selection rate and LHC filling scheme, simulated data is not needed to  
476 evaluate it. The HLT1 and HLT2 efficiency, however, do require simulated data as  
477 the efficiencies depend on variables to which we do not have access after the HLT2.

478 The efficiency for the HLT1 and HLT2 selection is combined into a single trigger  
479 efficiency, defined by the number of true signal decays passing the trigger and those

Table 4.3: Efficiency  $1/\rho_{\text{Truth}}$  of the truth matching requirement applied to the simulated data, as discussed in Section 4.2.2.

Mode	$1/\rho_{\text{Truth}} [\%]$
$D^0 \rightarrow K^-\pi^+$	$97.75 \pm 0.07$
$D^+ \rightarrow K^-\pi^+\pi^+$	$96.99 \pm 0.14$
$D_s^+ \rightarrow \phi\pi^+$	$99.08 \pm 0.24$
$D^{*+} \rightarrow D^0\pi^+, D^0 \rightarrow K^-\pi^+$	$97.26 \pm 0.13$

480 entering

$$\epsilon_{\text{Trigger}} = \epsilon_{\text{L0}} \times \frac{N_{\text{Triggered}|\text{Reconstructed}}}{N_{\text{Reconstructed}|\text{DaughtersInLHCb}}}.$$
 (4.6)

481 As detailed in Section 4.7, the PID efficiency is evaluated using a data-driven method  
482 and so is not included in the trigger efficiency.

#### 483 4.4 Offline selection

484 As in the case of the trigger efficiency, the efficiency of the offline selection  $\epsilon_{\text{Offline}}$  can  
485 only be evaluated on simulated data, and is the ratio of truth-matched signal decays  
486 passing the selection to those entering it

$$\epsilon_{\text{Offline}} = \frac{N_{\text{Offline}|\text{Triggered}}}{N_{\text{Triggered}|\text{Reconstructed}}}.$$
 (4.7)

487 Here, the offline selection is defined as the rectangular selection applied on the  
488 candidates that come out the various HLT2 lines, excluding any PID requirements.

#### 489 4.5 Combination of efficiencies

490 Aside from the acceptance and PID efficiencies, all selection criteria are estimated on  
491 the same simulated data sample for each decay mode. Hence, the number of events  
492 passing a certain stage in the selection is fully correlated to the number of events  
493 entering in the next stage. To avoid having to include these correlations explicitly,  
494 the final efficiency  $\epsilon_{\text{MC}}$  is computed in one step, incorporating all selections evaluated  
495 on the simulated data.

496 Tables 4.4 and C.7–C.9 give the per-bin efficiencies, derived from the MC, for  
497 each mode.

Table 4.4: Total MC selection efficiency for  $D^0 \rightarrow K^-\pi^+$  in bins of  $D^0$   $p_T$  and  $y$ .

$p_T$ [MeV/c]	$y$				
	[2, 2.5]	[2.5, 3]	[3, 3.5]	[3.5, 4]	[4, 4.5]
[9000, 10000]	$9.23^{+0.84}_{-0.78}$	$17.54^{+1.30}_{-1.23}$	$14.63^{+1.48}_{-1.37}$	$2.16^{+0.98}_{-0.68}$	$0.00^{+0.92}_{-0.00}$
[8000, 9000]	$8.57^{+0.64}_{-0.60}$	$16.19^{+0.96}_{-0.92}$	$16.13^{+1.14}_{-1.08}$	$3.89^{+0.88}_{-0.72}$	$0.00^{+0.42}_{-0.00}$
[7000, 8000]	$7.25^{+0.45}_{-0.43}$	$16.42^{+0.70}_{-0.68}$	$17.19^{+0.87}_{-0.84}$	$7.20^{+0.78}_{-0.71}$	$0.00^{+0.22}_{-0.00}$
[6000, 7000]	$6.83^{+0.32}_{-0.30}$	$15.22^{+0.50}_{-0.48}$	$17.13^{+0.61}_{-0.59}$	$9.94^{+0.62}_{-0.59}$	$0.08^{+0.14}_{-0.06}$
[5000, 6000]	$5.87^{+0.21}_{-0.21}$	$13.78^{+0.33}_{-0.33}$	$15.82^{+0.41}_{-0.40}$	$12.44^{+0.46}_{-0.44}$	$1.24^{+0.22}_{-0.19}$
[4000, 5000]	$4.57^{+0.13}_{-0.13}$	$11.66^{+0.22}_{-0.21}$	$12.83^{+0.25}_{-0.25}$	$11.24^{+0.29}_{-0.28}$	$2.71^{+0.20}_{-0.19}$
[3000, 4000]	$3.00^{+0.08}_{-0.08}$	$8.83^{+0.13}_{-0.13}$	$9.93^{+0.15}_{-0.15}$	$8.74^{+0.17}_{-0.17}$	$3.30^{+0.14}_{-0.13}$
[2000, 3000]	$1.65^{+0.04}_{-0.04}$	$5.51^{+0.08}_{-0.08}$	$6.52^{+0.09}_{-0.09}$	$5.54^{+0.10}_{-0.09}$	$2.63^{+0.08}_{-0.08}$
[1000, 2000]	$0.85^{+0.03}_{-0.03}$	$3.23^{+0.05}_{-0.05}$	$4.04^{+0.06}_{-0.06}$	$3.16^{+0.06}_{-0.06}$	$1.55^{+0.05}_{-0.05}$
[0, 1000]	$0.62^{+0.03}_{-0.03}$	$2.43^{+0.05}_{-0.05}$	$3.27^{+0.06}_{-0.06}$	$2.60^{+0.07}_{-0.07}$	$1.19^{+0.07}_{-0.06}$

## 4.6 Propagation of uncertainties

Due to the finite size of the MC sample, the selection efficiency carries a statistical uncertainty, which translates to a systematic uncertainty on the cross-section measurement. As binomial uncertainties fail to model this uncertainty correctly in case of very low or very high efficiencies and for small sample sizes, the uncertainties are estimated from the posteriori probability for  $\epsilon$ , assuming a binomial distribution for the number of passing events given the total number of events and  $\epsilon$  and a flat prior in  $\epsilon$ .<sup>2</sup> This posteriori probability is also used in the MC error propagation to obtain the uncertainties on the measured cross-sections, as discussed in Section 1.3.

Because of this, the uncertainties given in the various tables in this section are not propagated directly, and are only given for illustration.

## 4.7 Particle identification

The signal Monte Carlo samples that have been used in the previous sections cannot be used alone to determine the efficiencies of the PID requirements used in this

<sup>2</sup>The posteriori probability for  $\epsilon$  is given by  $P(\epsilon) \propto \epsilon^p(1 - \epsilon)^{t-p}$  with  $p(t)$  being the number of passing (total) events. This is the Beta function with  $\alpha = p + 1$  and  $\beta = t - p + 1$ .

512 analysis, as there is a large disagreement between the PID modelling between MC  
513 and real data. Instead, a data-driven method to estimate the efficiencies is used, and  
514 will be described and applied in this section. The method employed in this analysis  
515 follows the well-known PIDCALIB approach but reimplements most steps to account  
516 for small calibration sample size.

517 **4.7.1 Overview**

518 The PID efficiency is computed in the same way as in the  $\sqrt{s} = 13$  TeV analysis, the  
519 formalism of which is described in great detail in the corresponding analysis note [7].  
520 The procedure itself shall be briefly summarised here, and then the results will be  
521 given.

522 The PID efficiency is computed with the following steps, where ‘calibration tracks’  
523 are tracks of a known particle species which have no PID requirements made on  
524 them, and ‘reference tracks’ are a sample of tracks for which the efficiency is to be  
525 determined:

- 526 1. The calibration tracks are binned in a set of variables which are assumed to  
527 fully parameterise the PID efficiency, with a granularity that is assumed to be  
528 sufficiently fine such that the PID efficiency is single-valued within a bin;
- 529 2. The PID cut for which the efficiency is to be determined is applied to the  
530 calibration tracks;
- 531 3. The PID efficiency is then defined per bin as the ratio of calibration tracks  
532 passing the PID requirements to the number of calibration tracks before the  
533 requirement;
- 534 4. Each reference track is assigned an efficiency depending on which bin it falls in  
535 to.

536 For a given final state, this procedure is performed on each track, and the total  
537 efficiency is the product of the per-track efficiencies.

538 There are two assumptions in this procedure: the set of variables in which the tracks  
539 are binned are assumed to fully parameterise the PID efficiency; and the binning is  
540 sufficiently fine such that there is no variation in the PID efficiency across the bin.  
541 (There is a subtlety here in that if the calibration and reference distributions are  
542 identical within a bin, it does not matter if the efficiency varies within the bin, as it  
543 will vary in the same way for both samples.) We chose to parameterise the efficiency  
544 with the track momentum  $p$ , track pseudorapidity  $\eta$ , and the number of hits in the

545 SPD sub-detector `nSPDHits`, which is used as a measure of the event multiplicity  
 546 (how ‘busy’ the event is). The validity of these assumptions will be assessed in the  
 547 context of systematic effects, discussed in Section 7.4.

548 The kaon and pion calibration tracks are taken from  $D^{*+}$ -tagged  $D^0 \rightarrow K^-\pi^+$   
 549 decays, selected without the use of particle identification information from data  
 550 from the same data-taking period as in this analysis. These calibration samples  
 551 are found to have a small overlap with our signal sample. The fully selected data  
 552 sample (including all PID selection criteria) is chosen as the reference sample. This  
 553 approach is valid if the efficiency is non-zero for the region in phase-space covered  
 554 by the selected sample (as is the case in this analysis due to the loose requirements  
 555 imposed on  $\text{DLL}_{K-\pi}$ ). Weighting every reference event by the inverse of the efficiency,  
 556 one obtains the number of events before the PID selection and the efficiency can be  
 557 computed. Contributions from combinatorial background and secondary decays are  
 558 removed from the reference sample on a statistical basis using the `sPlot` technique [13],  
 559 with sWeights computed from the  $\ln \chi_{\text{IP}}^2$  fit described in Section 5.

#### 560 4.7.2 Binning of the calibration sample

561 The efficiency look-up tables binned in `p-eta-nSPDHits` are the key ingredient for the  
 562 calibration procedure. The usual PIDCALIB procedure uses a global fit the entire  
 563 calibration sample and assigns every event a signal weight using the `sPlot` technique.  
 564 Due to the small size of the 5 TeV calibration sample, this approach cannot be used  
 565 as for any sensibly fine binning, statistical fluctuations in combination with sWeights  
 566 lead to unphysical efficiencies in some of the bins. To prevent this, but also to get a  
 567 better handle on the statistical uncertainties in every bin of the calibration sample,  
 568 an unbinned likelihood fit is performed separately in each bin of the calibration table.  
 569 This fit is performed in three dimensions:  $\Delta m = m(D^{*+}) - m(D^0)$ ,  $m = m(D^0)$   
 570 and a flag  $f$  indicating whether the event in the calibration sample passed or failed  
 571 the PID selection. The following fit models are used:

572  $m$  Double-gaussian for signal and wrong slow pion and a first order polynomial for  
 573 the combinatorial background.

574  $\Delta m$  Double-gaussian for signal. Combinatorial and wrong slow pion background are  
 575 modelled using:

$$\text{PDF}(\Delta m) \propto \sqrt{\frac{x}{b} - 1} \cdot \exp\left(\frac{a}{b}x\right) ,$$

576 where  $b = 139.57 \text{ MeV}/c^2$  is fixed to the mass of the  $\pi^\pm$ .

577     $f$  The cut flag is modelled using an Bernoulli PDF:

$$\text{PDF}(f) = \varepsilon^f (1 - \varepsilon)^{1-f}.$$

578    Independent  $\varepsilon$  are used for the modelling of the signal as well as the wrong slow  
 579    pion and combinatorial background, resulting in different efficiencies for the  
 580    three components. However, only the signal efficiency is of interest and hence  
 581    referred to simply as  $\varepsilon$ .

582    An example fit is shown in Figure 4.3. The result of the fit is an estimate  $\hat{\varepsilon}$  for the  
 583    efficiency in a bin. To estimate the uncertainty, the sample is bootstrapped and  
 584    the fit is repeated 10,000 times for each of these bootstrap samples. This has the  
 585    benefit that the obtained efficiencies are all within the physically allowed region of  
 586     $0 \leq \hat{\varepsilon} \leq 1$  (unlike the classic PIDCALIB procedure, where binomial uncertainties can  
 587    lead to a significant extension of the distribution of the estimator past the physical  
 588    boundaries). These 10,000 values per bin are then used in the Monte Carlo error  
 589    propagation approach described before to obtain the efficiency in each bin of the  
 590    charm meson production measurement and the correlation between different bins.

591    This approach also allows to study the statistical correlation between the  $K^\pm$  and  
 592     $\pi^\pm$  calibration data (as tracks for both are taken from the same sample a correlation is  
 593    possible). Figure 4.4 shows the distribution of the linear correlation for every possible  
 594    combination of  $K^\pm$  and  $\pi^\pm$  calibration table bins. No significant correlation is found.

595    The bin boundaries are identical to those of 13 TeV measurement. The boundaries  
 596    for the tables are as follows for  $K^\pm$ :

Variable	Limits	Boundaries
$p$	$3 \leq p < 100 \text{ GeV}/c$	7.5, 11, 18, 27, 35, 40, 48, 63
$\eta$	$2 \leq \eta < 5$	2.645, 3.4, 3.6, 4.0
nSPDHits	$0 \leq \text{nSPDHits} < \infty$	212, 400

598    And for  $\pi^\pm$ :

Variable	Limits	Boundaries
$p$	$3 \leq p < 100 \text{ GeV}/c$	12, 14, 32, 63
$\eta$	$2 \leq \eta < 5$	2.4, 2.5, 2.8, 3.7, 4.1
nSPDHits	$0 \leq \text{nSPDHits} < \infty$	276, 500

### 600    4.7.3 Results

601    The central values of the PID efficiencies are computed for each charm hadron in a  
 602    given  $p_T$ - $y$  bin by multiplying together the PID efficiencies of all of the child tracks.

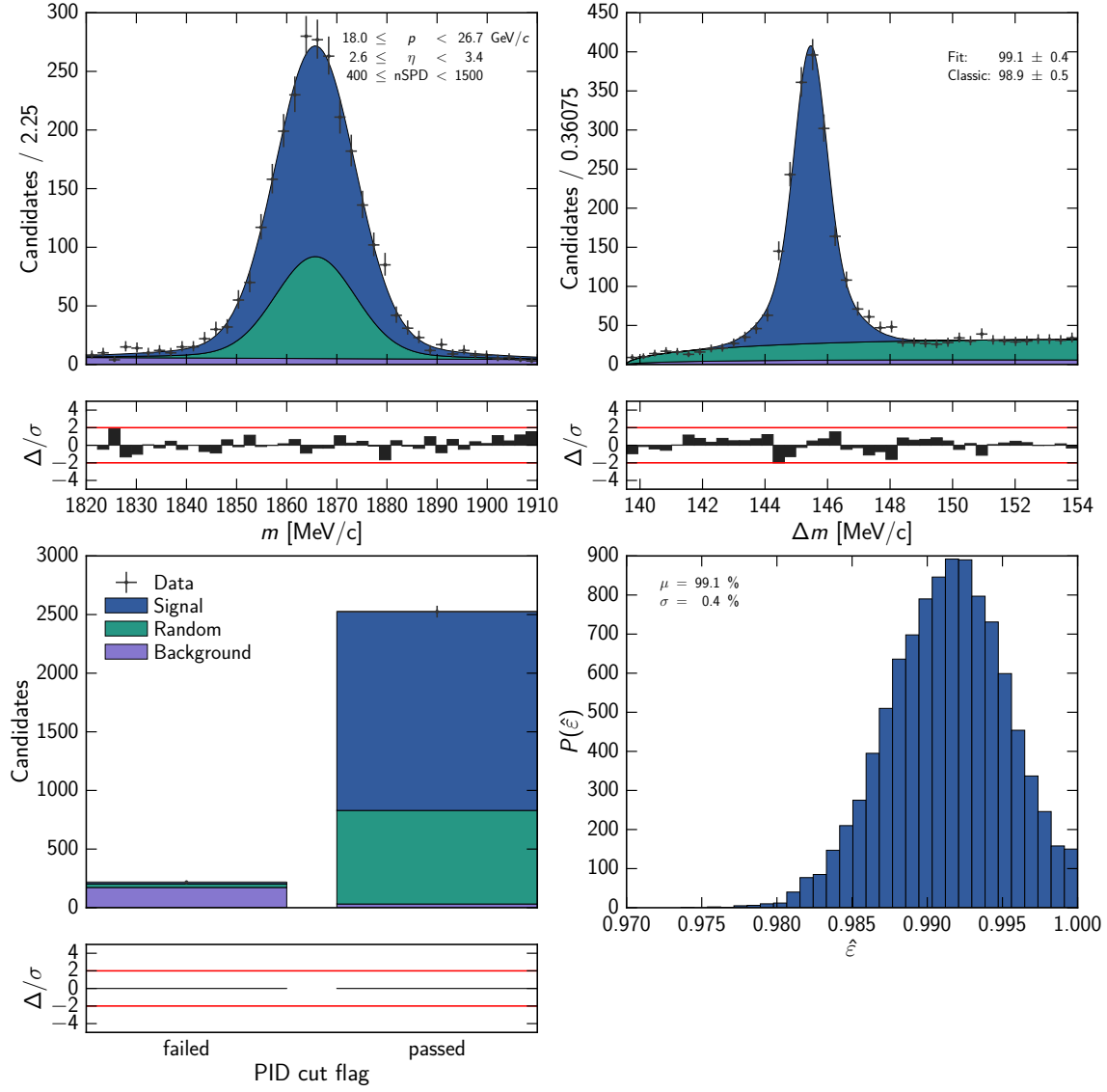


*Figure 4.3: Illustration of the per bin performed in the kaon calibration sample with  $DLL_{K-\pi} > 5$  as the cut. The bin boundaries are given in the top left, the obtained efficiency in that bin compared with the classic PIDCALIB number in the top right (uncertainties statistical only). Bottom right shows the distribution of  $\hat{\varepsilon}$  obtained from bootstrapping the data and repeating the fit procedure.*

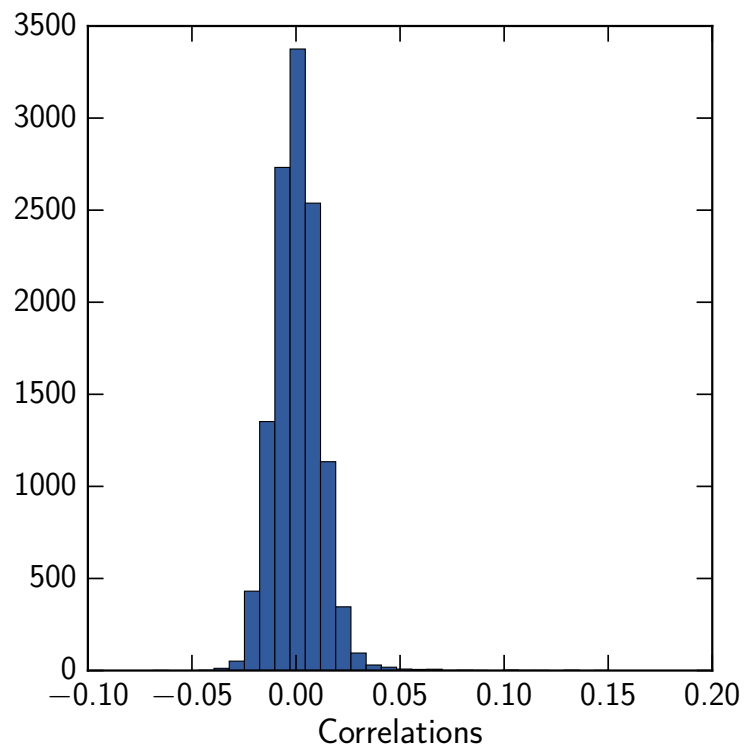


*Figure 4.4: Distribution of the linear correlation coefficients for all pair-wise combination of  $K^\pm$  and  $\pi^\pm$  calibration table bins.*

*Table 4.5: Total PID selection efficiency for  $D^0 \rightarrow K^-\pi^+$  in bins of  $D^0$   $p_T$  and  $y$ . Shown uncertainties are due to the size of the calibration sample, estimated by bootstrapping the calibration sample.*

$p_T$ [MeV/c]	$y$				
	[2, 2.5]	[2.5, 3]	[3, 3.5]	[3.5, 4]	[4, 4.5]
[9000, 10000]	94.44 ± 0.37	85.61 ± 0.46	81.54 ± 0.51		
[8000, 9000]	95.17 ± 0.25	90.41 ± 0.28	82.01 ± 0.46	67.93 ± 0.65	
[7000, 8000]	97.12 ± 0.15	93.92 ± 0.18	85.06 ± 0.34	68.09 ± 0.55	
[6000, 7000]	97.80 ± 0.11	95.99 ± 0.14	88.26 ± 0.24	71.90 ± 0.42	
[5000, 6000]	97.88 ± 0.11	97.44 ± 0.08	92.32 ± 0.15	75.97 ± 0.35	53.04 ± 0.63
[4000, 5000]	97.28 ± 0.13	97.86 ± 0.07	95.16 ± 0.10	79.69 ± 0.29	58.33 ± 0.58
[3000, 4000]	96.55 ± 0.15	97.70 ± 0.08	96.56 ± 0.08	85.02 ± 0.20	64.87 ± 0.55
[2000, 3000]	95.61 ± 0.21	96.85 ± 0.11	96.79 ± 0.08	90.18 ± 0.16	69.44 ± 0.49
[1000, 2000]	94.65 ± 0.29	95.53 ± 0.17	96.39 ± 0.12	93.17 ± 0.17	79.27 ± 0.37
[0, 1000]	94.09 ± 0.39	94.30 ± 0.26	96.35 ± 0.14	94.47 ± 0.21	85.17 ± 0.44

603 The statistical uncertainty on the reference sample size is already incorporated in  
 604 the uncertainty on the fit yields. Therefore, the uncertainties given in the tables  
 605 are due to the size of the calibration sample and constitute one of the systematic  
 606 uncertainties in this measurement.

607 The obtained PID efficiencies using the calibration procedure described above are  
 608 given in bins of charm hadron  $p_T$  and  $y$  in Table 4.5 and Tables C.10–C.12.

## 609 4.8 Signal window efficiency

610 As described in Section 5, the number of prompt signal candidates is measured by  
 611 fitting the  $\ln \chi_{\text{IP}}^2$  distribution of candidates in a signal window defined in the mass  
 612 distribution. This requirement removes some signal candidates. The efficiency of the  
 613 requirement is evaluated by computing the fractional integral of the signal component  
 614 of the model fitted to the mass distribution, where the fractional integral across the  
 615 entire fitted mass range is defined to be unity. In the case of the  $D^{*+}$  measurement,  
 616 there is an additional requirement that the candidates used in the  $\ln \chi_{\text{IP}}^2$  fit fall in  
 617 a signal window defined in the  $\delta m = m(D^{*+}) - m(D^0)$  distribution. The efficiency  
 618 of this  $\delta m$  signal window requirement is computed in the same way as for the mass  
 619 signal window requirement, except the signal component of the model fitted to the  
 620  $\delta m$  distribution is used.

*Table 4.6: Signal window requirement efficiencies, in percent, for  $D^0 \rightarrow K^-\pi^+$ .*

$p_T$ [MeV/c]	[2, 2.5]	[2.5, 3]	[3, 3.5]	$y$ [3.5, 4]	[4, 4.5]
[9000, 10000]	96.36 ± 0.44	96.82 ± 0.35	96.31 ± 0.55	97.74 ± 0.21	97.74 ± 0.21
[8000, 9000]	97.07 ± 0.34	96.97 ± 0.28	95.50 ± 0.52	96.17 ± 1.29	97.74 ± 0.23
[7000, 8000]	97.28 ± 0.27	96.91 ± 0.28	96.30 ± 0.34	93.65 ± 0.67	97.74 ± 0.25
[6000, 7000]	97.43 ± 0.23	97.14 ± 0.26	96.50 ± 0.29	95.22 ± 0.55	97.74 ± 0.22
[5000, 6000]	97.49 ± 0.21	97.39 ± 0.25	96.41 ± 0.28	95.01 ± 0.38	93.52 ± 0.80
[4000, 5000]	97.64 ± 0.23	97.49 ± 0.24	96.82 ± 0.21	95.40 ± 0.30	93.94 ± 0.61
[3000, 4000]	97.78 ± 0.21	97.60 ± 0.26	97.04 ± 0.24	95.89 ± 0.25	93.28 ± 0.28
[2000, 3000]	97.86 ± 0.20	97.70 ± 0.24	97.22 ± 0.24	95.91 ± 0.26	94.00 ± 0.38
[1000, 2000]	97.96 ± 0.21	97.80 ± 0.23	97.32 ± 0.26	96.39 ± 0.25	94.82 ± 0.42
[0, 1000]	97.96 ± 0.20	97.88 ± 0.22	97.51 ± 0.25	96.65 ± 0.29	95.43 ± 0.62

621     The integral of a probability density function is a number. To assign an uncertainty  
 622 to this number, the fractional integral is recomputed in a series of 500 pseudo-  
 623 experiments. Within each toy study, each shape parameter is assigned a value  
 624 sampled from a Gaussian distribution with a mean as the ‘nominal’ value of that  
 625 parameter, the value found by the fit, and with a width as the uncertainty on that  
 626 nominal value. Correlations between the different shape parameters are taken into  
 627 account. The variance on the deviation of the integrals, with respect to the integral  
 628 computed using the nominal shape parameter values, is taken as the square of the  
 629 uncertainty on the nominal integral value.

630     As the shape of some mass signal models are  $p_T$ - $y$  bin dependent, as described in  
 631 Section 5.5, the signal window efficiency is computed separately in each  $p_T$ - $y$  bin.  
 632 Tables 4.6 and C.13–C.15 give the per-bin efficiencies for each mode.

## 633 5 Yield extraction

634 The number of fully selected prompt signal candidates, for a given charm hadron in  
635 a given  $p_T$ - $y$  bin, is determined by a one-dimensional binned extended maximum  
636 likelihood fit to the charm hadron  $\ln \chi_{\text{IP}}^2$  distribution in the mass signal region of the  
637 fully selected dataset. This is performed simultaneously across all  $p_T$ - $y$  bins using  
638 the ROOFIT framework.

639 In this section we will define how the  $\ln \chi_{\text{IP}}^2$  fits are constructed, are the mass  
640 signal and background regions are defined, and how the mass fits are performed,  
641 which provide input to the  $\ln \chi_{\text{IP}}^2$  fits. The implementation of the fitter is the same  
642 as used for the 13 TeV measurement, hence the fit validation is not repeated and pull  
643 plots for the signal yield can be found in Ref. [7].

### 644 5.1 Definition of species

645 The species of interest for this analysis is ‘prompt’ signal, that is a charm hadron  
646 originating from the  $pp$  interaction point, whilst a signal decay originating from the  
647 decay of a long-lived  $b$ -hadron is ‘secondary’ signal. Combinatorial background is  
648 comprised of random combinations of tracks which have satisfied the full selection  
649 criteria. For the  $D^{*+}$  measurement, two additional species of data are considered:  
650 ‘random soft pion’ background, where a background soft pion from the event has  
651 been combined with the relevant ‘prompt’ signal charm hadron to form a fake prompt  
652 resonant candidate, and ‘secondary soft pion’ background, where a background soft  
653 pion from the event has been combined with the relevant ‘secondary’ signal charm  
654 hadron to form a fake secondary resonant candidate.

### 655 5.2 Overview

656 The prompt signal yield in each  $p_T$ - $y$  bin is measured by a binned extended maximum  
657 likelihood fit to the  $\ln \chi_{\text{IP}}^2$  distribution. This variable can discriminate between prompt  
658 and secondary signal as the generating probability density functions (PDFs) will be  
659 displaced with respect to one another (charm hadrons produced via  $b$ -decays will  
660 not point back to the PV, in general). The combinatorial background, however, is  
661 harder to discriminate against and model in  $\ln \chi_{\text{IP}}^2$ . Instead, a non-parametric model  
662 is taken from the mass sidebands, which is then normalised in the  $\ln \chi_{\text{IP}}^2$  fit to the  
663 number of combinatorial background candidates measured in the signal region with a  
664 fit to the charm hadron mass.

665 For all cases but the  $D^{*+}$  measurement, it is the mass of the charm hadron  
666 that is used to discriminate all signal from combinatorial background. For the  $D^{*+}$

667 measurement, the delta mass distribution, the difference between the reconstructed  
 668  $D^{*+}$  mass and the reconstructed  $D^0$  mass  $\delta m = m(D^{*+}) - m(D^0)$ , is used instead.

### 669 5.3 Mass fit

670 For each one-dimensional mass and  $\delta m$  fit, we assign one PDF per discriminatory  
 671 species: signal and combinatorial background. In both the mass and  $\delta m$  distributions,  
 672 the prompt and secondary signal shapes are assumed to be identical, and for the  $\delta m$   
 673 fits the combinatorial background is assumed to be indistinguishable from random  
 674 soft pion backgrounds. The total PDF is constructed as the sum of the per-species  
 675 PDFs, weighted by the respective species' yields

$$f(m) = \sum_{\text{Species}} N_{\text{Species}} \cdot f_{\text{Species}}(m), \quad (5.1)$$

$$f(\delta m) = \sum_{\text{Species}} N_{\text{Species}} \cdot f_{\text{Species}}(\delta m). \quad (5.2)$$

676 For every mass fit, the background PDF is taken to be a first-order polynomial,  
 677 and the signal PDF is mode-dependent, given in Section 5.5.

678 The joint combinatorial and random soft pion background in the  $\delta m$  fits is an  
 679 empirical function of the form

$$R(x; \delta m_0, A, B) = e^{B \cdot \delta m} \cdot (x - \delta m_0)^A, \quad (5.3)$$

680 where  $\delta m_0$  is a threshold value fixed to the charged pion rest mass  $m_{\pi^\pm} = 139.57$  MeV [14]  
 681 and the parameter  $B$  is fixed to zero. The signal PDF is the sum of three normal  
 682 distributions, sharing a common mean but allowed to have varying widths.

683 One such PDF,  $f(m)$  or  $f(\delta m)$ , is constructed per  $p_T$ - $y$  bin, and the likelihood is  
 684 formed as the product of these such that each PDF is fitted simultaneously when the  
 685 negative log-likelihood is minimised.

### 686 5.4 $\ln \chi_{\text{IP}}^2$ fit

687 The prompt and secondary signal distributions are modelled by continuous, paramet-  
 688 ric PDFs. Rather than attempting to parameterise the combinatorial background  
 689 distribution, a kernel density estimate (KDE) PDF, or ‘template’, is created from  
 690 the  $\ln \chi_{\text{IP}}^2$  distribution in the lower and upper sidebands of the reconstructed charm  
 691 hadron mass. In the case of the  $D^{*+}$  measurements, the upper sideband of the  $\delta m$   
 692 distribution is used instead. This approach assumes that the  $\ln \chi_{\text{IP}}^2$  shape in the

693 signal region is the same as that in the sidebands, *i.e.* that the mass and  $\ln \chi_{\text{IP}}^2$  are  
 694 uncorrelated in the background sample.

695 The ‘signal region’ in each long-lived charm hadron mass distribution is defined as  
 696 a 40 MeV-wide window centred on the nominal rest mass of the given charm hadron,  
 697 taken to be  $m_{D^0} = 1864.84$  MeV,  $m_{D^+} = 1869.61$  MeV, and  $m_{D_s^+} = 1968.30$  MeV [14].  
 698 The ‘lower sideband’ is a 20 MeV-wide window centred 50 MeV below the centre of the  
 699 signal window, and the ‘upper sideband’ is a 20 MeV-wide window centred 50 MeV  
 700 above the centre of the signal window. For the  $D^{*+}$  measurements, the ‘signal  
 701 region’ is defined as a window 6 MeV wide, centred on the nominal  $\delta m$  value of  
 702 145.43 MeV [14]. The ‘upper sideband’, or just ‘sideband’ as a ‘lower sideband’ region  
 703 is not defined, is defined as the region from 4.5 MeV to 9 MeV above the centre of  
 704 the signal region. Figures 5.1–5.4 show the signal and sideband regions for each  
 705 mode. A comparison between the  $\ln \chi_{\text{IP}}^2$  distributions in the two sidebands is shown  
 706 in Appendix A.

707 The integral of the  $\ln \chi_{\text{IP}}^2$  background template PDF is constrained to be near  
 708 the number of background candidates in the signal region. This is measured with  
 709 the binned extended maximum likelihood fit to the charm hadron mass distribution,  
 710 or the  $\delta m$  distribution in the  $D^0$  mass signal region for the  $D^{*+}$  measurements, as  
 711 described in Section 5.3. To avoid any complications due to correlations between the  
 712 background template PDF and the fitted data, only the data in signal region is used  
 713 in the  $\ln \chi_{\text{IP}}^2$  fit. For the  $D^{*+}$  measurements, this signal region requirement is made  
 714 in both the  $D^0$  mass and the  $\delta m$  distributions.

715 For each one-dimensional  $\ln \chi_{\text{IP}}^2$  fit, we assign one PDF per discriminatory species:  
 716 prompt signal, secondary signal, and combinatorial background. The total PDFs  
 717 are constructed as the sum of per-species PDFs, weighted by the respective species’  
 718 yields

$$f(\ln \chi_{\text{IP}}^2) = \sum_{\text{Species}} N_{\text{Species}} \cdot f_{\text{Species}}(\ln \chi_{\text{IP}}^2). \quad (5.4)$$

719 The constraint on the background yield is applied by multiplying  $f(\ln \chi_{\text{IP}}^2)$  by a  
 720 normal distribution whose mean is the number of background candidates  $N$  measured  
 721 by the mass fit and whose width is the uncertainty on  $N$  returned by the fitter.

722 One such PDF,  $f(\ln \chi_{\text{IP}}^2)$ , and background constraint is constructed per  $p_{\text{T}}\text{-}y$  bin,  
 723 and the likelihood is formed as the product of these such that each PDF is fitted  
 724 simultaneously when the negative log-likelihood is minimised. The benefit of this  
 725 construction is that some shape parameters can be shared across bins, reducing the  
 726 uncertainty on the fit parameters. Which parameters are shared across bins and  
 727 which are fitted independently is mode-dependent, given in Section 5.5.

728 We choose to model the prompt signal  $\ln \chi_{\text{IP}}^2$  distribution with a modified normal

729 distribution  $H$ , where the width is allowed to be asymmetric with respect to the  
 730 mean and the tails are described by exponential functions

$$H(x; \mu, \sigma, \epsilon, \rho_L, \rho_R) = \begin{cases} \exp\left(\frac{\rho_L^2}{2} + \rho_L \frac{x-\mu}{(1-\epsilon)\sigma}\right) & x < \mu - (\rho_L \sigma(1-\epsilon)), \\ \exp\left(-\left(\frac{x-\mu}{\sqrt{2}\sigma(1-\epsilon)}\right)^2\right) & \mu - (\rho_L \sigma(1-\epsilon)) \leq x < \mu, \\ \exp\left(-\left(\frac{x-\mu}{\sqrt{2}\sigma(1+\epsilon)}\right)^2\right) & \mu \leq x < \mu + (\rho_R \sigma(1+\epsilon)), \\ \exp\left(\frac{\rho_R^2}{2} - \rho_R \frac{x-\mu}{(1+\epsilon)\sigma}\right) & x \geq \mu + (\rho_R \sigma(1+\epsilon)), \end{cases} \quad (5.5)$$

731 where the parameter  $\mu$  is the mode of the distribution,  $\sigma$  is the average of the left  
 732 and right widths,  $\epsilon$  is the asymmetry of the left and right widths, and  $\rho_{L(R)}$  is the  
 733 exponent for the left (right) tail. The secondary signal distribution is modelled by a  
 734 normal distribution  $G$  with mean  $\mu$  and width  $\sigma$

$$G(x; \mu, \sigma) = e^{-\frac{(x-\mu)^2}{2\sigma^2}}. \quad (5.6)$$

735 These shapes are motivated by the  $\ln \chi_{\text{IP}}^2$  distributions for prompt and secondary  
 736 signal decays observed in the MC samples.

737 Given the large number of parameters to be fitted, some shape parameters are  
 738 fixed to values obtained from ‘prefits’ to samples of prompt and secondary signal MC.  
 739 The set of parameters that are fixed is mode-dependent, given in Section 5.5.

## 740 5.5 Mode-specific details

741 As different modes exhibit different features in the mass,  $\delta m$ , and  $\ln \chi_{\text{IP}}^2$  distributions,  
 742 several aspects of the fits are different between modes. This sections gives the list  
 743 of parameters that are split between  $p_{\text{T}}\text{-}y$  bins, and the list of parameters that are  
 744 allowed to float after the fit to MC data, for each mode.

745 We initially assume no knowledge of which parameters should be independent (to  
 746 be ‘split’) across the  $p_{\text{T}}\text{-}y$  bins, nor of whether the  $\ln \chi_{\text{IP}}^2$  distribution is well-modelled  
 747 by the MC, and so we adjust the parameterisation to best describe the data. For  
 748 the mass fits, all parameters are initially made to be the same across all  $p_{\text{T}}\text{-}y$  bins,  
 749 and are then split one by one when it is observed that a feature varies across the  
 750 bins, such as the width of the signal peak. All parameters of the  $\ln \chi_{\text{IP}}^2$  fits are first  
 751 kept fixed to values found from the fits to the simulated data, and then individual  
 752 parameters are floated if the total PDF does not model the data well. Parameters  
 753 are then split across  $p_{\text{T}}\text{-}y$  bins in the same manner as in the mass fits.

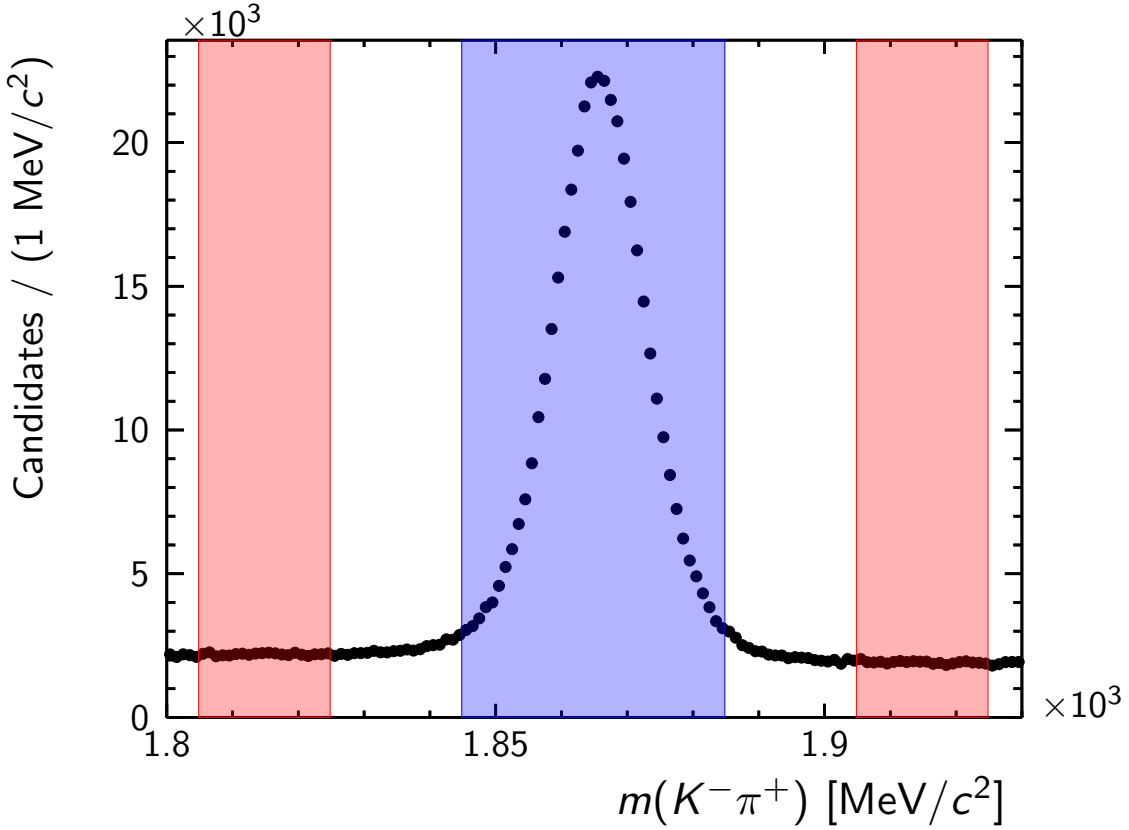


*Figure 5.1: Definition of signal window, in blue, and sidebands, in red, for  $D^0 \rightarrow K^-\pi^+$  candidates. The signal window is  $\pm 20\text{ MeV}$  either side of the nominal  $D^0$  mass of  $1864.84\text{ MeV}$  [14]. The upper and lower sidebands are each  $20\text{ MeV}$  wide, with the lower sideband ending  $40\text{ MeV}$  below the nominal  $D^0$  mass and the upper sideband beginning  $40\text{ MeV}$  above the nominal  $D^0$  mass. The full dataset is shown.*

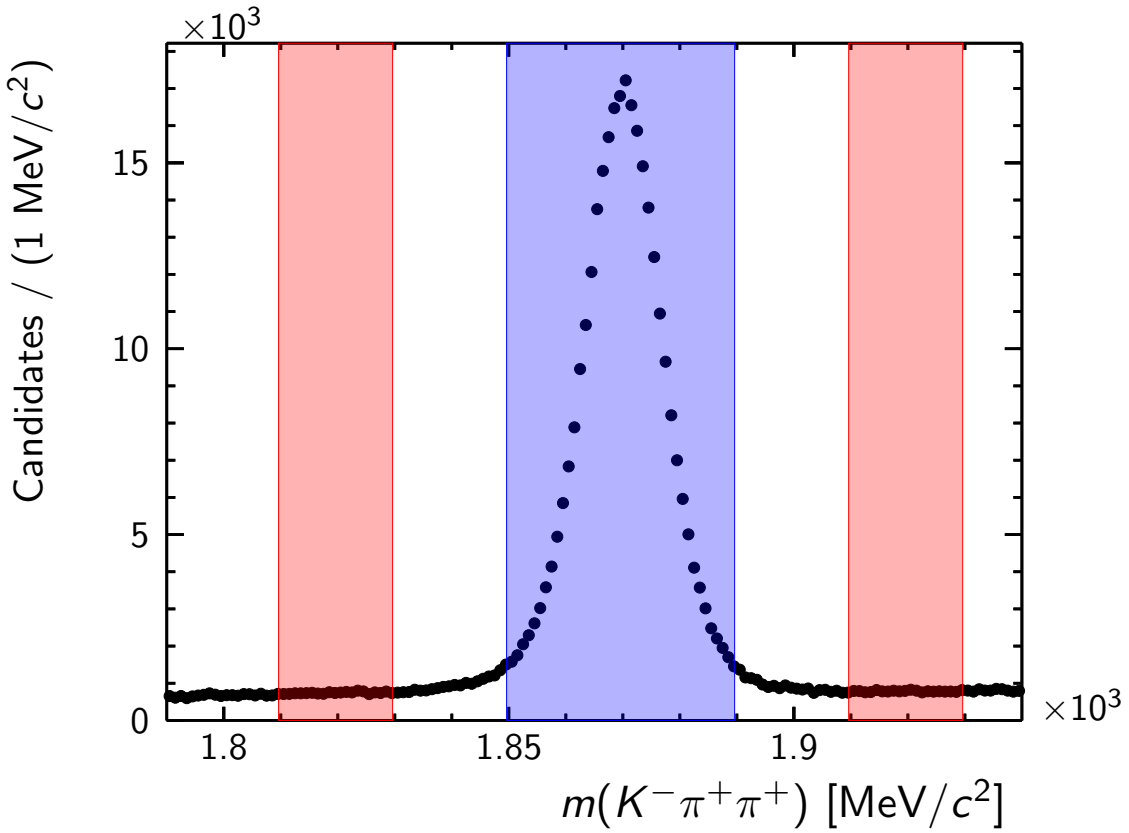


*Figure 5.2: Definition of signal window, in blue, and sidebands, in red, for  $D^+ \rightarrow K^-\pi^+\pi^+$  candidates. The signal window is  $\pm 20$  MeV either side of the nominal  $D^+$  mass of 1869.61 MeV [14]. The upper and lower sidebands are each 20 MeV wide, with the lower sideband ending 40 MeV below the nominal  $D^+$  mass and the upper sideband beginning 40 MeV above the nominal  $D^+$  mass. The full dataset is shown.*

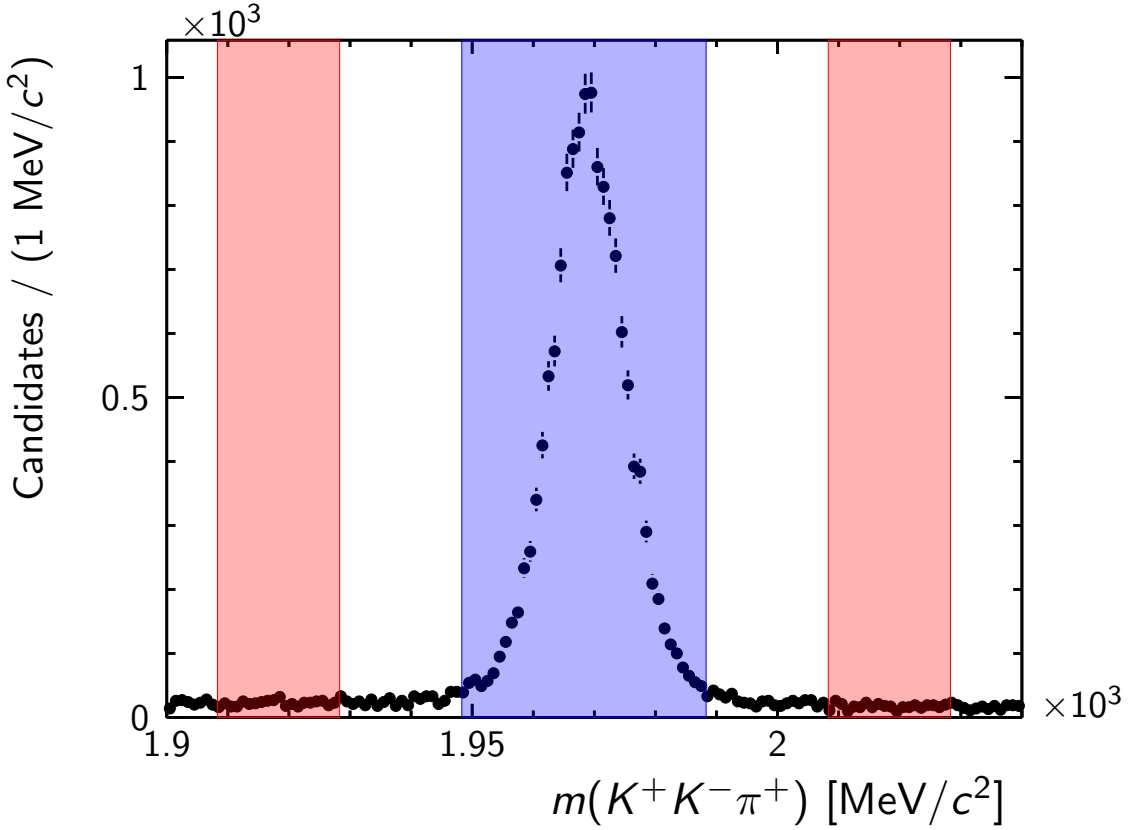


*Figure 5.3: Definition of signal window, in blue, and sidebands, in red, for  $D_s^+ \rightarrow \phi\pi^+$  candidates. The signal window is  $\pm 20$  MeV either side of the nominal  $D_s^+$  mass of  $1968.30$  MeV [14]. The upper and lower sidebands are each  $20$  MeV wide, with the lower sideband ending  $40$  MeV below the nominal  $D_s^+$  mass and the upper sideband beginning  $40$  MeV above the nominal  $D_s^+$  mass. The full dataset is shown.*

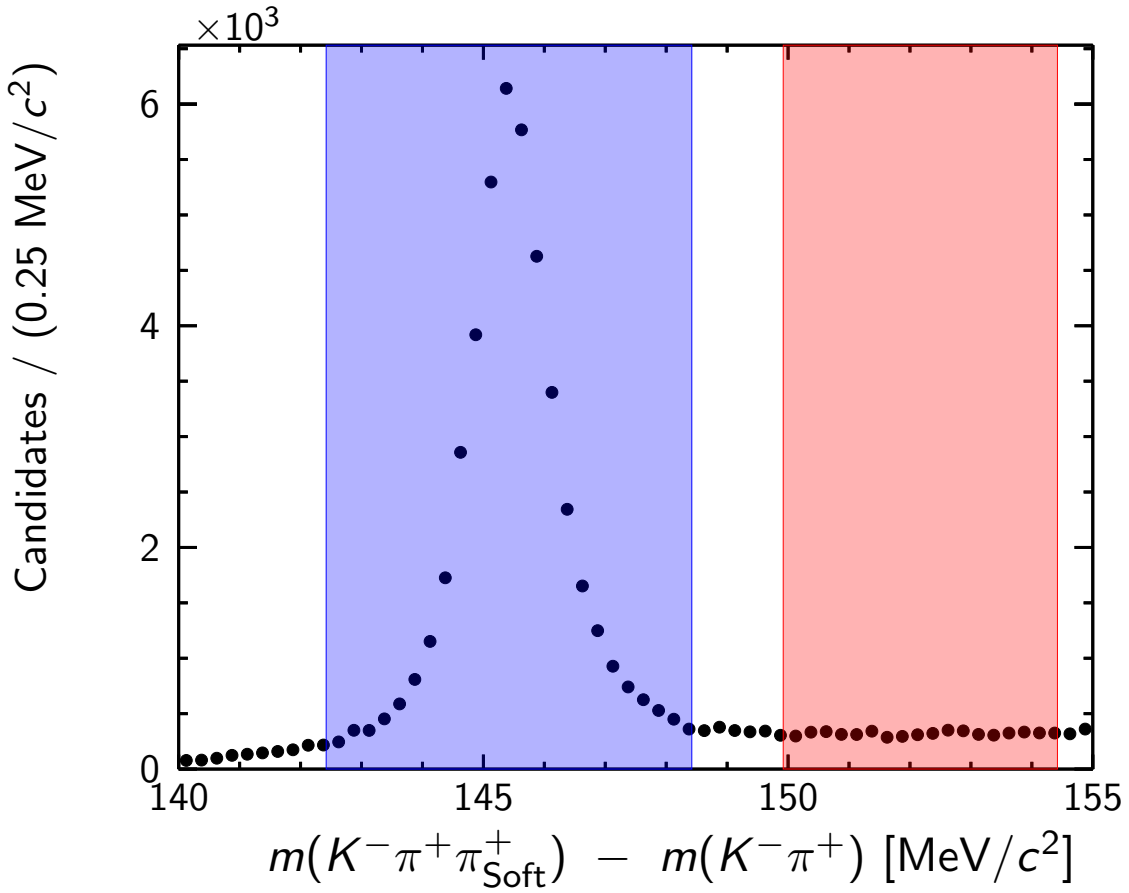


Figure 5.4: Definition of signal window, in blue, and sidebands, in red, for  $D^{*+} \rightarrow D^0\pi^+$ , with  $D^0 \rightarrow K^-\pi^+$ , candidates. The signal window is  $\pm 3$  MeV either side of the nominal  $\delta m = m(D^{*+}) - m(D^0)$  mass of 145.43 MeV [14]. The upper sideband is 4.5 MeV wide, beginning 4.5 MeV above the nominal  $\delta m$  value. The full dataset within the  $D^0$  signal region, defined in Section 5.2 and shown in Figure 5.1, is shown.

754 **Fit details for  $D^0$**

755 For the  $D^0 \rightarrow K^-\pi^+$  mode, the signal shape in the mass fit is the sum of a normal  
756 and a Crystal Ball distribution, sharing a common mean but allowed to have different  
757 widths. The mean and width of the signal mass PDF are split across  $p_T\text{-}y$  bins, as  
758 is the slope of the background mass PDF. The mean of the  $\ln \chi_{\text{IP}}^2$  prompt signal  
759 PDF and the width of the secondary signal PDF are also split across  $p_T\text{-}y$  bins. The  
760 mean and width of the prompt signal  $\ln \chi_{\text{IP}}^2$  PDF and all parameters of the secondary  
761 signal  $\ln \chi_{\text{IP}}^2$  PDF are floated in the fit, and all other  $\ln \chi_{\text{IP}}^2$  shape parameters fixed to  
762 the values from MC.

763 Prefits to the prompt signal and secondary signal data samples in  $\ln \chi_{\text{IP}}^2$  are given  
764 in Figure 5.5.

765 **Fit details for  $D^+$**

766 For the  $D^+ \rightarrow K^-\pi^+\pi^+$  mode, the signal shape in the mass fit is the sum of a normal  
767 and a Crystal Ball distribution, sharing a common mean but allowed to have different widths. The mean of the signal mass PDF as well as the width of the Crystal  
768 Ball component in the mass PDF are split across  $p_T\text{-}y$  bins, as is the slope of the  
769 background mass PDF. The mean of the  $\ln \chi_{\text{IP}}^2$  prompt signal and secondary signal  
770 distributions are split across  $p_T\text{-}y$  bins. The mean and tail parameters of the signal  
771  $\ln \chi_{\text{IP}}^2$  PDF, are floated during the final fit, with all other shape parameters fixed to  
772 the values from MC.

774 Prefits to the prompt signal and secondary signal data samples in  $\ln \chi_{\text{IP}}^2$  are given  
775 in Figure 5.6.

776 **Fit details for  $D_s^+$**

777 For the  $D_s^+ \rightarrow \phi\pi^+$  mode, the signal shape in the mass fit is the sum of two normal  
778 distributions, sharing a common mean but allowed to have different widths. The  
779 mean and width of the signal mass PDF and the slope of the background mass PDF,  
780 along with the mean of the  $\ln \chi_{\text{IP}}^2$  prompt signal PDF, are split across  $p_T\text{-}y$  bins.  
781 The mean of the prompt signal  $\ln \chi_{\text{IP}}^2$  PDF and all parameters of the secondary PDF  
782 are floated during the final fit, with all other shape parameters fixed to the values  
783 from MC.

784 Prefits to the prompt signal and secondary signal data samples in  $\ln \chi_{\text{IP}}^2$  are given  
785 in Figure 5.7.

786 **Fit details for  $D^{*+}$**

787 For the  $D^{*+}$ -tagged  $D^0 \rightarrow K^- \pi^+$  mode, the width of the widest component of the  
788 signal model, described in Section 5.3, is split across  $p_T$ - $y$  bins, along with the mean  
789 of the prompt signal  $\ln \chi_{\text{IP}}^2$  PDF. The mean of the prompt signal  $\ln \chi_{\text{IP}}^2$  PDF and all  
790 parameters of the secondary PDF are floated during the final fit, with all other shape  
791 parameters fixed to the values from MC.

792 Prefits to the prompt signal and secondary signal data samples in  $D^0 \ln \chi_{\text{IP}}^2$  are  
793 given in Figure 5.8.

794 **5.6 Fit results**

795 For each fit, the covariance matrix is checked to be positive definite, and the goodness-  
796 of-fit within each  $p_T$ - $y$  bin is checked visually to ensure that the negative log-likelihood  
797 converge to a sensible minimum. Integrated mass,  $\delta m$ , and  $\ln \chi_{\text{IP}}^2$  fits are given in  
798 Figures 5.9–5.17. Prompt signal yields per  $p_T$ - $y$  bin are given in Tables 5.1–5.4

799 The  $\ln \chi_{\text{IP}}^2$  fits in each  $p_T$ - $y$  have been omitted from this section for brevity, but  
800 are given in Appendix B.

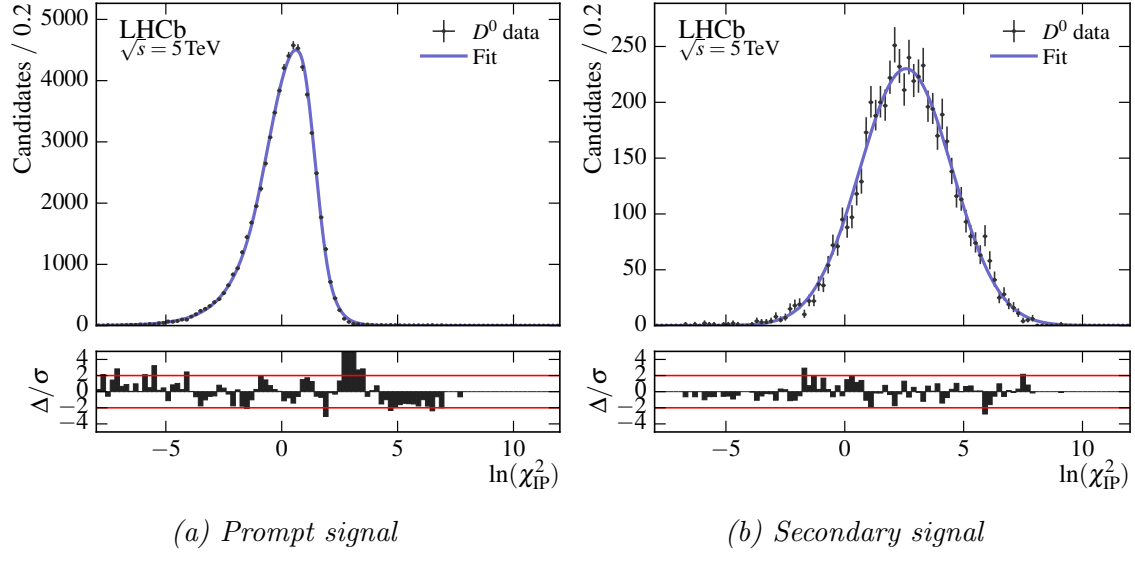


Figure 5.5: Integrated  $\ln \chi_{\text{IP}}^2$  prefits for  $D^0 \rightarrow K^- \pi^+$  in the prompt signal and secondary signal sample. The data and fit curves shown are the sum of the individual  $p_{\text{T}}\text{-}y$  bin contributions.

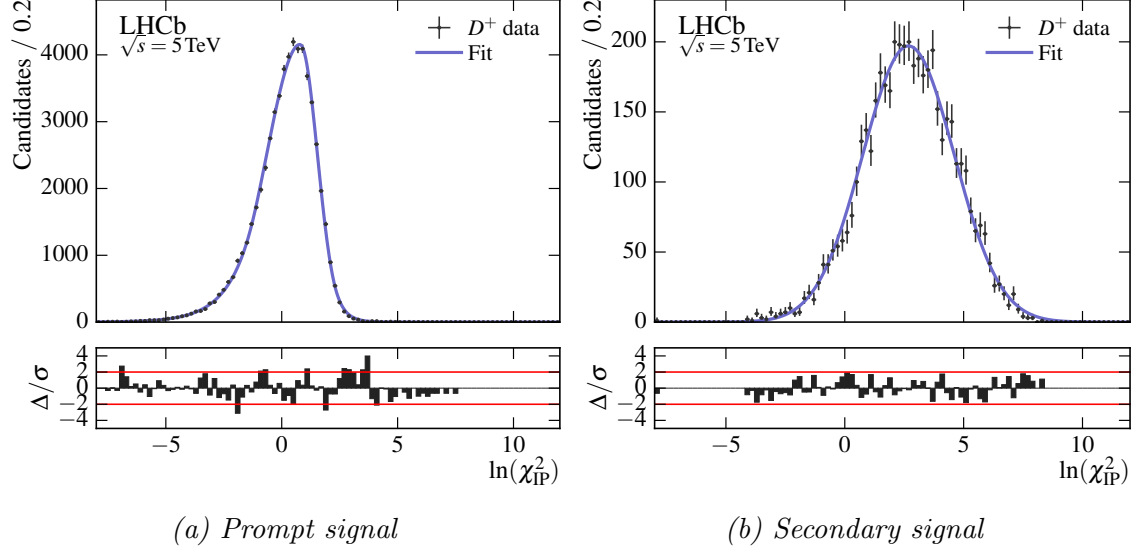


Figure 5.6: Integrated  $\ln \chi_{\text{IP}}^2$  prefits for  $D^+ \rightarrow K^- \pi^+ \pi^+$  in the prompt signal and secondary signal sample. The data and fit curves shown are the sum of the individual  $p_{\text{T}}\text{-}y$  bin contributions.

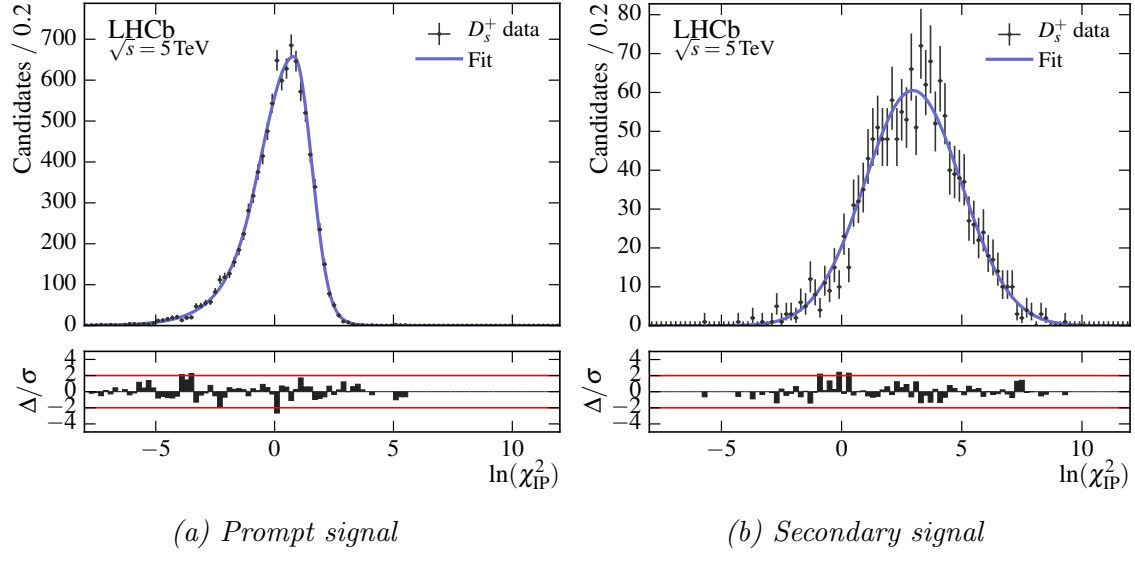


Figure 5.7: Integrated  $\ln \chi^2_{\text{IP}}$  prefits for  $D^+ \rightarrow \phi \pi^+$  in the prompt signal and secondary signal sample. The data and fit curves shown are the sum of the individual  $p_T$ - $y$  bin contributions.

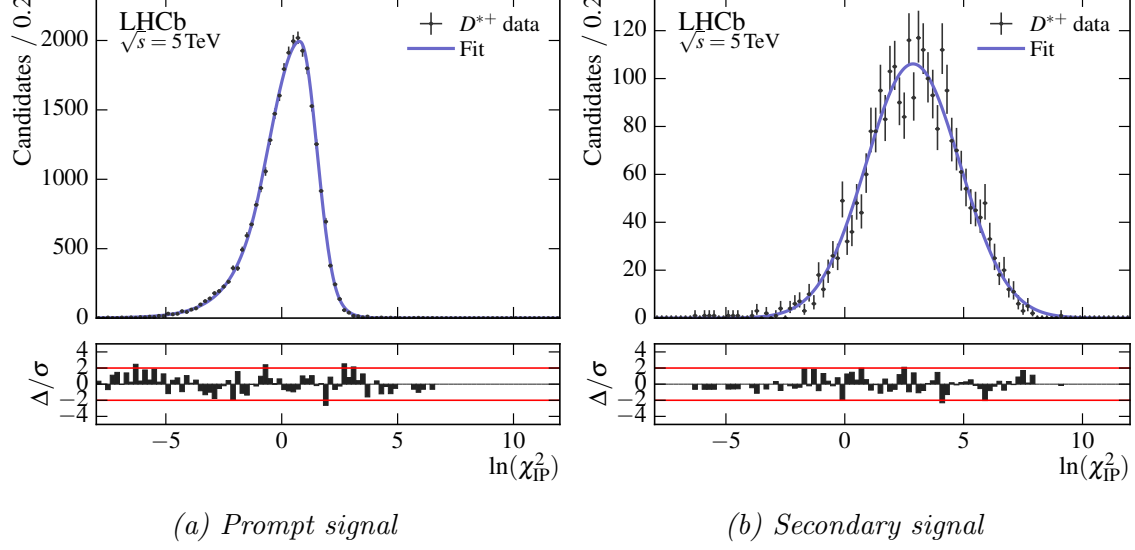


Figure 5.8: Integrated  $\ln \chi^2_{\text{IP}}$  prefits for  $D^{*+} \rightarrow D^0 \pi^+$ , with  $D^0 \rightarrow K^- \pi^+$ , in the prompt signal and secondary signal sample. The data and fit curves shown are the sum of the individual  $p_T$ - $y$  bin contributions.

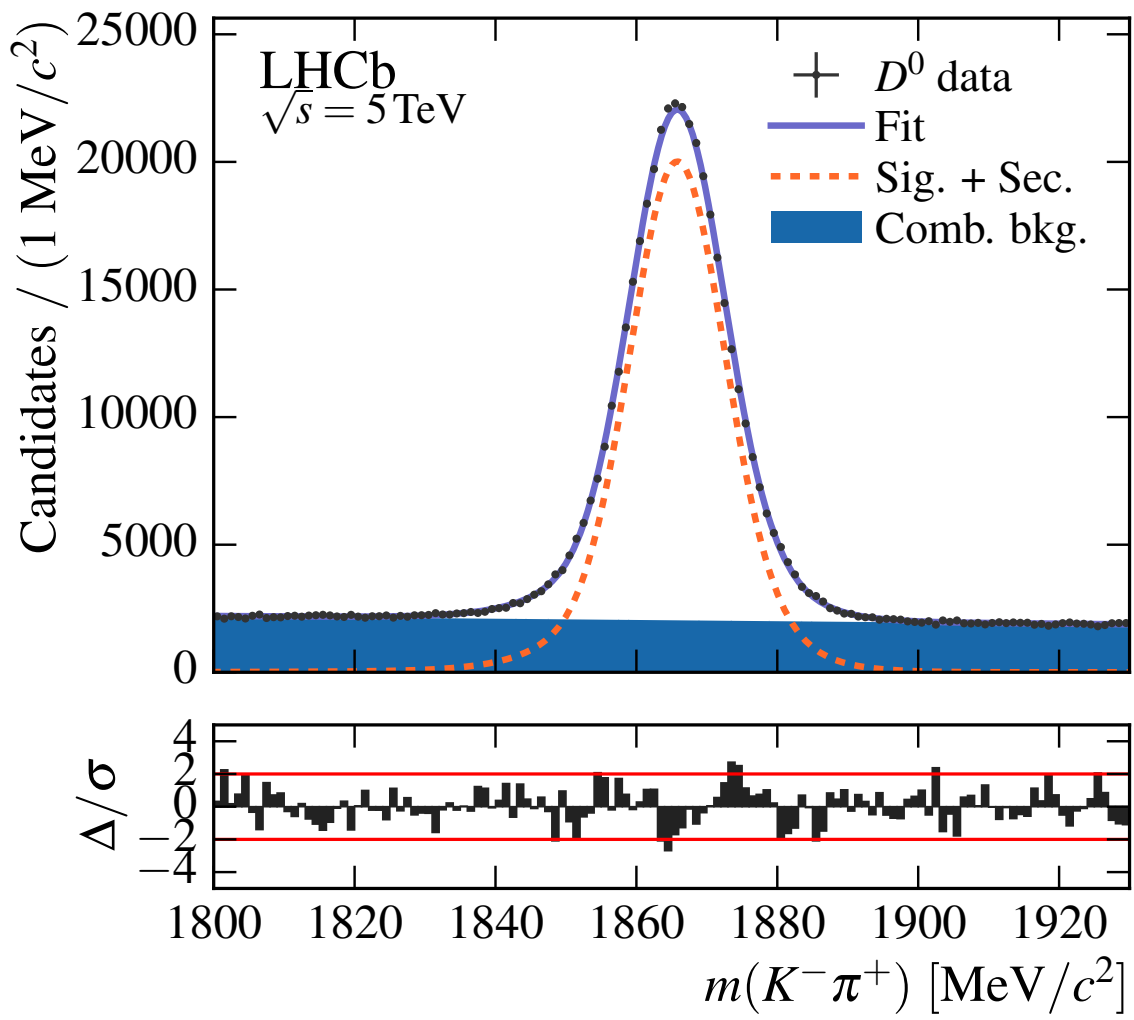


Figure 5.9: Integrated mass fit result for  $D^0 \rightarrow K^-\pi^+$ . The data and curve shown are the sum across all  $\text{pt-}y$  bins. Per-bin fits are given in Appendix B.1.

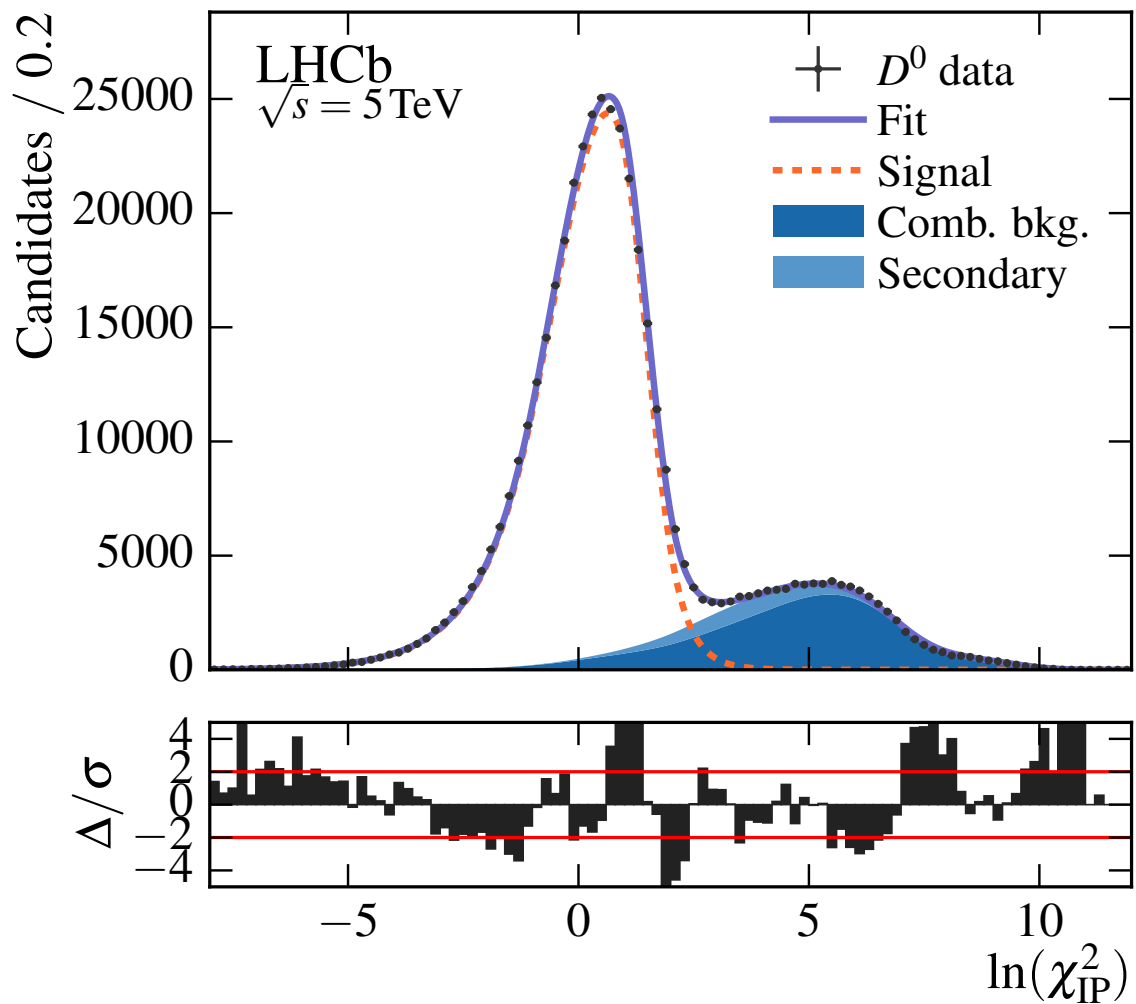


Figure 5.10: Integrated  $\ln \chi^2_{\text{IP}}$  fit result for  $D^0 \rightarrow K^- \pi^+$ . The data and curve shown are the sum across all  $p_{\text{T}}\text{-}y$  bins. Per-bin fits are given in Appendix B.1.

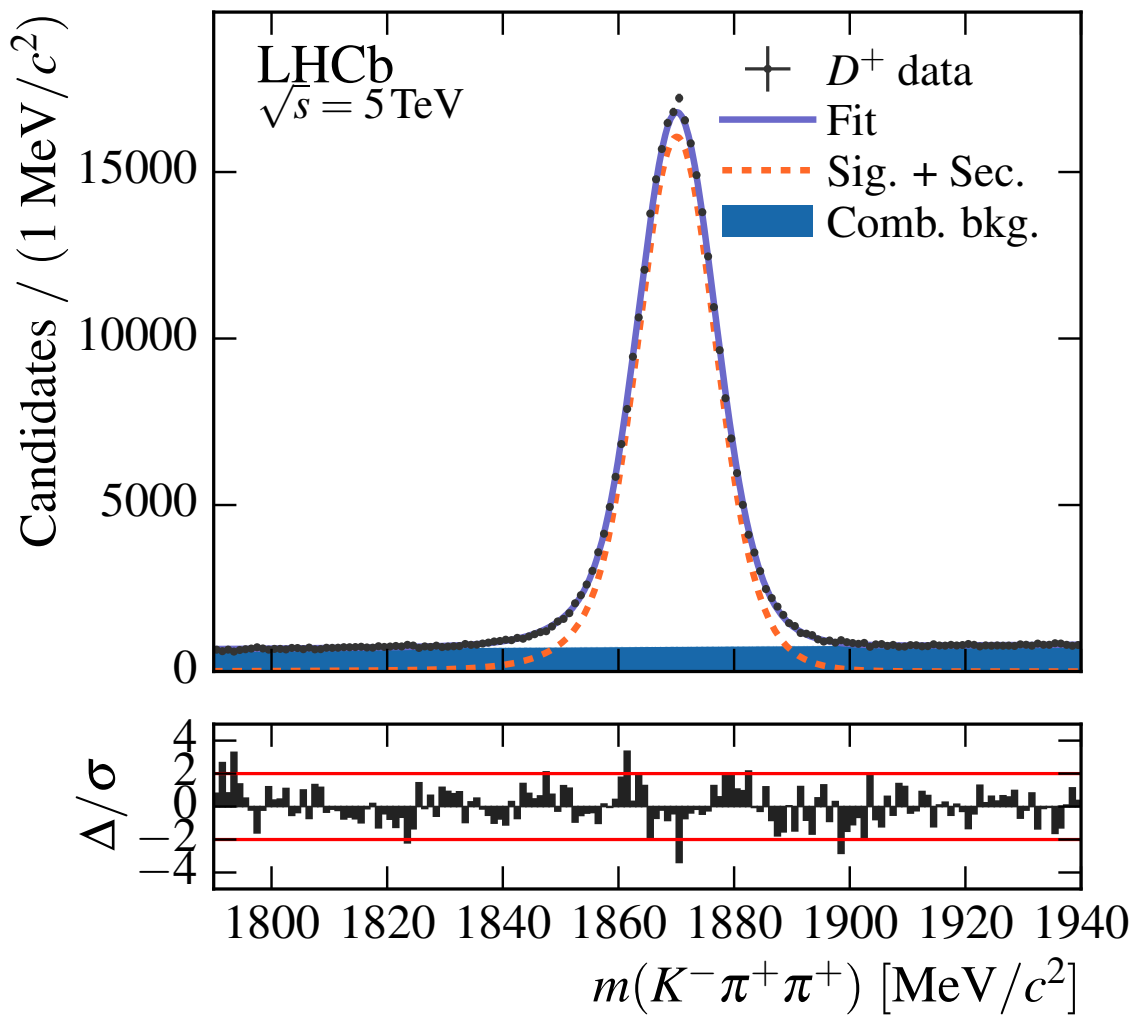


Figure 5.11: Integrated mass fit result for  $D^+ \rightarrow K^-\pi^+\pi^+$ . The data and curve shown are the sum across all  $p_T$ - $y$  bins. Per-bin fits are given in Appendix B.2.

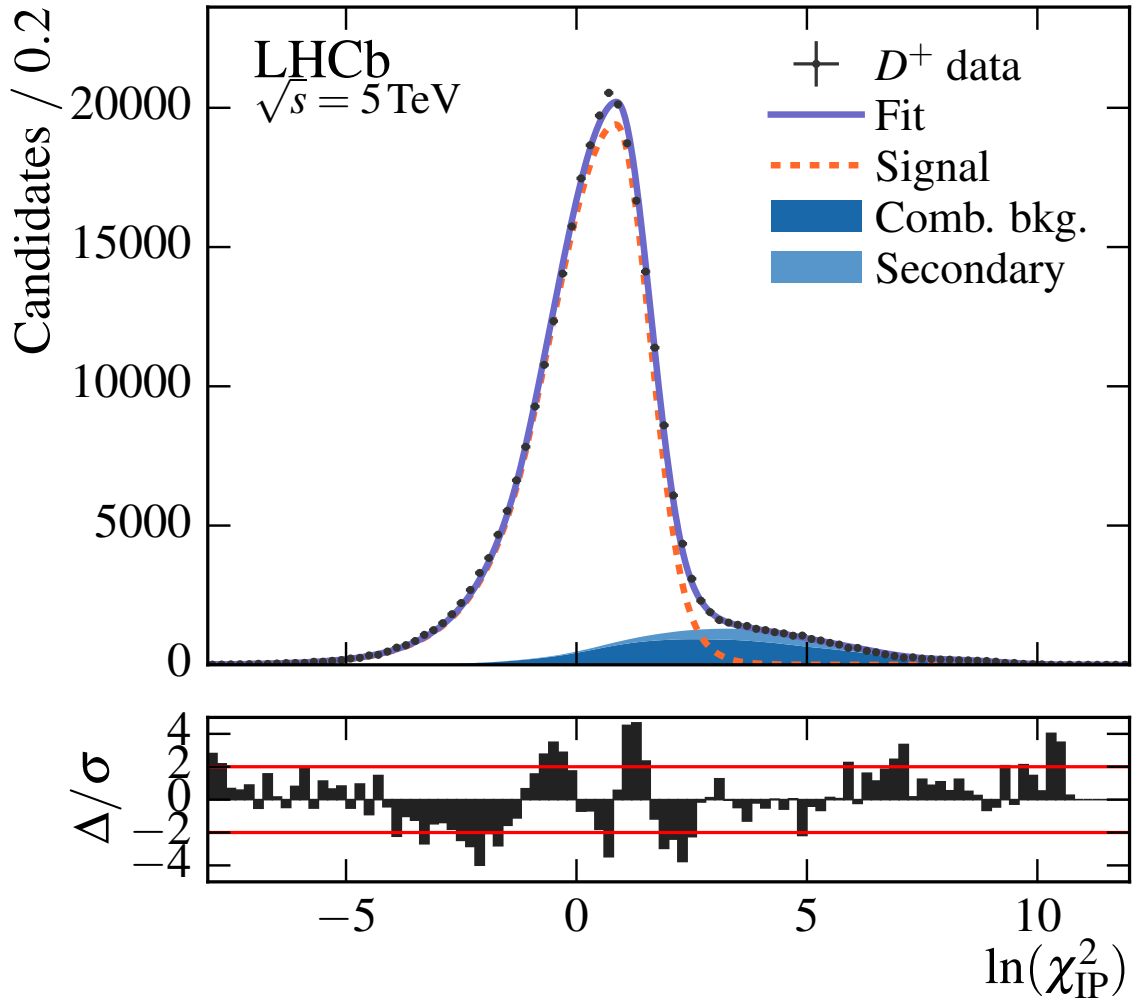


Figure 5.12: Integrated  $\ln \chi^2_{\text{IP}}$  fit result for  $D^+ \rightarrow K^- \pi^+ \pi^+$ . The data and curve shown are the sum across all  $p_T$ - $y$  bins. Per-bin fits are given in Appendix B.2.

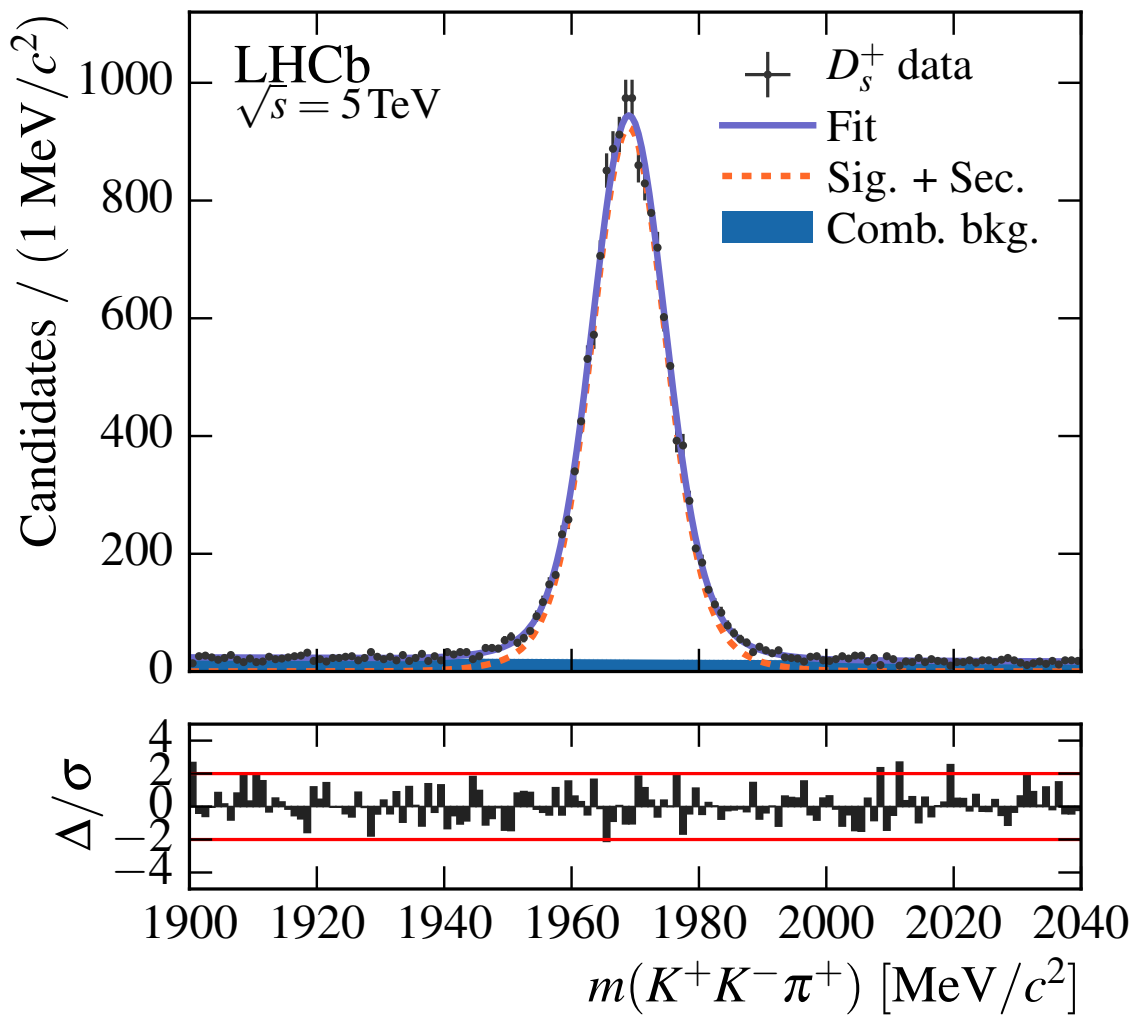


Figure 5.13: Integrated mass fit result for  $D_s^+ \rightarrow \phi\pi^+$ . The data and curve shown are the sum across all  $\text{pt}\text{-}y$  bins. Per-bin fits are given in Appendix B.3.

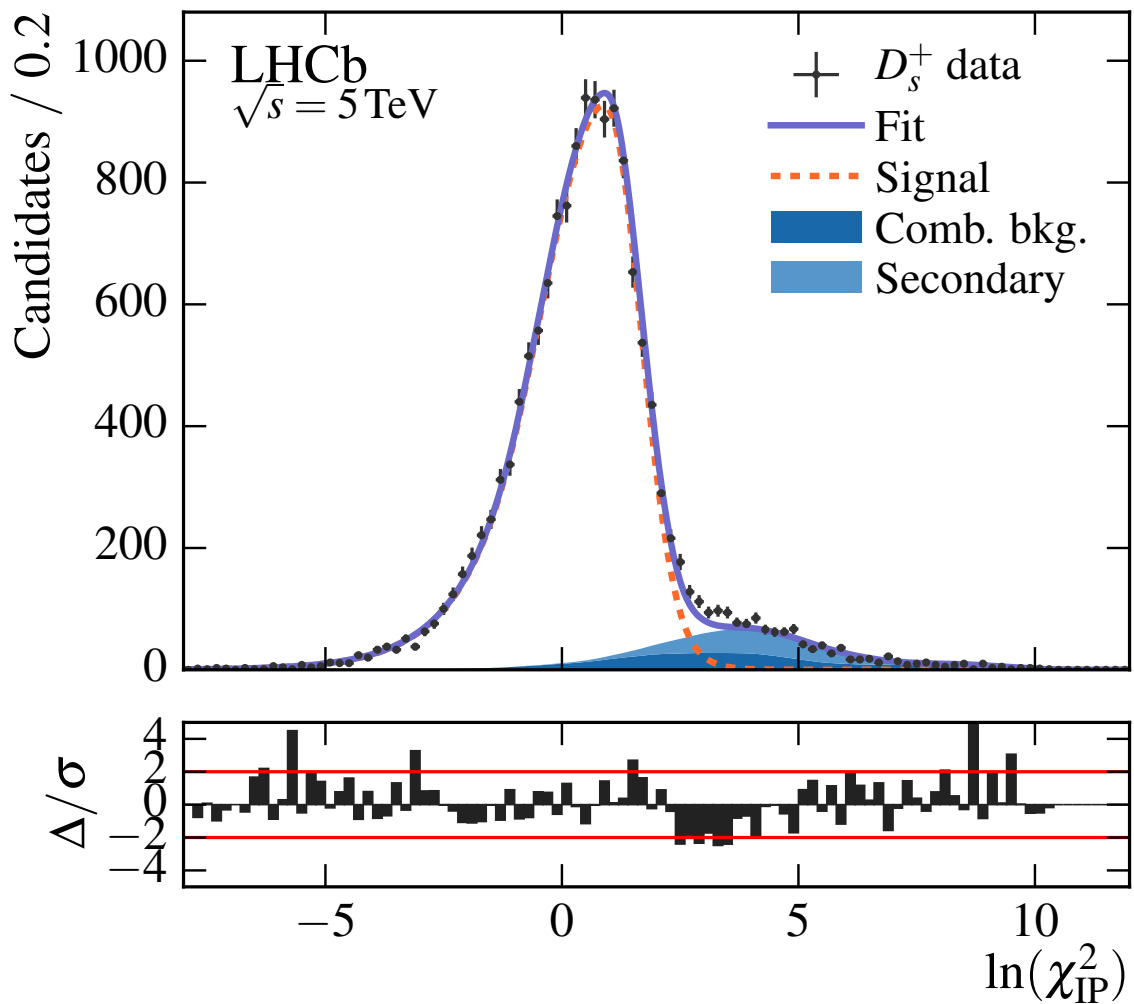


Figure 5.14: Integrated  $\ln \chi^2_{\text{IP}}$  fit result for  $D_s^+ \rightarrow \phi \pi^+$ . The data and curve shown are the sum across all pt-y bins. Per-bin fits are given in Appendix B.3.

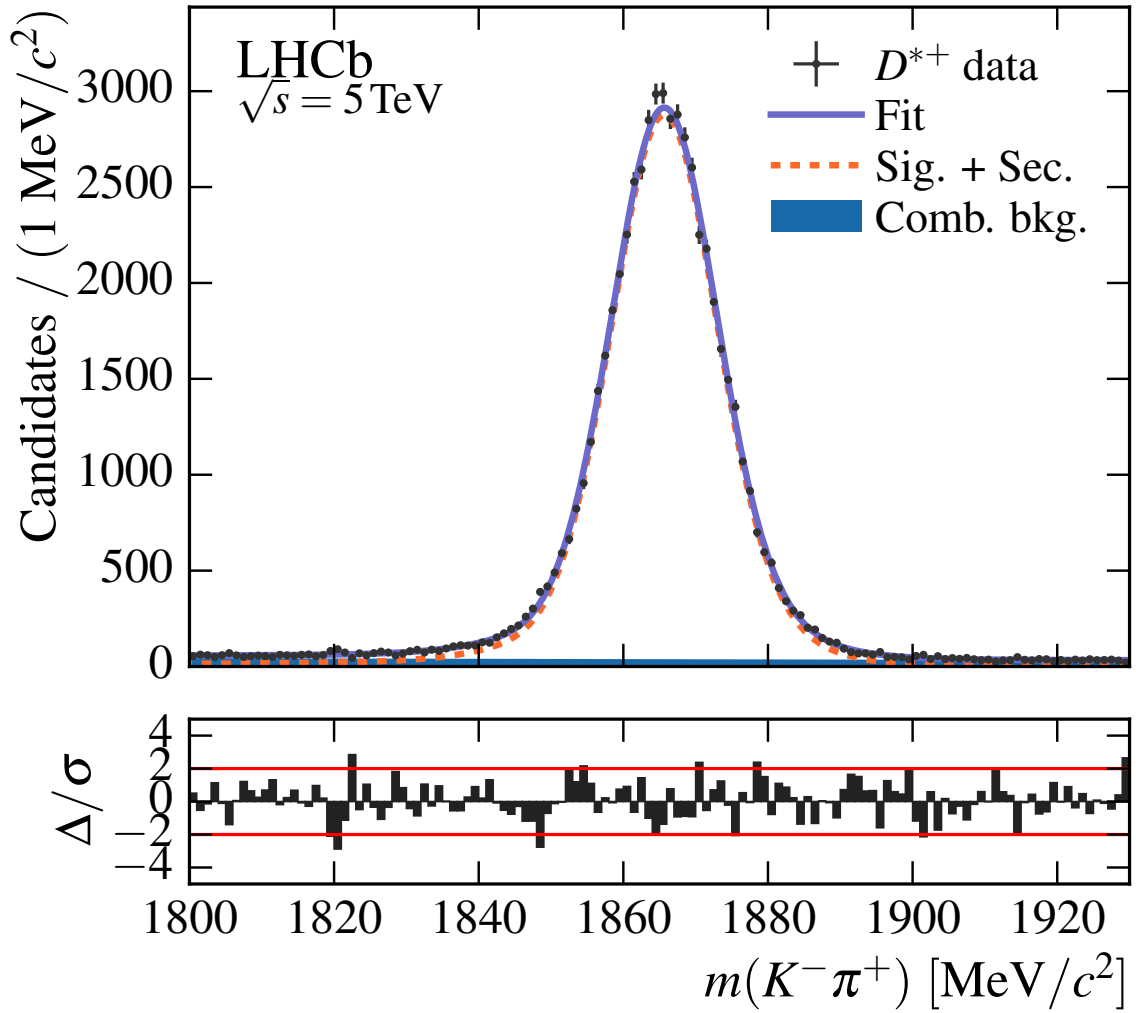


Figure 5.15: Integrated  $D^0$  mass fit result for  $D^{*+} \rightarrow D^0\pi^+$  with  $D^0 \rightarrow K^-\pi^+$ . The data and curve shown are the sum across all  $p_{\text{T}}\text{-}y$  bins. Per-bin fits are given in Appendix B.4.

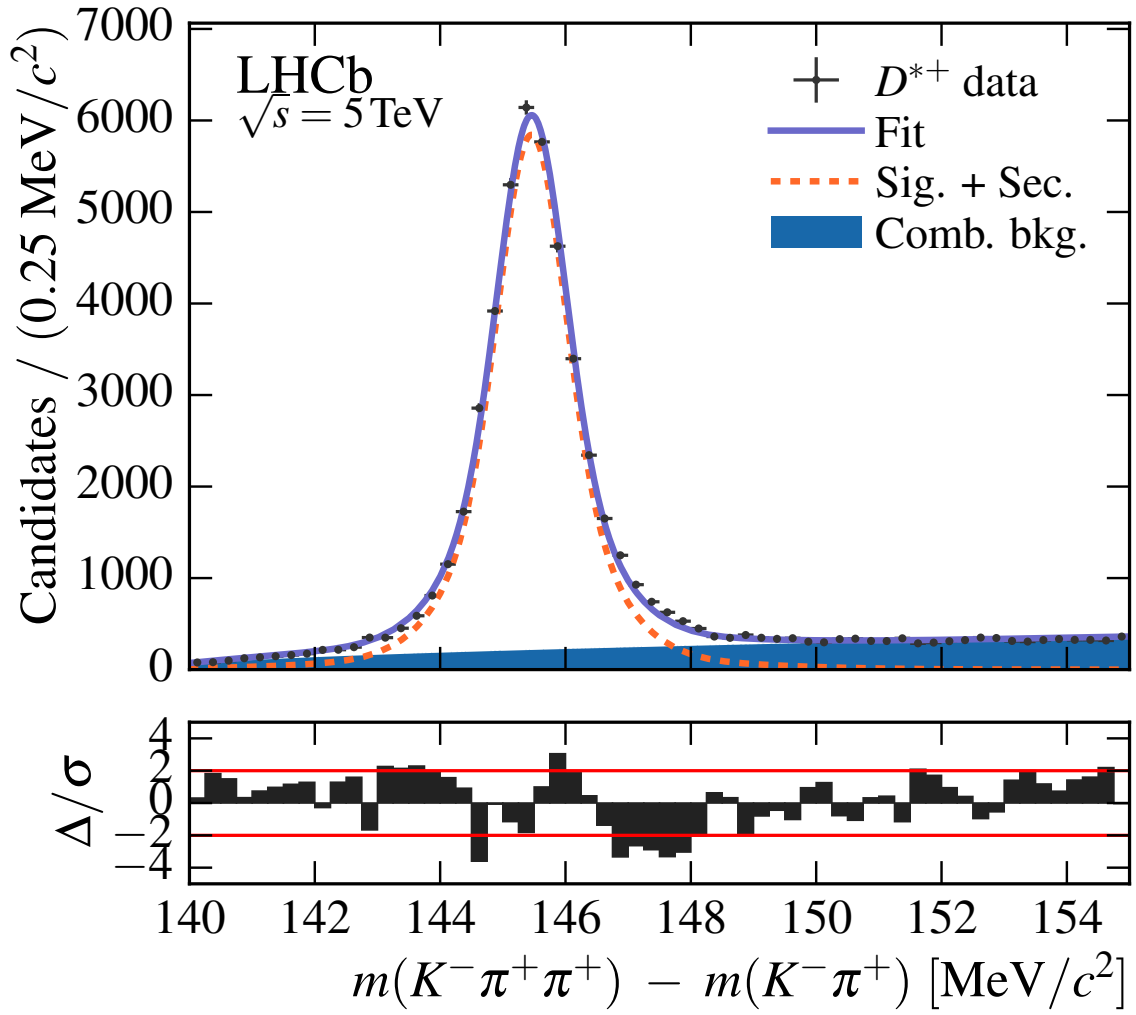


Figure 5.16: Integrated  $\delta m$  fit result for  $D^{*+} \rightarrow D^0\pi^+$  with  $D^0 \rightarrow K^-\pi^+$ . The data and curve shown are the sum across all  $p_{\text{T}}\text{-}y$  bins. Per-bin fits are given in Appendix B.4.

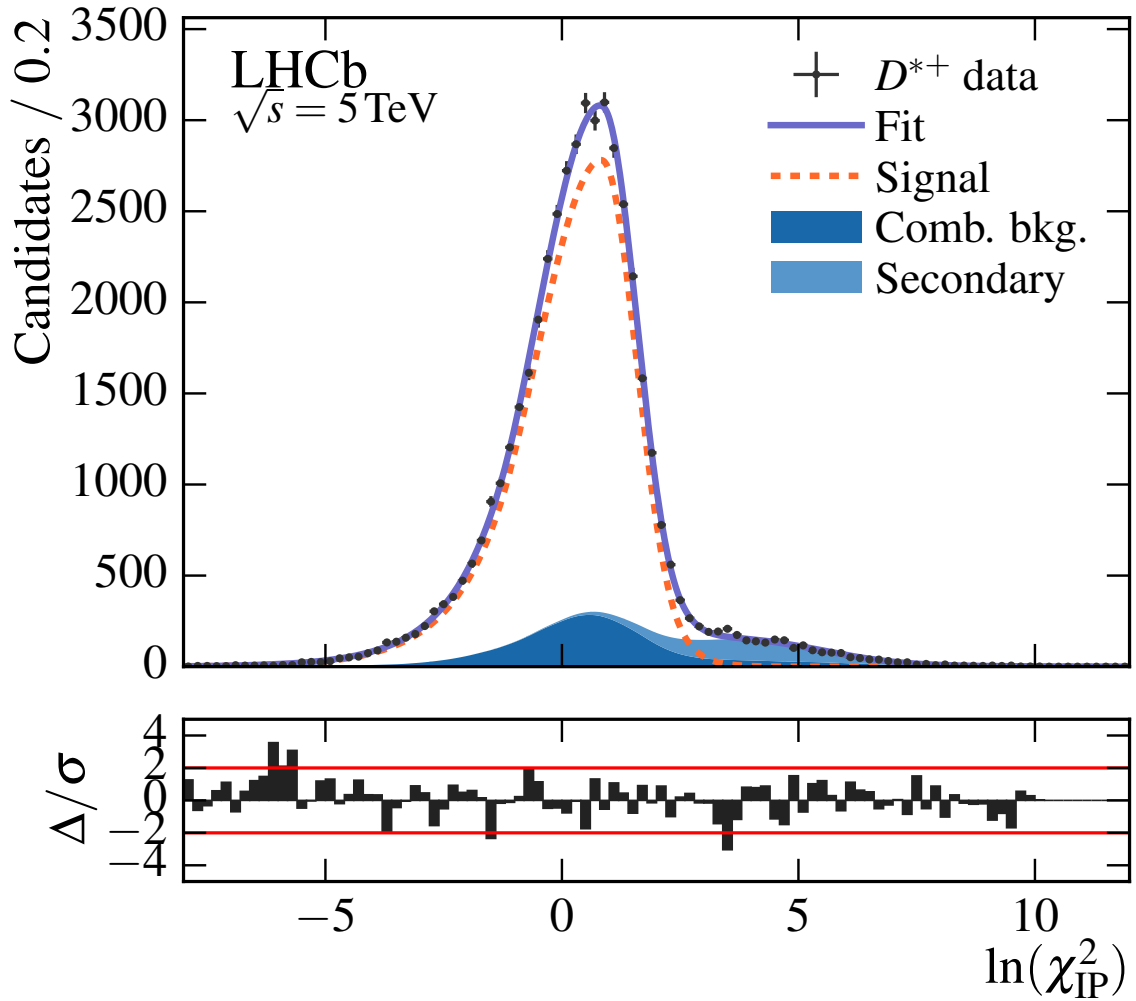


Figure 5.17: Integrated fit result for  $D^{*+} \rightarrow D^0\pi^+$  with  $D^0 \rightarrow K^-\pi^+$ . The data and curve shown are the sum across all  $p_T$ - $y$  bins. Per-bin fits are given in Appendix B.4.

Table 5.1: Prompt signal yields for  $D^0 \rightarrow K^- \pi^+$  in  $D^0$   $p_T$ - $y$  bins.

$p_T$ [MeV/ $c$ ]	$y$				
	[2, 2.5]	[2.5, 3]	[3, 3.5]	[3.5, 4]	[4, 4.5]
[0, 1000]	4027.8 ± 64.8	15171.9 ± 128.1	17368.1 ± 142.8	10814.8 ± 122.3	2805.7 ± 68.0
[1000, 2000]	8836.6 ± 95.2	29341.4 ± 174.2	29501.7 ± 177.3	17438.1 ± 141.2	4406.1 ± 72.7
[2000, 3000]	10255.1 ± 103.0	28468.9 ± 172.0	25519.1 ± 165.1	14296.7 ± 126.0	3323.5 ± 60.4
[3000, 4000]	8959.2 ± 96.2	20200.5 ± 145.1	16582.0 ± 133.6	8831.1 ± 97.1	1551.5 ± 40.6
[4000, 5000]	6199.0 ± 80.3	11572.5 ± 110.4	8930.7 ± 97.5	4450.6 ± 68.7	458.8 ± 21.8
[5000, 6000]	3762.5 ± 62.8	6211.7 ± 81.2	4618.0 ± 70.2	1860.9 ± 44.5	51.6 ± 7.3
[6000, 7000]	2352.3 ± 49.4	3196.8 ± 58.4	2400.7 ± 50.3	708.6 ± 27.1	
[7000, 8000]	1376.5 ± 37.8	1808.8 ± 43.9	1235.4 ± 36.1	199.1 ± 14.4	
[8000, 9000]	813.0 ± 29.4	1007.7 ± 32.9	596.4 ± 25.0	50.3 ± 7.1	
[9000, 10000]	526.1 ± 23.4	590.5 ± 25.0	268.3 ± 16.9		

Table 5.2: Prompt signal yields for  $D^+ \rightarrow K^-\pi^+\pi^+$  in  $D^+$   $p_{\text{T}}\text{-}y$  bins.

$p_{\text{T}}[\text{MeV}/c]$	$y$				
	[2, 2.5]	[2.5, 3]	[3, 3.5]	[3.5, 4]	[4, 4.5]
[0, 1000]		$166.6 \pm 15.4$	$444.9 \pm 26.5$	$385.4 \pm 26.9$	$95.9 \pm 28.4$
[1000, 2000]	$955.9 \pm 31.5$	$9288.3 \pm 101.7$	$14132.1 \pm 128.5$	$9654.5 \pm 108.7$	$2279.8 \pm 56.4$
[2000, 3000]	$4778.5 \pm 70.7$	$26280.5 \pm 168.6$	$30520.8 \pm 185.1$	$19620.0 \pm 151.4$	$4599.4 \pm 73.1$
[3000, 4000]	$6175.7 \pm 80.3$	$22426.6 \pm 155.0$	$22393.2 \pm 158.6$	$13631.7 \pm 125.7$	$3232.8 \pm 60.0$
[4000, 5000]	$5237.5 \pm 74.1$	$13531.2 \pm 120.8$	$12404.1 \pm 117.7$	$7070.2 \pm 89.1$	$1337.9 \pm 38.2$
[5000, 6000]	$3580.8 \pm 61.2$	$7645.4 \pm 91.0$	$6473.0 \pm 84.2$	$3396.3 \pm 61.2$	$432.3 \pm 21.4$
[6000, 7000]	$2381.8 \pm 49.9$	$4276.6 \pm 68.1$	$3468.5 \pm 61.4$	$1462.2 \pm 39.9$	$119.9 \pm 11.5$
[7000, 8000]	$1557.9 \pm 40.6$	$2484.8 \pm 51.4$	$1850.7 \pm 44.9$	$684.2 \pm 27.0$	
[8000, 9000]	$1005.9 \pm 32.4$	$1424.4 \pm 39.2$	$960.7 \pm 32.3$	$274.6 \pm 17.1$	
[9000, 10000]	$624.1 \pm 25.7$	$833.4 \pm 30.1$	$554.1 \pm 24.3$	$99.0 \pm 10.1$	

55

Table 5.3: Prompt signal yields for  $D_s^+ \rightarrow \phi\pi^+$  in  $D_s^+$   $p_{\text{T}}\text{-}y$  bins.

$p_{\text{T}}[\text{MeV}/c]$	$y$				
	[2, 2.5]	[2.5, 3]	[3, 3.5]	[3.5, 4]	[4, 4.5]
[1000, 2000]	$44.8 \pm 6.9$	$297.0 \pm 17.9$	$300.2 \pm 18.8$	$149.8 \pm 13.7$	$24.7 \pm 5.7$
[2000, 3000]	$365.7 \pm 19.5$	$1355.1 \pm 37.4$	$1238.1 \pm 36.4$	$585.6 \pm 25.6$	$102.3 \pm 11.1$
[3000, 4000]	$467.8 \pm 22.0$	$1279.0 \pm 36.5$	$1062.2 \pm 33.8$	$582.4 \pm 24.8$	$120.0 \pm 11.3$
[4000, 5000]	$403.1 \pm 20.4$	$856.3 \pm 30.1$	$689.1 \pm 27.2$	$341.7 \pm 18.9$	$68.0 \pm 8.4$
[5000, 6000]	$258.4 \pm 16.6$	$425.0 \pm 20.9$	$426.2 \pm 21.1$	$183.4 \pm 13.9$	$25.5 \pm 5.0$
[6000, 7000]	$173.9 \pm 13.3$	$269.1 \pm 16.8$	$193.3 \pm 14.3$	$88.3 \pm 9.8$	
[7000, 8000]	$128.1 \pm 11.5$	$155.5 \pm 12.6$	$113.5 \pm 10.9$	$49.2 \pm 7.1$	
[8000, 9000]	$60.8 \pm 8.3$	$82.9 \pm 9.4$	$63.2 \pm 8.3$	$22.7 \pm 4.7$	
[9000, 10000]	$49.2 \pm 7.4$	$57.3 \pm 7.6$	$34.6 \pm 5.9$		

Table 5.4: Prompt signal yields for  $D^{*+} \rightarrow D^0\pi^+$ , with  $D^0 \rightarrow K^-\pi^+$ , in  $D^{*+}$   $p_T$ - $y$  bins.

$p_T$ [MeV/ $c$ ]	[2, 2.5]	[2.5, 3]	$y$ [3, 3.5]	[3.5, 4]	[4, 4.5]
[1000, 2000]		667.9 $\pm$ 30.3	2783.1 $\pm$ 63.7	1822.4 $\pm$ 51.6	386.5 $\pm$ 23.0
[2000, 3000]	124.6 $\pm$ 12.4	2243.5 $\pm$ 52.7	4797.0 $\pm$ 79.6	2614.8 $\pm$ 60.5	568.1 $\pm$ 27.4
[3000, 4000]	451.8 $\pm$ 22.2	2861.5 $\pm$ 57.9	3813.9 $\pm$ 68.3	1857.6 $\pm$ 48.5	330.2 $\pm$ 20.5
[4000, 5000]	555.8 $\pm$ 24.8	2173.6 $\pm$ 49.4	2240.1 $\pm$ 50.7	1109.2 $\pm$ 35.8	105.4 $\pm$ 11.8
[5000, 6000]	467.4 $\pm$ 22.3	1318.3 $\pm$ 38.6	1112.2 $\pm$ 35.3	500.0 $\pm$ 24.1	33.3 $\pm$ 1.0
[6000, 7000]	357.2 $\pm$ 19.4	801.4 $\pm$ 29.4	604.6 $\pm$ 25.8	213.6 $\pm$ 15.4	
[7000, 8000]	224.0 $\pm$ 15.3	464.7 $\pm$ 22.4	334.1 $\pm$ 18.9	77.7 $\pm$ 9.1	
[8000, 9000]	139.9 $\pm$ 12.0	278.4 $\pm$ 17.3	185.9 $\pm$ 14.0	31.8 $\pm$ 5.6	
[9000, 10000]	113.6 $\pm$ 10.9	160.5 $\pm$ 13.0	118.4 $\pm$ 11.0		

## 6 Results

The cross-sections for prompt  $D^0$ ,  $D^+$ ,  $D_s^+$ , and  $D^{*+}$  hadrons in  $pp$  collisions at  $\sqrt{s} = 5 \text{ TeV}$  are given in Tables 6.3–6.6 in bins of charm hadron  $p_T$  and  $y$  as measured in the proton-proton collision rest frame. The cross-sections have been computed as

$$\sigma_i(H_c) = \frac{1}{\Delta p_T \Delta y} \cdot \frac{N_i(H_c \rightarrow f)}{\epsilon_i(H_c \rightarrow f) \cdot \mathcal{B}(H_c \rightarrow f) \cdot \mathcal{L}}, \quad (6.1)$$

in units of  $\mu\text{b GeV}^{-1}$ . Figures 6.2–6.5 show the results in  $y$  bins as a function of  $p_T$ , compared with the three theory predictions described in Section 1.2. In all cases, as throughout this note, the inclusion of the charge conjugate meson is implied.

### 6.1 Integrated cross-sections

We provide integrated cross-section per mode by summing the per-bin measurements within the fiducial  $p_T$ - $y$  volume  $0 \leq p_T < 8 \text{ GeV}$  and  $2 \leq y < 4.5$ .

To correct the integrated cross-sections for bins without a measurement, a multiplicative extrapolation factor is calculated using the POWHEG+NNPDF3.0L predictions for  $D^0$  and  $D^+$ , the FONLL predictions for  $D^{*+}$ , and the GMVFNS predictions for  $D_s^+$ . This is computed as the ratio between the sum of all per-bin cross-sections within the measurement volume and the sum of all per-bin cross-sections within the measurement volume that have a corresponding measurement. The uncertainty on the extrapolation factor is taken as the difference between factors computed using the upper and lower bounds of the theory predictions, and this uncertainty is propagated to the integrated cross-sections as a systematic uncertainty. The obtained integrated cross-sections are given in Table 6.1.

### 6.2 Total $c\bar{c}$ cross-section

For each measurement presented in Section 6.1, we compute the total  $c\bar{c}$  cross-section within the fiducial  $p_T$ - $y$  volume by scaling the measurement by the reciprocal of the respective *fragmentation fraction*. These are taken from the 2008 edition of the Particle Data Group booklet [15], and are given in Table 6.2.

For each integrated cross-section from Section 6.1, the total  $c\bar{c}$  cross-section is computed from the fragmentation fractions as

$$\sigma(c\bar{c}) = \sigma(H_c + \bar{H}_c)/2f(c \rightarrow H_c), \quad (6.2)$$

where  $H_c$  is a charm meson and  $\bar{H}_c$  is its charge conjugate. The factor 1/2 comes from the fragmentation fractions measuring the charm quark fragmentation to a single

*Table 6.1: Prompt charm production cross-sections in the kinematic ranges given. The computation of the extrapolation factors is described in the text. The first uncertainty on the cross-section is statistical, and the second is systematic and includes the contribution from the extrapolation factor. No extrapolation factor is given for  $D_s^+$  as a measurement is available in every bin of the integrated kinematic volume.*

			Extrapolation factor	Cross-section ( $\mu\text{b}$ )		
$D^0$	$0 < p_T < 8 \text{ GeV}/c$	$2 < y < 4.5$	$1.0013 \pm 0.0019$	$1635 \pm 4 \pm 89$		
$D^+$	$0 < p_T < 8 \text{ GeV}/c$	$2 < y < 4.5$	$1.108 \pm 0.049$	$619 \pm 6 \pm 56$		
$D^0$	$1 < p_T < 8 \text{ GeV}/c$	$2 < y < 4.5$	$1.0017 \pm 0.0020$	$1190 \pm 3 \pm 64$		
$D^+$	$1 < p_T < 8 \text{ GeV}/c$	$2 < y < 4.5$	$1.00062 \pm 0.00099$	$456 \pm 3 \pm 34$		
$D_s^+$	$1 < p_T < 8 \text{ GeV}/c$	$2 < y < 4.5$	$1.0734 \pm 0.0080$	$195 \pm 4 \pm 19$		
$D^{*+}$	$1 < p_T < 8 \text{ GeV}/c$	$2 < y < 4.5$	$1.122 \pm 0.046$	$467 \pm 6 \pm 40$		
$D^0$	$0 < p_T < 8 \text{ GeV}/c$	$2.5 < y < 4$	—	$943 \pm 2 \pm 49$		
$D^+$	$0 < p_T < 8 \text{ GeV}/c$	$2.5 < y < 4$	—	$369 \pm 5 \pm 29$		
$D^0$	$1 < p_T < 8 \text{ GeV}/c$	$2.5 < y < 4$	—	$681 \pm 2 \pm 35$		
$D^+$	$1 < p_T < 8 \text{ GeV}/c$	$2.5 < y < 4$	—	$265.4 \pm 0.9 \pm 19.1$		
$D_s^+$	$1 < p_T < 8 \text{ GeV}/c$	$2.5 < y < 4$	—	$117 \pm 2 \pm 11$		
$D^{*+}$	$1 < p_T < 8 \text{ GeV}/c$	$2.5 < y < 4$	—	$286 \pm 3 \pm 22$		

*Table 6.2: Charm hadron fragmentation fractions, taken from [15]. Here,  $H_c$  refers to a single charge of charm meson.*

$H_c$	$f(c \rightarrow H_c)$
$D^0$	$0.565 \pm 0.032$
$D^+$	$0.246 \pm 0.020$
$D_s^+$	$0.224 \pm 0.028$
$D^{*+}$	$0.080 \pm 0.017$

830 charge, whereas we measure the integrated cross-sections combined for both mesons  
831 and anti-mesons.

832 The average  $c\bar{c}$  cross-section is computed using the method of the ‘best unbiased  
833 linear estimator’ (BLUE) [16]. This method combines a set of  $N$  measurements  $m_i$   
834 in to an average  $m$  using per-measurement weights  $\alpha_i$

$$m = \sum_i^N \alpha_i m_i. \quad (6.3)$$

835 This linear relation is where the ‘linear’ name comes from. The ‘unbiased’ name  
836 comes from the constraint on the set of weights that  $\sum_i \alpha_i = 1$ , and ‘best’ comes  
837 from the choice of the weights being such that the covariance of the average  $\sigma^2$  is  
838 minimal

$$\sigma^2 = \alpha^T C \alpha, \quad (6.4)$$

839 where  $C$  is the covariance matrix of the input measurements, and  $\alpha$  is the vector of  
840 weights  $\alpha_i$ . The vector of weights optimising this equation can be computed from  $C$   
841 as

$$\alpha = \frac{C^{-1} u}{u^T C^{-1} u} \quad (6.5)$$

842 where  $u$  is a vector of length  $N$  whose components are all unity.

843 Only the  $D^0$  and  $D^+$   $c\bar{c}$  measurements enter in the average  $c\bar{c}$  cross-section, as the  
844  $D_s^+$  and  $D^{*+}$  measurements do not improve the statistical precision. Figure 6.1 shows  
845 the results for the total  $c\bar{c}$  cross-sections for using only  $D^0$  data, only  $D^+$  data, and  
846 the average of the two measurements, which is computed using the BLUE method to  
847 be

$$\sigma(pp \rightarrow c\bar{c}X)_{p_T < 8 \text{ GeV}/c, 2.0 < y < 4.5} = 1395 \pm 5 \pm 80 \pm 67 \mu\text{b}.$$

## 848 6.3 Relative cross-sections

849 The absolute cross-sections measurements given above allows several relative mea-  
850 surements to be made.

### 851 6.3.1 Relative to 13 TeV measurements

852 Relative measurements between our  $\sqrt{s} = 5$  TeV measurements and those made on  
853 data taken in 2015 at a centre-of-mass energy of 13 TeV are of particular interest  
854 to the theory community, as they can predict these ratios with considerably higher  
855 precision than absolute quantities due to cancellations in parton density function

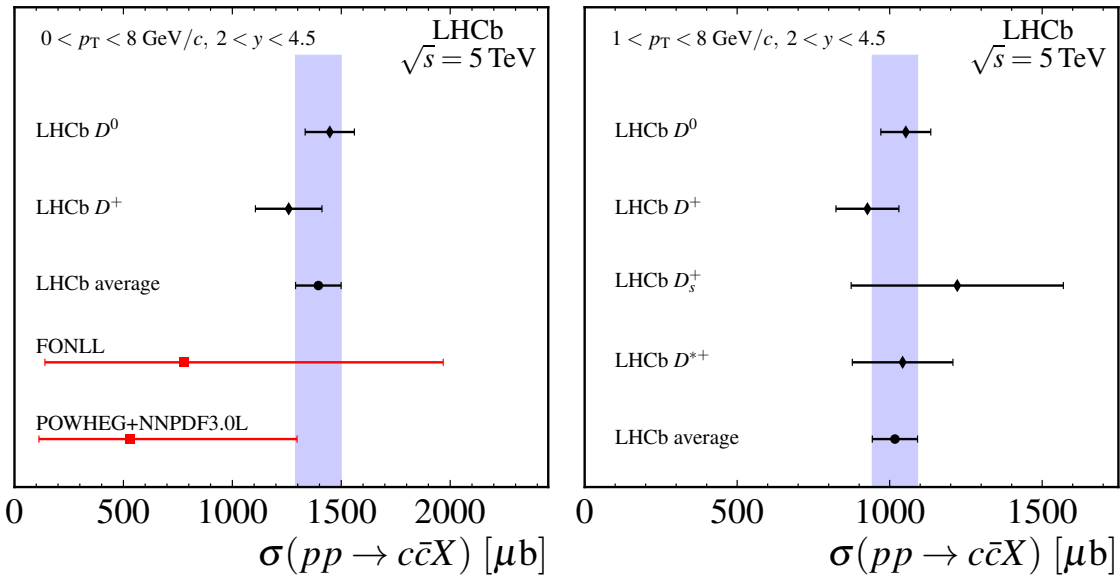


*Figure 6.1: Integrated cross-section measurements (black diamonds) as well as their average (black circle and blue band) shown (left) based on the  $D^0$  and  $D^+$  cross-sections and theory predictions (red squares) [1, 2] for  $0 < p_T < 8 \text{ GeV}/c$  and (right) for all four mesons for  $1 < p_T < 8 \text{ GeV}/c$ . The “absolute” predictions are based on calculations of the 13 TeV cross-section, while the “scaled” predictions are based on calculations of the 13 to 7 TeV ratio multiplied with the LHCb measurement.*

856    uncertainties. As we make our absolute measurements in a binning compatible with  
857    the 13 TeV measurement, that is with exactly aligned bin boundaries, the relative  
858    measurement is quite straightforward. The uncertainties on the ratio are computed  
859    by taking in to account the correlations between the two measurements, as described  
860    in Section 7.11.

861    The ratios between cross-sections at  $\sqrt{s} = 5$  TeV and 13 TeV are given in Figures  
862    6.6, Figures 6.7, Figures 6.8, and Figures 6.9 for  $D^0 \rightarrow K^-\pi^+$ ,  $D^+ \rightarrow K^-\pi^+\pi^+$ ,  
863     $D_s^+ \rightarrow \phi\pi^+$ , and  $D^{*+} \rightarrow D^0\pi^+$  with  $D^0 \rightarrow K^-\pi^+$ . The corresponding numerical  
864    values are given in Tables 6.7–6.10.

### 865    6.3.2 Relative between charm mesons

866    Besides computing the ratios between the differential cross-section measurements  
867    at different energies, one can also obtain production ratios between different charm  
868    mesons. These ratios also benefit from a large reduction in the systematic uncertainties  
869    as correlated sources cancel. These ratios are compared to measurements performed at  
870     $e^+e^-$  colliders. To reduce the uncertainty on the displayed measurements, the ratios  
871    are formed between cross-sections times branching ratios. Ratios with respect to  $D^0$   
872    are shown in Figure 6.10 while the remaining combinations are given in Figure 6.11.  
873    All numerical values are found in Tables 6.11–6.16.

Table 6.3: Differential cross-sections for prompt  $D^0$ , estimated using  $D^0 \rightarrow K^-\pi^+$ , in  $\mu b \text{ GeV}^{-1}$ .

$p_T$ [MeV/c]	$y$									
	[2, 2.5]		[2.5, 3]		[3, 3.5]		[3.5, 4]		[4, 4.5]	
[0, 1000]	$255^{+4}_{-4}$ $^{+31}_{-25}$	$206^{+2}_{-2}$ $^{+12}_{-13}$	$171.6^{+1.4}_{-1.4}$ $^{+9.6}_{-9.6}$	$147.9^{+1.7}_{-1.7}$ $^{+9.0}_{-8.6}$	$111^{+3}_{-3}$ $^{+10}_{-10}$					
[1000, 2000]	$389^{+4}_{-4}$ $^{+34}_{-30}$	$289^{+2}_{-2}$ $^{+17}_{-16}$	$231^{+1}_{-1}$ $^{+13}_{-12}$	$194^{+2}_{-2}$ $^{+11}_{-11}$	$137.0^{+2.3}_{-2.3}$ $^{+9.6}_{-8.4}$					
[2000, 3000]	$213^{+2}_{-2}$ $^{+14}_{-14}$	$157.6^{+1.0}_{-1.0}$ $^{+8.3}_{-8.8}$	$121.8^{+0.8}_{-0.8}$ $^{+7.0}_{-6.1}$	$92.6^{+0.8}_{-0.8}$ $^{+5.6}_{-5.1}$	$65.7^{+1.2}_{-1.2}$ $^{+4.5}_{-4.0}$					
[3000, 4000]	$95.7^{+1.0}_{-1.0}$ $^{+5.5}_{-5.9}$	$68.0^{+0.5}_{-0.5}$ $^{+3.8}_{-3.5}$	$52.0^{+0.4}_{-0.4}$ $^{+2.9}_{-2.7}$	$37.8^{+0.4}_{-0.4}$ $^{+2.3}_{-2.1}$	$24.9^{+0.7}_{-0.7}$ $^{+2.2}_{-2.0}$					
[4000, 5000]	$41.6^{+0.5}_{-0.5}$ $^{+2.6}_{-2.4}$	$29.1^{+0.3}_{-0.3}$ $^{+1.7}_{-1.5}$	$22.0^{+0.2}_{-0.2}$ $^{+1.3}_{-1.1}$	$15.68^{+0.24}_{-0.24}$ $^{+0.95}_{-0.87}$	$9.4^{+0.4}_{-0.4}$ $^{+1.8}_{-1.3}$					
[5000, 6000]	$19.2^{+0.3}_{-0.3}$ $^{+1.3}_{-1.1}$	$13.23^{+0.17}_{-0.17}$ $^{+0.80}_{-0.73}$	$9.52^{+0.14}_{-0.14}$ $^{+0.61}_{-0.54}$	$6.22^{+0.15}_{-0.15}$ $^{+0.46}_{-0.41}$	$2.51^{+0.35}_{-0.35}$ $^{+0.94}_{-0.61}$					
[6000, 7000]	$10.24^{+0.21}_{-0.21}$ $^{+0.74}_{-0.66}$	$6.24^{+0.11}_{-0.11}$ $^{+0.41}_{-0.37}$	$4.76^{+0.10}_{-0.10}$ $^{+0.32}_{-0.28}$	$3.10^{+0.12}_{-0.12}$ $^{+0.37}_{-0.30}$						
[7000, 8000]	$5.64^{+0.15}_{-0.15}$ $^{+0.47}_{-0.43}$	$3.34^{+0.08}_{-0.08}$ $^{+0.23}_{-0.22}$	$2.53^{+0.07}_{-0.07}$ $^{+0.20}_{-0.18}$	$1.28^{+0.09}_{-0.09}$ $^{+0.28}_{-0.20}$						
[8000, 9000]	$2.85^{+0.10}_{-0.10}$ $^{+0.27}_{-0.25}$	$1.94^{+0.06}_{-0.06}$ $^{+0.16}_{-0.15}$	$1.37^{+0.06}_{-0.06}$ $^{+0.15}_{-0.13}$	$0.60^{+0.08}_{-0.08}$ $^{+0.18}_{-0.14}$						
[9000, 10000]	$1.76^{+0.08}_{-0.08}$ $^{+0.19}_{-0.18}$	$1.11^{+0.05}_{-0.05}$ $^{+0.11}_{-0.10}$	$0.68^{+0.04}_{-0.04}$ $^{+0.11}_{-0.09}$							

Table 6.4: Differential cross-sections for prompt  $D^+$ , estimated using  $D^+ \rightarrow K^-\pi^+\pi^+$ , in  $\mu b\text{ GeV}^{-1}$ .

$p_T$ [MeV/c]	$y$										
	[2, 2.5]		[2.5, 3]		[3, 3.5]		[3.5, 4]		[4, 4.5]		
63	[0, 1000]		94 $\pm$ 9	21	57.7 $\pm$ 3.4	8.0	54.6 $\pm$ 3.8	7.5			
	[1000, 2000]	131 $\pm$ 4	23	106.8 $\pm$ 1.2	9.4	90.4 $\pm$ 0.8	7.6	73.1 $\pm$ 0.8	5.2	55.2 $\pm$ 1.4	5.5
	[2000, 3000]	84.4 $\pm$ 1.2	9.8	60.7 $\pm$ 0.4	4.5	48.2 $\pm$ 0.3	3.5	37.8 $\pm$ 0.3	3.0	24.8 $\pm$ 0.4	2.2
	[3000, 4000]	37.0 $\pm$ 0.5	3.6	27.5 $\pm$ 0.2	1.8	21.4 $\pm$ 0.2	1.7	15.8 $\pm$ 0.1	1.2	9.77 $\pm$ 0.18	0.84
	[4000, 5000]	18.5 $\pm$ 0.3	1.7	11.98 $\pm$ 0.11	0.77	8.93 $\pm$ 0.08	0.67	6.61 $\pm$ 0.08	0.47	3.61 $\pm$ 0.10	0.30
	[5000, 6000]	8.07 $\pm$ 0.14	0.57	5.34 $\pm$ 0.06	0.38	4.18 $\pm$ 0.05	0.31	2.98 $\pm$ 0.05	0.23	1.59 $\pm$ 0.08	0.17
	[6000, 7000]	4.07 $\pm$ 0.09	0.36	2.65 $\pm$ 0.04	0.20	1.97 $\pm$ 0.03	0.15	1.32 $\pm$ 0.04	0.11	0.633 $\pm$ 0.061	0.091
	[7000, 8000]	2.31 $\pm$ 0.06	0.22	1.43 $\pm$ 0.03	0.11	1.040 $\pm$ 0.025	0.086	0.778 $\pm$ 0.031	0.084		
	[8000, 9000]	1.60 $\pm$ 0.05	0.17	0.807 $\pm$ 0.022	0.070	0.528 $\pm$ 0.018	0.048	0.317 $\pm$ 0.020	0.046		
	[9000, 10000]	0.735 $\pm$ 0.030	0.084	0.420 $\pm$ 0.015	0.040	0.309 $\pm$ 0.014	0.034	0.170 $\pm$ 0.017	0.035		

Table 6.5: Differential cross-sections for prompt  $D_s^+$ , estimated using  $D_s^+ \rightarrow \phi\pi^+$ , in  $\mu b \text{ GeV}^{-1}$ .

$p_T$ [MeV/c]	$y$											
	[2, 2.5]		[2.5, 3]		[3, 3.5]		[3.5, 4]		[4, 4.5]			
[1000, 2000]	$36^{+} \quad 5^{+}$	$5^{-} \quad 8^{+}$	$45.7^{+} \quad 2.8^{+}$	$5.9^{-} \quad 5.2$	$36.1^{+} \quad 2.3^{+}$	$4.7^{-} \quad 4.1$	$28.2^{+} \quad 2.6^{+}$	$4.1^{-} \quad 3.4$				
[2000, 3000]	$42.0^{+} \quad 2.2^{+}$	$8.5^{-} \quad 6.5$	$30.0^{+} \quad 0.8^{+}$	$3.1^{-} \quad 2.8$	$22.5^{+} \quad 0.7^{+}$	$2.1^{-} \quad 2.0$	$16.8^{+} \quad 0.7^{+}$	$1.7^{-} \quad 1.6$	$9.9^{+} \quad 1.1^{+}$	$1.7^{-} \quad 1.4$		
[3000, 4000]	$19.1^{+} \quad 0.9^{+}$	$2.9^{-} \quad 2.2$	$13.1^{+} \quad 0.4^{+}$	$1.2^{-} \quad 1.2$	$9.21^{+} \quad 0.29^{+}$	$0.93^{-} \quad 0.75$	$7.15^{+} \quad 0.30^{+}$	$0.69^{-} \quad 0.64$	$4.36^{+} \quad 0.41^{+}$	$0.57^{-} \quad 0.51$		
[4000, 5000]	$9.6^{+} \quad 0.5^{+}$	$1.3^{-} \quad 1.0$	$6.02^{+} \quad 0.21^{+}$	$0.57^{-} \quad 0.54$	$4.71^{+} \quad 0.19^{+}$	$0.47^{-} \quad 0.41$	$3.07^{+} \quad 0.17^{+}$	$0.32^{-} \quad 0.29$	$2.11^{+} \quad 0.26^{+}$	$0.30^{-} \quad 0.27$		
[5000, 6000]	$3.78^{+} \quad 0.24^{+}$	$0.43^{-} \quad 0.45$	$2.40^{+} \quad 0.12^{+}$	$0.25^{-} \quad 0.21$	$2.15^{+} \quad 0.11^{+}$	$0.23^{-} \quad 0.20$	$1.33^{+} \quad 0.10^{+}$	$0.15^{-} \quad 0.14$	$0.77^{+} \quad 0.15^{+}$	$0.14^{-} \quad 0.12$		
[6000, 7000]	$2.25^{+} \quad 0.17^{+}$	$0.32^{-} \quad 0.27$	$1.44^{+} \quad 0.09^{+}$	$0.17^{-} \quad 0.14$	$0.91^{+} \quad 0.07^{+}$	$0.11^{-} \quad 0.09$	$0.608^{+} \quad 0.067^{+}$	$0.084^{-} \quad 0.073$				
[7000, 8000]	$1.25^{+} \quad 0.11^{+}$	$0.20^{-} \quad 0.17$	$0.754^{+} \quad 0.061^{+}$	$0.095^{-} \quad 0.089$	$0.513^{+} \quad 0.049^{+}$	$0.072^{-} \quad 0.061$	$0.384^{+} \quad 0.055^{+}$	$0.078^{-} \quad 0.062$				
[8000, 9000]	$0.59^{+} \quad 0.08^{+}$	$0.11^{-} \quad 0.09$	$0.339^{+} \quad 0.038^{+}$	$0.046^{-} \quad 0.043$	$0.270^{+} \quad 0.035^{+}$	$0.044^{-} \quad 0.036$						
[9000, 10000]	$0.446^{+} \quad 0.067^{+}$	$0.099^{-} \quad 0.089$	$0.359^{+} \quad 0.048^{+}$	$0.068^{-} \quad 0.065$	$0.145^{+} \quad 0.025^{+}$	$0.029^{-} \quad 0.025$						

Table 6.6: Differential cross-sections for prompt  $D^{*+}$ , estimated using  $D^{*+} \rightarrow D^0\pi^+$  with  $D^0 \rightarrow K^-\pi^+$ , in  $\mu b \text{ GeV}^{-1}$ .

$p_T$ [MeV/c]	$y$									
	[2, 2.5]		[2.5, 3]		[3, 3.5]		[3.5, 4]		[4, 4.5]	
69	[1000, 2000]		$123^{+}_{-}$ $6^{+}_{-}$ $12^{+}_{-}$	$89.6^{+}_{-}$ $2.1^{+}_{-}$ $7.0^{+}_{-}$	$76.0^{+}_{-}$ $2.2^{+}_{-}$ $5.9^{+}_{-}$	$51.5^{+}_{-}$ $3.1^{+}_{-}$ $4.3^{+}_{-}$				
	[2000, 3000]	$79^{+}_{-}$ $8^{+}_{-}$ $12^{+}_{-}$	$64.8^{+}_{-}$ $1.5^{+}_{-}$ $5.4^{+}_{-}$	$54.5^{+}_{-}$ $0.9^{+}_{-}$ $4.0^{+}_{-}$	$36.8^{+}_{-}$ $0.8^{+}_{-}$ $2.7^{+}_{-}$	$26.7^{+}_{-}$ $1.3^{+}_{-}$ $2.9^{+}_{-}$				
	[3000, 4000]	$43.0^{+}_{-}$ $2.1^{+}_{-}$ $3.9^{+}_{-}$	$30.0^{+}_{-}$ $0.6^{+}_{-}$ $2.1^{+}_{-}$	$25.0^{+}_{-}$ $0.4^{+}_{-}$ $1.9^{+}_{-}$	$16.0^{+}_{-}$ $0.4^{+}_{-}$ $1.2^{+}_{-}$	$10.80^{+}_{-}$ $0.67^{+}_{-}$ $0.94^{+}_{-}$				
	[4000, 5000]	$22.5^{+}_{-}$ $1.0^{+}_{-}$ $1.9^{+}_{-}$	$13.6^{+}_{-}$ $0.3^{+}_{-}$ $1.0^{+}_{-}$	$10.82^{+}_{-}$ $0.24^{+}_{-}$ $0.85^{+}_{-}$	$8.14^{+}_{-}$ $0.26^{+}_{-}$ $0.70^{+}_{-}$	$4.4^{+}_{-}$ $0.5^{+}_{-}$ $1.0^{+}_{-}$				
	[5000, 6000]	$10.5^{+}_{-}$ $0.5^{+}_{-}$ $0.9^{+}_{-}$	$6.19^{+}_{-}$ $0.18^{+}_{-}$ $0.46^{+}_{-}$	$4.62^{+}_{-}$ $0.15^{+}_{-}$ $0.37^{+}_{-}$	$3.02^{+}_{-}$ $0.15^{+}_{-}$ $0.26^{+}_{-}$	$2.25^{+}_{-}$ $0.07^{+}_{-}$ $0.44^{+}_{-}$				
	[6000, 7000]	$6.00^{+}_{-}$ $0.32^{+}_{-}$ $0.63^{+}_{-}$	$3.11^{+}_{-}$ $0.11^{+}_{-}$ $0.26^{+}_{-}$	$2.28^{+}_{-}$ $0.10^{+}_{-}$ $0.18^{+}_{-}$	$1.52^{+}_{-}$ $0.11^{+}_{-}$ $0.14^{+}_{-}$					
	[7000, 8000]	$2.72^{+}_{-}$ $0.19^{+}_{-}$ $0.31^{+}_{-}$	$1.67^{+}_{-}$ $0.08^{+}_{-}$ $0.14^{+}_{-}$	$1.32^{+}_{-}$ $0.07^{+}_{-}$ $0.12^{+}_{-}$	$0.81^{+}_{-}$ $0.10^{+}_{-}$ $0.12^{+}_{-}$					
	[8000, 9000]	$1.47^{+}_{-}$ $0.13^{+}_{-}$ $0.19^{+}_{-}$	$0.867^{+}_{-}$ $0.054^{+}_{-}$ $0.076^{+}_{-}$	$0.625^{+}_{-}$ $0.047^{+}_{-}$ $0.063^{+}_{-}$	$0.39^{+}_{-}$ $0.07^{+}_{-}$ $0.13^{+}_{-}$					
	[9000, 10000]	$1.00^{+}_{-}$ $0.10^{+}_{-}$ $0.14^{+}_{-}$	$0.570^{+}_{-}$ $0.046^{+}_{-}$ $0.060^{+}_{-}$	$0.592^{+}_{-}$ $0.055^{+}_{-}$ $0.093^{+}_{-}$						

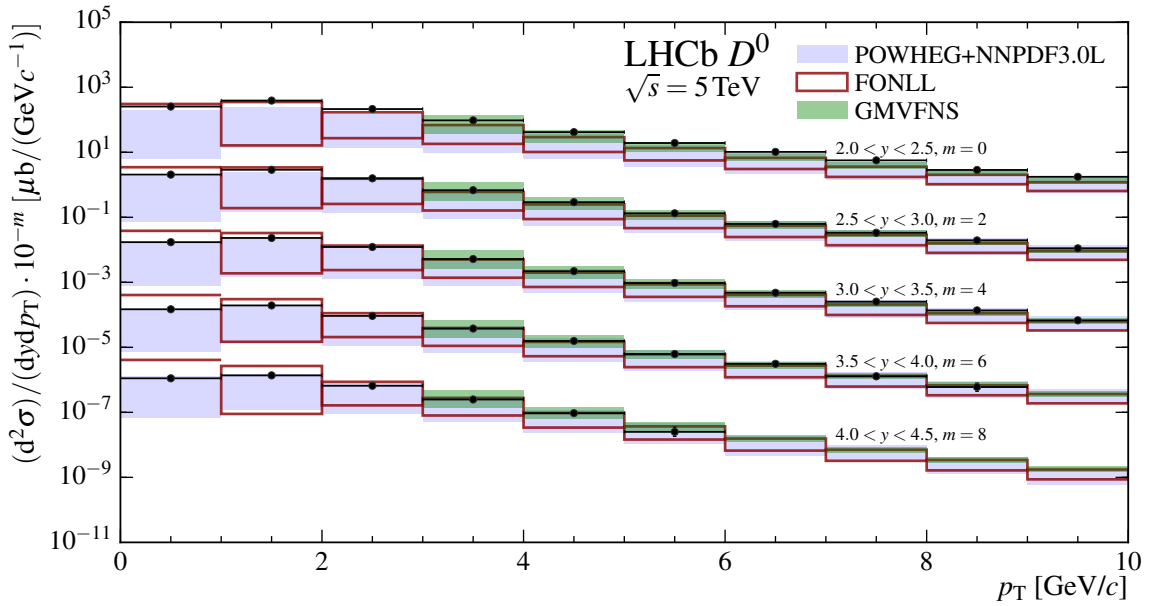


Figure 6.2: Differential cross-sections for prompt  $D^0$ , estimated using  $D^0 \rightarrow K^-\pi^+$ , in  $\mu\text{b GeV}^{-1}$ .

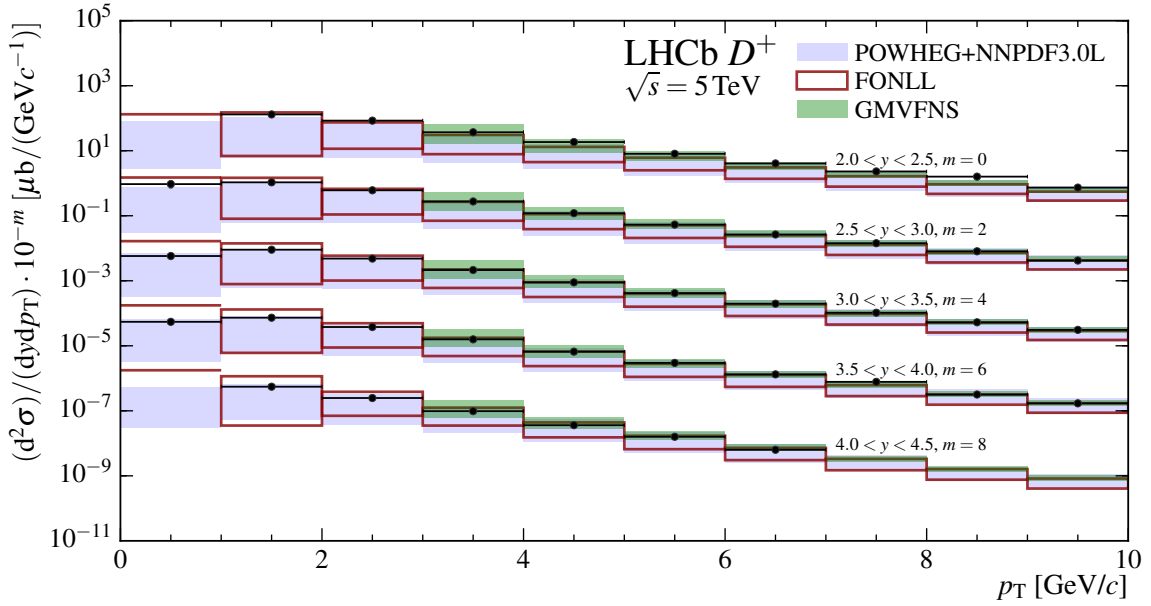


Figure 6.3: Differential cross-sections for prompt  $D^+$ , estimated using  $D^+ \rightarrow K^-\pi^+\pi^+$ , in  $\mu\text{b GeV}^{-1}$ .

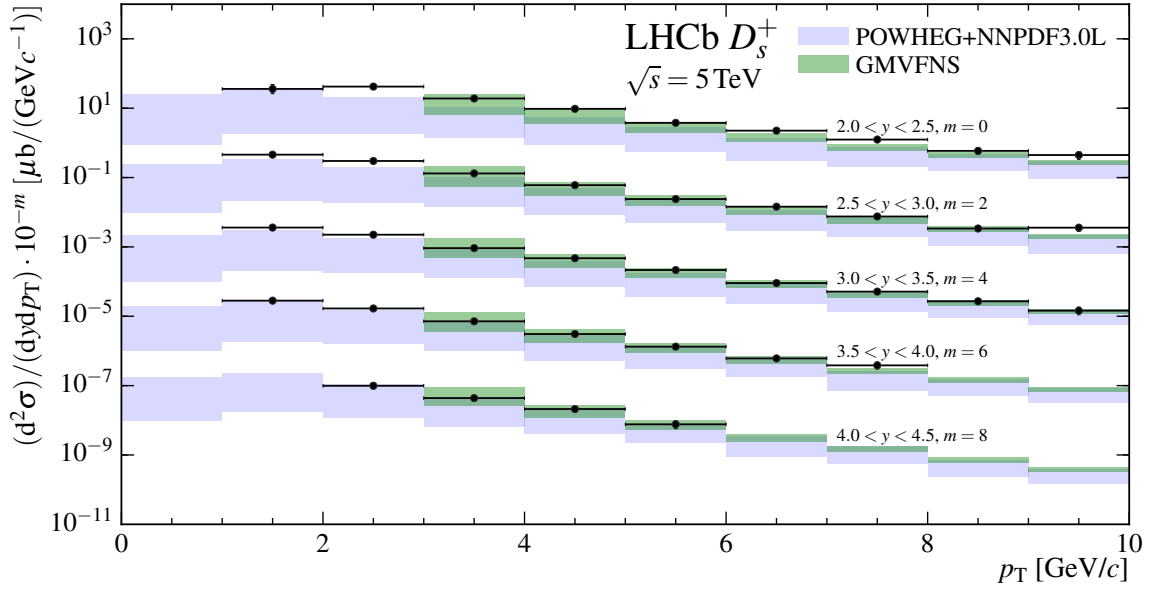


Figure 6.4: Differential cross-sections for prompt  $D_s^+$ , estimated using  $D_s^+ \rightarrow \phi\pi^+$ , in  $\mu\text{b GeV}^{-1}$ .

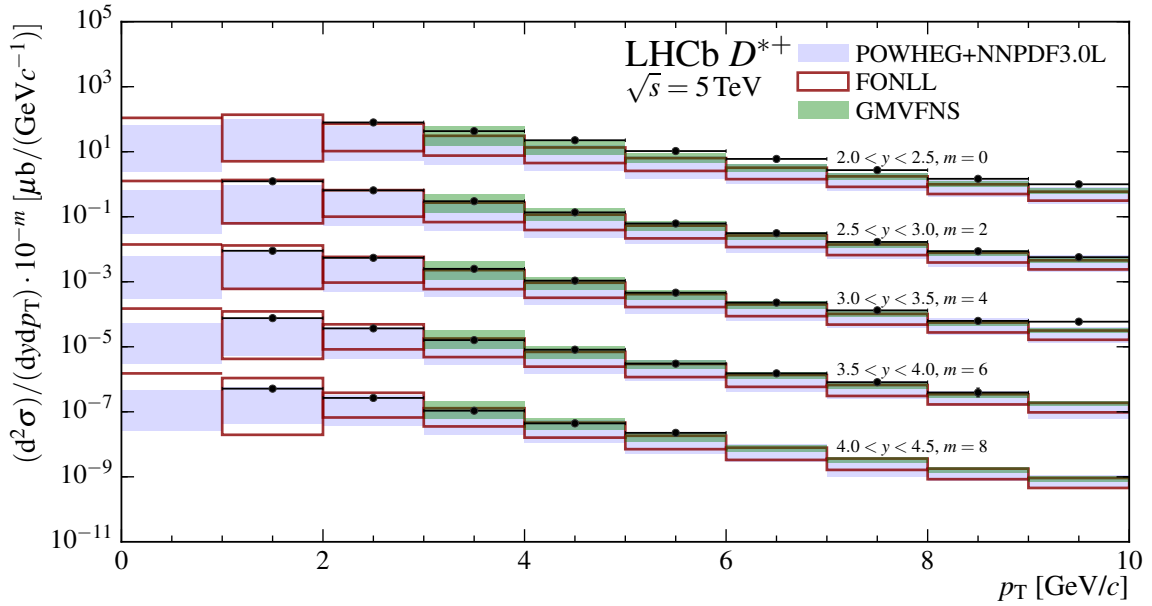


Figure 6.5: Differential cross-sections for prompt  $D^{*+}$ , estimated using  $D^{*+} \rightarrow D^0\pi^+$  with  $D^0 \rightarrow K^-\pi^+$ , in  $\mu\text{b GeV}^{-1}$ .

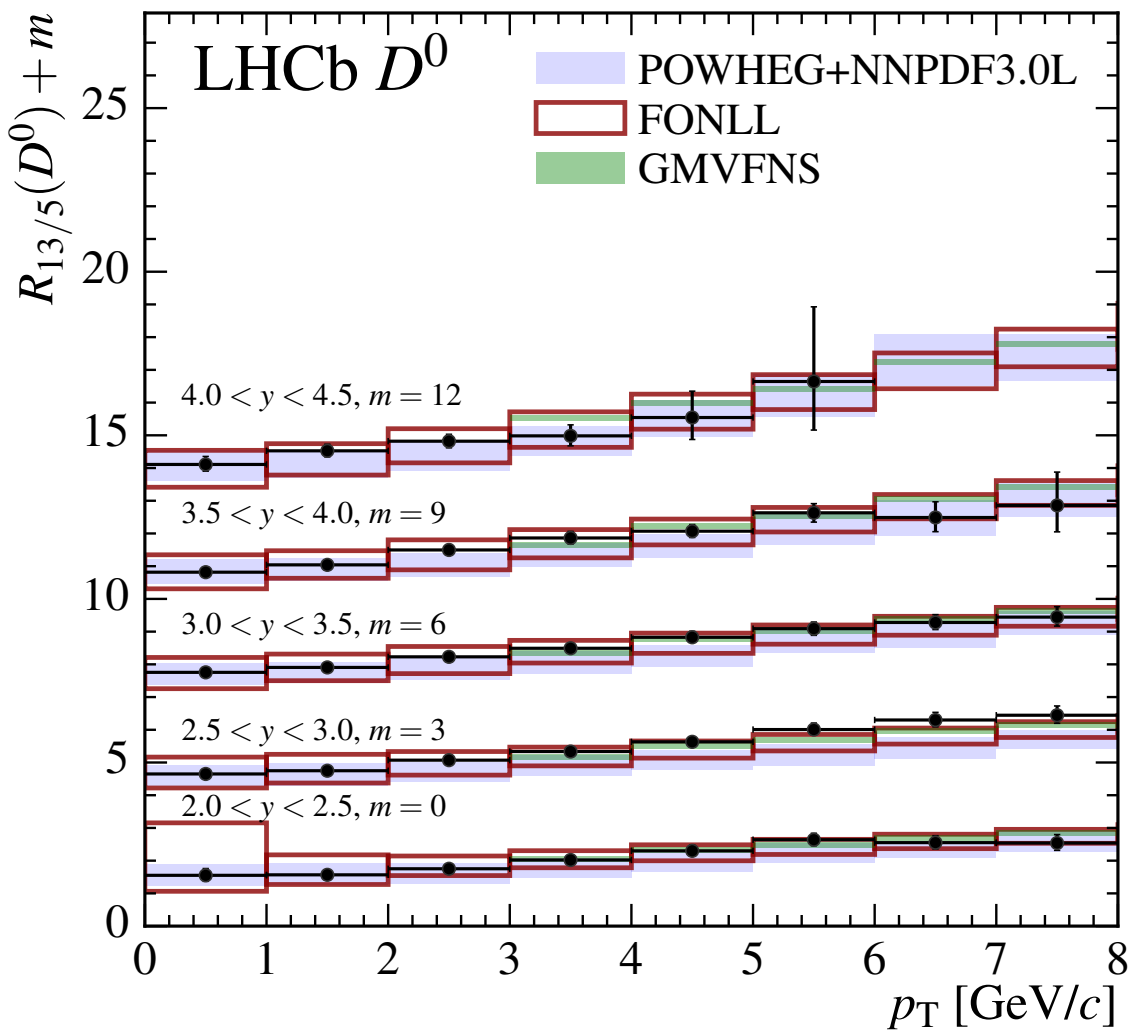


Figure 6.6: Cross-sections relative between 13 TeV and 5 TeV for  $D^0$  estimated using the  $D^0 \rightarrow K^- \pi^+$  cross-section results.

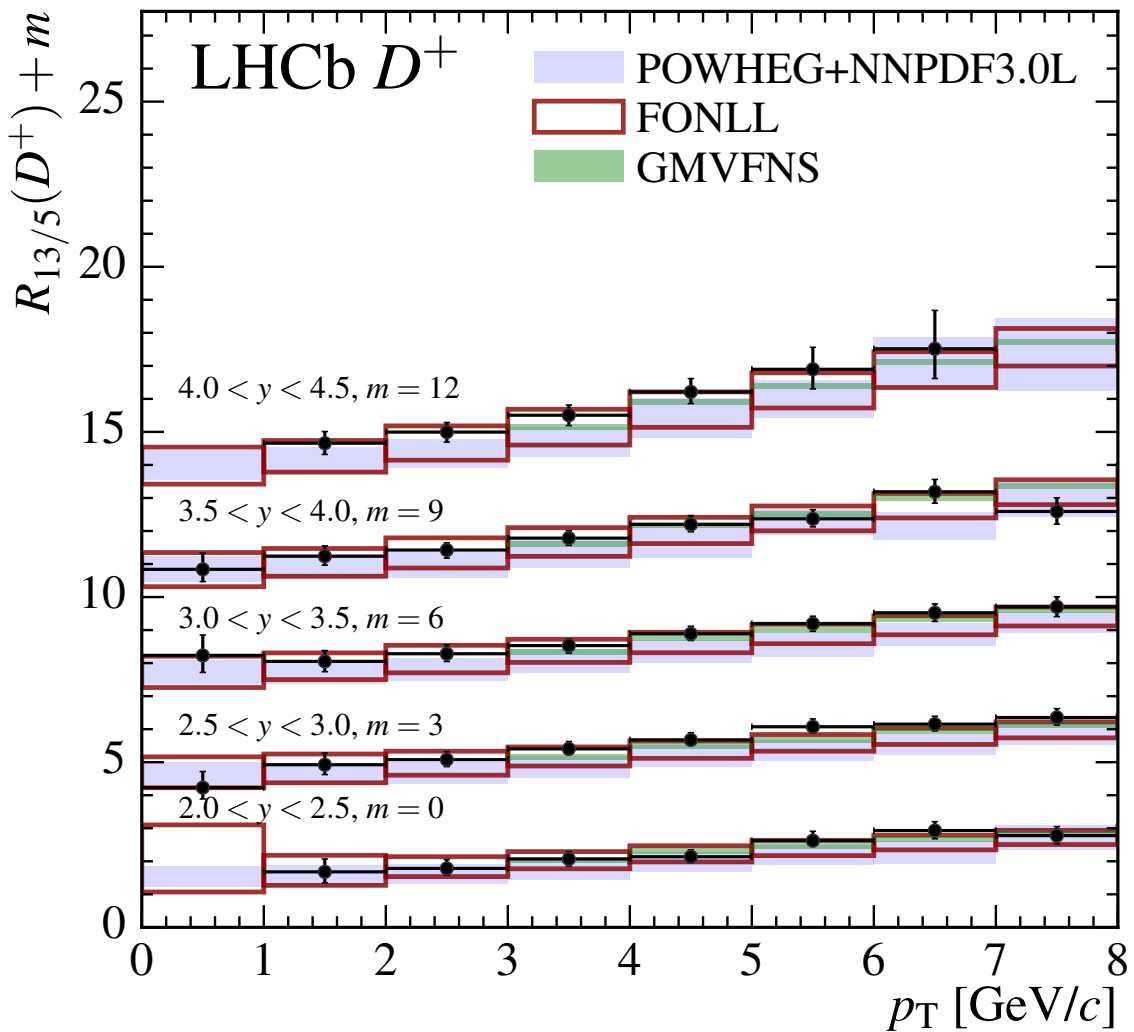


Figure 6.7: Cross-sections relative between 13 TeV and 5 TeV for  $D^+$  estimated using the  $D^+ \rightarrow K^- \pi^+ \pi^+$  cross-section results.

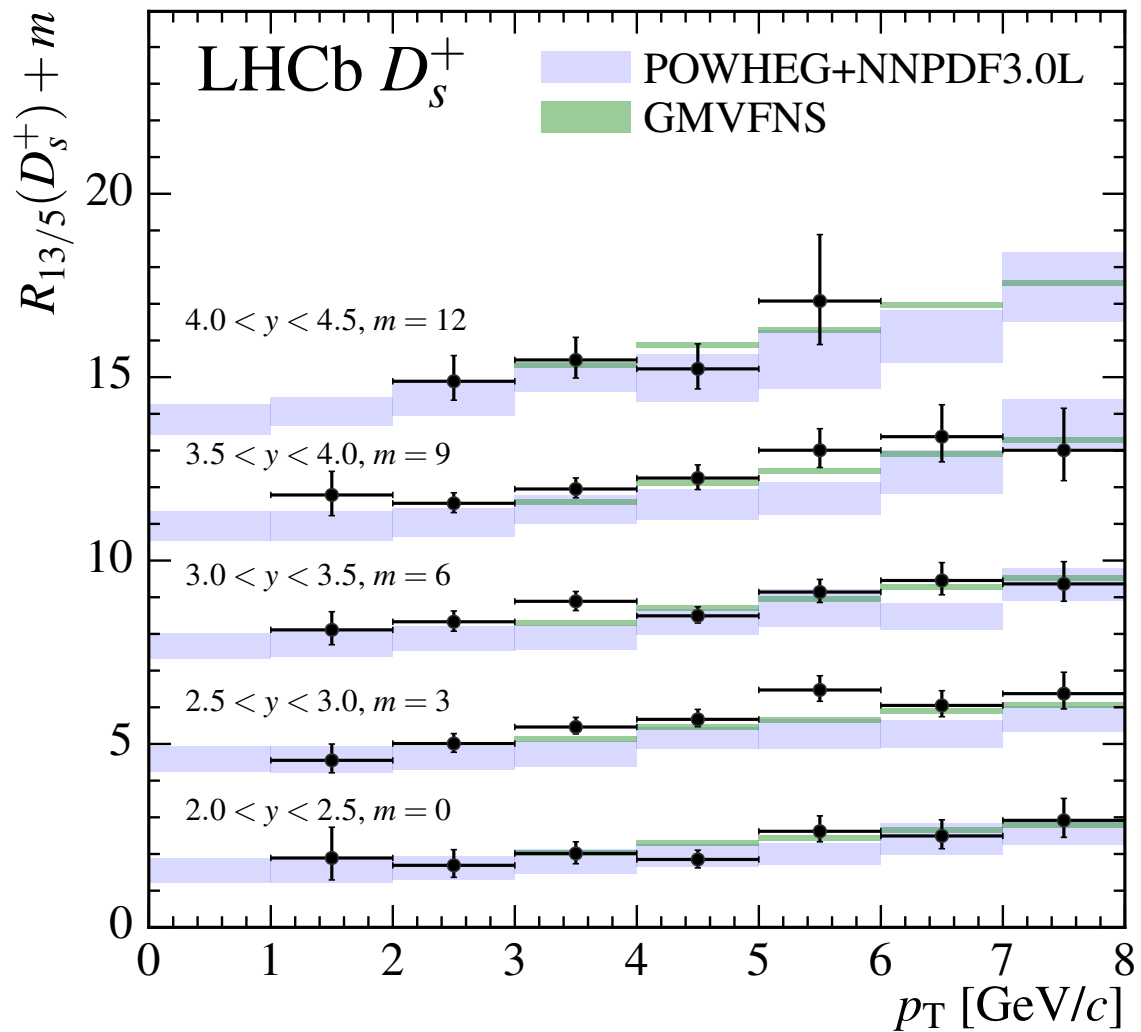


Figure 6.8: Cross-sections relative between 13 TeV and 5 TeV for  $D_s^+$  estimated using the  $D_s^+ \rightarrow \phi\pi^+$  cross-section results.

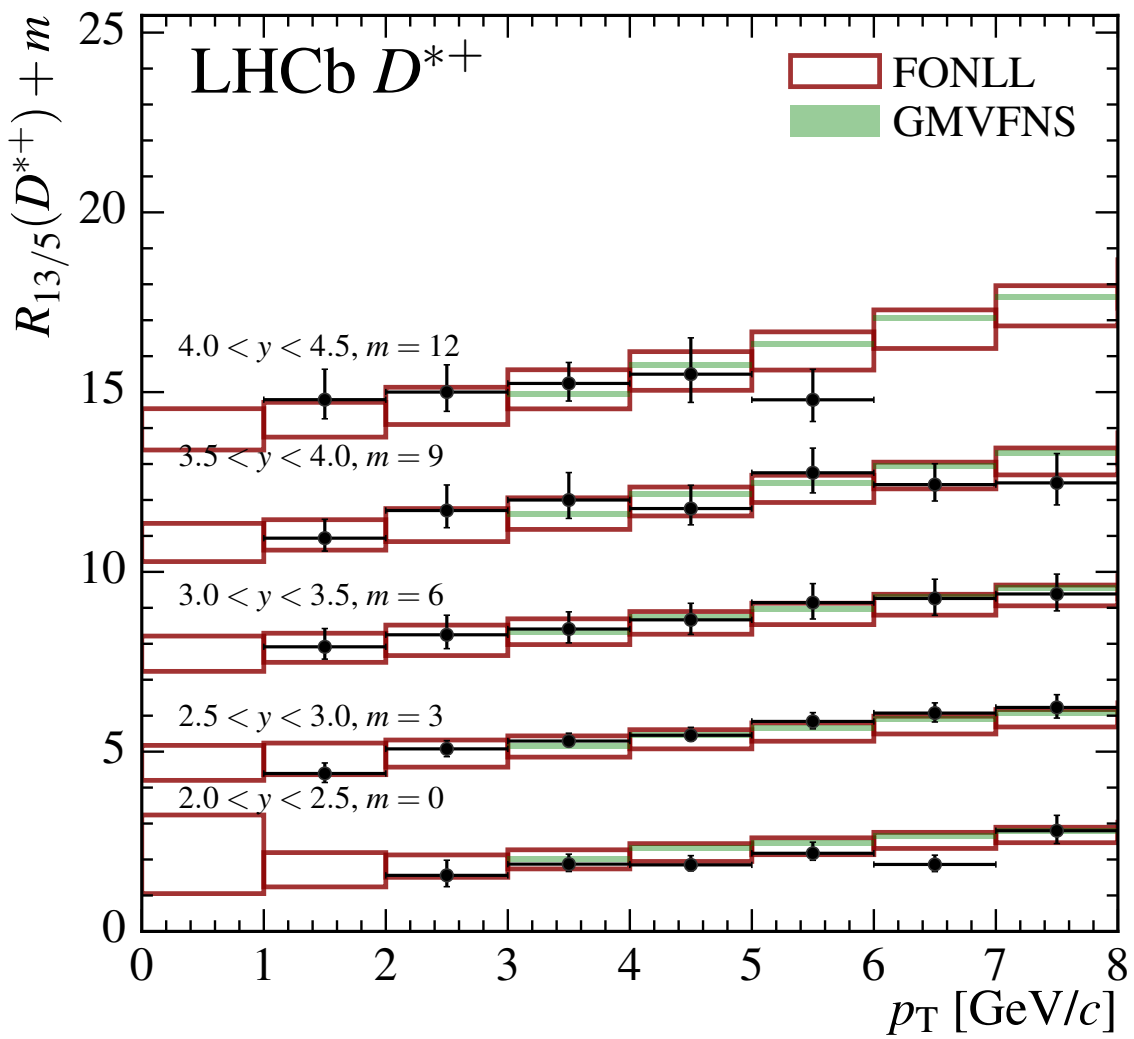


Figure 6.9: Cross-sections relative between 13 TeV and 5 TeV for  $D^{*+}$  estimated using the  $D^{*+} \rightarrow D^0\pi^+$  with  $D^0 \rightarrow K^-\pi^+$  cross-section results.

Table 6.7: Relative cross-sections for prompt  $D^0 \rightarrow K^- \pi^+$  in  $\mu b \text{ GeV}^{-1}$ .

$p_T$ [MeV/c]	$y$				
	[2, 2.5]	[2.5, 3]	[3, 3.5]	[3.5, 4]	[4, 4.5]
[0, 1000]	$1.55^{+0.03+0.21}_{-0.03-0.18}$	$1.65^{+0.02+0.14}_{-0.01-0.10}$	$1.76^{+0.02+0.13}_{-0.02-0.10}$	$1.82^{+0.02+0.13}_{-0.02-0.12}$	$2.11^{+0.06+0.24}_{-0.05-0.20}$
[1000, 2000]	$1.57^{+0.02+0.16}_{-0.02-0.14}$	$1.75^{+0.01+0.13}_{-0.01-0.11}$	$1.91^{+0.01+0.12}_{-0.01-0.11}$	$2.04^{+0.02+0.15}_{-0.02-0.11}$	$2.53^{+0.04+0.20}_{-0.04-0.18}$
[2000, 3000]	$1.75^{+0.02+0.15}_{-0.02-0.13}$	$2.07^{+0.01+0.14}_{-0.01-0.11}$	$2.23^{+0.02+0.13}_{-0.02-0.13}$	$2.50^{+0.02+0.16}_{-0.02-0.14}$	$2.82^{+0.06+0.20}_{-0.05-0.20}$
[3000, 4000]	$2.02^{+0.02+0.16}_{-0.02-0.12}$	$2.33^{+0.02+0.14}_{-0.02-0.13}$	$2.49^{+0.02+0.15}_{-0.02-0.13}$	$2.86^{+0.03+0.20}_{-0.03-0.18}$	$2.98^{+0.08+0.33}_{-0.08-0.29}$
[4000, 5000]	$2.30^{+0.03+0.17}_{-0.03-0.14}$	$2.63^{+0.03+0.16}_{-0.03-0.14}$	$2.83^{+0.03+0.18}_{-0.03-0.15}$	$3.07^{+0.05+0.20}_{-0.05-0.19}$	$3.54^{+0.18+0.78}_{-0.17-0.65}$
[5000, 6000]	$2.64^{+0.05+0.19}_{-0.05-0.18}$	$3.01^{+0.04+0.19}_{-0.04-0.17}$	$3.09^{+0.05+0.20}_{-0.05-0.20}$	$3.63^{+0.09+0.26}_{-0.09-0.27}$	$4.6^{+0.8+2.1}_{-0.6-1.4}$
[6000, 7000]	$2.55^{+0.06+0.20}_{-0.05-0.19}$	$3.30^{+0.06+0.22}_{-0.06-0.20}$	$3.28^{+0.07+0.23}_{-0.07-0.21}$	$3.49^{+0.14+0.46}_{-0.13-0.41}$	
[7000, 8000]	$2.54^{+0.07+0.25}_{-0.07-0.21}$	$3.44^{+0.09+0.27}_{-0.08-0.23}$	$3.44^{+0.11+0.30}_{-0.10-0.26}$	$3.86^{+0.31+0.97}_{-0.27-0.76}$	

Table 6.8: Relative cross-sections for prompt  $D^+ \rightarrow K^-\pi^+\pi^+$  in  $\mu b \text{ GeV}^{-1}$ .

$p_T$ [MeV/c]	$y$				
	[2, 2.5]	[2.5, 3]	[3, 3.5]	[3.5, 4]	[4, 4.5]
$\gamma_3$	[0, 1000]	$1.23^{+0.14+0.47}_{-0.11-0.32}$	$2.23^{+0.15+0.60}_{-0.14-0.50}$	$1.84^{+0.15+0.47}_{-0.13-0.35}$	
	[1000, 2000]	$1.68^{+0.07+0.38}_{-0.06-0.33}$	$1.92^{+0.02+0.35}_{-0.02-0.30}$	$2.05^{+0.02+0.33}_{-0.02-0.31}$	$2.24^{+0.03+0.31}_{-0.03-0.27}$
	[2000, 3000]	$1.78^{+0.03+0.27}_{-0.03-0.21}$	$2.08^{+0.01+0.25}_{-0.01-0.21}$	$2.28^{+0.01+0.27}_{-0.01-0.23}$	$2.42^{+0.02+0.22}_{-0.02-0.24}$
	[3000, 4000]	$2.07^{+0.03+0.22}_{-0.03-0.21}$	$2.40^{+0.02+0.22}_{-0.02-0.17}$	$2.53^{+0.02+0.20}_{-0.02-0.23}$	$2.78^{+0.03+0.22}_{-0.03-0.22}$
	[4000, 5000]	$2.14^{+0.03+0.20}_{-0.03-0.18}$	$2.67^{+0.03+0.22}_{-0.03-0.16}$	$2.89^{+0.03+0.23}_{-0.03-0.20}$	$3.20^{+0.04+0.27}_{-0.04-0.22}$
	[5000, 6000]	$2.62^{+0.05+0.28}_{-0.05-0.16}$	$3.07^{+0.04+0.24}_{-0.04-0.19}$	$3.19^{+0.04+0.22}_{-0.04-0.23}$	$3.37^{+0.07+0.27}_{-0.06-0.24}$
	[6000, 7000]	$2.93^{+0.07+0.26}_{-0.07-0.24}$	$3.15^{+0.05+0.23}_{-0.05-0.20}$	$3.52^{+0.07+0.26}_{-0.06-0.26}$	$4.19^{+0.12+0.35}_{-0.12-0.32}$
	[7000, 8000]	$2.78^{+0.08+0.26}_{-0.07-0.25}$	$3.35^{+0.08+0.26}_{-0.07-0.22}$	$3.71^{+0.10+0.29}_{-0.09-0.28}$	$3.59^{+0.16+0.38}_{-0.14-0.36}$

Table 6.9: Relative cross-sections for prompt  $D_s^+ \rightarrow \phi\pi^+$  in  $\mu b GeV^{-1}$ .

$p_T$ [MeV/c]	$y$				
	[2, 2.5]	[2.5, 3]	[3, 3.5]	[3.5, 4]	[4, 4.5]
[1000, 2000]	$1.89^{+0.36+0.76}_{-0.28-0.53}$	$1.55^{+0.12+0.43}_{-0.10-0.33}$	$2.11^{+0.16+0.47}_{-0.14-0.38}$	$2.79^{+0.32+0.56}_{-0.28-0.49}$	
[2000, 3000]	$1.69^{+0.10+0.42}_{-0.10-0.31}$	$2.01^{+0.06+0.27}_{-0.06-0.23}$	$2.33^{+0.08+0.28}_{-0.07-0.25}$	$2.56^{+0.12+0.26}_{-0.12-0.23}$	$2.89^{+0.38+0.59}_{-0.30-0.42}$
[3000, 4000]	$2.01^{+0.10+0.30}_{-0.10-0.26}$	$2.46^{+0.08+0.25}_{-0.07-0.18}$	$2.89^{+0.10+0.25}_{-0.09-0.23}$	$2.95^{+0.14+0.27}_{-0.13-0.20}$	$3.47^{+0.38+0.48}_{-0.32-0.38}$
[4000, 5000]	$1.85^{+0.11+0.23}_{-0.09-0.21}$	$2.67^{+0.10+0.25}_{-0.10-0.18}$	$2.49^{+0.11+0.22}_{-0.10-0.17}$	$3.25^{+0.20+0.30}_{-0.18-0.26}$	$3.23^{+0.47+0.49}_{-0.38-0.39}$
[5000, 6000]	$2.62^{+0.19+0.38}_{-0.17-0.24}$	$3.47^{+0.19+0.34}_{-0.17-0.26}$	$3.14^{+0.17+0.30}_{-0.16-0.24}$	$4.01^{+0.34+0.48}_{-0.30-0.37}$	$5.1^{+1.3+1.2}_{-0.9-0.8}$
[6000, 7000]	$2.49^{+0.22+0.38}_{-0.19-0.29}$	$3.05^{+0.21+0.34}_{-0.19-0.24}$	$3.46^{+0.29+0.40}_{-0.25-0.30}$	$4.38^{+0.57+0.66}_{-0.46-0.51}$	
[7000, 8000]	$2.92^{+0.31+0.51}_{-0.26-0.38}$	$3.37^{+0.31+0.50}_{-0.27-0.32}$	$3.36^{+0.37+0.48}_{-0.31-0.36}$	$4.01^{+0.70+0.91}_{-0.54-0.63}$	

74

Table 6.10: Relative cross-sections for prompt  $D^{*+} \rightarrow D^0\pi^+$  with  $D^0 \rightarrow K^-\pi^+$  in  $\mu b GeV^{-1}$ .

$p_T$ [MeV/c]	$y$				
	[2, 2.5]	[2.5, 3]	[3, 3.5]	[3.5, 4]	[4, 4.5]
[1000, 2000]		$1.39^{+0.07+0.28}_{-0.07-0.24}$	$1.92^{+0.05+0.51}_{-0.04-0.34}$	$1.94^{+0.06+0.52}_{-0.06-0.35}$	$2.79^{+0.18+0.83}_{-0.16-0.51}$
[2000, 3000]	$1.56^{+0.19+0.38}_{-0.16-0.27}$	$2.08^{+0.05+0.22}_{-0.05-0.21}$	$2.25^{+0.04+0.54}_{-0.04-0.38}$	$2.71^{+0.07+0.71}_{-0.06-0.47}$	$3.00^{+0.16+0.74}_{-0.14-0.52}$
[3000, 4000]	$1.87^{+0.10+0.26}_{-0.09-0.18}$	$2.30^{+0.05+0.21}_{-0.05-0.15}$	$2.41^{+0.05+0.48}_{-0.04-0.38}$	$3.00^{+0.08+0.76}_{-0.08-0.51}$	$3.24^{+0.22+0.54}_{-0.20-0.45}$
[4000, 5000]	$1.85^{+0.09+0.24}_{-0.08-0.15}$	$2.46^{+0.06+0.21}_{-0.06-0.16}$	$2.67^{+0.06+0.46}_{-0.06-0.40}$	$2.76^{+0.09+0.64}_{-0.09-0.45}$	$3.50^{+0.45+0.91}_{-0.36-0.70}$
[5000, 6000]	$2.17^{+0.11+0.29}_{-0.10-0.16}$	$2.84^{+0.09+0.23}_{-0.08-0.19}$	$3.15^{+0.11+0.52}_{-0.10-0.45}$	$3.76^{+0.19+0.66}_{-0.18-0.53}$	$2.79^{+0.17+0.83}_{-0.17-0.58}$
[6000, 7000]	$1.86^{+0.11+0.23}_{-0.10-0.17}$	$3.07^{+0.12+0.26}_{-0.11-0.22}$	$3.26^{+0.15+0.52}_{-0.13-0.45}$	$3.43^{+0.27+0.51}_{-0.24-0.39}$	
[7000, 8000]	$2.80^{+0.21+0.37}_{-0.18-0.30}$	$3.23^{+0.17+0.31}_{-0.15-0.25}$	$3.39^{+0.21+0.51}_{-0.19-0.43}$	$3.48^{+0.47+0.66}_{-0.37-0.49}$	

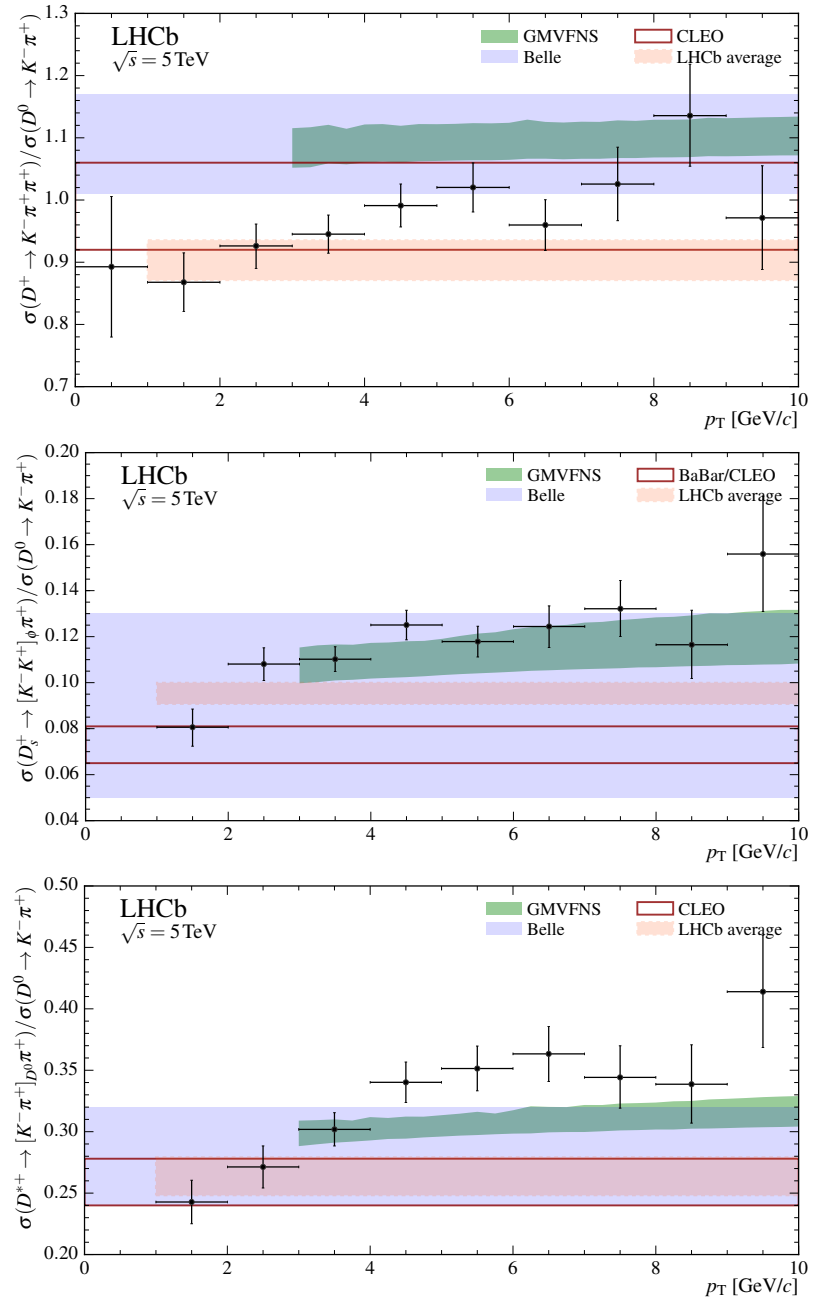


Figure 6.10: Ratios of cross-section measurements of (top)  $D^+$ , (middle)  $D_s^+$ , and (bottom)  $D^{*+}$  mesons with respect to the  $D^0$  cross-sections. The blue bands indicate the corresponding ratios of fragmentation fractions. The ratios are given as a function of  $p_T$  and different symbols indicate different ranges in  $y$ .

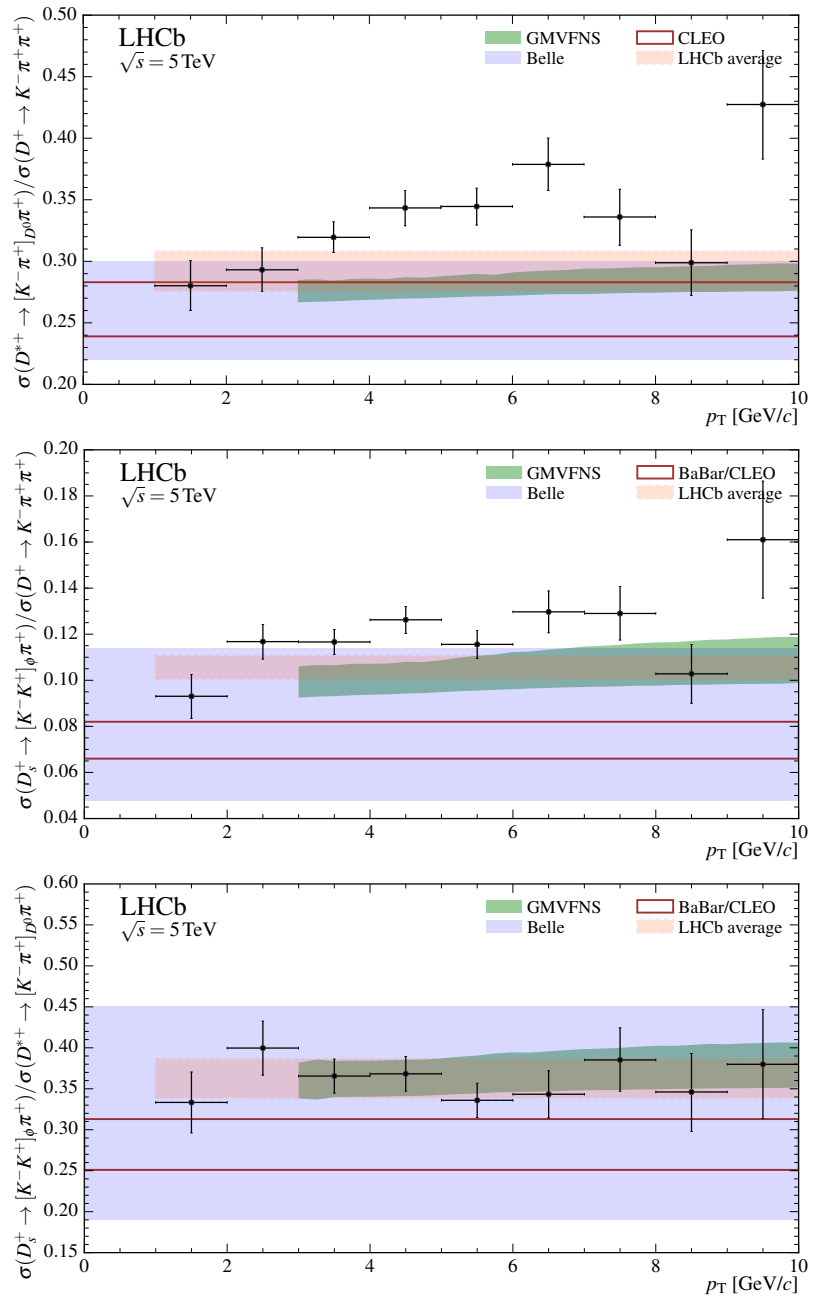


Figure 6.11: Ratios of cross-section measurements of (top)  $D^{*+}$ , and (middle)  $D_s^+$  mesons with respect to  $D^+$  cross-sections, and (bottom)  $D_s^+$  over  $D^{*+}$  mesons. The blue bands indicate the corresponding ratios of fragmentation fractions. The ratios are given as a function of  $p_T$  and different symbols indicate different ranges in  $y$ .

Table 6.11: The ratios of differential production cross-sections in  $10^{-2}$  for prompt  $D^+$  and  $D^0$  mesons in bins of  $(y, p_T)$ . The first uncertainty is statistical, and the second is the total systematic.

$p_T$ [MeV/c]	$y$				
	[2, 2.5]	[2.5, 3]	[3, 3.5]	[3.5, 4]	[4, 4.5]
77	[0, 1000]		$108 \pm 10 + 23$	$79.1 \pm 4.8 + 9.5$	$87 \pm 6 + 11$
	[1000, 2000]	$79 \pm 3 + 13$	$86.9 \pm 1.1 + 4.5$	$92.0 \pm 1.0 + 4.5$	$88.6 \pm 1.2 + 3.7$
	[2000, 3000]	$93.1 \pm 1.7 + 8.2$	$90.6 \pm 0.8 + 3.4$	$93.1 \pm 0.8 + 3.2$	$96.1 \pm 1.1 + 4.4$
	[3000, 4000]	$91.1 \pm 1.5 + 6.9$	$95.1 \pm 0.9 + 2.5$	$96.9 \pm 1.0 + 4.0$	$98.2 \pm 1.4 + 4.2$
	[4000, 5000]	$104.8 \pm 2.0 + 6.7$	$96.8 \pm 1.3 + 2.8$	$95.7 \pm 1.4 + 4.1$	$99.2 \pm 2.0 + 4.4$
	[5000, 6000]	$98.6 \pm 2.4 + 4.6$	$95.0 \pm 1.7 + 4.0$	$103.3 \pm 2.1 + 5.0$	$112.8 \pm 3.4 + 7.3$
	[6000, 7000]	$93.4 \pm 2.8 + 6.8$	$100.1 \pm 2.5 + 5.5$	$97.5 \pm 2.7 + 5.6$	$100 \pm 5 + 11$
	[7000, 8000]	$96.3 \pm 3.7 + 9.2$	$100.9 \pm 3.3 + 6.9$	$96.6 \pm 3.8 + 7.4$	$143 \pm 12 + 30$
	[8000, 9000]	$132 \pm 7 + 16$	$97.6 \pm 4.3 + 8.8$	$91 \pm 5 + 10$	$124 \pm 22 + 44$
	[9000, 10000]	$99 \pm 6 + 14$	$89 \pm 5 + 10$	$108 \pm 9 + 19$	

Table 6.12: The ratios of differential production cross-sections in  $10^{-2}$  for prompt  $D_s^+$  and  $D^0$  mesons in bins of  $(y, p_T)$ . The first uncertainty is statistical, and the second is the total systematic.

$p_T$ [MeV/c]	$y$				
	[2, 2.5]	[2.5, 3]	[3, 3.5]	[3.5, 4]	[4, 4.5]
$\gamma_\infty$	$5.3^{+0.8+1.5}_{-0.8-1.1}$	$9.13^{+0.55+0.80}_{-0.55-0.77}$	$9.02^{+0.56+0.83}_{-0.57-0.73}$	$8.38^{+0.76+0.98}_{-0.77-0.82}$	
	$11.4^{+0.6+2.0}_{-0.6-1.6}$	$11.00^{+0.31+0.56}_{-0.31-0.52}$	$10.66^{+0.32+0.44}_{-0.32-0.58}$	$10.48^{+0.47+0.56}_{-0.47-0.67}$	$8.7^{+1.0+1.3}_{-1.0-1.2}$
	$11.5^{+0.6+1.4}_{-0.6-1.0}$	$11.15^{+0.33+0.40}_{-0.32-0.58}$	$10.23^{+0.33+0.47}_{-0.34-0.42}$	$10.94^{+0.47+0.58}_{-0.49-0.64}$	$10.1^{+1.0+1.1}_{-1.0-1.2}$
	$13.3^{+0.7+1.3}_{-0.7-1.1}$	$11.94^{+0.43+0.54}_{-0.44-0.64}$	$12.37^{+0.51+0.63}_{-0.51-0.64}$	$11.31^{+0.65+0.69}_{-0.65-0.75}$	$12.9^{+1.7+2.5}_{-1.7-2.4}$
	$11.3^{+0.7+0.9}_{-0.7-1.1}$	$10.45^{+0.54+0.67}_{-0.52-0.57}$	$13.03^{+0.68+0.82}_{-0.66-0.84}$	$12.3^{+1.0+1.0}_{-1.0-1.1}$	$17.6^{+4.8+6.8}_{-3.9-5.0}$
	$12.7^{+1.0+1.5}_{-1.0-1.4}$	$13.4^{+0.9+1.1}_{-0.8-1.0}$	$10.99^{+0.84+0.93}_{-0.84-0.89}$	$11.3^{+1.3+1.6}_{-1.3-1.5}$	
	$12.8^{+1.2+1.8}_{-1.2-1.6}$	$13.0^{+1.1+1.3}_{-1.1-1.3}$	$11.7^{+1.2+1.4}_{-1.2-1.3}$	$17.3^{+2.9+4.7}_{-2.7-3.7}$	
	$11.9^{+1.7+2.2}_{-1.7-1.9}$	$10.1^{+1.2+1.3}_{-1.2-1.2}$	$11.4^{+1.6+1.8}_{-1.5-1.6}$		
	$14.7^{+2.3+3.4}_{-2.3-2.9}$	$18.7^{+2.7+3.5}_{-2.5-3.4}$	$12.4^{+2.3+2.9}_{-2.2-2.5}$		

Table 6.13: The ratios of differential production cross-sections in  $10^{-2}$  for prompt  $D^{*+}$  and  $D^0$  mesons in bins of  $(y, p_T)$ . The first uncertainty is statistical, and the second is the total systematic.

$p_T$ [MeV/c]	$y$				
	[2, 2.5]	[2.5, 3]	[3, 3.5]	[3.5, 4]	[4, 4.5]
[1000, 2000]		$28.8 \pm 1.3 \pm 2.2$	$26.2 \pm 0.6 \pm 1.3$	$26.5 \pm 0.8 \pm 1.4$	$25.4 \pm 1.6 \pm 1.8$
[2000, 3000]	$25.2 \pm 2.5 \pm 3.5$	$27.8 \pm 0.7 \pm 1.5$	$30.3 \pm 0.5 \pm 1.3$	$26.9 \pm 0.7 \pm 1.2$	$27.5 \pm 1.5 \pm 2.6$
[3000, 4000]	$30.4 \pm 1.5 \pm 2.2$	$29.9 \pm 0.6 \pm 1.1$	$32.5 \pm 0.7 \pm 1.5$	$28.7 \pm 0.8 \pm 1.4$	$29.4 \pm 2.0 \pm 2.6$
[4000, 5000]	$36.7 \pm 1.7 \pm 2.2$	$31.7 \pm 0.8 \pm 1.3$	$33.4 \pm 0.9 \pm 1.7$	$35.2 \pm 1.3 \pm 2.3$	$31.6 \pm 4.0 \pm 9.0$
[5000, 6000]	$36.9 \pm 1.8 \pm 2.3$	$31.7 \pm 1.0 \pm 1.6$	$32.8 \pm 1.2 \pm 1.8$	$32.9 \pm 1.8 \pm 2.4$	$61 \pm 10 \pm 25$
[6000, 7000]	$39.6 \pm 2.3 \pm 3.7$	$33.8 \pm 1.4 \pm 2.1$	$32.5 \pm 1.6 \pm 2.1$	$33.2 \pm 2.7 \pm 3.8$	
[7000, 8000]	$32.7 \pm 2.4 \pm 3.7$	$34.0 \pm 1.9 \pm 2.7$	$35.3 \pm 2.3 \pm 3.0$	$43.0 \pm 6.1 \pm 9.8$	
[8000, 9000]	$34.8 \pm 3.2 \pm 4.7$	$30.2 \pm 2.2 \pm 2.9$	$31.0 \pm 2.8 \pm 3.7$	$44 \pm 11 \pm 22$	
[9000, 10000]	$38.5 \pm 4.2 \pm 6.4$	$34.9 \pm 3.2 \pm 4.2$	$59 \pm 7 \pm 12$		

Table 6.14: The ratios of differential production cross-sections in  $10^{-2}$  for prompt  $D_s^+$  and  $D^+$  mesons in bins of  $(y, p_T)$ . The first uncertainty is statistical, and the second is the total systematic.

80

$p_T$ [MeV/c]	$y$				
	[2, 2.5]	[2.5, 3]	[3, 3.5]	[3.5, 4]	[4, 4.5]
[1000, 2000]	$6.7^{+1.1+2.2}_{-1.0-1.6}$	$10.51^{+0.65+0.85}_{-0.64-0.83}$	$9.80^{+0.62+0.81}_{-0.62-0.71}$	$9.5^{+0.9+1.1}_{-0.9-0.9}$	
[2000, 3000]	$12.2^{+0.7+2.3}_{-0.7-1.8}$	$12.14^{+0.34+0.52}_{-0.34-0.45}$	$11.45^{+0.35+0.43}_{-0.34-0.50}$	$10.90^{+0.48+0.47}_{-0.48-0.73}$	$9.8^{+1.1+1.4}_{-1.1-1.3}$
[3000, 4000]	$12.6^{+0.6+1.4}_{-0.6-1.2}$	$11.72^{+0.35+0.47}_{-0.34-0.45}$	$10.56^{+0.34+0.39}_{-0.34-0.45}$	$11.13^{+0.49+0.52}_{-0.49-0.61}$	$11.0^{+1.1+1.1}_{-1.0-1.1}$
[4000, 5000]	$12.7^{+0.7+1.2}_{-0.7-1.1}$	$12.33^{+0.45+0.61}_{-0.44-0.51}$	$12.94^{+0.52+0.57}_{-0.53-0.69}$	$11.40^{+0.65+0.68}_{-0.64-0.73}$	$14.3^{+1.8+1.8}_{-1.8-1.6}$
[5000, 6000]	$11.5^{+0.8+1.1}_{-0.8-0.9}$	$11.00^{+0.56+0.68}_{-0.56-0.55}$	$12.62^{+0.65+0.70}_{-0.64-0.80}$	$10.95^{+0.86+0.87}_{-0.86-0.88}$	$11.8^{+2.4+2.1}_{-2.4-1.8}$
[6000, 7000]	$13.6^{+1.1+1.5}_{-1.1-1.4}$	$13.34^{+0.87+0.99}_{-0.85-0.98}$	$11.26^{+0.85+0.89}_{-0.84-0.91}$	$11.3^{+1.3+1.3}_{-1.3-1.2}$	
[7000, 8000]	$13.2^{+1.2+1.8}_{-1.2-1.7}$	$12.9^{+1.1+1.2}_{-1.1-1.3}$	$12.1^{+1.2+1.3}_{-1.2-1.2}$	$12.1^{+1.8+2.4}_{-1.8-1.9}$	
[8000, 9000]	$9.0^{+1.3+1.6}_{-1.3-1.5}$	$10.3^{+1.2+1.2}_{-1.2-1.2}$	$12.6^{+1.7+1.7}_{-1.7-1.6}$		
[9000, 10000]	$14.9^{+2.3+3.4}_{-2.3-2.9}$	$20.9^{+2.9+3.8}_{-2.8-3.7}$	$11.5^{+2.1+2.3}_{-2.0-2.0}$		

Table 6.15: The ratios of differential production cross-sections in  $10^{-2}$  for prompt  $D^{*+}$  and  $D^+$  mesons in bins of  $(y, p_T)$ . The first uncertainty is statistical, and the second is the total systematic.

$p_T$ [MeV/c]	$y$				
	[2, 2.5]	[2.5, 3]	[3, 3.5]	[3.5, 4]	[4, 4.5]
[1000, 2000]		$33.2^{+1.6+2.3}_{-1.5-2.3}$	$28.5^{+0.7+0.8}_{-0.7-1.7}$	$29.9^{+0.9+1.3}_{-0.9-1.9}$	$26.8^{+1.7+2.0}_{-1.7-2.9}$
[2000, 3000]	$27.1^{+2.7+4.2}_{-2.7-4.1}$	$30.7^{+0.8+1.4}_{-0.8-0.9}$	$32.5^{+0.6+0.9}_{-0.6-1.8}$	$28.0^{+0.7+0.6}_{-0.7-2.0}$	$31.0^{+1.6+2.7}_{-1.5-3.4}$
[3000, 4000]	$33.4^{+1.7+2.4}_{-1.7-3.1}$	$31.4^{+0.7+1.1}_{-0.7-1.0}$	$33.6^{+0.6+0.9}_{-0.6-1.9}$	$29.2^{+0.8+1.0}_{-0.8-2.1}$	$31.8^{+2.1+2.1}_{-2.0-2.4}$
[4000, 5000]	$35.0^{+1.6+2.1}_{-1.6-3.0}$	$32.7^{+0.8+1.3}_{-0.8-1.1}$	$34.9^{+0.8+1.3}_{-0.8-1.9}$	$35.4^{+1.2+2.0}_{-1.2-2.9}$	$35.1^{+4.1+8.2}_{-4.1-5.5}$
[5000, 6000]	$37.4^{+1.9+2.9}_{-1.9-2.8}$	$33.3^{+1.1+1.5}_{-1.1-1.4}$	$31.8^{+1.1+1.4}_{-1.1-1.9}$	$29.2^{+1.5+1.7}_{-1.5-2.0}$	$40.8^{+2.5+8.4}_{-2.3-6.9}$
[6000, 7000]	$42.5^{+2.5+3.6}_{-2.4-3.6}$	$33.7^{+1.4+1.8}_{-1.3-1.9}$	$33.3^{+1.6+1.9}_{-1.5-2.2}$	$33.1^{+2.6+2.5}_{-2.5-3.0}$	
[7000, 8000]	$33.9^{+2.5+3.5}_{-2.4-3.4}$	$33.7^{+1.8+2.2}_{-1.8-2.1}$	$36.5^{+2.3+2.6}_{-2.2-2.8}$	$30.0^{+3.8+4.7}_{-3.6-3.9}$	
[8000, 9000]	$26.4^{+2.4+3.6}_{-2.4-3.1}$	$31.0^{+2.1+2.3}_{-2.1-2.4}$	$34.1^{+2.9+2.9}_{-2.8-3.2}$	$36^{+7+12}_{-6-8}$	
[9000, 10000]	$39.0^{+4.2+5.9}_{-4.1-5.1}$	$39.1^{+3.6+3.9}_{-3.5-4.1}$	$55.0^{+5.8+9.4}_{-5.5-7.7}$		

Table 6.16: The ratios of differential production cross-sections in  $10^{-2}$  for prompt  $D_s^+$  and  $D^{*+}$  mesons in bins of  $(y, p_T)$ . The first uncertainty is statistical, and the second is the total systematic.

$p_T$ [MeV/c]	$y$				
	[2, 2.5]	[2.5, 3]	[3, 3.5]	[3.5, 4]	[4, 4.5]
[1000, 2000]		$31.7^{+2.5+3.4}_{-2.3-2.9}$	$34.4^{+2.3+3.6}_{-2.3-2.1}$	$31.6^{+3.0+4.7}_{-3.0-2.7}$	
[2000, 3000]	$45^{+6+12}_{-5-7}$	$39.5^{+1.5+1.9}_{-1.4-2.2}$	$35.2^{+1.2+2.3}_{-1.2-1.5}$	$39.0^{+1.9+3.6}_{-1.9-2.2}$	$31.6^{+3.9+6.3}_{-3.7-4.4}$
[3000, 4000]	$37.8^{+2.7+5.5}_{-2.5-3.5}$	$37.3^{+1.3+1.6}_{-1.3-1.7}$	$31.5^{+1.2+2.2}_{-1.1-1.3}$	$38.0^{+1.9+3.6}_{-1.9-2.1}$	$34.5^{+3.9+4.2}_{-3.8-3.5}$
[4000, 5000]	$36.3^{+2.6+4.7}_{-2.4-2.8}$	$37.7^{+1.6+2.1}_{-1.6-1.9}$	$37.1^{+1.7+2.7}_{-1.7-2.0}$	$32.2^{+2.0+3.5}_{-2.0-2.4}$	$40.8^{+7.4+9.3}_{-6.3-8.1}$
[5000, 6000]	$30.7^{+2.6+3.5}_{-2.4-2.7}$	$33.0^{+1.9+2.3}_{-1.8-1.9}$	$39.7^{+2.4+3.3}_{-2.3-2.5}$	$37.5^{+3.5+3.9}_{-3.3-3.1}$	$29.0^{+5.8+7.4}_{-5.7-5.6}$
[6000, 7000]	$32.0^{+3.1+4.3}_{-3.0-3.6}$	$39.6^{+2.9+3.6}_{-2.8-3.1}$	$33.8^{+2.9+3.4}_{-2.8-2.7}$	$34.1^{+4.7+4.9}_{-4.3-3.6}$	
[7000, 8000]	$39.1^{+4.6+6.2}_{-4.4-5.1}$	$38.4^{+3.7+4.0}_{-3.6-4.0}$	$33.1^{+3.8+4.3}_{-3.5-3.5}$	$40.3^{+8.1+9.5}_{-7.1-7.1}$	
[8000, 9000]	$34.2^{+5.7+6.8}_{-5.4-5.5}$	$33.4^{+4.4+4.3}_{-4.2-3.7}$	$36.9^{+5.7+6.0}_{-5.4-4.7}$		
[9000, 10000]	$38.1^{+7.2+9.6}_{-6.5-7.7}$	$54^{+9+11}_{-8-10}$	$20.9^{+4.3+4.9}_{-3.9-4.1}$		

*Table 7.1: Relative error on the  $D^0$  cross-section in each kinematic bin due to the statistical uncertainty.*

$p_T$ [MeV/c]	$y$				
	[2, 2.5]	[2.5, 3]	[3, 3.5]	[3.5, 4]	[4, 4.5]
[0, 1000]	1.60	0.84	0.82	1.13	2.41
[1000, 2000]	1.07	0.59	0.60	0.81	1.64
[2000, 3000]	1.00	0.60	0.64	0.88	1.81
[3000, 4000]	1.07	0.71	0.80	1.09	2.61
[4000, 5000]	1.29	0.95	1.09	1.53	4.73
[5000, 6000]	1.66	1.30	1.51	2.38	14.09
[6000, 7000]	2.09	1.82	2.09	3.81	
[7000, 8000]	2.73	2.41	2.90	7.20	
[8000, 9000]	3.60	3.24	4.17	14.01	
[9000, 10000]	4.43	4.21	6.26		

## 7 Systematic uncertainties

This section will describe and evaluate the systematic uncertainties in the analysis. Each of the sources for systematic uncertainties discussed below gives rise to one of the terms on the right side of equation 1.1 (or one of the its components in case of the efficiency). These uncertainties are then propagated by adding an additive nuisance parameter on the respective term. Monte Carlo error propagation is used to propagate the uncertainties, as discussed in Section 1.3. For comparison, the relative statistical uncertainty is also given in Tables 7.1, D.1, D.2, and D.3 for  $D^0 \rightarrow K^-\pi^+$ ,  $D^+ \rightarrow K^-\pi^+\pi^+$ ,  $D_s^+ \rightarrow \phi\pi^+$ , and  $D^{*+} \rightarrow D^0\pi^+$  with  $D^0 \rightarrow K^-\pi^+$ .

### 7.1 Finite Monte Carlo sample size

This analysis relies on Monte Carlo samples to estimate most of the efficiencies, and as these samples are of finite size the efficiencies carry a non-zero statistical uncertainty. This is propagated to the measurement as a systematic uncertainty. As the set of MC events is unique for each  $p_T$ - $y$  bin and mode, this systematic uncertainty is fully uncorrelated between bins and between modes. As already discussed in Section 4.5, the posteriori probability for the estimated efficiency is described by the Beta distribution, and hence the corresponding nuisance parameter is modelled by this distribution after shifting it such that the most probable value coincides with zero.

Table 7.2: Relative error on the  $D^0$  cross-section in each kinematic bin due to the finite size of the Monte Carlo sample.

$p_T$ [MeV/c]	$y$				
	[2, 2.5]	[2.5, 3]	[3, 3.5]	[3.5, 4]	[4, 4.5]
[0, 1000]	3.19	1.49	1.38	1.84	4.00
[1000, 2000]	2.19	1.09	1.01	1.29	2.35
[2000, 3000]	1.91	1.01	0.99	1.26	2.30
[3000, 4000]	1.87	1.08	1.11	1.42	3.00
[4000, 5000]	2.10	1.33	1.40	1.80	5.20
[5000, 6000]	2.59	1.72	1.85	2.62	11.42
[6000, 7000]	3.28	2.33	2.52	4.39	
[7000, 8000]	4.37	3.11	3.46	7.27	
[8000, 9000]	5.37	4.07	5.03	14.51	
[9000, 10000]	6.40	5.11	7.05		

893     The resulting relative systematic uncertainties are given in Tables 7.2, D.4, D.5,  
 894     and D.6 for  $D^0 \rightarrow K^-\pi^+$ ,  $D^+ \rightarrow K^-\pi^+\pi^+$ ,  $D_s^+ \rightarrow \phi\pi^+$ , and  $D^{*+} \rightarrow D^0\pi^+$  with  
 895      $D^0 \rightarrow K^-\pi^+$ .

## 896     7.2 Monte Carlo modelling

897     If the simulated data does not correctly model the selection variables, the selection  
 898     efficiencies that are evaluated with MC will be wrong. Small deviations of the MC  
 899     from the distributions in data can lead to small deviations from the true efficiencies,  
 900     and these deviations need to be evaluated and assigned as systematic uncertainties.  
 901     In order to extract the signal distribution for a specified variable the sPlot method  
 902     was used [13]. The resulting histograms which compare the simulated distribution to  
 903     those obtained from data are shown in the Figures in Appendix

904     To assess the uncertainty, the following procedure is performed for each selection  
 905     variable:

- 906       1. For a given selection variable  $x$ , find the cut value  $y$  on  $x$  which rejects half of  
     907       the simulated data;
- 908       2. Apply the cut value  $y$  on  $x$  in the *real data*, counting the number of signal  
     909       candidates passing the requirement as the sum of signal sWeights divided by

Table 7.3: Relative error on all kinematic bins due to the Monte Carlo modelling systematic.

Mode	Relative error
$D^0 \rightarrow K^- \pi^+$	1.97%
$D^+ \rightarrow K^- \pi^+ \pi^+$	1.35%
$D_s^+ \rightarrow \phi \pi^+$	0.31%
$D^{*+} \rightarrow D^0 \pi^+$ with $D^0 \rightarrow K^- \pi^+$	0.95%

910 the PID selection efficiencies

$$N_{\text{Passed}} = \sum_N^i I(i) \frac{w_{i,\text{signal}}}{\epsilon_{PID}}, \quad (7.1)$$

911 where  $I(i)$  is 1 if the value of  $x$  for the  $i$ th event passes the requirement on  $x$ ,  
912 and is zero otherwise;

913 3. The efficiency-corrected signal yield corresponding to the requirement on  $x$   
914 is  $2N_{\text{Passed}}$ , which should equal the number of signal candidates before the  
915 requirement  $y$ , if the MC describes the data. The quantity

$$\Delta = 2N_{\text{Passed}} - \sum_N^i \frac{w_{i,\text{signal}}}{\epsilon_{PID}}. \quad (7.2)$$

916 is then a handle on the mis-modelling of the data in the MC.

917 This procedure is integrated across all  $p_T$ - $y$  bins as the MC sample sizes are too  
918 small to make precise differential measurements.

919 To account for correlations between variables, which may lead to double-counting  
920 of the mis-modelling if neglected, the procedure is repeated ten thousand times per  
921 selection variable, using bootstrapped real data, deciding how many times an event  
922 enters a bootstrap sample by sampling from a Poisson distribution with a mean of 1.  
923 The total systematic uncertainty on the efficiency-corrected signal yield due to MC  
924 mis-modelling is the mean of the ten thousand samples. We assign an uncertainty of  
925 zero if the deviation is not statistically significant.

926 The  $p_T$ - $y$  -integrated systematic uncertainty is given for each mode in Table 7.3

### 927 7.3 Monte Carlo truth matching

928 Due to the finite size of the Monte Carlo sample, the truth matching efficiency defined  
929 in Section 4.2.2 carries a statistical uncertainty. This uncertainty is propagated as a

*Table 7.4: Relative error on the cross-sections in all kinematic bins due to the finite size of the Monte Carlo sample used to compute the truth matching efficiency.*

Mode	Relative error
$D^0 \rightarrow K^- \pi^+$	0.08%
$D^+ \rightarrow K^- \pi^+ \pi^+$	0.19%
$D_s^+ \rightarrow \phi \pi^+$	0.29%
$D^{*+} \rightarrow D^0 \pi^+$ with $D^0 \rightarrow K^- \pi^+$	0.22%

930 systematic uncertainty on the cross-sections.

931 As the MC sample size is too small to compute the truth match systematic in  
932  $p_T$ - $y$  bins, an integrated value is computed. The values for each mode are given in  
933 Table 7.4.

## 934 7.4 PID calibration

935 Four common sources are typically mentioned when discussing systematic uncertainties  
936 in the PIDCALIB approach:

- 937 1. Mismodelling in the reference sample: the chosen reference sample does not  
938 correctly model the kinematics. This does not apply to this analysis as a purely  
939 data-driven approach is used where the actual data is reweighted.
- 940 2. Uncertainty due to the  $s\mathcal{P}lot$  technique in the calibration sample: We perform  
941 fits in each calibration bin separately, hence this does not apply here.
- 942 3. Limited sample size of the calibration sample: This is incorporated as described  
943 before by bootstrapping the calibration sample before each fit and including  
944 the variation of the obtained efficiency in each as part of the Monte Carlo error  
945 propagation.
- 946 4. The chosen binning scheme can bias the efficiency if the distributions of the  
947 reference and calibration sample within a bin are significantly different. The  
948 treatment of this uncertainty will be discussed in the following.

949 To estimate the effect of the binning systematic, we employ an alternative method  
950 using the boosted decision tree based reweighting algorithm of the `hep_ml` package.  
951 An efficiency can be seen as the weight that has to be assigned to  
952 an event before the selection criteria to have the obtained distribution agree with the  
953 one obtained after the cut.

Table 7.5: Relative error on the  $D^0$  cross-section in each kinematic bin due to the finite size of the PID calibration sample.

$p_T$ [MeV/c]	$y$				
	[2, 2.5]	[2.5, 3]	[3, 3.5]	[3.5, 4]	[4, 4.5]
[0, 1000]	0.46	0.29	0.15	0.23	0.57
[1000, 2000]	0.34	0.19	0.12	0.18	0.52
[2000, 3000]	0.23	0.11	0.08	0.18	0.79
[3000, 4000]	0.16	0.08	0.08	0.25	0.93
[4000, 5000]	0.13	0.07	0.11	0.38	1.08
[5000, 6000]	0.11	0.08	0.17	0.49	1.37
[6000, 7000]	0.12	0.13	0.30	0.61	
[7000, 8000]	0.15	0.19	0.45	0.83	
[8000, 9000]	0.27	0.31	0.63	1.03	
[9000, 10000]	0.42	0.54	0.67		

Therefore, we trained the BDT classifier to discriminate between the distributions in the calibration sample before and after the  $\text{DLL}_{K-\pi}$  cut being applied to the track. As training variables, we use  $p$ ,  $\eta$  and `nSPDHits`, while additional variables can be included, no significant change was observed if  $\phi$ ,  $p_T$  or the number of tracks were added in addition to the nominal three variables.

The trained reweighter is then used to predict the efficiencies for every event in the reference sample and the efficiency in each  $p_T$ - $y$  bin is obtained as before. The difference in obtained efficiency to the nominal method using a binned calibration sample is then taken as the systematic uncertainty.

The resulting relative systematic uncertainties due to the finite size of the PID calibration sample are given in Tables 7.5, D.7, D.8, and D.9 for  $D^0 \rightarrow K^-\pi^+$ ,  $D^+ \rightarrow K^-\pi^+\pi^+$ ,  $D_s^+ \rightarrow \phi\pi^+$ , and  $D^{*+} \rightarrow D^0\pi^+$  with  $D^0 \rightarrow K^-\pi^+$ . The corresponding tables for the relative systematic uncertainties due to the choice of binning are given in Tables 7.6, D.10, D.11, and D.12.

## 7.5 Luminosity

There is an uncertainty on the luminosity measurement provided by the luminosity group, which we will propagate as a systematic uncertainty on our measurement. The relative uncertainty on the luminosity measurement is expected to be around 5%. As of 14<sup>th</sup> June 2016, the luminosity calibration for this dataset is not available, and so

*Table 7.6: Relative error on the  $D^0$  cross-section in each kinematic bin due to the choice of PID calibration binning.*

$p_T$ [MeV/c]	$y$				
	[2, 2.5]	[2.5, 3]	[3, 3.5]	[3.5, 4]	[4, 4.5]
[0, 1000]	7.92	1.03	0.28	0.71	3.74
[1000, 2000]	4.57	1.01	0.23	0.26	1.49
[2000, 3000]	2.14	0.60	0.02	0.53	0.52
[3000, 4000]	0.86	0.34	0.23	1.51	4.86
[4000, 5000]	0.31	0.03	0.68	0.09	12.97
[5000, 6000]	0.33	0.19	1.13	2.76	26.13
[6000, 7000]	0.26	0.40	0.06	6.89	
[7000, 8000]	0.04	1.09	2.52	14.42	
[8000, 9000]	0.74	1.95	4.79	16.23	
[9000, 10000]	0.37	2.84	8.96		

973 the luminosity reported in this note is incorrect.

## 974 7.6 Tracking efficiency correction

975 There is an uncertainty on the tracking correction, discussed in Section 4.2.1, provided  
 976 by the tracking group, which we will propagate as a systematic uncertainty on our  
 977 measurement. There are several potential sources for systematic uncertainties:

- 978 • The uncertainties given in Figure 4.1 which incorporate the statistical uncer-  
 979 tainties from the calibration mode and differences between different methods  
 980 used to extract these factors.
- 981 • The correction table provides numbers estimated using muons. An additional  
 982 uncertainty of 1.1% (1.4%) is applied for kaons (pions) due to uncertainties in  
 983 the hadronic interactions. This is dominated by the uncertainty on the material  
 984 budget and hence full correlation between kaons and pions is assumed.
- 985 • An additional uncertainty of 0.4% is applied due to the reweighting procedure.

986 All of these sources are propagated using Monte Carlo error propagation and assuming  
 987 Gaussian distributions with the above mentioned relative widths for the different  
 988 contributions to the tracking systematic uncertainty. Even though different bins and  
 989 modes have different final state kinematics and hence access the table of correction

*Table 7.7: Relative error on the  $D^0$  cross-section in each kinematic bin due to the finite sample size and hadronic interaction uncertainty on the tracking efficiency correction measurement.*

$p_T$ [MeV/c]	$y$				
	[2, 2.5]	[2.5, 3]	[3, 3.5]	[3.5, 4]	[4, 4.5]
[0, 1000]	4.73	3.87	3.25	3.12	3.03
[1000, 2000]	4.42	3.55	3.19	3.11	3.10
[2000, 3000]	3.88	3.26	3.10	3.08	3.06
[3000, 4000]	3.40	3.14	3.05	3.04	3.06
[4000, 5000]	3.27	3.08	3.02	3.02	3.17
[5000, 6000]	3.15	3.03	3.01	3.03	3.26
[6000, 7000]	3.10	3.03	3.00	3.07	
[7000, 8000]	3.07	3.05	3.00	3.09	
[8000, 9000]	3.03	3.07	3.00	3.22	
[9000, 10000]	3.01	3.08	3.03		

990 factors for each track differently, the obtained uncertainty is driven by the global  
 991 factors for the reweighting and the hadronic interaction uncertainty and the results  
 992 are found to be highly correlated (at least 90%) between different bins and modes.

993 The resulting relative systematic uncertainties are given in Table 7.7 for  $D^0 \rightarrow K^-\pi^+$ ,  
 994 in Table D.13 for  $D^+ \rightarrow K^-\pi^+\pi^+$ , in Table D.14 for  $D_s^+ \rightarrow \phi\pi^+$ , and in  
 995 Table D.15 for  $D^{*+} \rightarrow D^0\pi^+$  with  $D^0 \rightarrow K^-\pi^+$ .

996 The posteriori distribution obtained from the toy propagation of the uncertainties  
 997 is then used as the distribution for the associated nuisance parameter after shifting it  
 998 such that the most probable value coincides with zero.

## 999 7.7 Branching fractions

1000 There is an uncertainty on the branching fractions, provided by the Particle Data  
 1001 Group [17], which we will propagate as a systematic uncertainty on our measurement.  
 1002 The numerical values used are listed in Table 7.8. We use these particular values as  
 1003 they are the same as those used in the  $\sqrt{s} = 13$  TeV charm production measurement,  
 1004 making the statistical treatment when computing ratios between centre-of-mass  
 1005 energies very easy (the branching fractions will cancel).

1006 As this measurement does not determine the resonant  $\phi \rightarrow K^+K^-$  contribution  
 1007 in the  $D_s^+ \rightarrow \phi\pi^+$  sample, but instead only selects events within a  $\pm 20$  MeV window

*Table 7.8: Branching ratios for the different modes [14]. Quoted uncertainties are propagated as systematic uncertainties in this measurement.*

Mode	$\mathcal{B}$ [%]
$D^0 \rightarrow K^- \pi^+$	$3.88 \pm 0.05$
$D^+ \rightarrow K^- \pi^+ \pi^+$	$9.13 \pm 0.19$
$D_s^+ \rightarrow \phi \pi^+$	$2.24 \pm 0.13$
$D^{*+} \rightarrow D^0 \pi^+$	$67.7 \pm 0.5$

around the  $\phi$  mass, as described in Section 3.3, a dedicated measurement by CLEO is used [11]. This measures the branching fraction of  $D_s^+ \rightarrow \phi \pi^+$ , where a ‘ $\phi$ ’ is identified by the same  $\pm 20$  MeV window definition.

## 7.8 Fit model

Other fit models may describe the well but give different results. The magnitude of the difference between the cross sections computed with other fit models and our ‘nominal’ model, described in Section 5, is assigned as a systematic uncertainty on the result. This corresponds to an uncertainty on what the true generating probability density function is for the observed data.

The resulting relative systematic uncertainties are given in Tables 7.9, D.16, D.17, and D.18 for  $D^0 \rightarrow K^- \pi^+$ ,  $D^+ \rightarrow K^- \pi^+ \pi^+$ ,  $D_s^+ \rightarrow \phi \pi^+$ , and  $D^{*+} \rightarrow D^0 \pi^+$  with  $D^0 \rightarrow K^- \pi^+$ .

## 7.9 Signal window

The signal window that is applied to the data entering the  $\ln \chi_{\text{IP}}^2$  fit, as described in Section 5, and this has an efficiency, as described in Section 4.8. The computation of this efficiency assumes the signal model is known, but the parameters of the model are fitted to the data, and so have an uncertainty, which results in a systematic uncertainty on the signal window efficiency.

This computation of the uncertainty on the signal window efficiency is given in Section 4.8. This uncertainty is propagated the cross-sections as the systematic uncertainty.

*Table 7.9: Relative error on the  $D^0$  cross-section in each kinematic bin due to the arbitrary choice of fit model.*

$p_T$ [MeV/c]	$y$				
	[2, 2.5]	[2.5, 3]	[3, 3.5]	[3.5, 4]	[4, 4.5]
[0, 1000]	0.45	0.45	0.52	1.31	2.74
[1000, 2000]	0.01	0.28	0.92	1.66	2.18
[2000, 3000]	0.17	0.50	1.15	1.82	1.77
[3000, 4000]	0.39	0.72	1.38	1.38	1.41
[4000, 5000]	0.71	1.19	1.41	1.29	1.12
[5000, 6000]	0.73	1.38	1.33	1.25	1.66
[6000, 7000]	0.91	1.45	1.14	1.29	
[7000, 8000]	1.37	1.30	1.17	1.18	
[8000, 9000]	1.48	1.16	1.36	1.33	
[9000, 10000]	1.74	1.43	0.84		

## 7.10 Correlations and summary

The different sources of systematic uncertainty discussed in this section can be grouped into different categories: global uncertainties which are correlated between all bins and all modes, uncertainties which are only correlated between the bins of one mode and those which are uncorrelated between bins and modes.

### Global uncertainties

- Branching ratio for  $D^0$  and  $D^{*+} \rightarrow D^0\pi^+$  for the same  $D^0$  final state.
- Luminosity
- Tracking correction

### Correlated between different bins

- Branching ratio
- Fit model
- PID calibration sample size
- PID binning

*Table 7.10: Overview of systematic uncertainties and their values, expressed as relative fractions of the cross-section measurements in percent (%). Uncertainties that are computed bin-by-bin are expressed as ranges giving the minimum to maximum values of the bin uncertainties. Ranges for the correlations are also given separately for bins and modes in percent.*

Sources	$D^0$ $K^-\pi^+$	$D^+$ $K^-\pi^+\pi^+$	$D_s^+$ $\phi\pi^+$	$D^{*+}$ $K^-\pi^+\pi^+$	Correlations bins	Correlations modes
Stat.	0–10	0–10	0–20	0–20	-	-
MC stat.	0–20	0–20	0–20	0–10	-	-
MC/data	0.3	0.7	0.6	2	-	-
MC/truth	0.07	0.1	0.3	0.3	-	-
Tracking	3–5	5–7	4–7	5–7	90–100	0–50
PID stat.	0–1	0–1	0–2	0–2	0–100	0–50
PID binning	0–30	0–10	0–20	0–20	-	-
Fit	0–3	0–3	0–3	0.0–1.0	-	-
Signal window	0–1	0–1	0–3	0–2	-	-
Branching ratios	1.2	2.1	5.8	1.5	100	0–95
Luminosity			3.8		100	100

## Uncorrelated

- Monte Carlo sample size

An overview of the uncertainties is given in Table 7.10. As we employ Monte Carlo error propagation, correlations due to a common input to the measurement of meson species (e.g. they all use the same tracking correction tables and systematic uncertainty due to detector material modelling) are implicitly included in the computation (also across different center-of-mass energies) the same Monte Carlo error propagation list is used.

## 7.11 Correlations between $\sqrt{s} = 5 \text{ TeV}$ and $13 \text{ TeV}$ measurements

The use of Monte Carlo error propagation allows a seamless treatment of correlations even between different years. Correlated systematic uncertainties are: the branching

1055 fractions, the luminosity and the tracking calibration. As the same numerical values  
1056 for the branching fractions are used, the corresponding systematic uncertainty is  
1057 fully correlated between the two years. The correlation between for the luminosity  
1058 uncertainty is taken to be 32% (luminosity working group) and the contributions  
1059 to tracking due to the uncertainty on the material budget are assumed to be fully  
1060 correlated.

1061    **8 Conclusion**

1062    A measurement of charm production in  $pp$  collisions at a centre-of-mass energy of  
1063     $\sqrt{s} = 5 \text{ TeV}$  has been performed with data collected with the LHCb detector. While  
1064    the shapes of the differential cross-sections for  $D^0$ ,  $D^+$ ,  $D_s^+$ , and  $D^{*+}$  mesons are  
1065    found to be in agreement with NLO predictions, the measured values tend to lie at  
1066    the upper edge of the predictions. This is a feature also common to the measurements  
1067    at  $\sqrt{s} = 7$  and  $13 \text{ TeV}$ , which indicates a general underestimation in the prediction  
1068    of the absolute value of prompt charm production in the forward region. The ratios  
1069    of the production cross-sections for centre-of-mass energies of  $13 \text{ TeV}$  and  $5 \text{ TeV}$  have  
1070    been measured and show consistency with theoretical predictions. The integrated  
1071    cross-sections for prompt open charm meson production in  $pp$  collisions at  $\sqrt{s} = 5 \text{ TeV}$   
1072    and in the range  $1 < p_T < 8 \text{ GeV}/c$  and  $2 < y < 4.5$  are

$$\begin{aligned}\sigma(pp \rightarrow D^0 X) &= 1190 \pm 3 \pm 64 \mu\text{b}, \\ \sigma(pp \rightarrow D^+ X) &= 456 \pm 3 \pm 34 \mu\text{b}, \\ \sigma(pp \rightarrow D_s^+ X) &= 195 \pm 4 \pm 19 \mu\text{b}, \\ \sigma(pp \rightarrow D^{*+} X) &= 467 \pm 6 \pm 40 \mu\text{b}.\end{aligned}$$

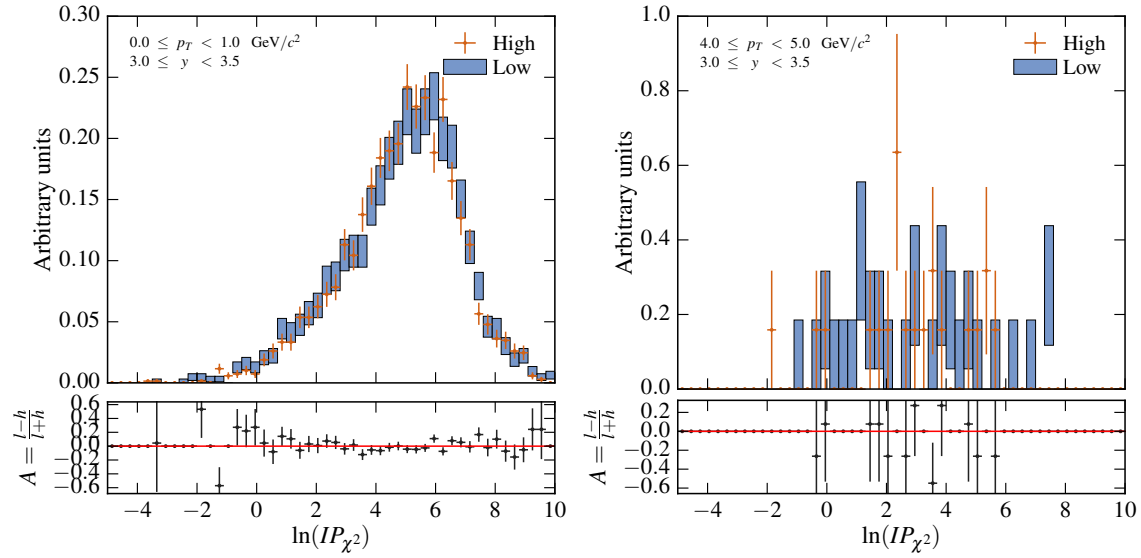


*Figure A.1: Comparison of the upper and lower sidebands for  $D^0 \rightarrow K^- \pi^+$  for two example bins.*

## A Comparison of upper and lower sidebands

To enhance the available statistic for the creation of the templates used in the  $\ln \chi_{\text{IP}}^2$  fit, both upper and lower sidebands are used. This can potentially lead to problems if both are significantly different as this will impact the modelling of the background distribution in the signal window.

To investigate this effect, the  $\ln \chi_{\text{IP}}^2$  distributions in the upper and lower sideband are compared in the  $p_T$ - $y$  bin of the measurement. Comparison plots are given in Figures A.1, A.2 and A.3. All show a good agreement between both distribution (in the limited statistic available in each  $p_T$ - $y$  bin).

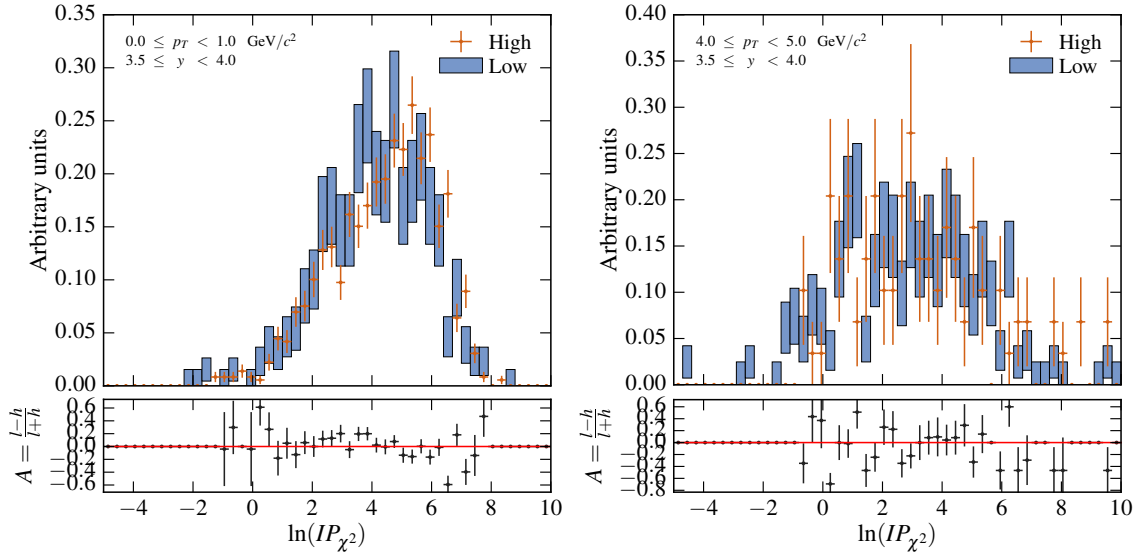


Figure A.2: Comparison of the upper and lower sidebands for  $D^+ \rightarrow K^-\pi^+\pi^+$  for two example bins.

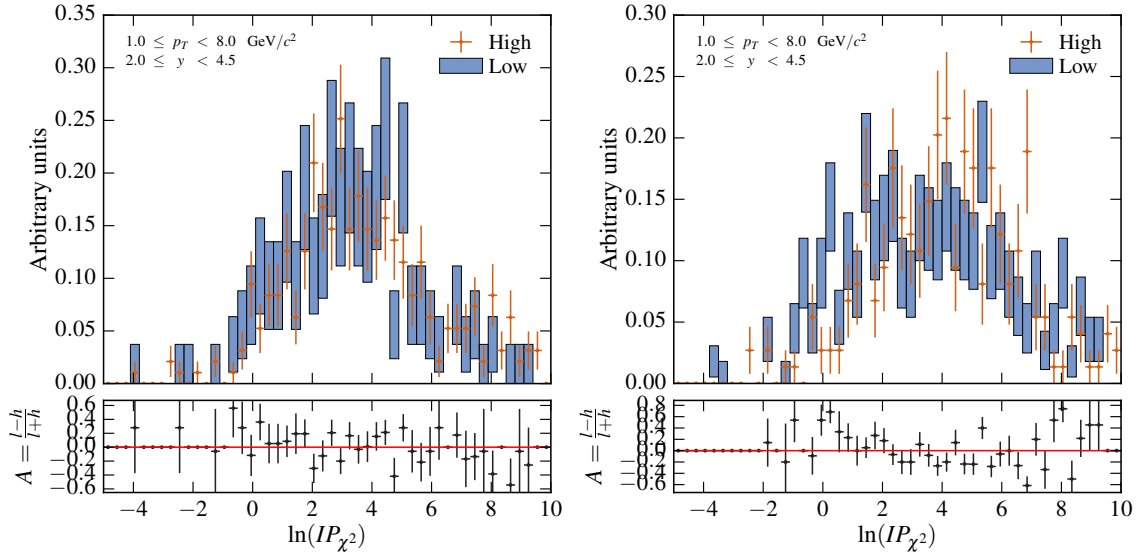


Figure A.3: Comparison of the upper and lower sidebands for  $D_s^+ \rightarrow \phi\pi^+$  (left) and of the  $D^{*+} \rightarrow D^0\pi^+$  with  $D^0 \rightarrow K^-\pi^+$  sideband with alternative sideband with  $155 \leq \delta m < 160$  MeV/ $c^2$ . Due to the very low background statistic in both modes,  $p_T\cdot y$  integrated distributions are shown.

1082 **B Per-bin  $\ln \chi^2_{\text{IP}}$  fits**

1083 This section presents the  $\ln \chi^2_{\text{IP}}$  fits described in Section 5 in  $p_{\text{T}}\text{-}y$  bins. The integrated  
1084 fits are given in Section 5.6.

1085 **B.1**  $D^0 \rightarrow K^- \pi^+$

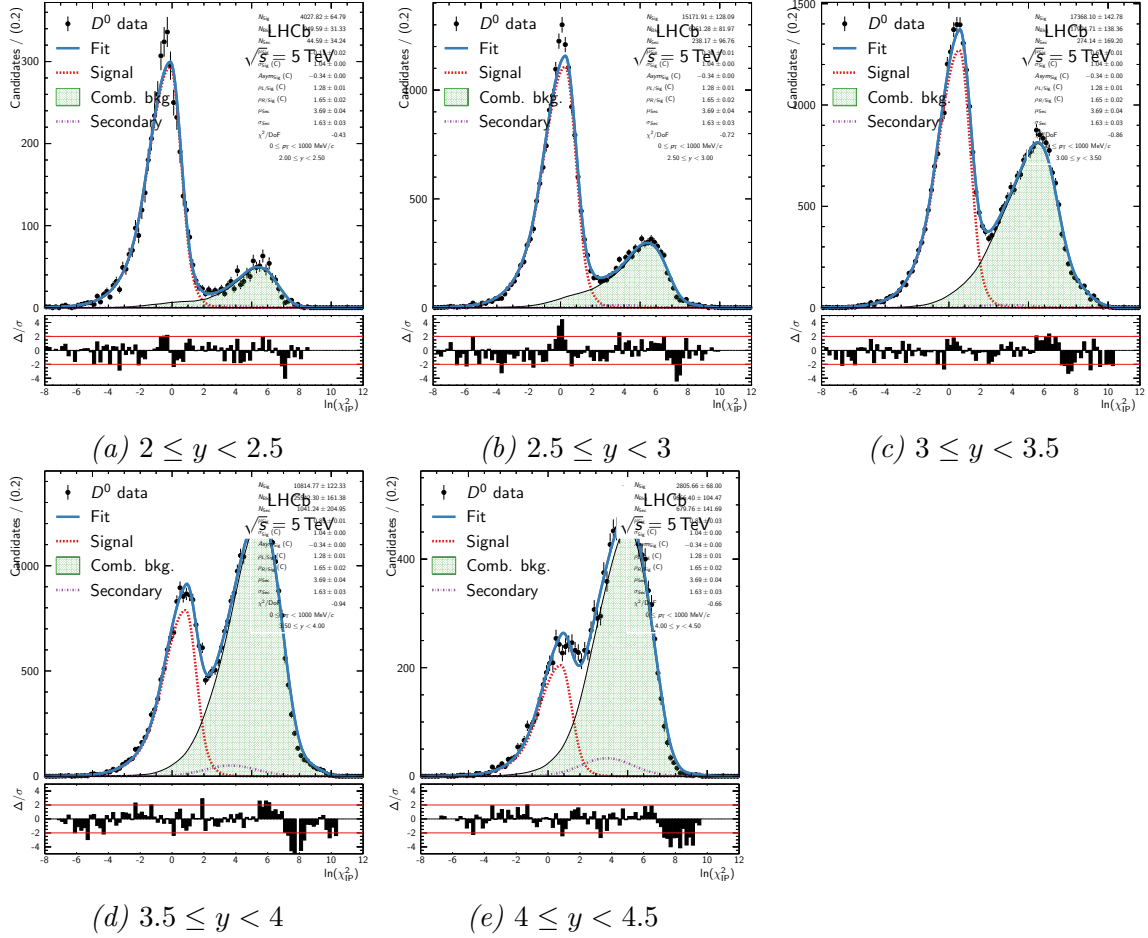


Figure B.1: Fits to the  $\ln \chi^2_{IP}$  distribution in the signal region of the  $D^0 \rightarrow K^- \pi^+$  data in bins of rapidity in the  $p_T$  range  $0 \leq p_T < 1 \text{ GeV}$ .

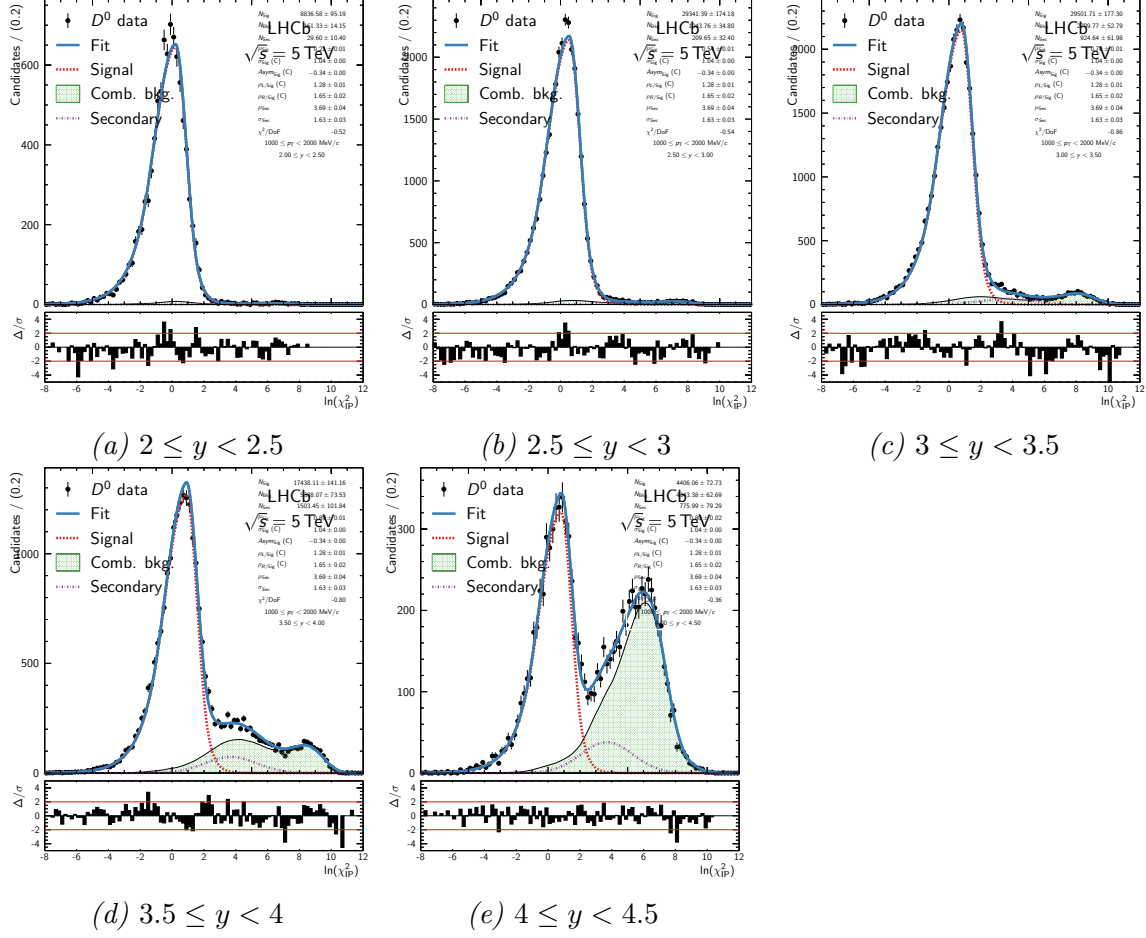


Figure B.2: Fits to the  $\ln \chi^2_{\text{IP}}$  distribution in the signal region of the  $D^0 \rightarrow K^- \pi^+$  data in bins of rapidity in the  $p_T$  range  $1 \leq p_T < 2 \text{ GeV}$ .

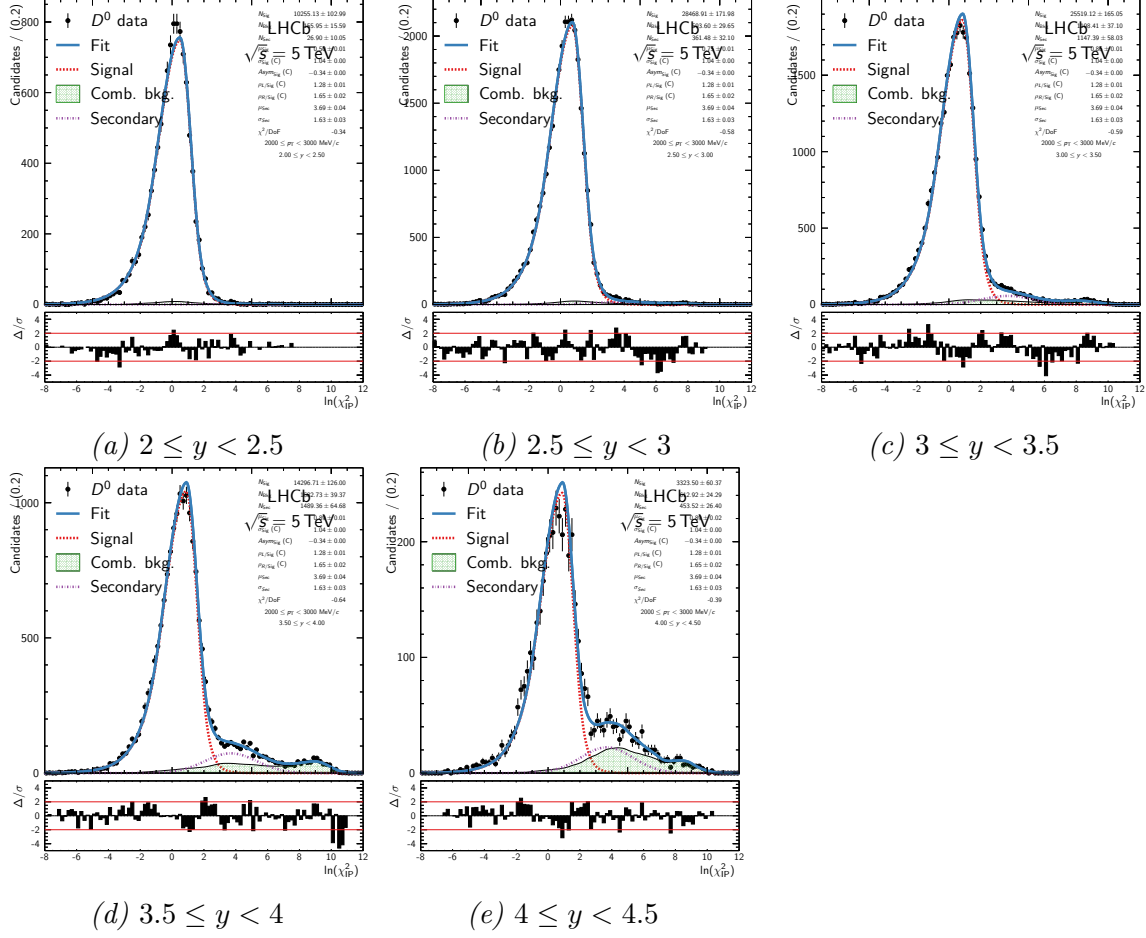
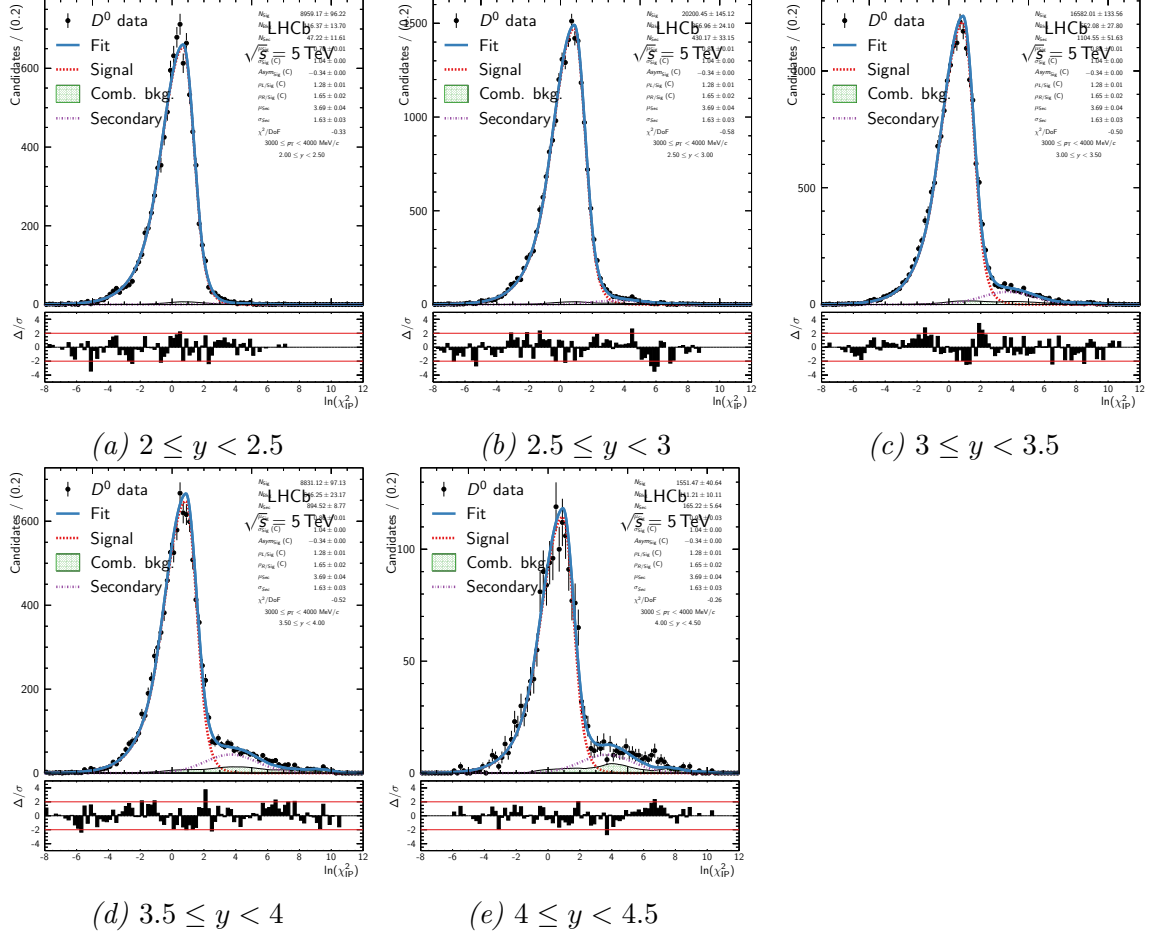


Figure B.3: Fits to the  $\ln \chi^2_{\text{IP}}$  distribution in the signal region of the  $D^0 \rightarrow K^- \pi^+$  data in bins of rapidity in the  $p_T$  range  $2 \leq p_T < 3 \text{ GeV}$ .



*Figure B.4: Fits to the  $\ln \chi_{\text{IP}}^2$  distribution in the signal region of the  $D^0 \rightarrow K^- \pi^+$  data in bins of rapidity in the  $p_T$  range  $3 \leq p_T < 4 \text{ GeV}$ .*

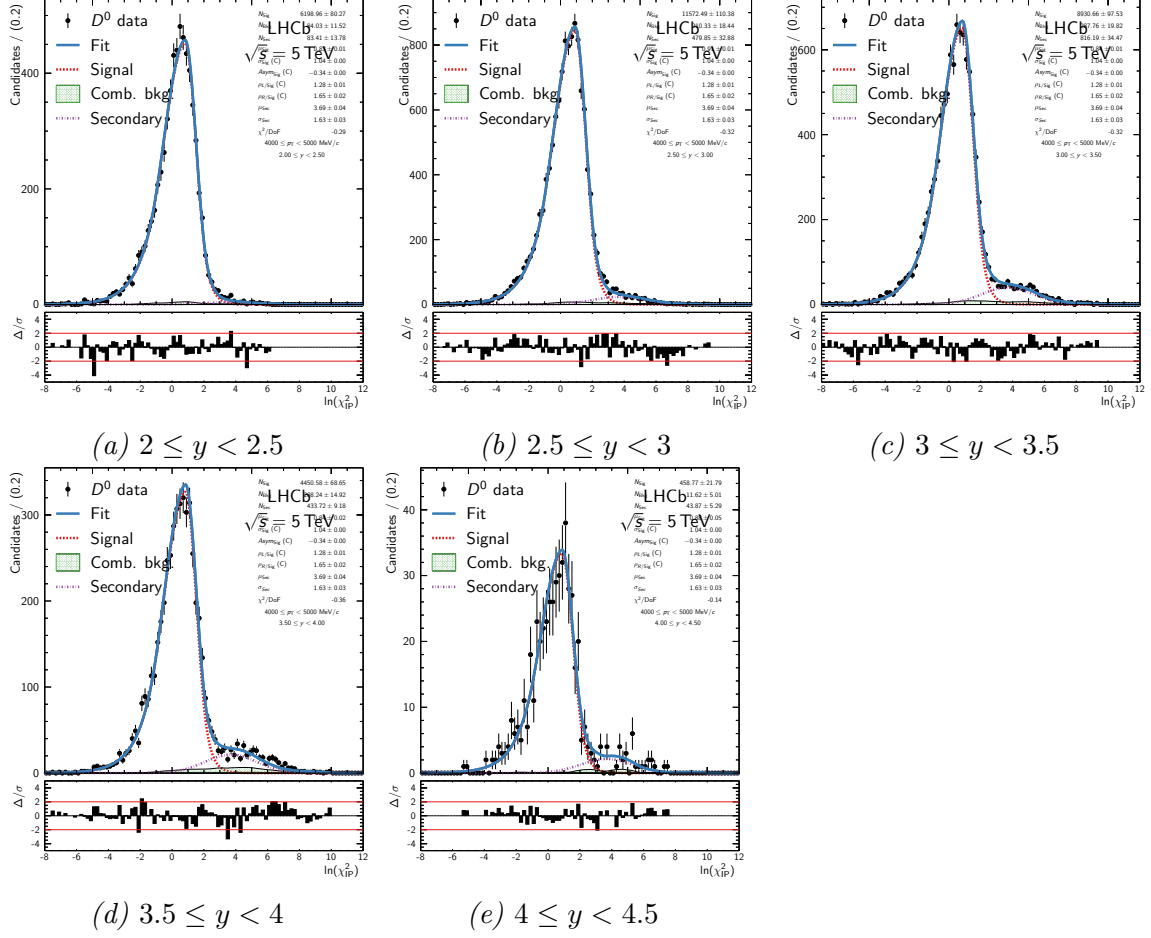


Figure B.5: Fits to the  $\ln \chi_{\text{IP}}^2$  distribution in the signal region of the  $D^0 \rightarrow K^- \pi^+$  data in bins of rapidity in the  $p_T$  range  $4 \leq p_T < 5 \text{ GeV}$ .

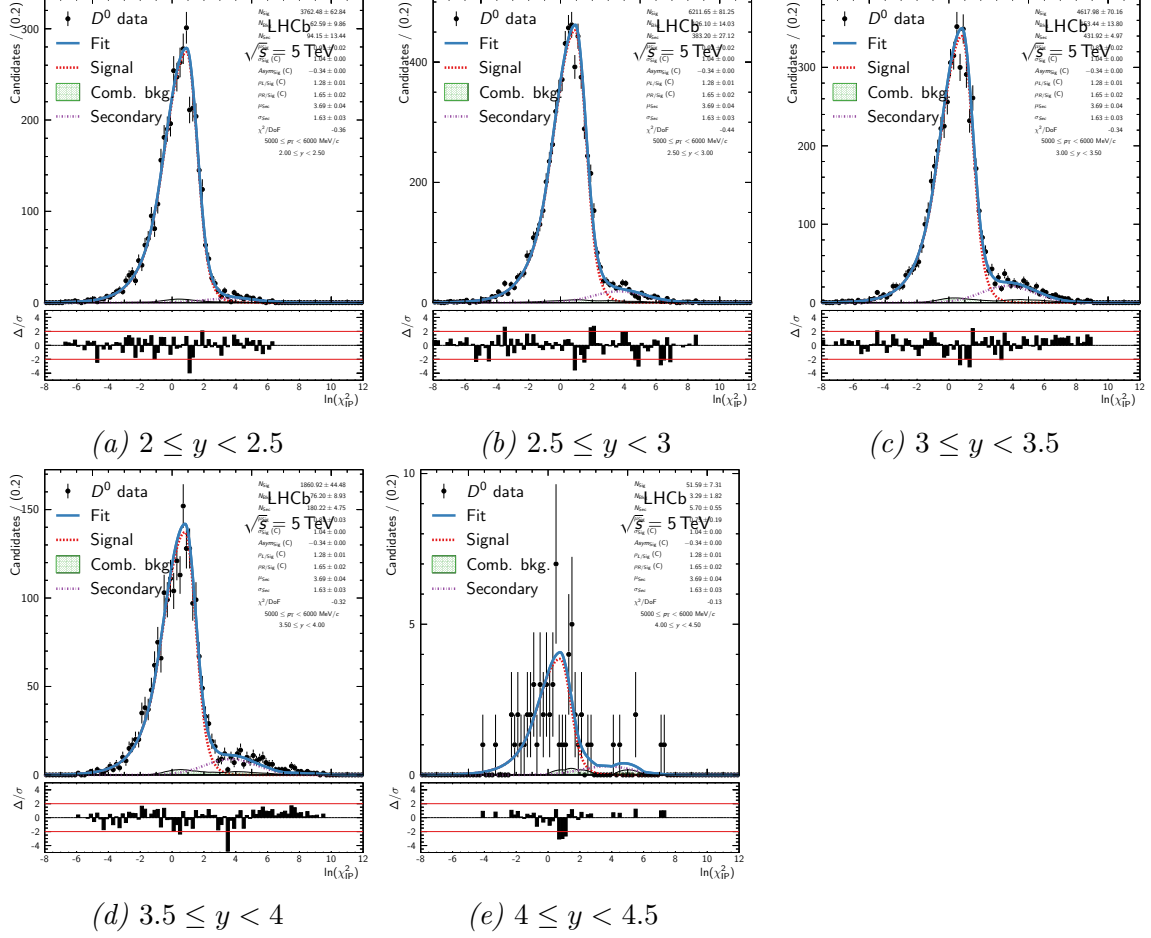


Figure B.6: Fits to the  $\ln \chi^2_{\text{IP}}$  distribution in the signal region of the  $D^0 \rightarrow K^- \pi^+$  data in bins of rapidity in the  $p_T$  range  $5 \leq p_T < 6 \text{ GeV}$ .

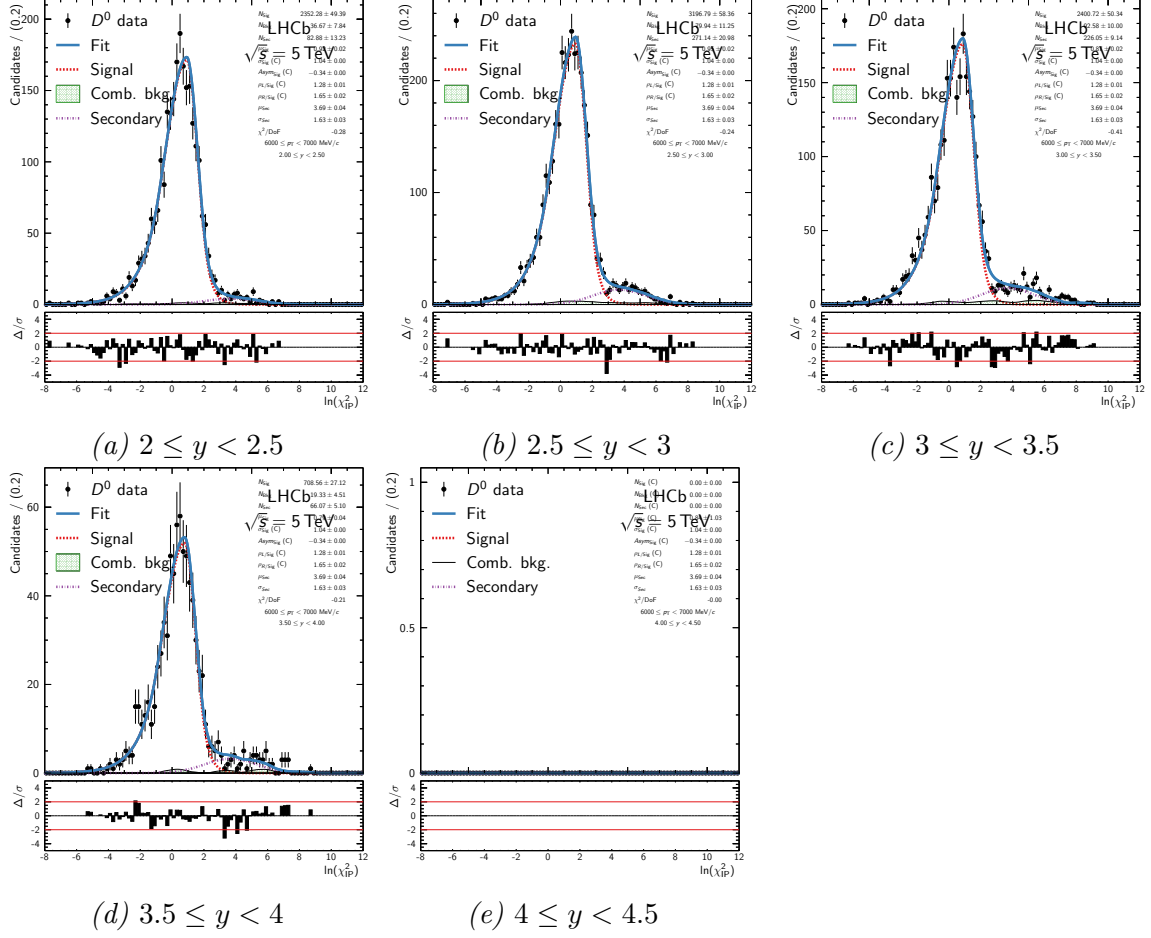


Figure B.7: Fits to the  $\ln \chi_{\text{IP}}^2$  distribution in the signal region of the  $D^0 \rightarrow K^- \pi^+$  data in bins of rapidity in the  $p_T$  range  $6 \leq p_T < 7 \text{ GeV}$ .

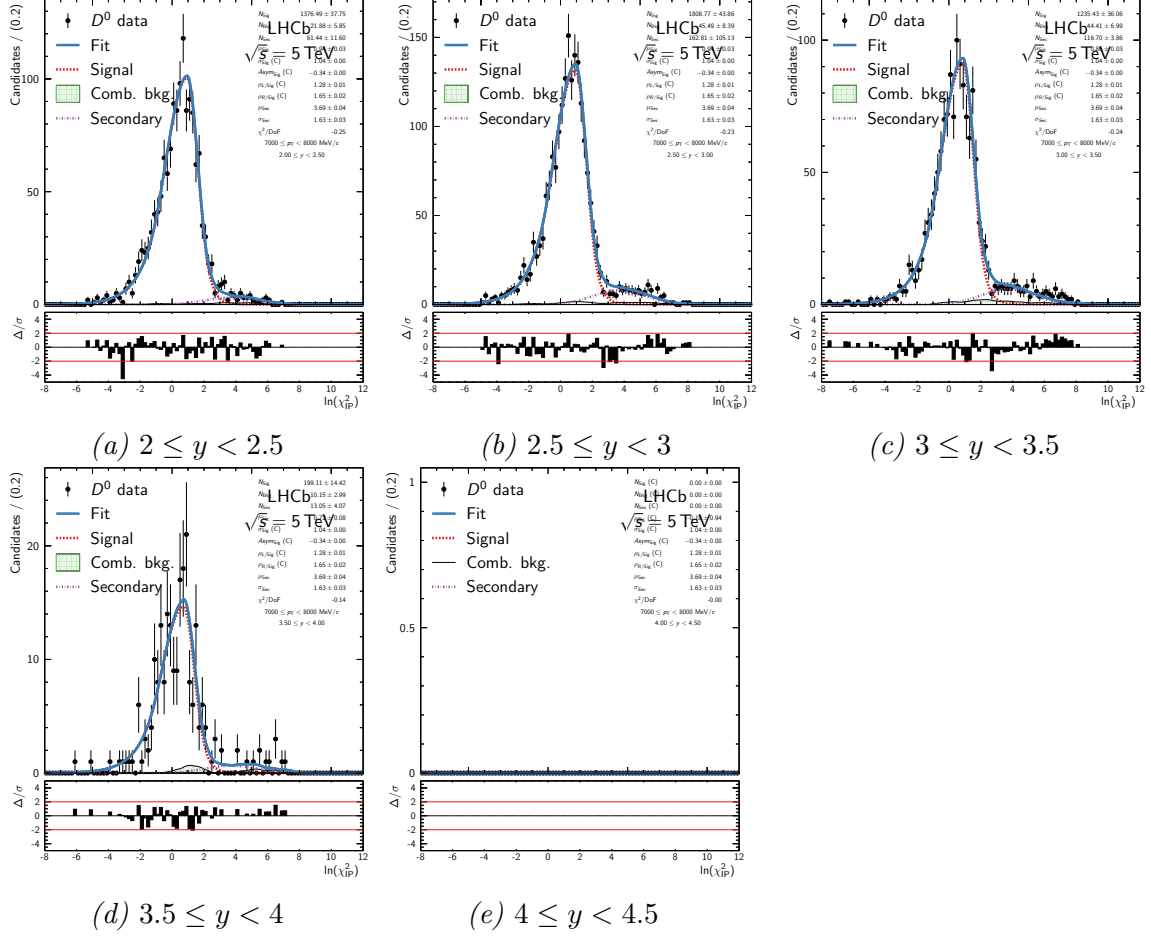


Figure B.8: Fits to the  $\ln \chi^2_{\text{IP}}$  distribution in the signal region of the  $D^0 \rightarrow K^- \pi^+$  data in bins of rapidity in the  $p_T$  range  $7 \leq p_T < 8 \text{ GeV}$ .

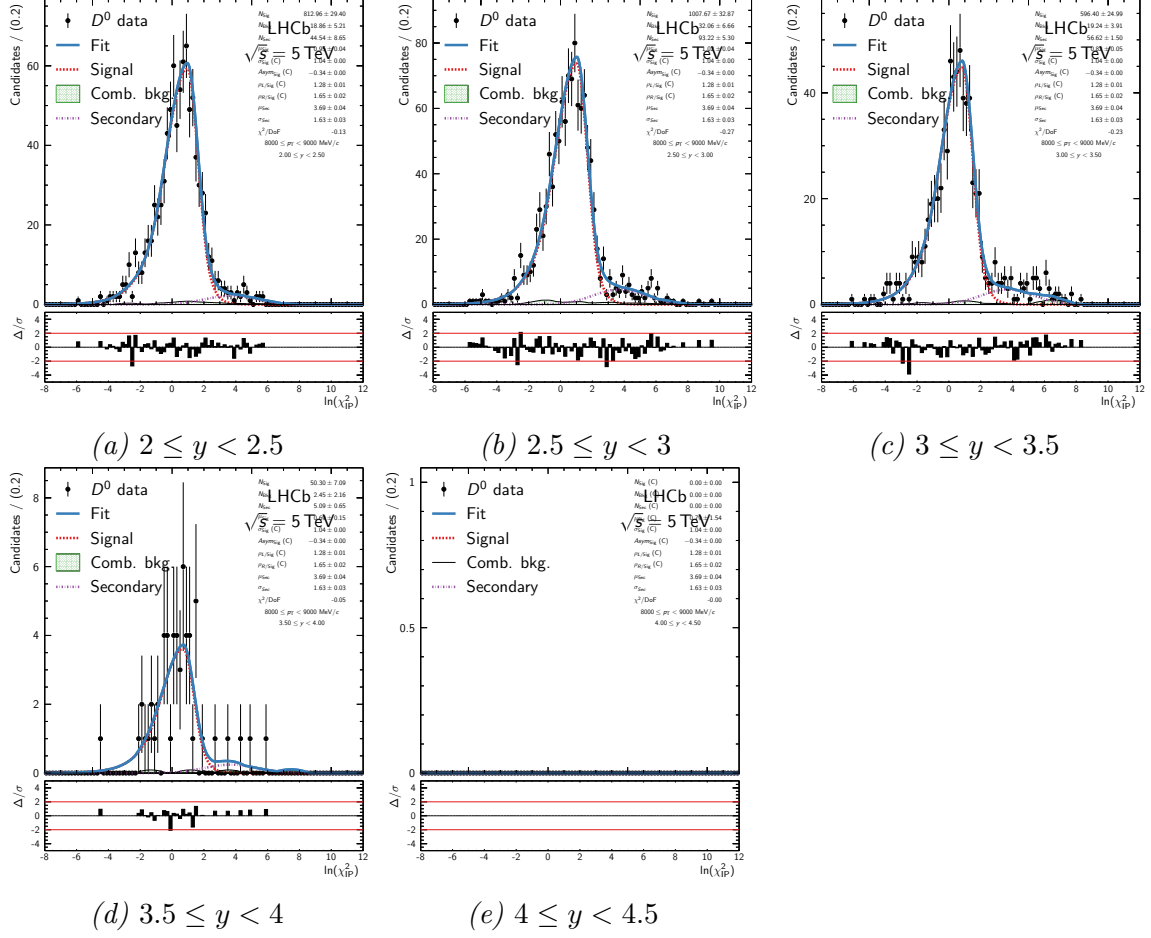


Figure B.9: Fits to the  $\ln \chi^2_{\text{IP}}$  distribution in the signal region of the  $D^0 \rightarrow K^- \pi^+$  data in bins of rapidity in the  $p_T$  range  $8 \leq p_T < 9 \text{ GeV}$ .

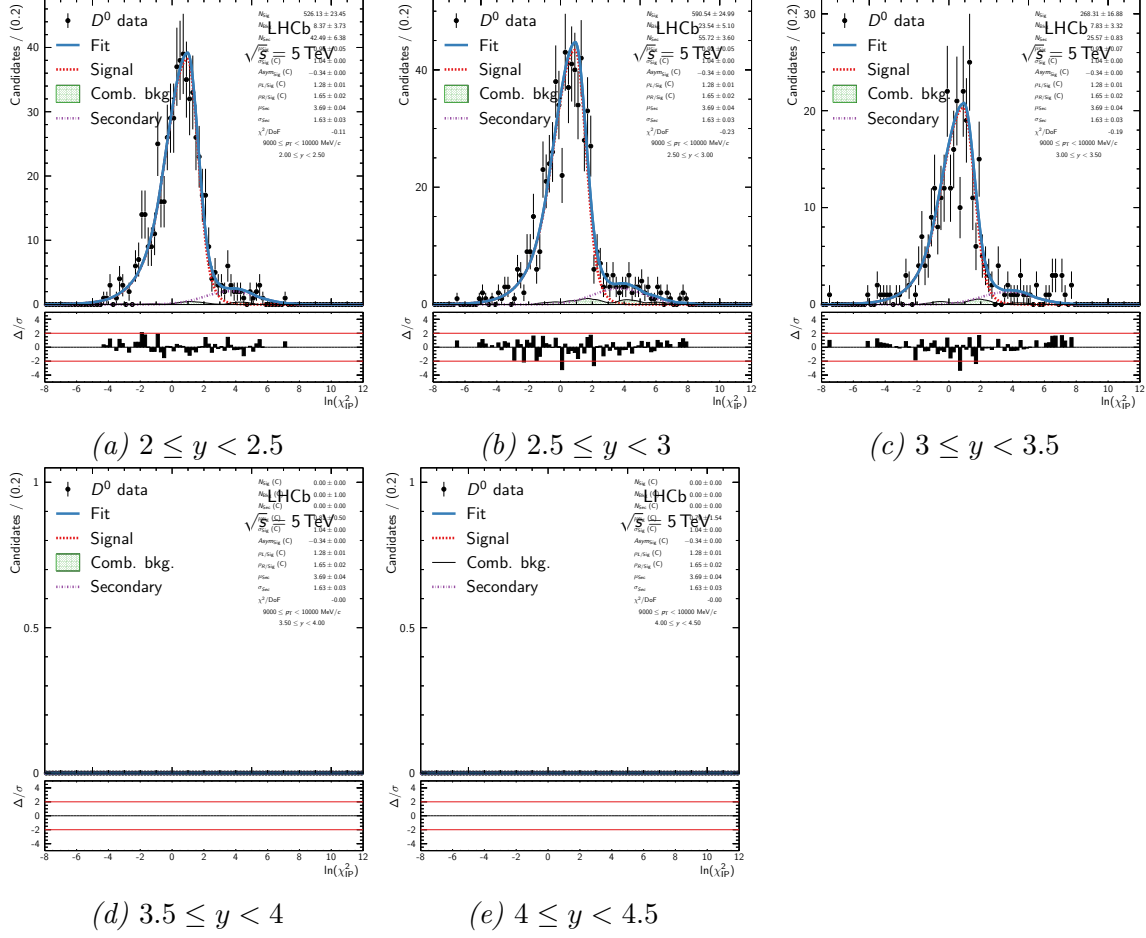


Figure B.10: Fits to the  $\ln \chi^2_{\text{IP}}$  distribution in the signal region of the  $D^0 \rightarrow K^- \pi^+$  data in bins of rapidity in the  $p_T$  range  $9 \leq p_T < 10 \text{ GeV}$ .

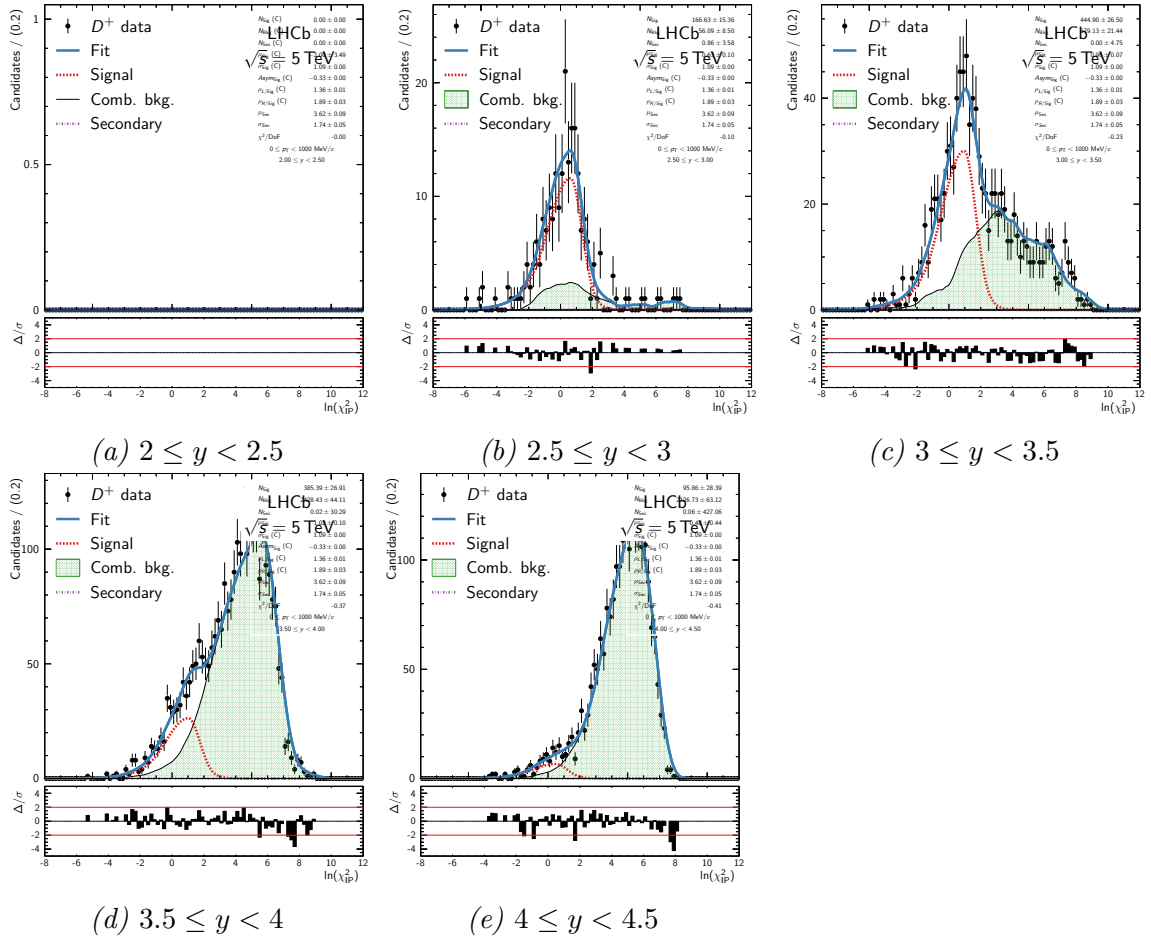


Figure B.11: Fits to the  $\ln \chi_{\text{IP}}^2$  distribution in the signal region of the  $D^+ \rightarrow K^- \pi^+ \pi^+$  data in bins of rapidity in the  $p_T$  range  $0 \leq p_T < 1 \text{ GeV}$ .

1086 **B.2**  $D^+ \rightarrow K^- \pi^+ \pi^+$

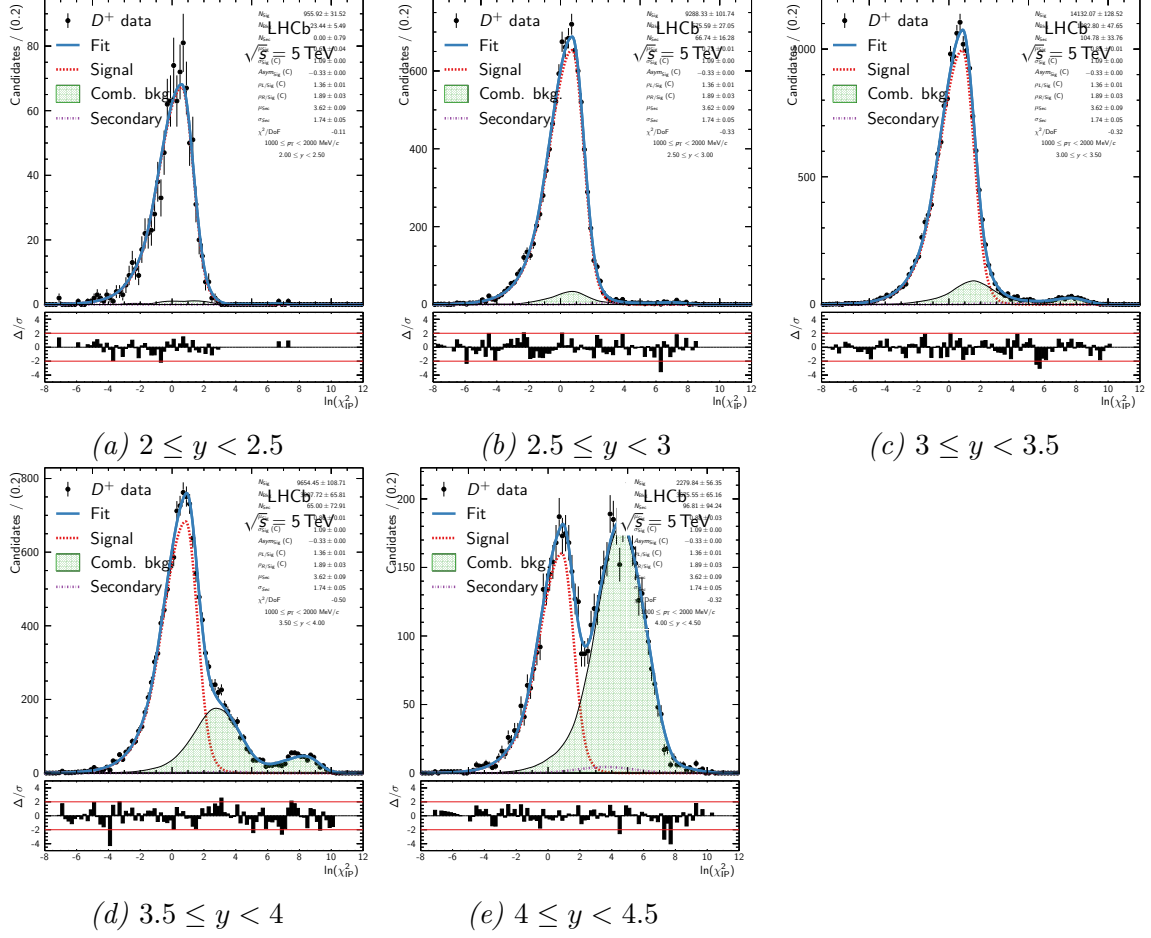


Figure B.12: Fits to the  $\ln \chi^2_{\text{IP}}$  distribution in the signal region of the  $D^+ \rightarrow K^- \pi^+ \pi^+$  data in bins of rapidity in the  $p_T$  range  $1 \leq p_T < 2 \text{ GeV}$ .

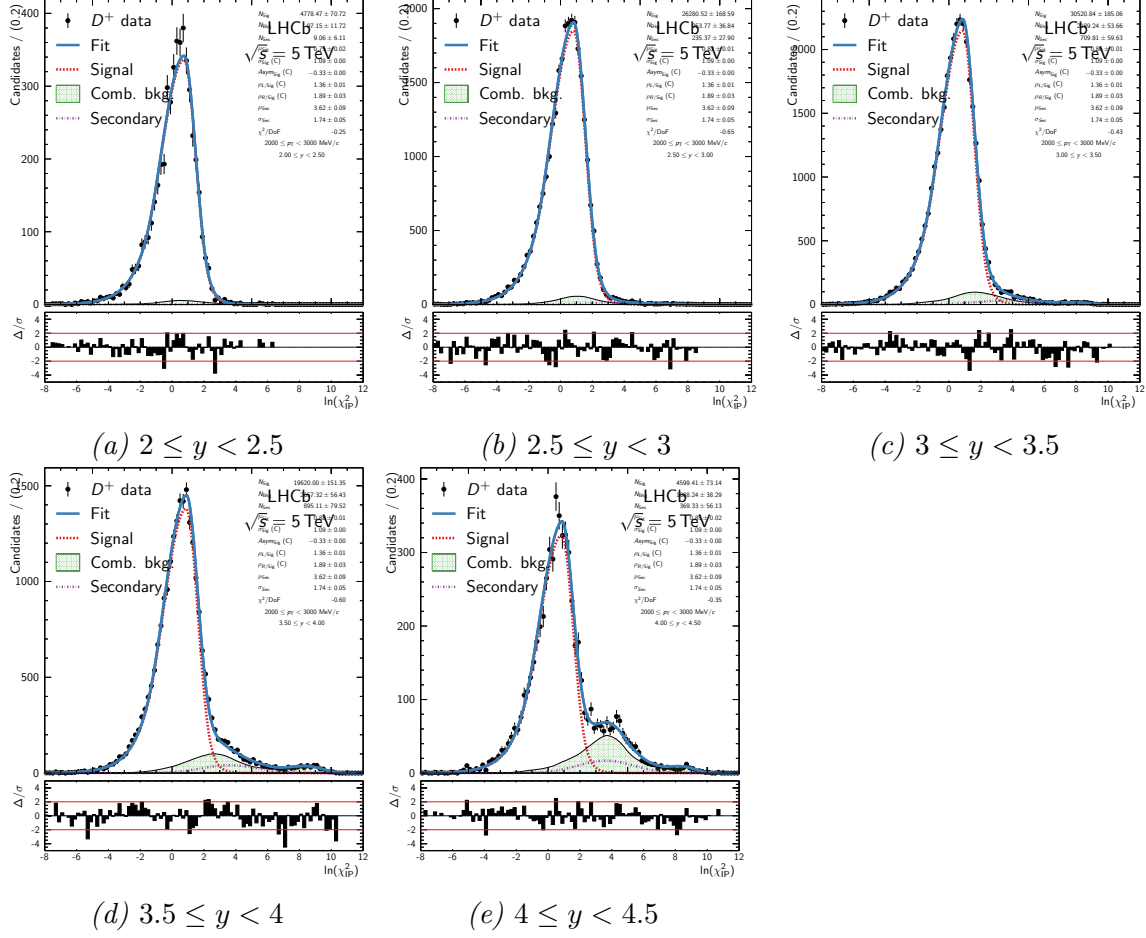


Figure B.13: Fits to the  $\ln \chi^2_{\text{IP}}$  distribution in the signal region of the  $D^+ \rightarrow K^- \pi^+ \pi^+$  data in bins of rapidity in the  $p_T$  range  $2 \leq p_T < 3 \text{ GeV}$ .

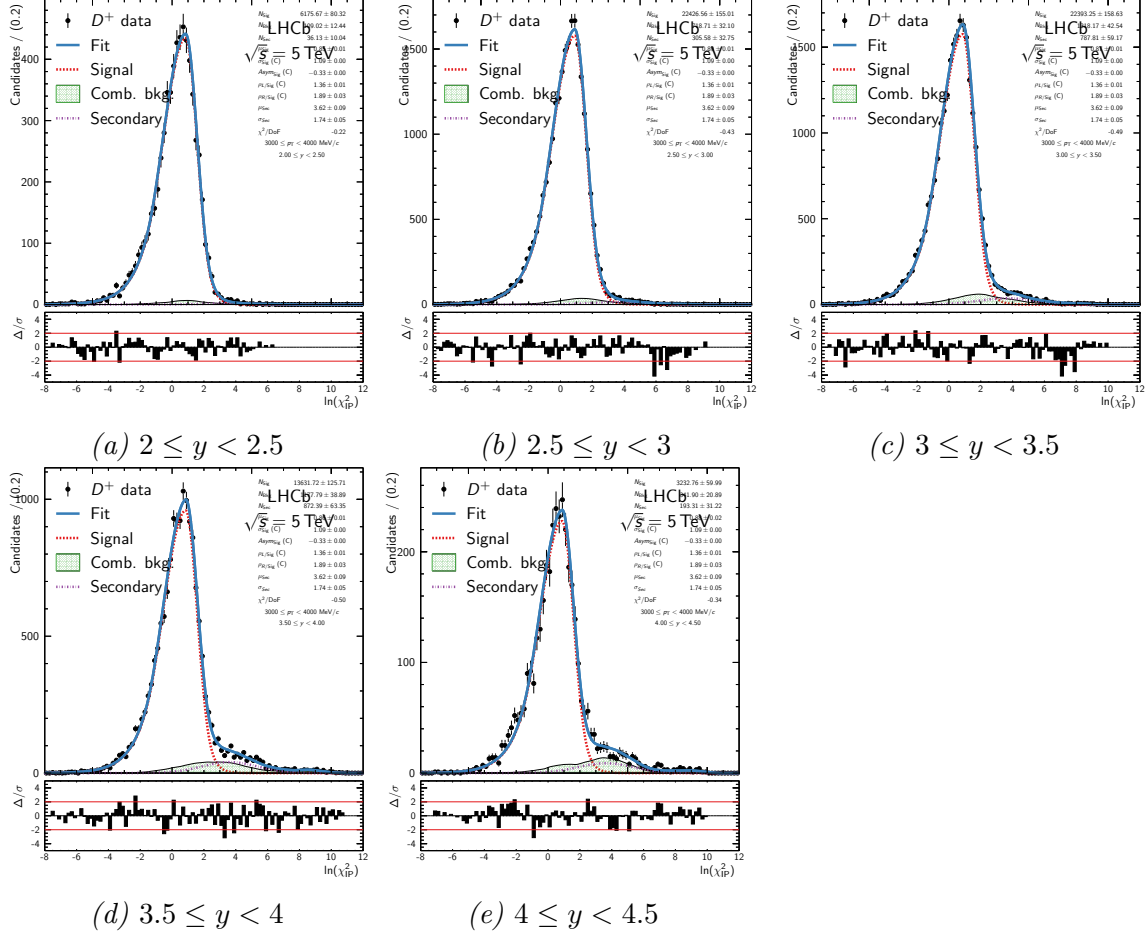


Figure B.14: Fits to the  $\ln \chi^2_{\text{IP}}$  distribution in the signal region of the  $D^+ \rightarrow K^- \pi^+ \pi^+$  data in bins of rapidity in the  $p_T$  range  $3 \leq p_T < 4 \text{ GeV}$ .

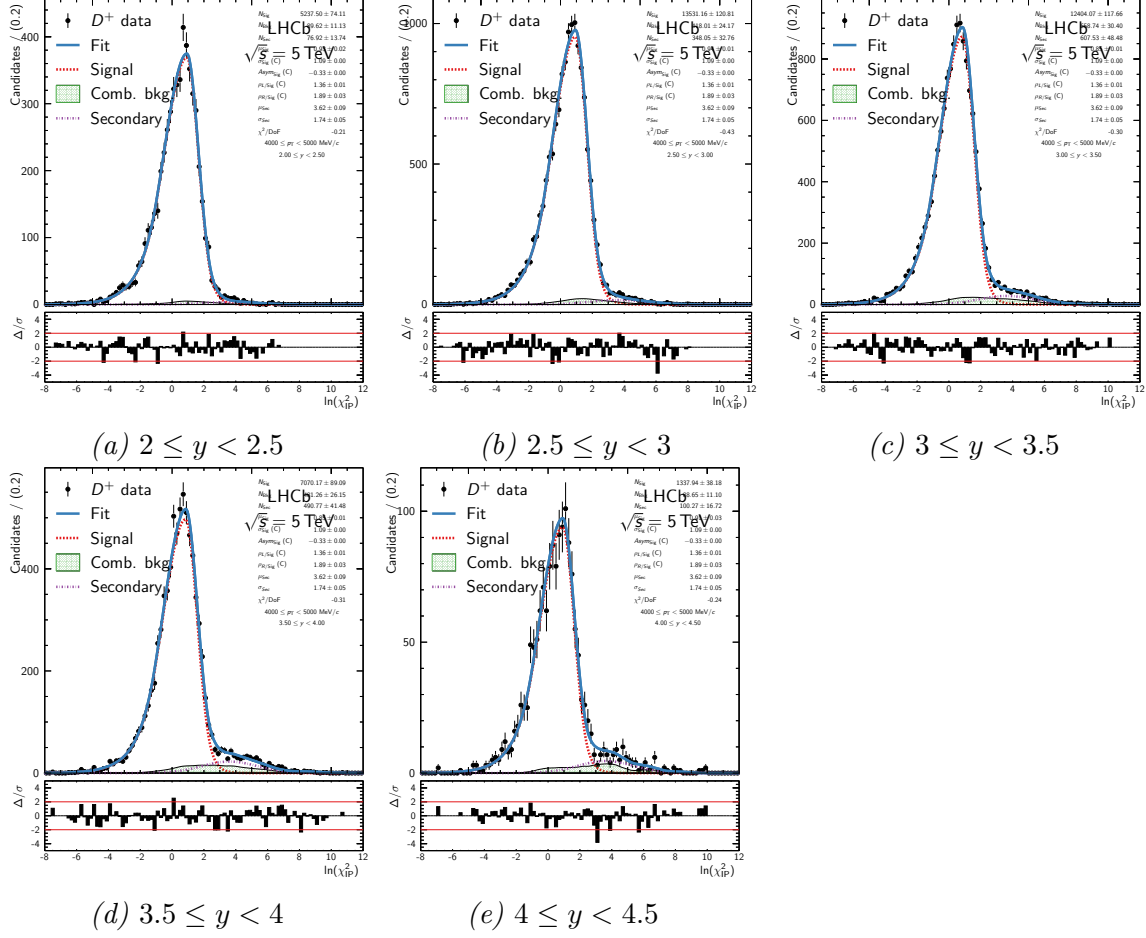


Figure B.15: Fits to the  $\ln \chi^2_{\text{IP}}$  distribution in the signal region of the  $D^+ \rightarrow K^- \pi^+ \pi^+$  data in bins of rapidity in the  $p_T$  range  $4 \leq p_T < 5 \text{ GeV}$ .

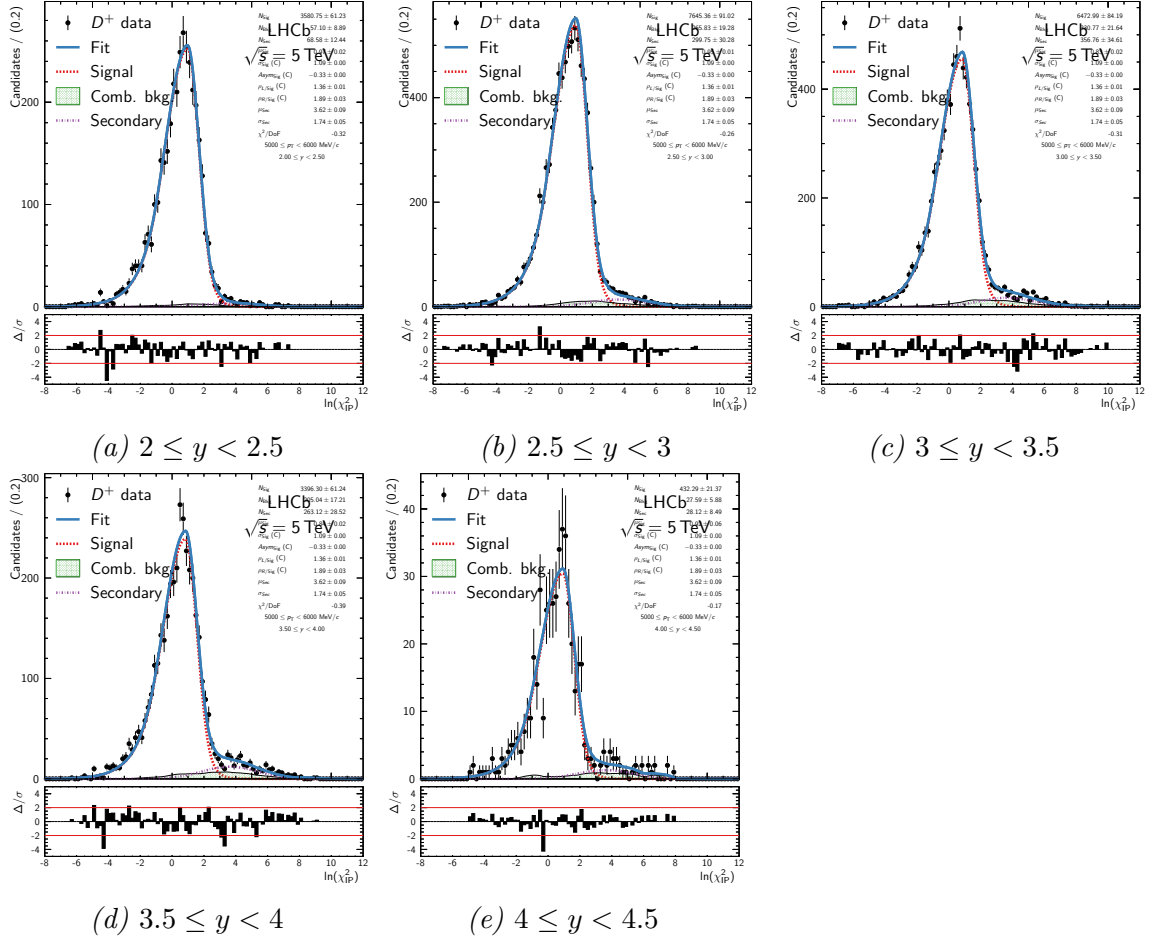


Figure B.16: Fits to the  $\ln \chi^2_{\text{IP}}$  distribution in the signal region of the  $D^+ \rightarrow K^- \pi^+ \pi^+$  data in bins of rapidity in the  $p_T$  range  $5 \leq p_T < 6 \text{ GeV}$ .

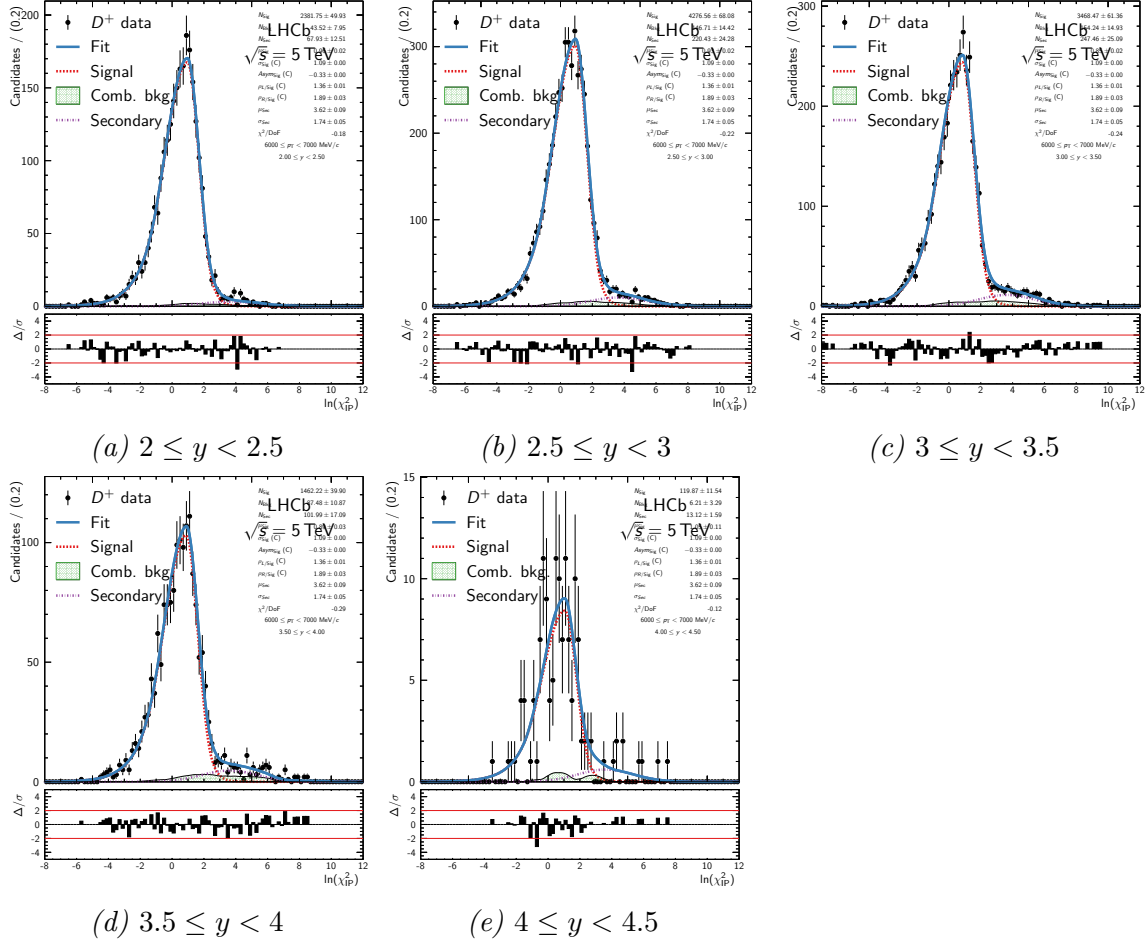


Figure B.17: Fits to the  $\ln \chi^2_{\text{IP}}$  distribution in the signal region of the  $D^+ \rightarrow K^- \pi^+ \pi^+$  data in bins of rapidity in the  $p_T$  range  $6 \leq p_T < 7 \text{ GeV}$ .

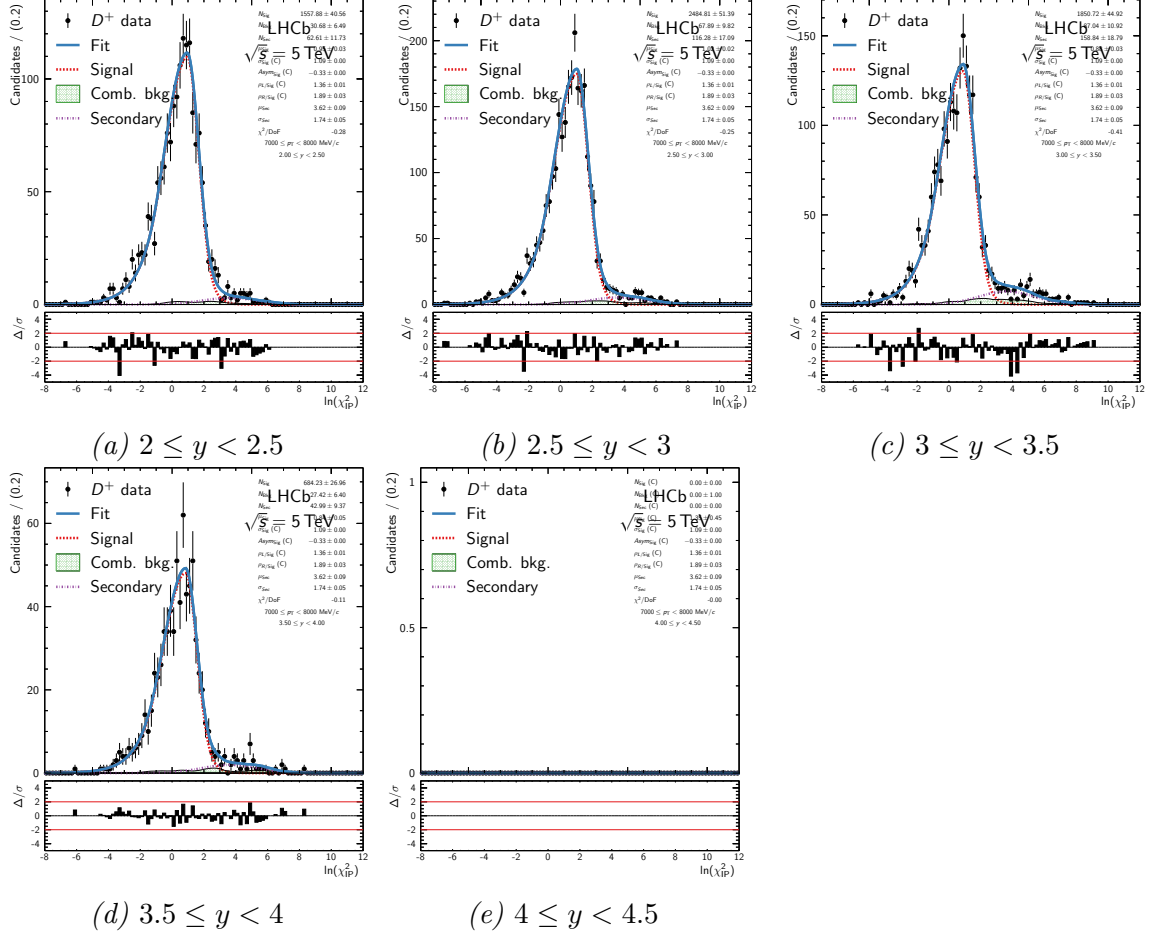


Figure B.18: Fits to the  $\ln \chi^2_{\text{IP}}$  distribution in the signal region of the  $D^+ \rightarrow K^- \pi^+ \pi^+$  data in bins of rapidity in the  $p_T$  range  $7 \leq p_T < 8 \text{ GeV}$ .

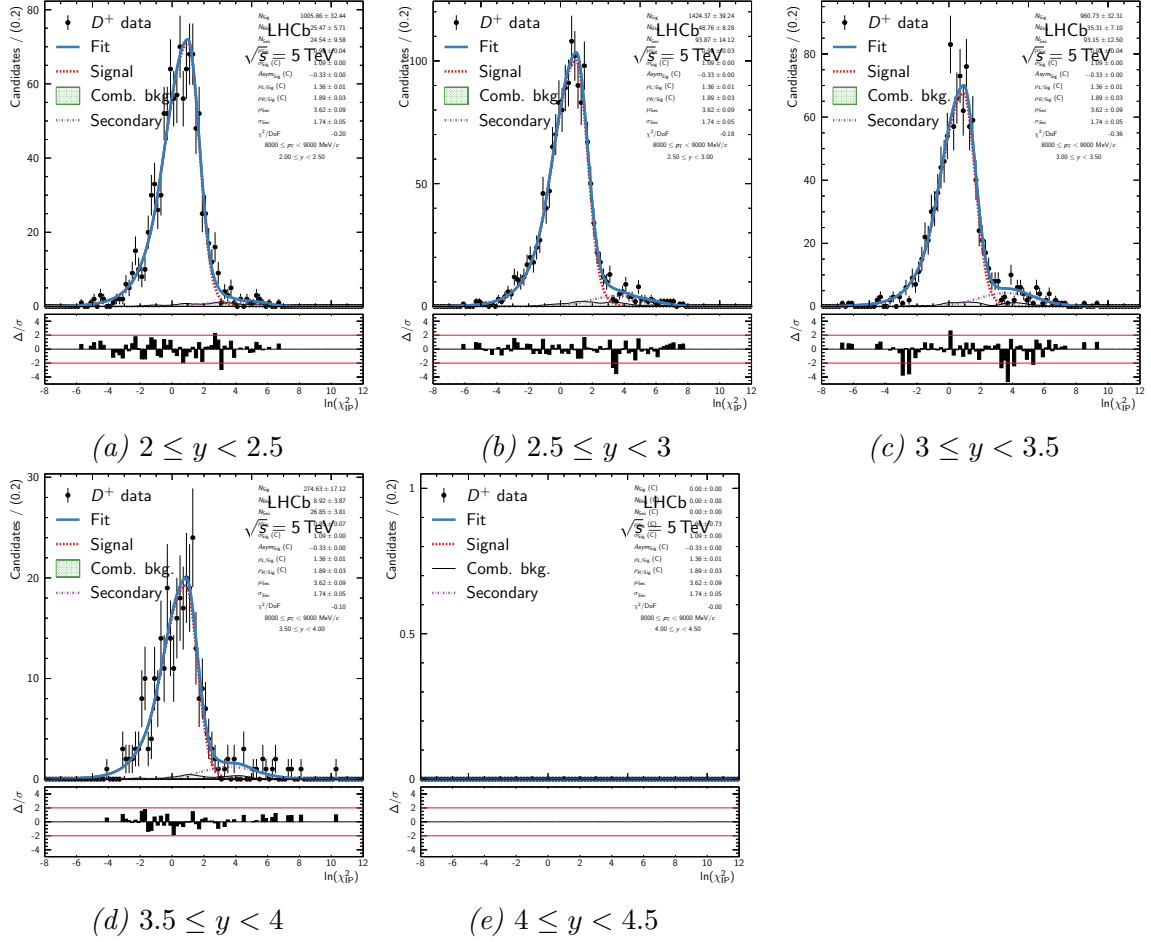


Figure B.19: Fits to the  $\ln \chi^2_{\text{IP}}$  distribution in the signal region of the  $D^+ \rightarrow K^- \pi^+ \pi^+$  data in bins of rapidity in the  $p_T$  range  $8 \leq p_T < 9 \text{ GeV}$ .

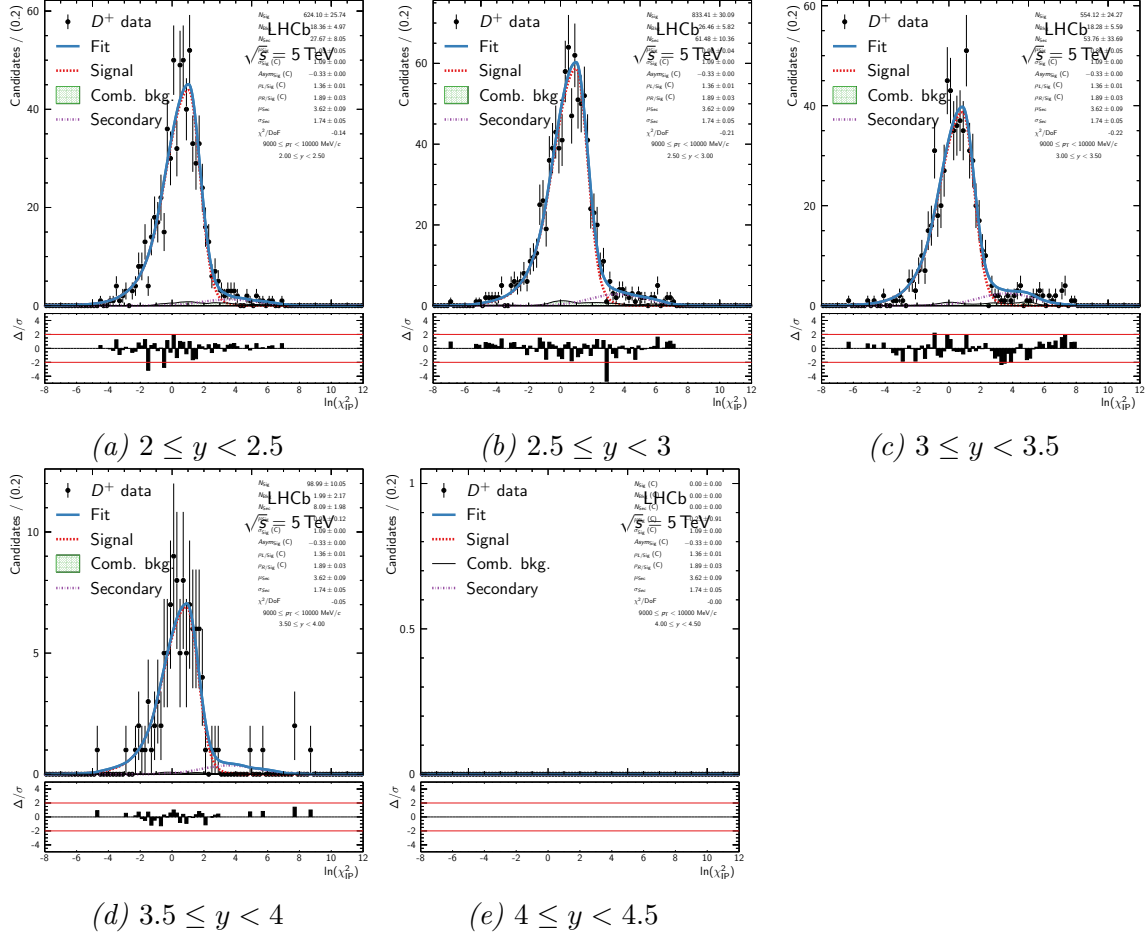


Figure B.20: Fits to the  $\ln \chi^2_{\text{IP}}$  distribution in the signal region of the  $D^+ \rightarrow K^- \pi^+ \pi^+$  data in bins of rapidity in the  $p_T$  range  $9 \leq p_T < 10 \text{ GeV}$ .

<sub>1087</sub> **B.3**  $D_s^+ \rightarrow \phi\pi^+$

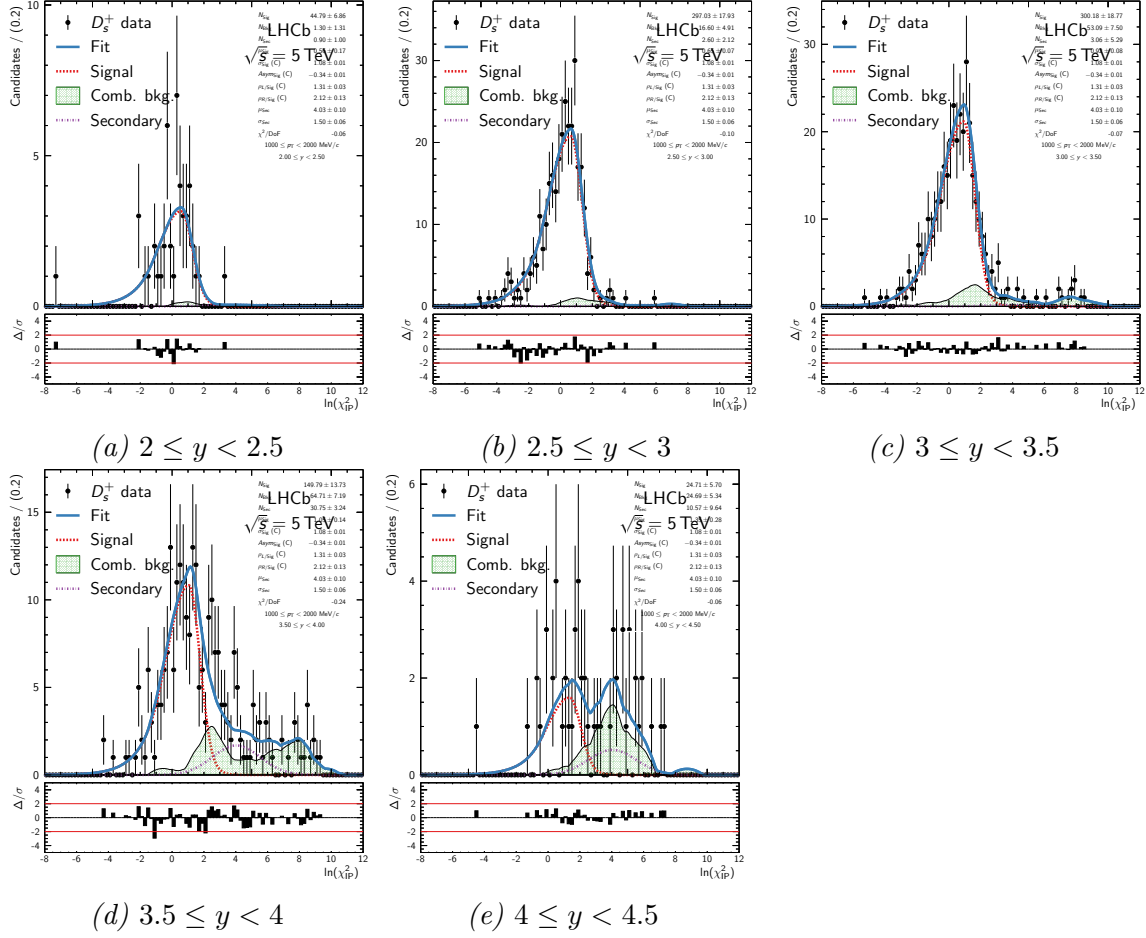


Figure B.21: Fits to the  $\ln \chi^2_{\text{IP}}$  distribution in the signal region of the  $D_s^+ \rightarrow \phi \pi^+$  data in bins of rapidity in the  $p_T$  range  $1 \leq p_T < 2 \text{ GeV}$ .

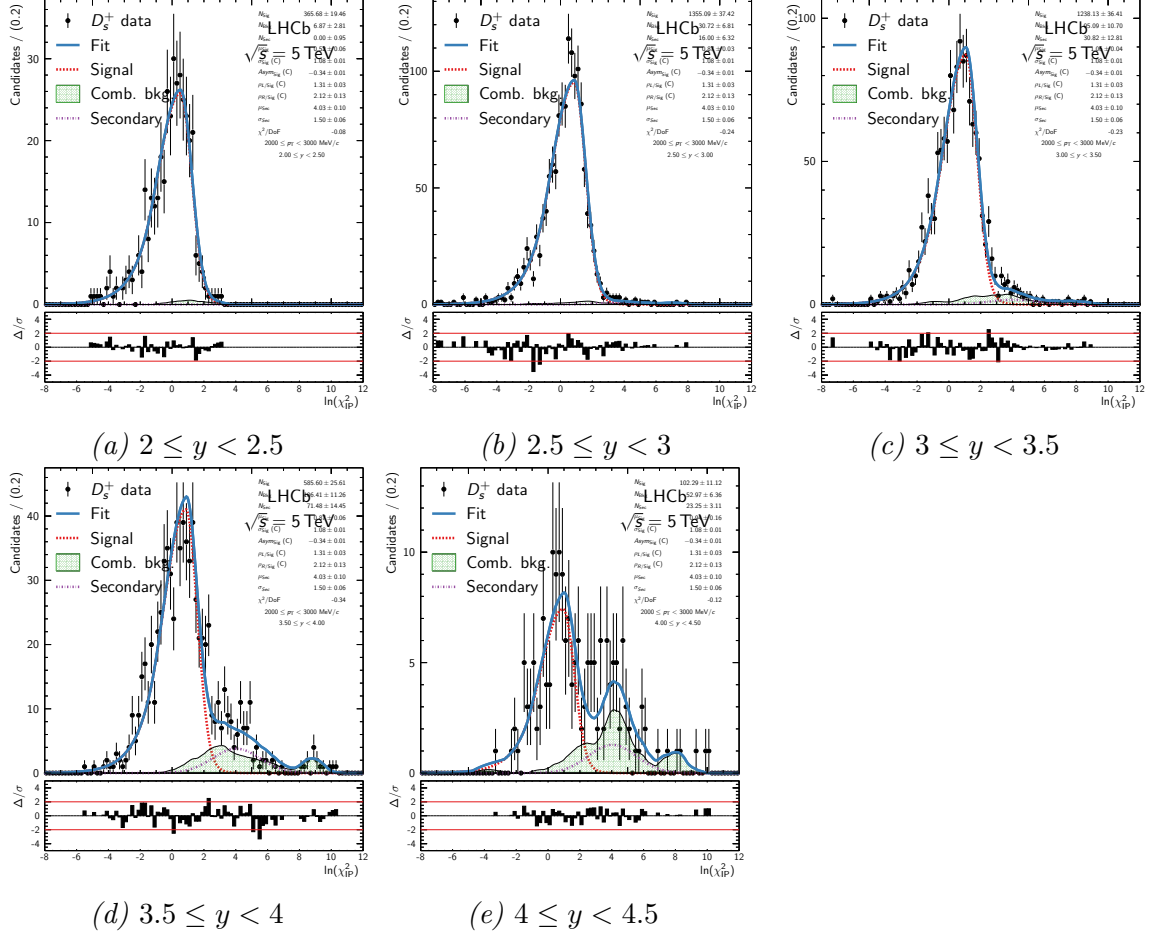


Figure B.22: Fits to the  $\ln \chi^2_{\text{IP}}$  distribution in the signal region of the  $D_s^+ \rightarrow \phi\pi^+$  data in bins of rapidity in the  $p_T$  range  $2 \leq p_T < 3 \text{ GeV}$ .

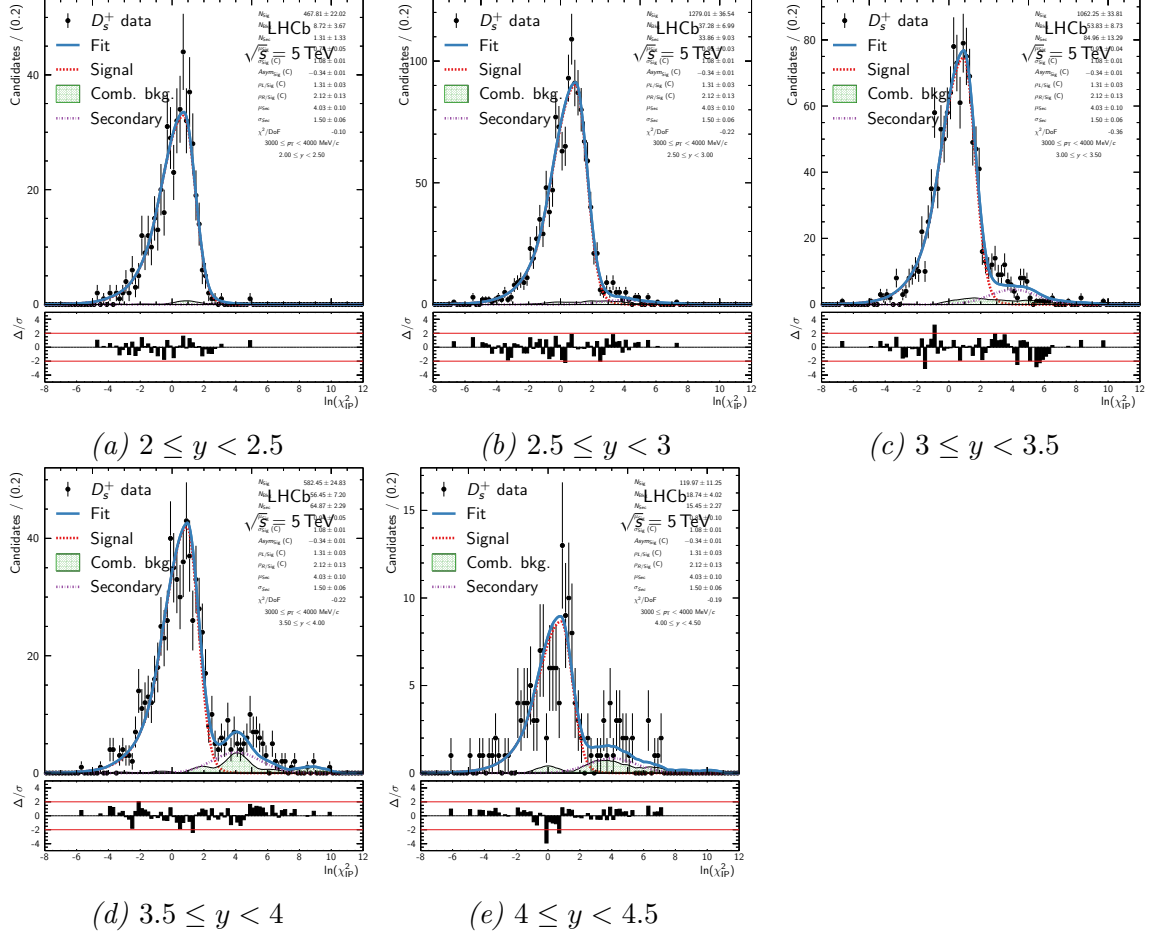


Figure B.23: Fits to the  $\ln \chi^2_{\text{IP}}$  distribution in the signal region of the  $D_s^+ \rightarrow \phi \pi^+$  data in bins of rapidity in the  $p_T$  range  $3 \leq p_T < 4 \text{ GeV}$ .

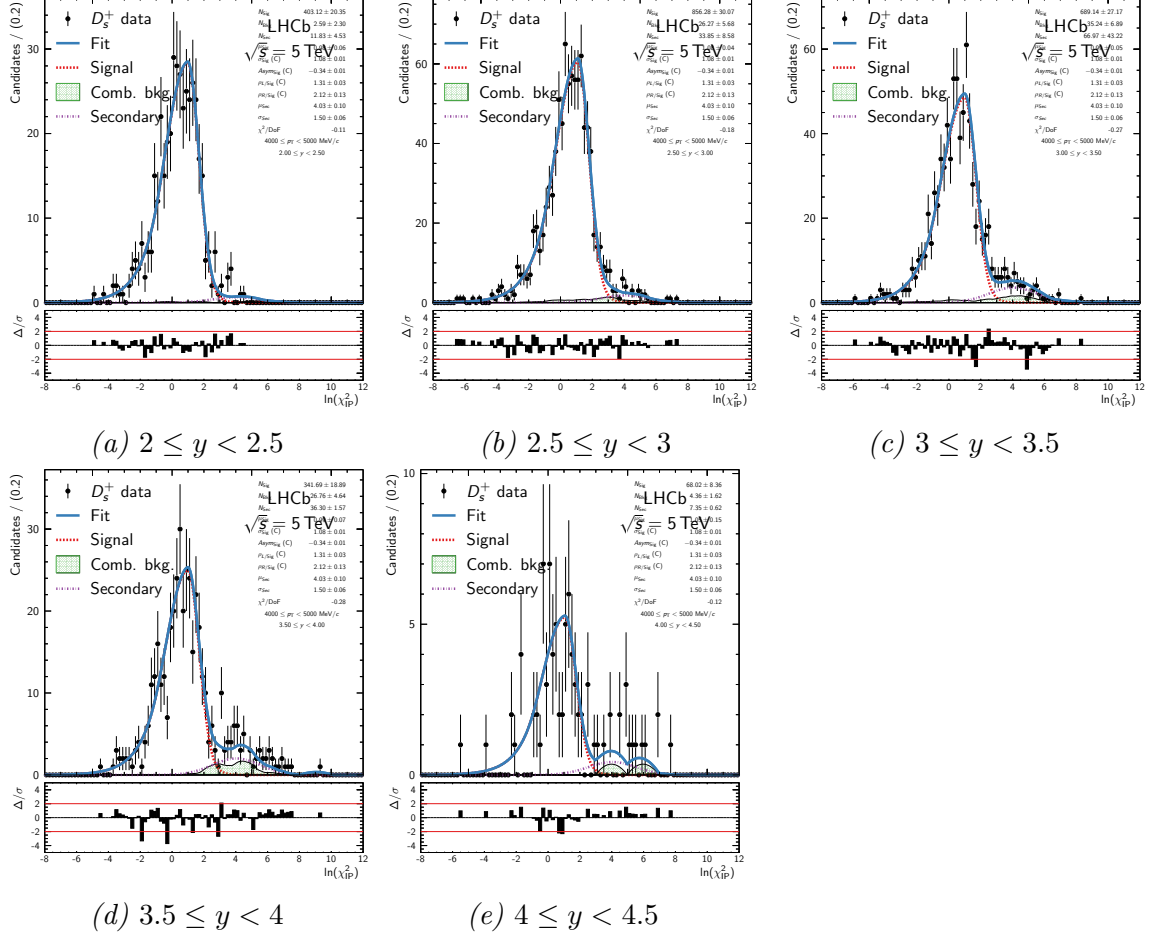


Figure B.24: Fits to the  $\ln \chi^2_{\text{IP}}$  distribution in the signal region of the  $D_s^+ \rightarrow \phi \pi^+$  data in bins of rapidity in the  $p_T$  range  $4 \leq p_T < 5 \text{ GeV}$ .

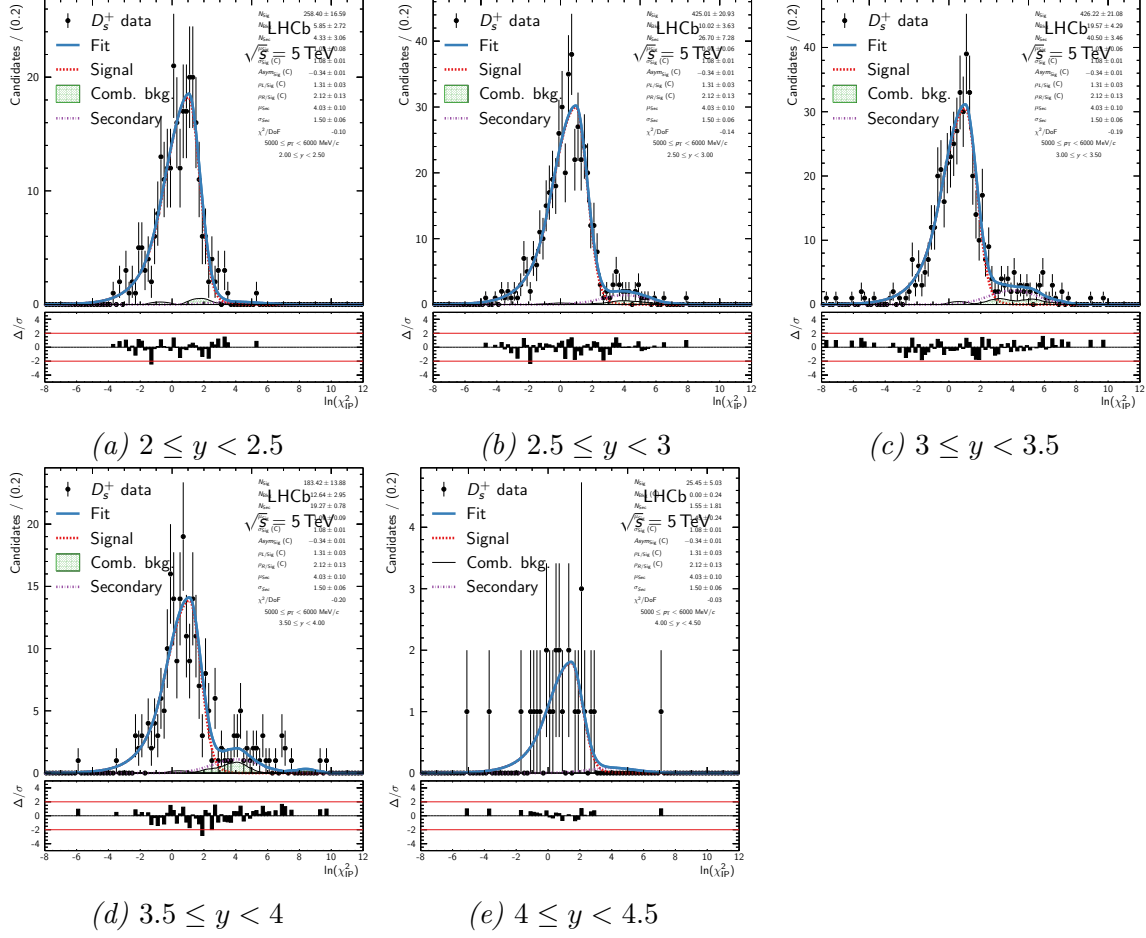


Figure B.25: Fits to the  $\ln \chi^2_{\text{IP}}$  distribution in the signal region of the  $D_s^+ \rightarrow \phi \pi^+$  data in bins of rapidity in the  $p_T$  range  $5 \leq p_T < 6 \text{ GeV}$ .

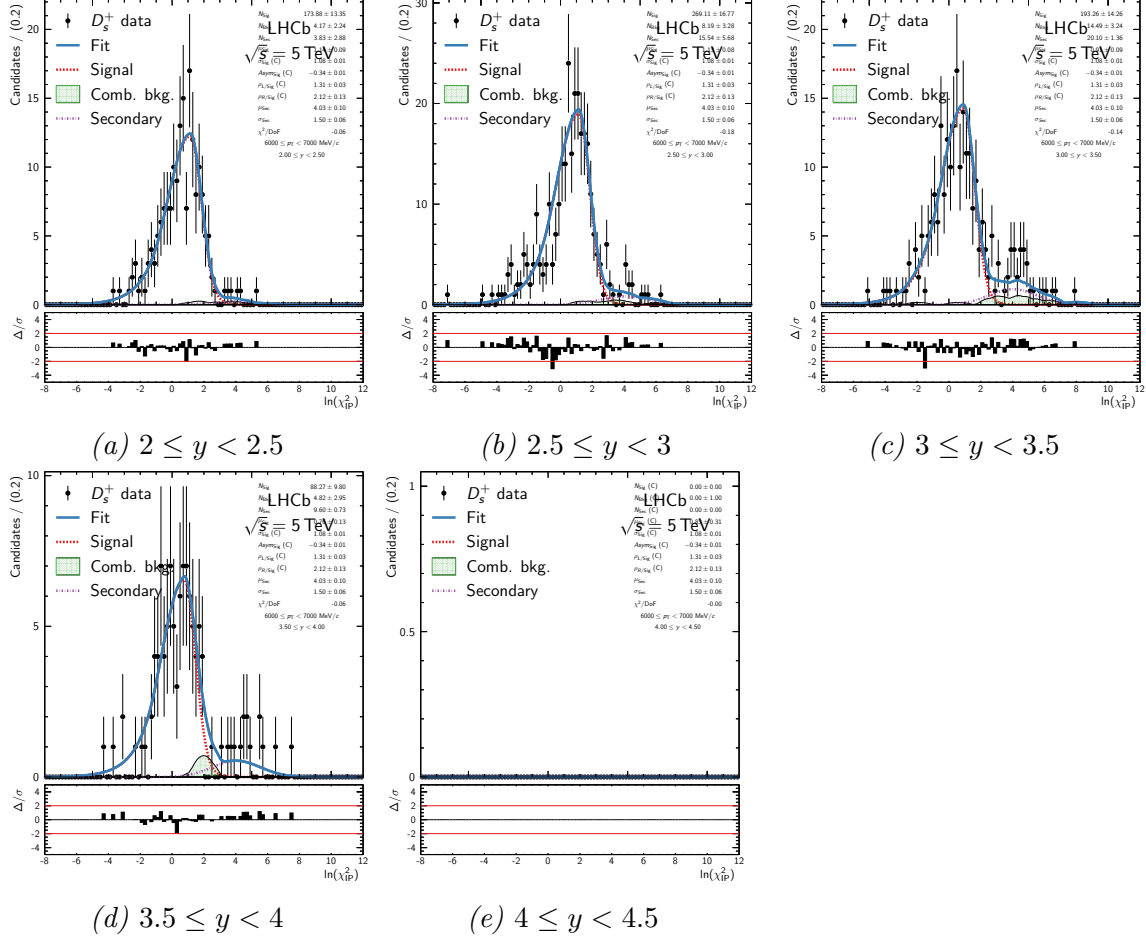


Figure B.26: Fits to the  $\ln \chi^2_{\text{IP}}$  distribution in the signal region of the  $D_s^+ \rightarrow \phi \pi^+$  data in bins of rapidity in the  $p_T$  range  $6 \leq p_T < 7 \text{ GeV}$ .

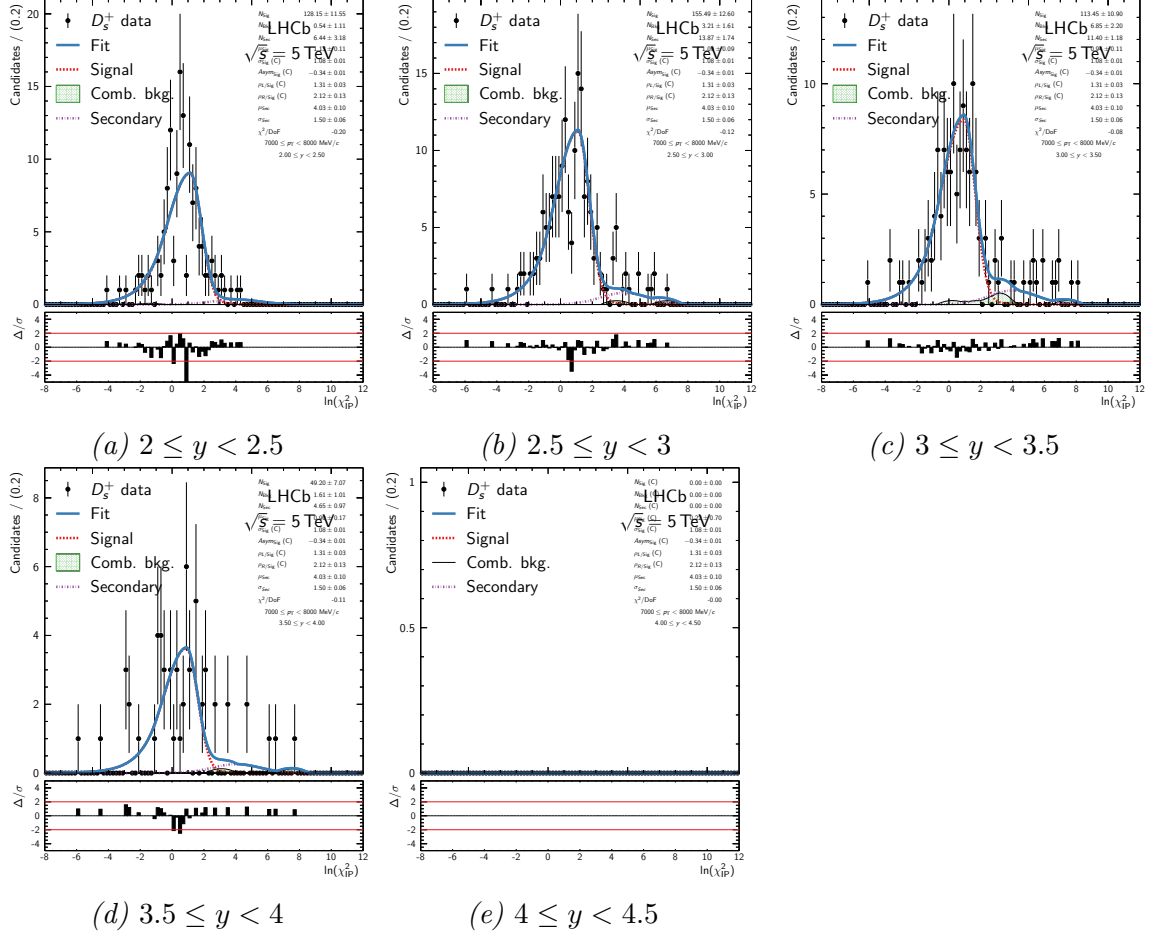


Figure B.27: Fits to the  $\ln \chi^2_{\text{IP}}$  distribution in the signal region of the  $D_s^+ \rightarrow \phi \pi^+$  data in bins of rapidity in the  $p_T$  range  $7 \leq p_T < 8 \text{ GeV}$ .

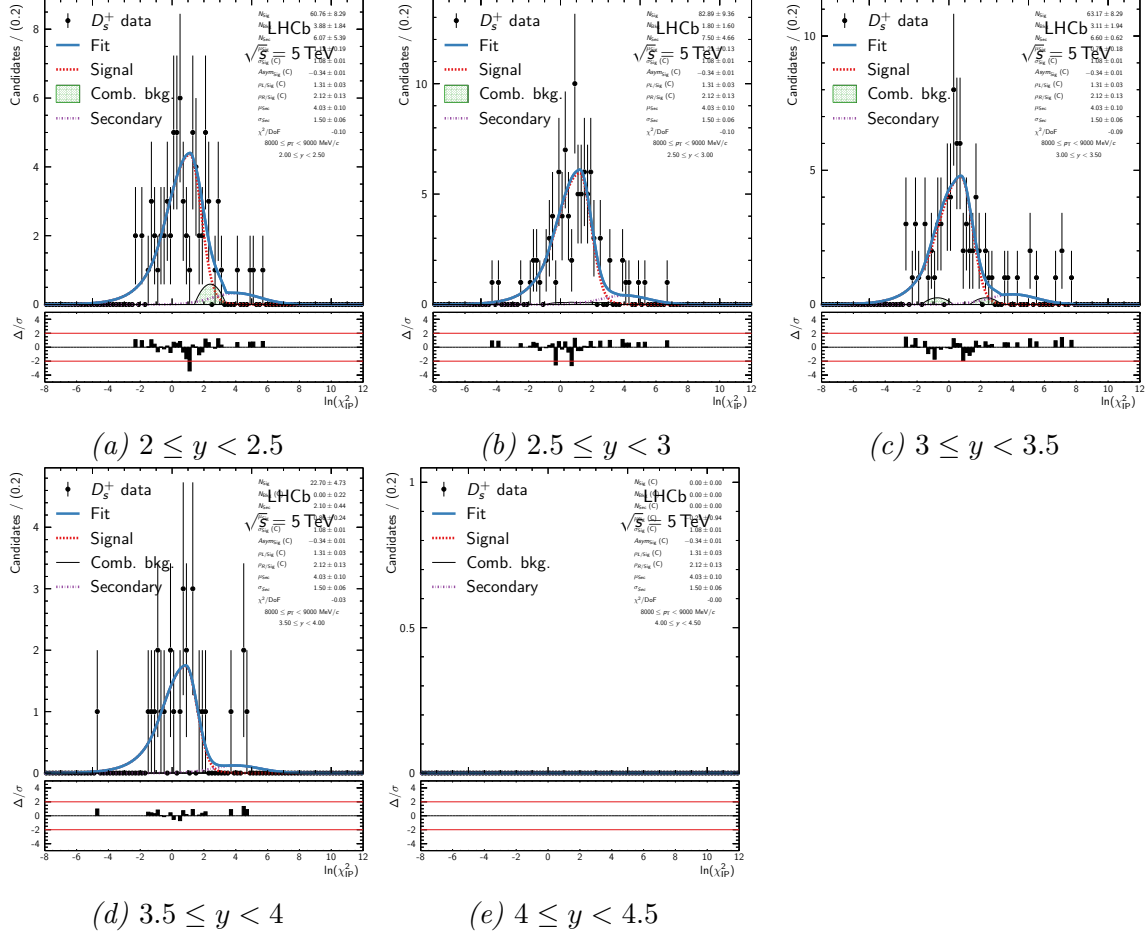


Figure B.28: Fits to the  $\ln \chi^2_{\text{IP}}$  distribution in the signal region of the  $D_s^+ \rightarrow \phi \pi^+$  data in bins of rapidity in the  $p_T$  range  $8 \leq p_T < 9 \text{ GeV}$ .

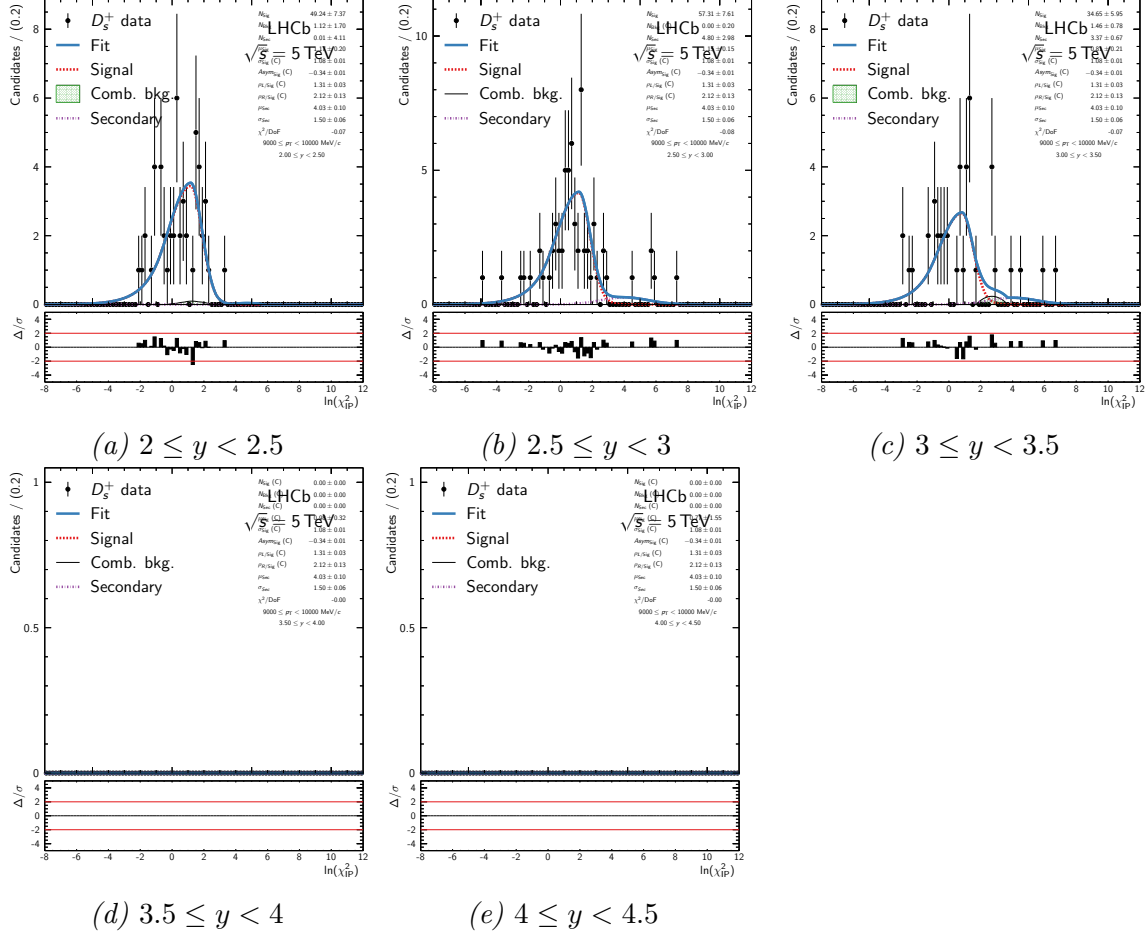


Figure B.29: Fits to the  $\ln \chi^2_{\text{IP}}$  distribution in the signal region of the  $D_s^+ \rightarrow \phi \pi^+$  data in bins of rapidity in the  $p_T$  range  $9 \leq p_T < 10 \text{ GeV}$ .

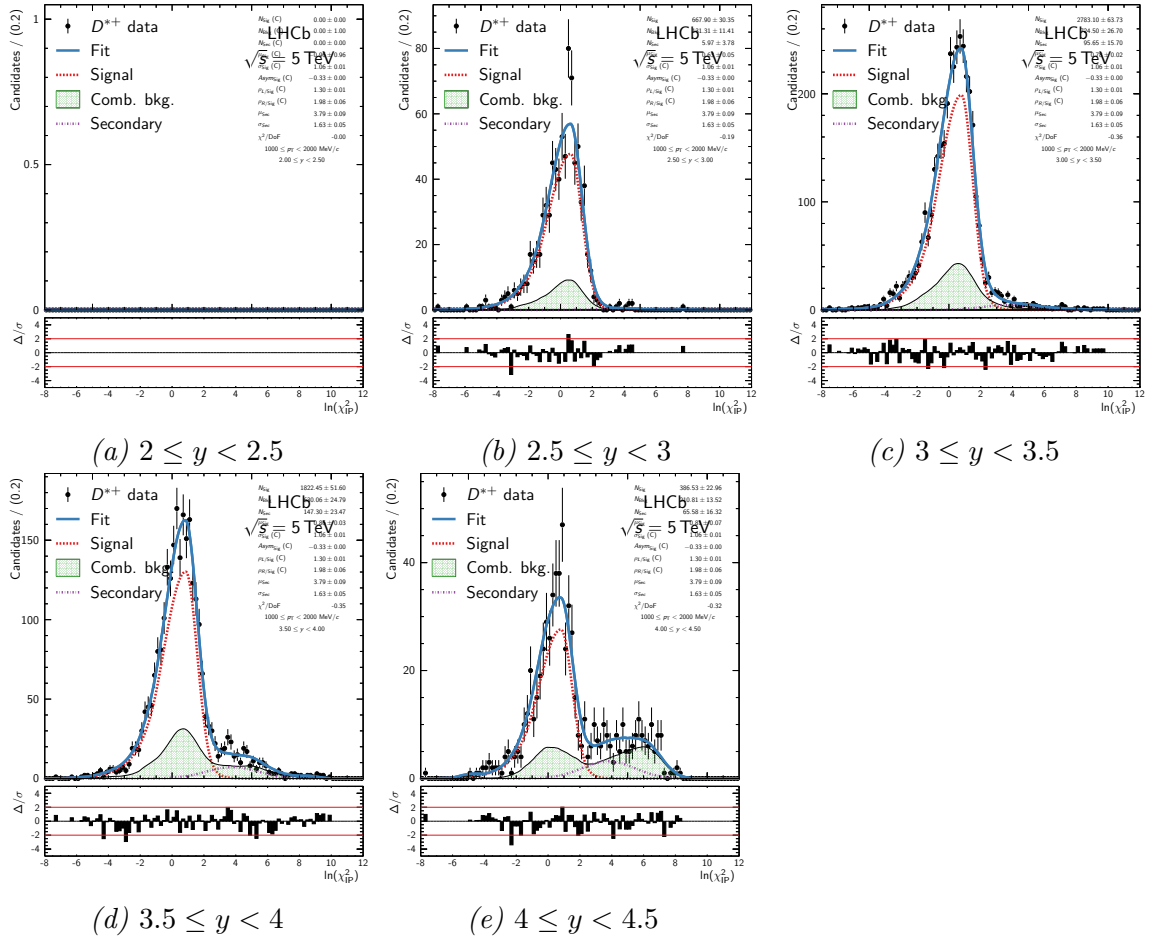


Figure B.30: Fits to the  $\ln \chi^2_{\text{IP}}$  distribution in the signal region of the  $D^{*+} \rightarrow D^0 \pi^+$ , with  $D^0 \rightarrow K^- \pi^+$ , data in bins of rapidity in the  $p_T$  range  $1 \leq p_T < 2 \text{ GeV}$ .

#### 1088 B.4 $D^{*+} \rightarrow D^0 \pi^+$ with $D^0 \rightarrow K^- \pi^+$

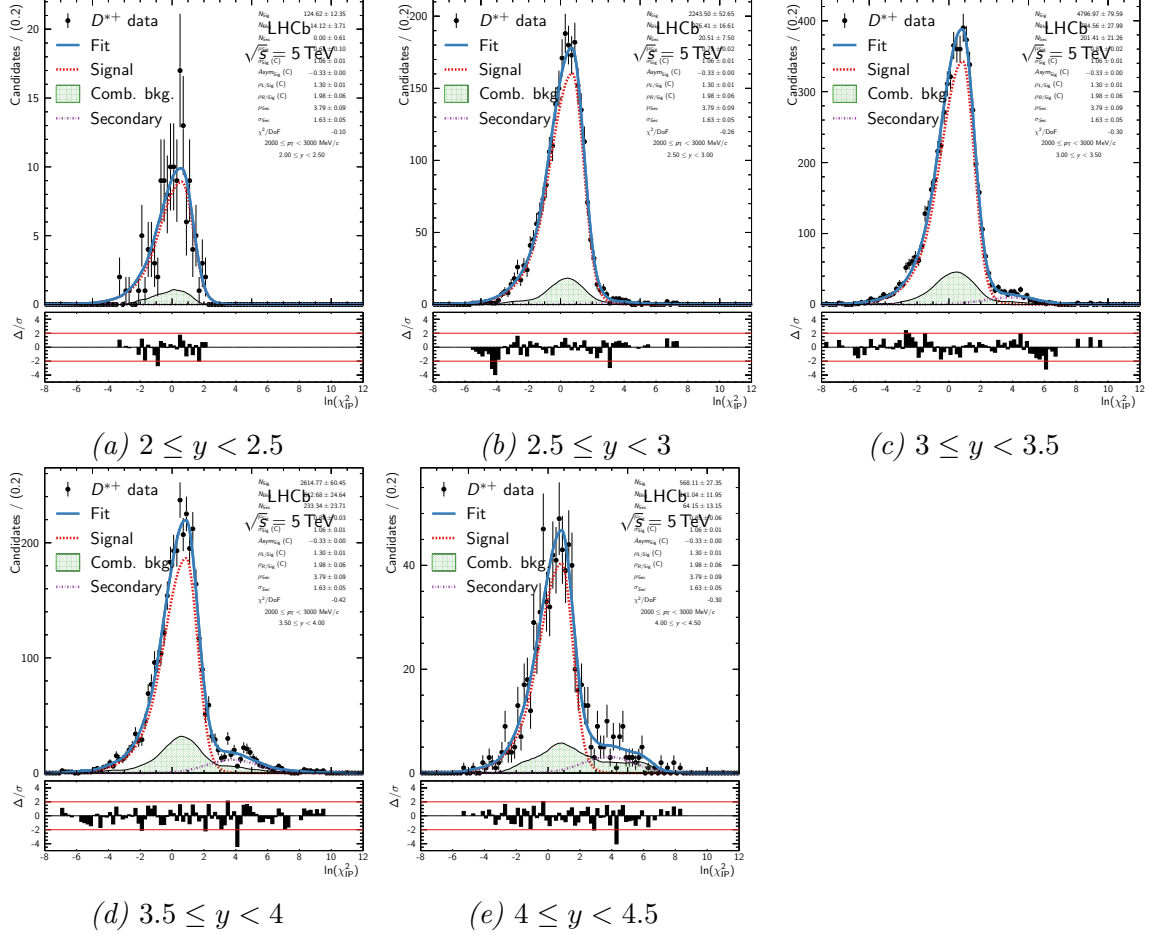


Figure B.31: Fits to the  $\ln \chi^2_{\text{IP}}$  distribution in the signal region of the  $D^{*+} \rightarrow D^0 \pi^+$ , with  $D^0 \rightarrow K^- \pi^+$ , data in bins of rapidity in the  $p_T$  range  $2 \leq p_T < 3 \text{ GeV}$ .

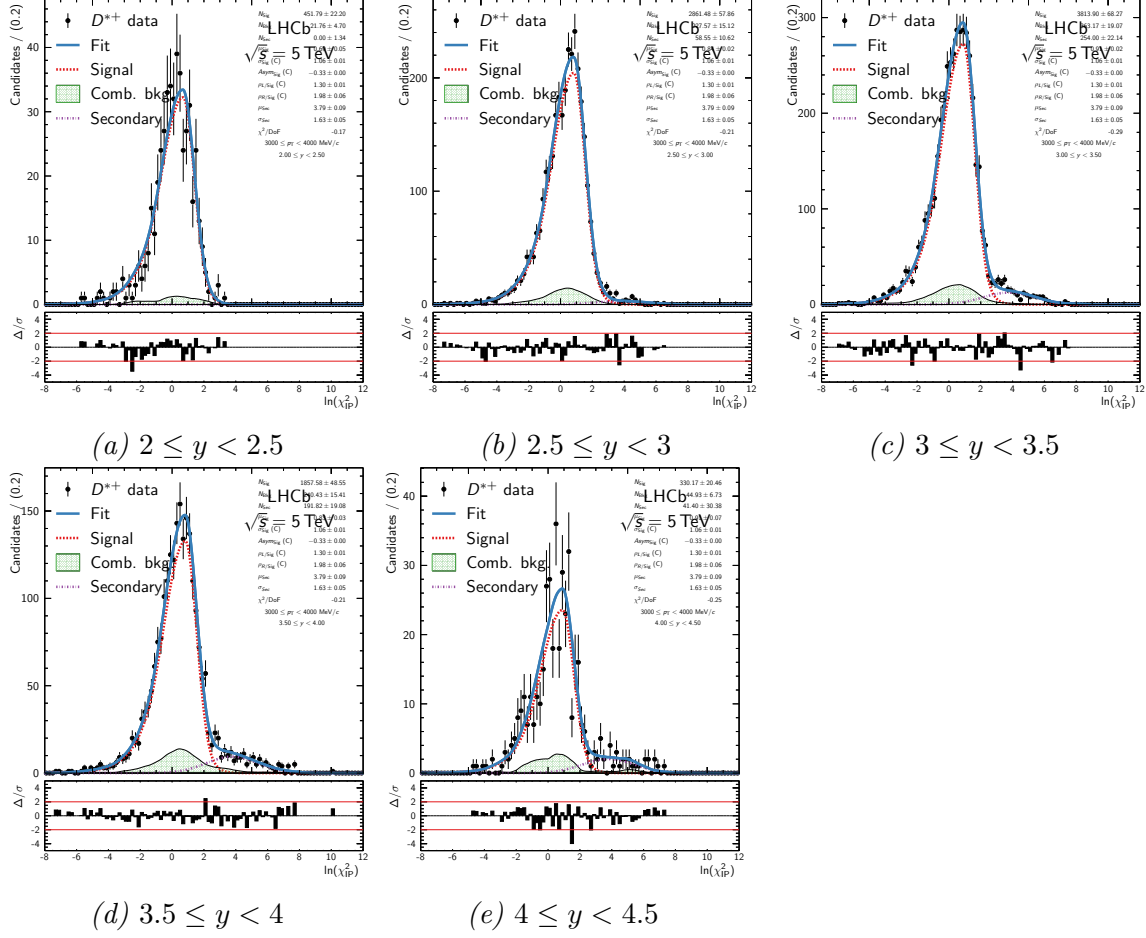


Figure B.32: Fits to the  $\ln \chi^2_{\text{IP}}$  distribution in the signal region of the  $D^{*+} \rightarrow D^0 \pi^+$ , with  $D^0 \rightarrow K^- \pi^+$ , data in bins of rapidity in the  $p_T$  range  $3 \leq p_T < 4 \text{ GeV}$ .

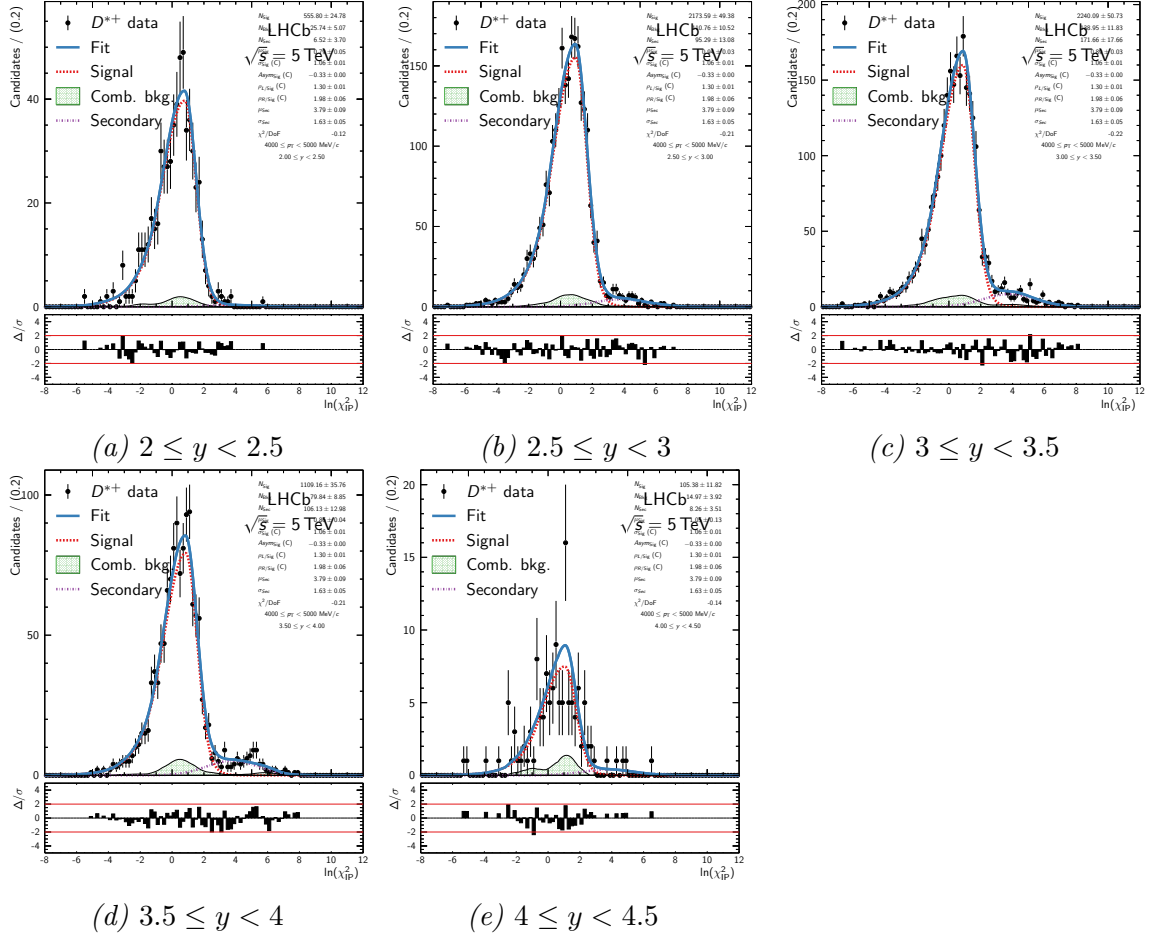


Figure B.33: Fits to the  $\ln \chi^2_{\text{IP}}$  distribution in the signal region of the  $D^{*+} \rightarrow D^0 \pi^+$ , with  $D^0 \rightarrow K^- \pi^+$ , data in bins of rapidity in the  $p_{\text{T}}$  range  $4 \leq p_{\text{T}} < 5 \text{ GeV}$ .

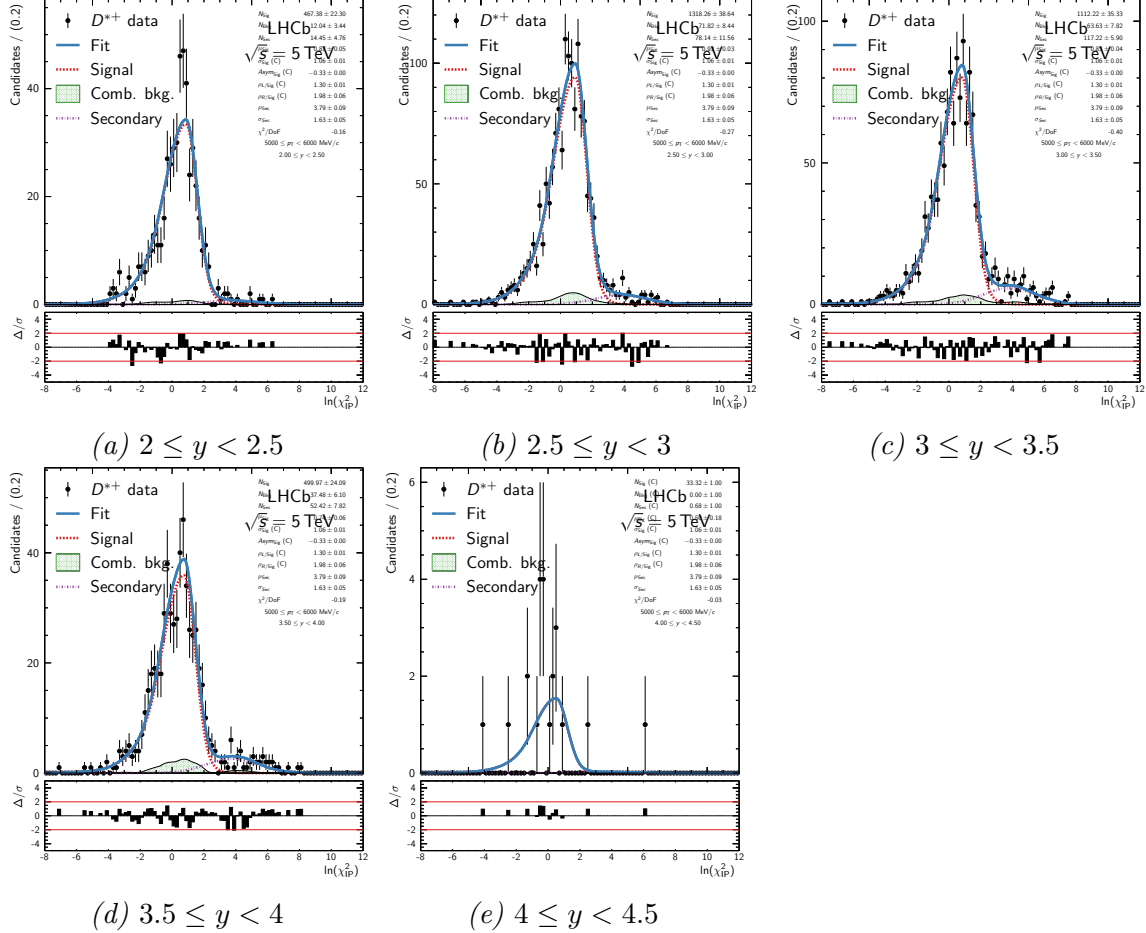


Figure B.34: Fits to the  $\ln \chi^2_{\text{IP}}$  distribution in the signal region of the  $D^{*+} \rightarrow D^0 \pi^+$ , with  $D^0 \rightarrow K^- \pi^+$ , data in bins of rapidity in the  $p_T$  range  $5 \leq p_T < 6 \text{ GeV}$ .

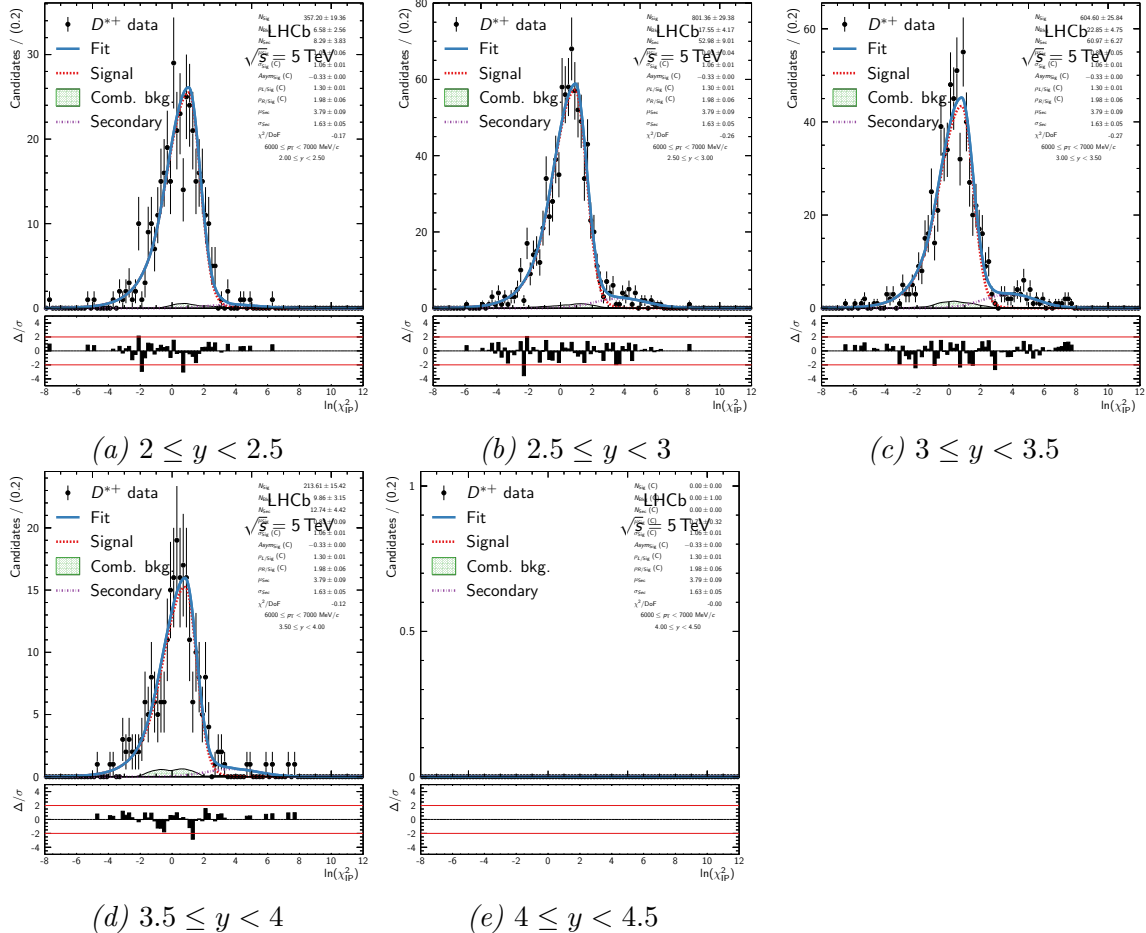


Figure B.35: Fits to the  $\ln \chi^2_{\text{IP}}$  distribution in the signal region of the  $D^{*+} \rightarrow D^0 \pi^+$ , with  $D^0 \rightarrow K^- \pi^+$ , data in bins of rapidity in the  $p_T$  range  $6 \leq p_T < 7 \text{ GeV}$ .

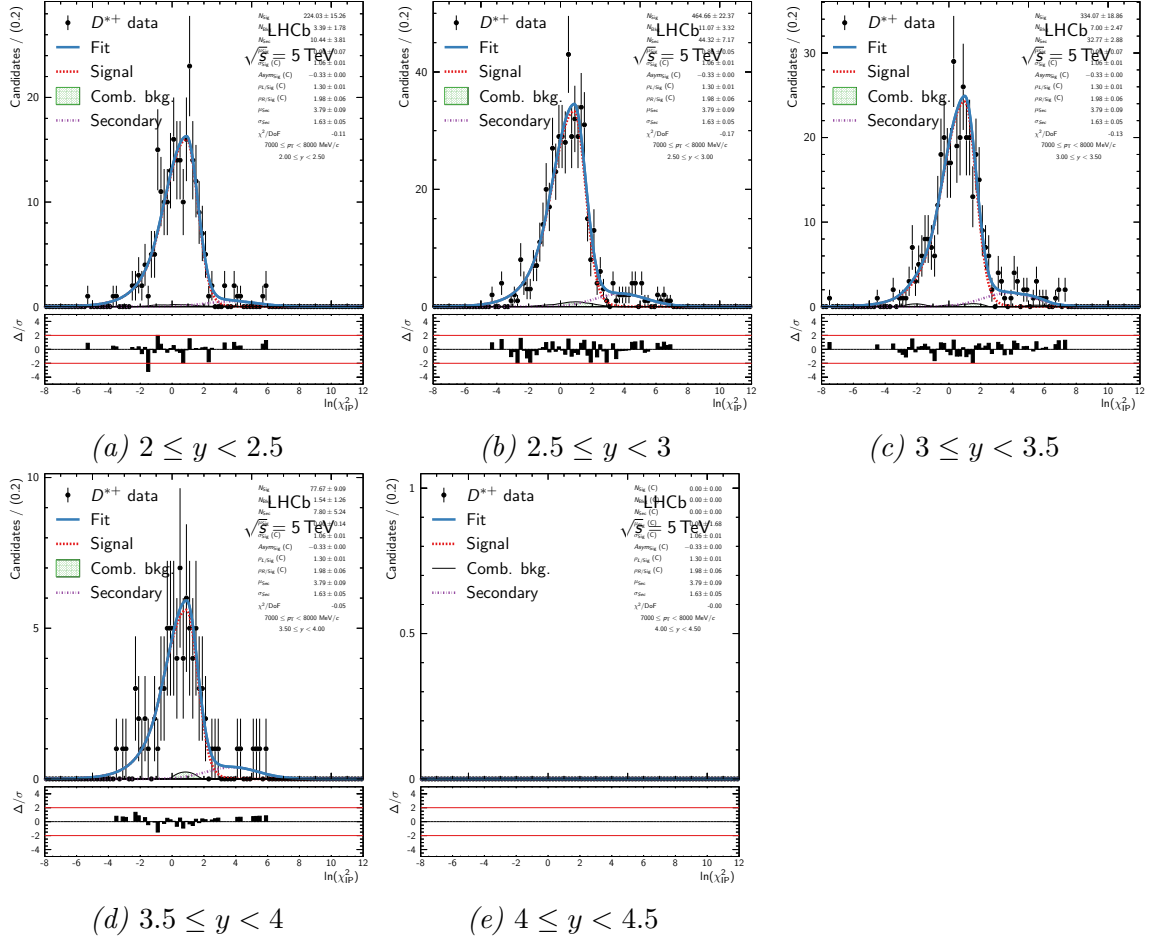


Figure B.36: Fits to the  $\ln \chi^2_{\text{IP}}$  distribution in the signal region of the  $D^{*+} \rightarrow D^0 \pi^+$ , with  $D^0 \rightarrow K^- \pi^+$ , data in bins of rapidity in the  $p_T$  range  $7 \leq p_T < 8 \text{ GeV}$ .

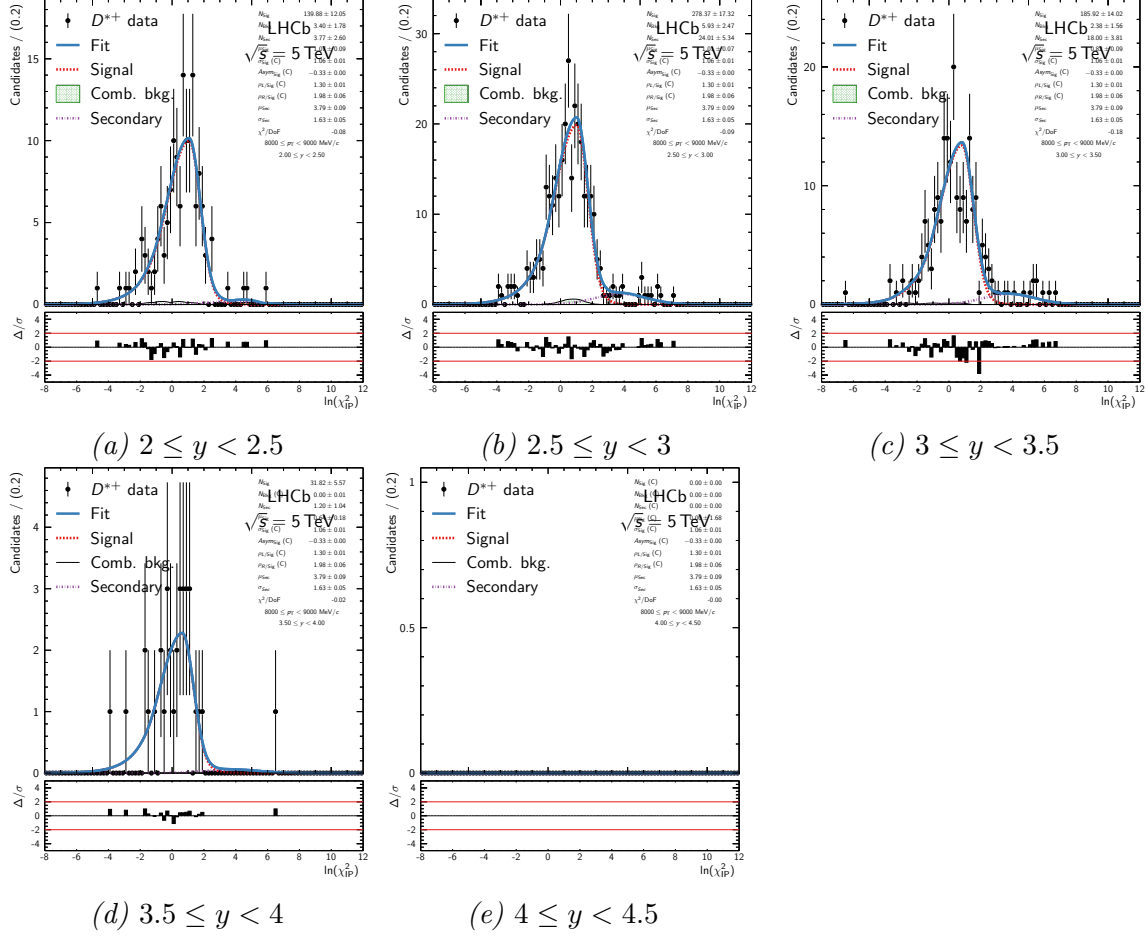


Figure B.37: Fits to the  $\ln \chi^2_{\text{IP}}$  distribution in the signal region of the  $D^{*+} \rightarrow D^0 \pi^+$ , with  $D^0 \rightarrow K^- \pi^+$ , data in bins of rapidity in the  $p_T$  range  $8 \leq p_T < 9 \text{ GeV}$ .

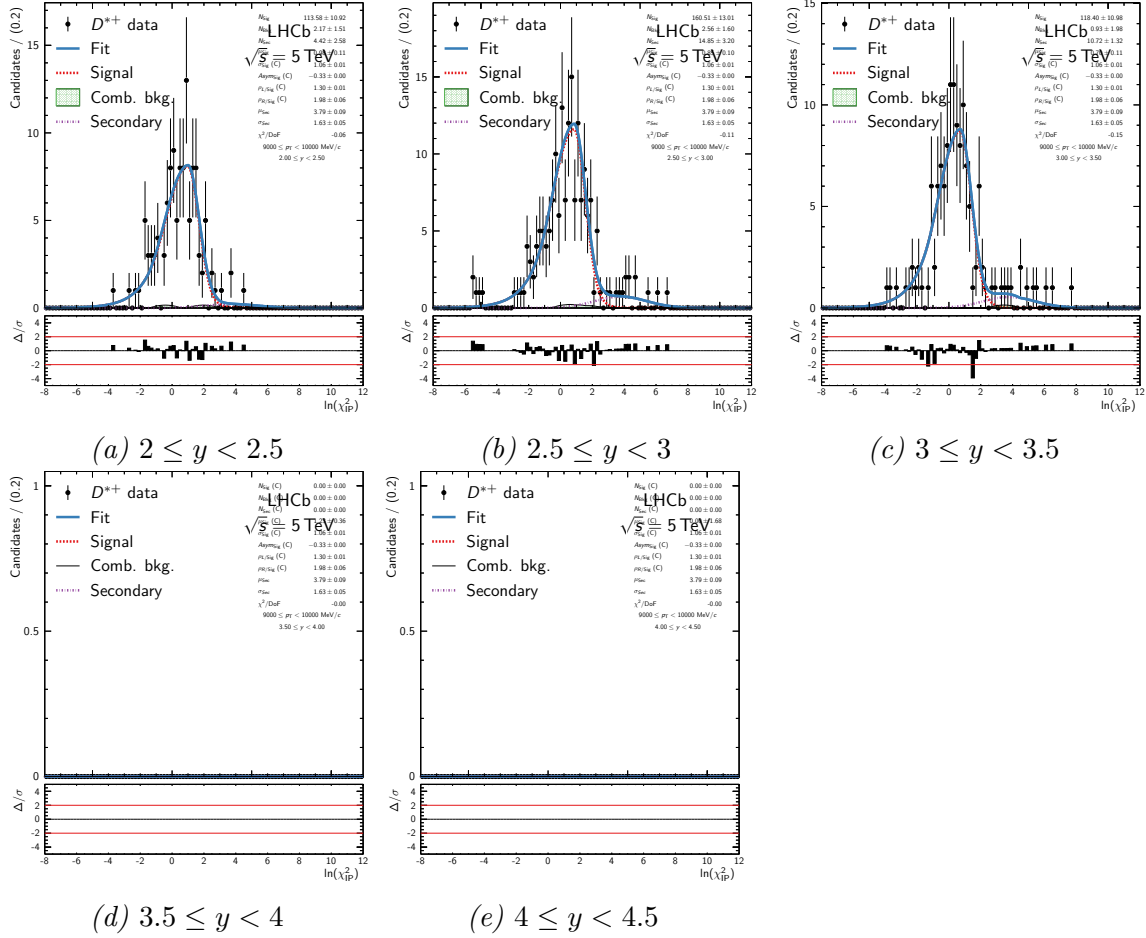


Figure B.38: Fits to the  $\ln \chi_{\text{IP}}^2$  distribution in the signal region of the  $D^{*+} \rightarrow D^0 \pi^+$ , with  $D^0 \rightarrow K^- \pi^+$ , data in bins of rapidity in the  $p_T$  range  $9 \leq p_T < 10 \text{ GeV}$ .

Table C.1: Acceptance efficiency for  $D^+ \rightarrow K^-\pi^+\pi^+$  in bins of  $D^0$   $p_T$  and  $y$ .

$p_T$ [MeV/c]	$y$				
	[2, 2.5]	[2.5, 3]	[3, 3.5]	[3.5, 4]	[4, 4.5]
[9000, 10000]	$99.21^{+0.24}_{-0.33}$	$99.86^{+0.10}_{-0.23}$	$100.00^{+0.00}_{-0.26}$	$100.00^{+0.00}_{-0.48}$	$98.08^{+1.03}_{-1.94}$
[8000, 9000]	$98.29^{+0.29}_{-0.35}$	$99.92^{+0.06}_{-0.14}$	$100.00^{+0.00}_{-0.15}$	$99.56^{+0.24}_{-0.45}$	$97.81^{+0.88}_{-1.40}$
[7000, 8000]	$98.33^{+0.23}_{-0.26}$	$99.95^{+0.04}_{-0.09}$	$99.93^{+0.05}_{-0.12}$	$99.77^{+0.13}_{-0.24}$	$99.48^{+0.28}_{-0.54}$
[6000, 7000]	$96.93^{+0.23}_{-0.25}$	$99.90^{+0.04}_{-0.07}$	$99.64^{+0.10}_{-0.13}$	$99.09^{+0.21}_{-0.27}$	$97.33^{+0.50}_{-0.61}$
[5000, 6000]	$95.33^{+0.22}_{-0.23}$	$99.93^{+0.03}_{-0.04}$	$99.78^{+0.06}_{-0.07}$	$99.11^{+0.15}_{-0.17}$	$97.45^{+0.34}_{-0.39}$
[4000, 5000]	$92.63^{+0.20}_{-0.20}$	$99.59^{+0.05}_{-0.06}$	$99.52^{+0.06}_{-0.07}$	$98.41^{+0.14}_{-0.15}$	$94.90^{+0.33}_{-0.35}$
[3000, 4000]	$88.11^{+0.17}_{-0.17}$	$99.01^{+0.06}_{-0.06}$	$99.22^{+0.06}_{-0.06}$	$97.47^{+0.12}_{-0.13}$	$92.07^{+0.27}_{-0.28}$
[2000, 3000]	$81.53^{+0.15}_{-0.15}$	$97.32^{+0.06}_{-0.07}$	$98.27^{+0.06}_{-0.06}$	$94.98^{+0.11}_{-0.12}$	$85.00^{+0.23}_{-0.23}$
[1000, 2000]	$72.87^{+0.12}_{-0.12}$	$93.07^{+0.07}_{-0.07}$	$96.25^{+0.06}_{-0.06}$	$89.91^{+0.11}_{-0.11}$	$72.98^{+0.19}_{-0.19}$
[0, 1000]	$66.81^{+0.14}_{-0.14}$	$88.78^{+0.10}_{-0.10}$	$92.95^{+0.08}_{-0.09}$	$83.53^{+0.14}_{-0.14}$	$60.24^{+0.21}_{-0.21}$

## 1089 C Efficiency tables

Table C.2: Acceptance efficiency for  $D_s^+ \rightarrow \phi\pi^+$  in bins of  $D^0$   $p_T$  and  $y$ .

$p_T$ [MeV/c]	$y$				
	[2, 2.5]	[2.5, 3]	[3, 3.5]	[3.5, 4]	[4, 4.5]
[9000, 10000]	$98.93^{+0.24}_{-0.30}$	$100.00^{+0.00}_{-0.11}$	$100.00^{+0.00}_{-0.17}$	$100.00^{+0.00}_{-0.31}$	$100.00^{+0.00}_{-0.84}$
[8000, 9000]	$98.93^{+0.19}_{-0.23}$	$99.89^{+0.06}_{-0.12}$	$99.68^{+0.13}_{-0.21}$	$100.00^{+0.00}_{-0.18}$	$99.34^{+0.36}_{-0.68}$
[7000, 8000]	$98.77^{+0.16}_{-0.18}$	$99.93^{+0.04}_{-0.07}$	$99.86^{+0.06}_{-0.11}$	$99.78^{+0.10}_{-0.17}$	$99.48^{+0.24}_{-0.41}$
[6000, 7000]	$98.13^{+0.15}_{-0.17}$	$99.97^{+0.02}_{-0.04}$	$99.95^{+0.03}_{-0.05}$	$99.84^{+0.06}_{-0.10}$	$99.34^{+0.20}_{-0.28}$
[5000, 6000]	$96.94^{+0.15}_{-0.15}$	$99.89^{+0.03}_{-0.04}$	$99.89^{+0.03}_{-0.04}$	$99.59^{+0.08}_{-0.10}$	$98.31^{+0.23}_{-0.27}$
[4000, 5000]	$95.76^{+0.12}_{-0.13}$	$99.73^{+0.03}_{-0.04}$	$99.63^{+0.05}_{-0.05}$	$99.22^{+0.08}_{-0.09}$	$97.39^{+0.20}_{-0.21}$
[3000, 4000]	$93.53^{+0.11}_{-0.11}$	$99.29^{+0.04}_{-0.04}$	$99.55^{+0.04}_{-0.04}$	$98.47^{+0.08}_{-0.08}$	$94.64^{+0.19}_{-0.19}$
[2000, 3000]	$89.73^{+0.10}_{-0.10}$	$97.92^{+0.05}_{-0.05}$	$98.43^{+0.05}_{-0.05}$	$95.40^{+0.09}_{-0.09}$	$86.25^{+0.19}_{-0.19}$
[1000, 2000]	$85.52^{+0.08}_{-0.08}$	$94.92^{+0.06}_{-0.06}$	$95.61^{+0.06}_{-0.06}$	$88.83^{+0.10}_{-0.10}$	$70.72^{+0.17}_{-0.17}$

Table C.3: Acceptance efficiency for  $D^{*+} \rightarrow D^0\pi^+$  with  $D^0 \rightarrow K^-\pi^+$  in bins of  $D^0$   $p_T$  and  $y$ .

$p_T$ [MeV/c]	$y$				
	[2, 2.5]	[2.5, 3]	[3, 3.5]	[3.5, 4]	[4, 4.5]
[9000, 10000]	$98.45^{+0.32}_{-0.40}$	$100.00^{+0.00}_{-0.13}$	$100.00^{+0.00}_{-0.19}$	$100.00^{+0.00}_{-0.37}$	$99.30^{+0.51}_{-1.19}$
[8000, 9000]	$98.37^{+0.26}_{-0.31}$	$100.00^{+0.00}_{-0.08}$	$100.00^{+0.00}_{-0.12}$	$100.00^{+0.00}_{-0.22}$	$99.63^{+0.27}_{-0.63}$
[7000, 8000]	$97.81^{+0.24}_{-0.26}$	$99.96^{+0.03}_{-0.07}$	$99.73^{+0.10}_{-0.16}$	$99.82^{+0.10}_{-0.18}$	$99.14^{+0.35}_{-0.56}$
[6000, 7000]	$96.71^{+0.22}_{-0.24}$	$99.77^{+0.06}_{-0.08}$	$99.97^{+0.02}_{-0.05}$	$99.56^{+0.13}_{-0.17}$	$99.16^{+0.24}_{-0.33}$
[5000, 6000]	$95.31^{+0.20}_{-0.21}$	$99.65^{+0.06}_{-0.07}$	$99.80^{+0.05}_{-0.07}$	$99.38^{+0.11}_{-0.13}$	$97.99^{+0.27}_{-0.31}$
[4000, 5000]	$92.96^{+0.18}_{-0.18}$	$99.13^{+0.07}_{-0.07}$	$99.76^{+0.04}_{-0.05}$	$98.71^{+0.12}_{-0.13}$	$95.34^{+0.29}_{-0.31}$
[3000, 4000]	$89.57^{+0.15}_{-0.15}$	$98.19^{+0.07}_{-0.08}$	$98.77^{+0.07}_{-0.07}$	$96.95^{+0.12}_{-0.13}$	$91.55^{+0.26}_{-0.26}$
[2000, 3000]	$84.77^{+0.13}_{-0.13}$	$96.23^{+0.07}_{-0.08}$	$98.25^{+0.06}_{-0.06}$	$95.45^{+0.10}_{-0.11}$	$86.97^{+0.21}_{-0.21}$
[1000, 2000]	$78.98^{+0.11}_{-0.11}$	$93.66^{+0.07}_{-0.07}$	$96.76^{+0.06}_{-0.06}$	$93.09^{+0.09}_{-0.09}$	$76.81^{+0.18}_{-0.18}$

Table C.4: Tracking efficiency correction for  $D^+ \rightarrow K^- \pi^+ \pi^+$ . Shown uncertainties are due to the size of the simulated sample.

$p_T$ [MeV/c]	[2, 2.5]	[2.5, 3]	[3, 3.5]	[3.5, 4]	[4, 4.5]
[9000, 10000]	$121.97 \pm 0.08$	$121.13 \pm 0.15$	$112.53 \pm 0.41$	$105.06 \pm 0.12$	$105.07 \pm 0.17$
[8000, 9000]	$122.16 \pm 0.08$	$121.03 \pm 0.12$	$112.32 \pm 0.32$	$105.07 \pm 0.11$	$105.39 \pm 0.11$
[7000, 8000]	$122.41 \pm 0.07$	$120.86 \pm 0.09$	$112.12 \pm 0.24$	$105.32 \pm 0.14$	$105.32 \pm 0.16$
[6000, 7000]	$122.58 \pm 0.05$	$120.57 \pm 0.08$	$112.05 \pm 0.14$	$105.40 \pm 0.06$	$105.16 \pm 0.07$
[5000, 6000]	$122.59 \pm 0.05$	$120.38 \pm 0.07$	$112.07 \pm 0.10$	$105.63 \pm 0.05$	$104.92 \pm 0.05$
[4000, 5000]	$122.14 \pm 0.05$	$120.21 \pm 0.05$	$111.89 \pm 0.07$	$106.08 \pm 0.04$	$104.89 \pm 0.03$
[3000, 4000]	$121.29 \pm 0.05$	$119.32 \pm 0.05$	$112.00 \pm 0.04$	$106.67 \pm 0.03$	$105.06 \pm 0.03$
[2000, 3000]	$120.33 \pm 0.05$	$117.82 \pm 0.04$	$111.59 \pm 0.03$	$107.18 \pm 0.03$	$105.34 \pm 0.02$
[1000, 2000]	$119.70 \pm 0.06$	$116.26 \pm 0.04$	$110.68 \pm 0.03$	$107.17 \pm 0.02$	$105.74 \pm 0.02$
[0, 1000]	$119.51 \pm 0.09$	$115.37 \pm 0.05$	$109.88 \pm 0.03$	$106.77 \pm 0.03$	$106.05 \pm 0.03$

Table C.5: Tracking efficiency correction for  $D_s^+ \rightarrow \phi \pi^+$ . Shown uncertainties are due to the size of the simulated sample.

$p_T$ [MeV/c]	[2, 2.5]	[2.5, 3]	[3, 3.5]	[3.5, 4]	[4, 4.5]
[9000, 10000]	$122.18 \pm 0.13$	$121.06 \pm 0.22$	$112.33 \pm 0.70$	$104.91 \pm 0.20$	$105.36 \pm 0.23$
[8000, 9000]	$122.49 \pm 0.13$	$120.92 \pm 0.16$	$111.71 \pm 0.43$	$105.03 \pm 0.18$	$105.00 \pm 0.15$
[7000, 8000]	$122.54 \pm 0.09$	$121.18 \pm 0.13$	$112.20 \pm 0.37$	$105.11 \pm 0.13$	$105.03 \pm 0.16$
[6000, 7000]	$122.80 \pm 0.09$	$121.37 \pm 0.13$	$111.24 \pm 0.32$	$105.55 \pm 0.09$	$104.97 \pm 0.14$
[5000, 6000]	$122.67 \pm 0.07$	$121.35 \pm 0.08$	$111.78 \pm 0.16$	$105.80 \pm 0.07$	$104.80 \pm 0.09$
[4000, 5000]	$122.41 \pm 0.05$	$120.91 \pm 0.08$	$111.63 \pm 0.11$	$106.27 \pm 0.05$	$104.80 \pm 0.06$
[3000, 4000]	$121.71 \pm 0.06$	$119.75 \pm 0.09$	$111.31 \pm 0.09$	$106.79 \pm 0.05$	$105.18 \pm 0.04$
[2000, 3000]	$120.43 \pm 0.10$	$117.69 \pm 0.07$	$110.28 \pm 0.06$	$106.99 \pm 0.04$	$105.77 \pm 0.04$
[1000, 2000]	$119.24 \pm 0.11$	$115.57 \pm 0.07$	$108.74 \pm 0.05$	$106.79 \pm 0.04$	$106.39 \pm 0.04$

Table C.6: Tracking efficiency correction for  $D^{*+} \rightarrow D^0\pi^+$  with  $D^0 \rightarrow K^-\pi^+$ . Shown uncertainties are due to the size of the simulated sample.

$p_T$ [MeV/c]	[2, 2.5]	[2.5, 3]	[3, 3.5]	[3.5, 4]	[4, 4.5]
[9000, 10000]	$121.55 \pm 0.06$	$121.76 \pm 0.08$	$111.43 \pm 0.31$	$105.78 \pm 0.10$	$106.30 \pm 0.08$
[8000, 9000]	$121.57 \pm 0.04$	$121.52 \pm 0.06$	$111.64 \pm 0.23$	$105.51 \pm 0.07$	$106.30 \pm 0.07$
[7000, 8000]	$121.53 \pm 0.04$	$121.00 \pm 0.05$	$111.47 \pm 0.17$	$105.42 \pm 0.06$	$106.04 \pm 0.05$
[6000, 7000]	$121.79 \pm 0.05$	$120.59 \pm 0.04$	$111.08 \pm 0.12$	$105.03 \pm 0.04$	$105.75 \pm 0.03$
[5000, 6000]	$121.99 \pm 0.05$	$120.13 \pm 0.04$	$110.67 \pm 0.08$	$104.78 \pm 0.03$	$105.59 \pm 0.03$
[4000, 5000]	$122.01 \pm 0.05$	$119.71 \pm 0.03$	$110.36 \pm 0.05$	$104.86 \pm 0.02$	$105.18 \pm 0.02$
[3000, 4000]	$121.63 \pm 0.06$	$119.03 \pm 0.03$	$110.11 \pm 0.03$	$105.24 \pm 0.02$	$104.82 \pm 0.02$
[2000, 3000]	$120.82 \pm 0.11$	$117.39 \pm 0.04$	$109.72 \pm 0.02$	$105.76 \pm 0.01$	$104.53 \pm 0.01$
[1000, 2000]	$120.59 \pm 0.90$	$114.17 \pm 0.07$	$109.17 \pm 0.02$	$106.20 \pm 0.01$	$104.59 \pm 0.01$

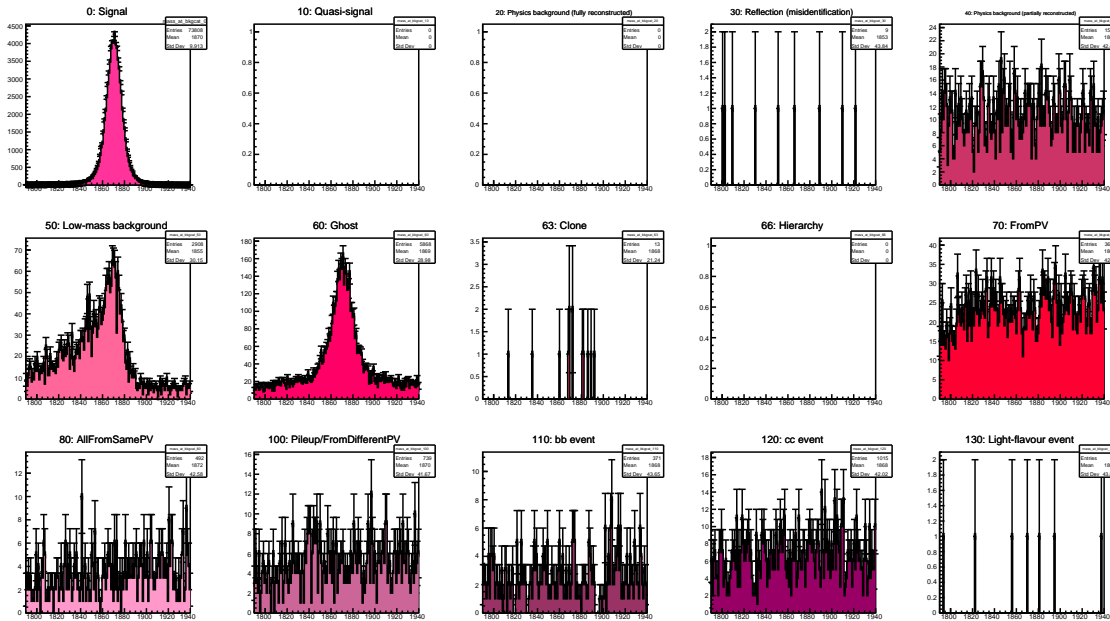
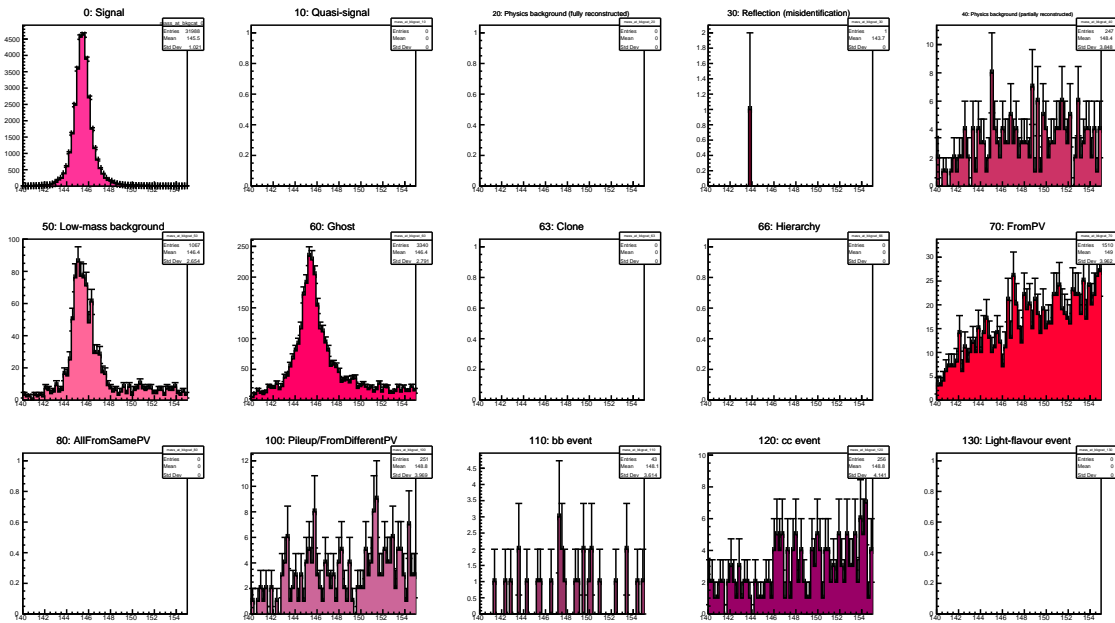


Figure C.1:  $D^+ \rightarrow K^-\pi^+\pi^+$  mass distributions for all the possible background categories values. Any signal-like peaking structures in background categories other than 0 or 10 indicate an inefficiency in the truth matching.



*Figure C.2:  $D^{*+} \rightarrow D^0\pi^+$ , with  $D^0 \rightarrow K^-\pi^+$ ,  $\delta m$  distributions for all the possible background categories values. Any signal-like peaking structures in background categories other than 0 or 10 indicate an inefficiency in the truth matching.*

Table C.7: Total MC selection efficiency for  $D^+ \rightarrow K^-\pi^+\pi^+$  in bins of  $D^0$   $p_T$  and  $y$ .

$p_T$ [MeV/c]	$y$				
	[2, 2.5]	[2.5, 3]	[3, 3.5]	[3.5, 4]	[4, 4.5]
[9000, 10000]	$9.65^{+0.85}_{-0.79}$	$23.55^{+1.39}_{-1.34}$	$24.70^{+1.70}_{-1.63}$	$10.22^{+1.61}_{-1.42}$	$0.00^{+0.83}_{-0.00}$
[8000, 9000]	$7.22^{+0.57}_{-0.53}$	$20.48^{+0.97}_{-0.94}$	$24.28^{+1.25}_{-1.21}$	$14.72^{+1.43}_{-1.33}$	$0.73^{+0.75}_{-0.39}$
[7000, 8000]	$7.69^{+0.44}_{-0.42}$	$19.85^{+0.71}_{-0.69}$	$23.19^{+0.91}_{-0.89}$	$14.75^{+1.01}_{-0.95}$	$0.76^{+0.43}_{-0.28}$
[6000, 7000]	$6.76^{+0.31}_{-0.29}$	$18.29^{+0.51}_{-0.50}$	$22.57^{+0.64}_{-0.63}$	$17.85^{+0.74}_{-0.72}$	$4.56^{+0.59}_{-0.53}$
[5000, 6000]	$5.25^{+0.20}_{-0.19}$	$16.23^{+0.35}_{-0.34}$	$19.35^{+0.42}_{-0.42}$	$17.55^{+0.50}_{-0.49}$	$5.82^{+0.42}_{-0.39}$
[4000, 5000]	$3.49^{+0.12}_{-0.11}$	$12.94^{+0.22}_{-0.22}$	$17.27^{+0.28}_{-0.28}$	$15.87^{+0.32}_{-0.31}$	$7.51^{+0.31}_{-0.30}$
[3000, 4000]	$2.20^{+0.07}_{-0.06}$	$9.57^{+0.14}_{-0.13}$	$13.06^{+0.17}_{-0.17}$	$12.52^{+0.20}_{-0.19}$	$6.44^{+0.19}_{-0.18}$
[2000, 3000]	$0.82^{+0.03}_{-0.03}$	$5.35^{+0.08}_{-0.07}$	$8.12^{+0.10}_{-0.10}$	$7.55^{+0.11}_{-0.11}$	$3.60^{+0.10}_{-0.10}$
[1000, 2000]	$0.12^{+0.01}_{-0.01}$	$1.16^{+0.03}_{-0.03}$	$2.11^{+0.04}_{-0.04}$	$2.03^{+0.05}_{-0.05}$	$0.89^{+0.04}_{-0.04}$
[0, 1000]	$0.00^{+0.00}_{-0.00}$	$0.02^{+0.01}_{-0.00}$	$0.11^{+0.01}_{-0.01}$	$0.11^{+0.01}_{-0.01}$	$0.08^{+0.02}_{-0.01}$

Table C.8: Total MC selection efficiency for  $D_s^+ \rightarrow \phi\pi^+$  in bins of  $D^0$   $p_T$  and  $y$ .

$p_T$ [MeV/c]	$y$				
	[2, 2.5]	[2.5, 3]	[3, 3.5]	[3.5, 4]	[4, 4.5]
[9000, 10000]	$4.97^{+1.06}_{-0.89}$	$7.37^{+1.40}_{-1.20}$	$13.17^{+2.32}_{-2.02}$	$8.44^{+2.53}_{-1.99}$	$0.00^{+1.85}_{-0.00}$
[8000, 9000]	$4.68^{+0.78}_{-0.67}$	$11.13^{+1.23}_{-1.13}$	$12.38^{+1.53}_{-1.39}$	$11.63^{+2.15}_{-1.85}$	$0.00^{+0.98}_{-0.00}$
[7000, 8000]	$4.66^{+0.57}_{-0.51}$	$9.33^{+0.85}_{-0.78}$	$11.16^{+1.12}_{-1.03}$	$9.62^{+1.37}_{-1.22}$	$0.76^{+0.78}_{-0.41}$
[6000, 7000]	$3.54^{+0.37}_{-0.33}$	$8.39^{+0.58}_{-0.55}$	$10.69^{+0.76}_{-0.72}$	$9.04^{+0.87}_{-0.80}$	$2.05^{+0.71}_{-0.53}$
[5000, 6000]	$3.21^{+0.25}_{-0.23}$	$8.01^{+0.41}_{-0.39}$	$9.77^{+0.52}_{-0.49}$	$8.35^{+0.58}_{-0.55}$	$3.71^{+0.57}_{-0.50}$
[4000, 5000]	$2.04^{+0.14}_{-0.14}$	$6.56^{+0.26}_{-0.25}$	$7.23^{+0.31}_{-0.30}$	$6.35^{+0.35}_{-0.33}$	$2.84^{+0.32}_{-0.29}$
[3000, 4000]	$1.25^{+0.08}_{-0.08}$	$4.66^{+0.16}_{-0.15}$	$5.77^{+0.19}_{-0.19}$	$4.62^{+0.20}_{-0.19}$	$2.01^{+0.17}_{-0.16}$
[2000, 3000]	$0.48^{+0.04}_{-0.04}$	$2.33^{+0.08}_{-0.08}$	$2.89^{+0.10}_{-0.10}$	$2.01^{+0.10}_{-0.09}$	$0.77^{+0.08}_{-0.07}$
[1000, 2000]	$0.07^{+0.01}_{-0.01}$	$0.37^{+0.03}_{-0.03}$	$0.47^{+0.03}_{-0.03}$	$0.34^{+0.03}_{-0.03}$	$0.08^{+0.02}_{-0.02}$

Table C.9: Total MC selection efficiency for  $D^{*+} \rightarrow D^0\pi^+$  with  $D^0 \rightarrow K^-\pi^+$  in bins of  $D^0$   $p_T$  and  $y$ .

$p_T$ [MeV/c]	$y$				
	[2, 2.5]	[2.5, 3]	[3, 3.5]	[3.5, 4]	[4, 4.5]
[9000, 10000]	$4.73 \pm 0.57$	$11.62 \pm 0.97$	$10.28 \pm 1.09$	$2.22 \pm 0.81$	$0.00 \pm 0.60$
[8000, 9000]	$3.83 \pm 0.40$	$13.16 \pm 0.77$	$14.51 \pm 0.95$	$5.42 \pm 0.86$	$0.00 \pm 0.31$
[7000, 8000]	$3.29 \pm 0.28$	$11.29 \pm 0.53$	$12.46 \pm 0.66$	$5.84 \pm 0.61$	$0.00 \pm 0.15$
[6000, 7000]	$2.40 \pm 0.18$	$10.25 \pm 0.37$	$12.51 \pm 0.48$	$8.05 \pm 0.49$	$0.46 \pm 0.20$
[5000, 6000]	$1.81 \pm 0.11$	$8.47 \pm 0.25$	$10.85 \pm 0.31$	$9.27 \pm 0.36$	$1.18 \pm 0.19$
[4000, 5000]	$1.04 \pm 0.06$	$6.35 \pm 0.15$	$9.16 \pm 0.20$	$7.46 \pm 0.22$	$1.93 \pm 0.15$
[3000, 4000]	$0.46 \pm 0.03$	$3.88 \pm 0.09$	$6.78 \pm 0.12$	$6.00 \pm 0.14$	$2.19 \pm 0.11$
[2000, 3000]	$0.07 \pm 0.01$	$1.47 \pm 0.04$	$3.94 \pm 0.07$	$3.57 \pm 0.08$	$1.52 \pm 0.06$
[1000, 2000]	$0.00 \pm 0.00$	$0.24 \pm 0.01$	$1.39 \pm 0.03$	$1.19 \pm 0.04$	$0.55 \pm 0.03$

Table C.10: Total PID selection efficiency for  $D^+ \rightarrow K^-\pi^+\pi^+$  in bins of  $D^+$   $p_T$  and  $y$ . Shown uncertainties are due to the size of the calibration sample, estimated by bootstrapping the calibration sample.

$p_T$ [MeV/c]	$y$				
	[2, 2.5]	[2.5, 3]	[3, 3.5]	[3.5, 4]	[4, 4.5]
[9000, 10000]	$96.47 \pm 0.19$	$93.01 \pm 0.24$	$87.21 \pm 0.34$	$73.69 \pm 0.60$	
[8000, 9000]	$96.57 \pm 0.18$	$94.96 \pm 0.15$	$89.59 \pm 0.26$	$76.29 \pm 0.46$	
[7000, 8000]	$96.71 \pm 0.19$	$96.33 \pm 0.11$	$91.46 \pm 0.20$	$78.44 \pm 0.40$	
[6000, 7000]	$96.48 \pm 0.20$	$96.98 \pm 0.10$	$93.20 \pm 0.16$	$80.63 \pm 0.32$	$56.24 \pm 0.68$
[5000, 6000]	$95.63 \pm 0.24$	$97.02 \pm 0.11$	$95.37 \pm 0.12$	$83.95 \pm 0.26$	$63.31 \pm 0.64$
[4000, 5000]	$94.80 \pm 0.28$	$96.48 \pm 0.13$	$96.20 \pm 0.11$	$87.28 \pm 0.21$	$68.56 \pm 0.55$
[3000, 4000]	$93.70 \pm 0.34$	$95.30 \pm 0.19$	$95.79 \pm 0.14$	$89.45 \pm 0.21$	$73.50 \pm 0.48$
[2000, 3000]	$92.64 \pm 0.41$	$93.25 \pm 0.31$	$94.37 \pm 0.24$	$90.73 \pm 0.28$	$79.18 \pm 0.44$
[1000, 2000]	$91.69 \pm 0.47$	$91.52 \pm 0.47$	$92.42 \pm 0.43$	$90.67 \pm 0.44$	$82.29 \pm 0.54$
[0, 1000]		$92.48 \pm 0.48$	$93.14 \pm 0.50$	$91.78 \pm 0.61$	$82.75 \pm 0.92$

Table C.11: Total PID selection efficiency for  $D_s^+ \rightarrow \phi\pi^+$  in bins of  $D_s^+$   $p_T$  and  $y$ . Shown uncertainties are due to the size of the calibration sample, estimated by bootstrapping the calibration sample.

$p_T$ [MeV/c]	$y$				
	[2, 2.5]	[2.5, 3]	[3, 3.5]	[3.5, 4]	[4, 4.5]
[9000, 10000]	98.12 $\pm$ 0.22	95.70 $\pm$ 0.21	86.04 $\pm$ 0.36		
[8000, 9000]	97.25 $\pm$ 0.25	96.83 $\pm$ 0.14	90.48 $\pm$ 0.30	69.09 $\pm$ 0.81	
[7000, 8000]	97.42 $\pm$ 0.24	97.35 $\pm$ 0.14	94.61 $\pm$ 0.18	68.55 $\pm$ 0.57	
[6000, 7000]	96.57 $\pm$ 0.33	97.57 $\pm$ 0.13	95.73 $\pm$ 0.14	81.65 $\pm$ 0.38	
[5000, 6000]	95.40 $\pm$ 0.35	97.33 $\pm$ 0.16	97.05 $\pm$ 0.11	84.43 $\pm$ 0.29	48.63 $\pm$ 0.82
[4000, 5000]	93.65 $\pm$ 0.54	95.74 $\pm$ 0.23	97.20 $\pm$ 0.14	89.04 $\pm$ 0.30	62.01 $\pm$ 0.67
[3000, 4000]	91.73 $\pm$ 0.64	93.48 $\pm$ 0.35	96.20 $\pm$ 0.20	89.87 $\pm$ 0.33	74.17 $\pm$ 0.71
[2000, 3000]	89.94 $\pm$ 0.79	89.41 $\pm$ 0.60	93.61 $\pm$ 0.35	90.66 $\pm$ 0.42	78.99 $\pm$ 0.72
[1000, 2000]	90.52 $\pm$ 0.88	85.22 $\pm$ 1.05	91.08 $\pm$ 0.70	89.10 $\pm$ 0.74	82.66 $\pm$ 1.07

Table C.12: Total PID selection efficiency for  $D^{*+} \rightarrow D^0\pi^+$ ,  $D^0 \rightarrow K^-\pi^+$  in bins of  $D^{*+}$   $p_T$  and  $y$ . Shown uncertainties are due to the size of the calibration sample, estimated by bootstrapping the calibration sample.

$p_T$ [MeV/c]	$y$				
	[2, 2.5]	[2.5, 3]	[3, 3.5]	[3.5, 4]	[4, 4.5]
[9000, 10000]	94.90 $\pm$ 0.34	92.80 $\pm$ 0.48	81.83 $\pm$ 0.59		
[8000, 9000]	97.28 $\pm$ 0.17	93.44 $\pm$ 0.30	85.77 $\pm$ 0.42	67.40 $\pm$ 0.63	
[7000, 8000]	98.10 $\pm$ 0.15	94.85 $\pm$ 0.19	86.19 $\pm$ 0.35	72.31 $\pm$ 0.60	
[6000, 7000]	98.23 $\pm$ 0.11	97.10 $\pm$ 0.10	89.31 $\pm$ 0.25	78.94 $\pm$ 0.46	
[5000, 6000]	98.07 $\pm$ 0.12	97.87 $\pm$ 0.10	94.18 $\pm$ 0.14	80.31 $\pm$ 0.43	58.86 $\pm$ 0.97
[4000, 5000]	97.27 $\pm$ 0.15	98.43 $\pm$ 0.09	95.88 $\pm$ 0.13	83.17 $\pm$ 0.26	59.10 $\pm$ 0.92
[3000, 4000]	96.93 $\pm$ 0.20	97.76 $\pm$ 0.12	96.54 $\pm$ 0.16	89.05 $\pm$ 0.20	69.39 $\pm$ 0.63
[2000, 3000]	97.51 $\pm$ 0.25	97.17 $\pm$ 0.15	96.63 $\pm$ 0.14	92.94 $\pm$ 0.20	73.64 $\pm$ 0.52
[1000, 2000]		96.69 $\pm$ 0.26	98.69 $\pm$ 0.18	95.50 $\pm$ 0.26	80.86 $\pm$ 0.50

Table C.13: Signal window requirement efficiencies, in percent, for  $D^+ \rightarrow K^-\pi^+\pi^+$ .

$p_T$ [MeV/c]	[2, 2.5]	[2.5, 3]	[3, 3.5]	$y$	[3.5, 4]	[4, 4.5]
[9000, 10000]	97.36 ± 0.18	96.76 ± 0.23	95.46 ± 0.51	95.07 ± 1.10	97.60 ± 0.09	
[8000, 9000]	97.11 ± 0.19	96.97 ± 0.16	96.21 ± 0.28	95.09 ± 0.72	97.60 ± 0.09	
[7000, 8000]	97.40 ± 0.12	97.06 ± 0.14	96.72 ± 0.19	93.36 ± 0.28	97.60 ± 0.09	
[6000, 7000]	97.53 ± 0.11	97.38 ± 0.10	96.66 ± 0.15	95.00 ± 0.36	93.17 ± 1.12	
[5000, 6000]	97.68 ± 0.10	97.52 ± 0.10	96.88 ± 0.12	95.48 ± 0.23	93.33 ± 0.23	
[4000, 5000]	97.74 ± 0.09	97.58 ± 0.09	97.01 ± 0.10	95.47 ± 0.18	93.36 ± 0.15	
[3000, 4000]	97.84 ± 0.08	97.66 ± 0.09	97.12 ± 0.10	95.88 ± 0.13	93.36 ± 0.13	
[2000, 3000]	97.97 ± 0.09	97.75 ± 0.09	97.26 ± 0.09	96.03 ± 0.12	94.07 ± 0.36	
[1000, 2000]	97.90 ± 0.10	97.83 ± 0.09	97.25 ± 0.10	96.26 ± 0.15	94.72 ± 0.62	
[0, 1000]	97.60 ± 0.09	97.72 ± 0.27	97.72 ± 0.23	97.75 ± 1.15	98.40 ± 2.44	

Table C.14: Signal window requirement efficiencies, in percent, for  $D_s^+ \rightarrow \phi\pi^+$ .

$p_T$ [MeV/c]	[2, 2.5]	[2.5, 3]	[3, 3.5]	$y$	[3.5, 4]	[4, 4.5]
[9000, 10000]	98.79 ± 0.27	98.62 ± 0.37	98.82 ± 0.25	98.83 ± 0.16	98.83 ± 0.17	
[8000, 9000]	98.88 ± 0.17	98.88 ± 0.18	98.83 ± 0.23	95.58 ± 1.39	98.83 ± 0.16	
[7000, 8000]	98.79 ± 0.21	98.80 ± 0.20	98.43 ± 0.44	97.75 ± 0.89	98.83 ± 0.16	
[6000, 7000]	98.88 ± 0.17	98.89 ± 0.17	98.85 ± 0.18	98.26 ± 0.66	98.83 ± 0.16	
[5000, 6000]	98.88 ± 0.17	98.89 ± 0.17	98.71 ± 0.19	97.96 ± 0.51	94.21 ± 2.37	
[4000, 5000]	98.90 ± 0.17	98.88 ± 0.17	98.78 ± 0.18	98.33 ± 0.29	94.86 ± 1.96	
[3000, 4000]	98.89 ± 0.17	98.88 ± 0.17	98.81 ± 0.17	98.28 ± 0.27	97.59 ± 0.92	
[2000, 3000]	98.89 ± 0.17	98.88 ± 0.16	98.85 ± 0.17	98.62 ± 0.21	98.12 ± 0.74	
[1000, 2000]	98.90 ± 0.17	98.87 ± 0.17	98.88 ± 0.17	98.35 ± 0.53	98.51 ± 1.77	

Table C.15: Signal window requirement efficiencies, in percent, for  $D^{*+} \rightarrow D^0\pi^+$ , with  $D^0 \rightarrow K^-\pi^+$ .

$p_T$ [MeV/c]	[2, 2.5]	[2.5, 3]	$y$ [3, 3.5]	[3.5, 4]	[4, 4.5]
[9000, 10000]	92.60 $\pm$ 0.90	93.68 $\pm$ 0.28	93.17 $\pm$ 0.54	93.95 $\pm$ 0.17	93.95 $\pm$ 0.16
[8000, 9000]	93.54 $\pm$ 0.37	93.70 $\pm$ 0.21	93.52 $\pm$ 0.53	91.85 $\pm$ 1.20	93.95 $\pm$ 0.17
[7000, 8000]	93.77 $\pm$ 0.23	93.57 $\pm$ 0.24	92.42 $\pm$ 0.55	93.84 $\pm$ 0.71	93.95 $\pm$ 0.17
[6000, 7000]	93.56 $\pm$ 0.27	93.86 $\pm$ 0.17	93.11 $\pm$ 0.31	92.21 $\pm$ 0.68	93.95 $\pm$ 0.17
[5000, 6000]	93.97 $\pm$ 0.18	93.74 $\pm$ 0.18	93.21 $\pm$ 0.22	93.12 $\pm$ 0.30	90.19 $\pm$ 1.50
[4000, 5000]	93.92 $\pm$ 0.16	93.91 $\pm$ 0.15	93.42 $\pm$ 0.19	92.61 $\pm$ 0.31	91.48 $\pm$ 0.95
[3000, 4000]	93.98 $\pm$ 0.16	93.89 $\pm$ 0.15	93.69 $\pm$ 0.17	92.81 $\pm$ 0.22	91.65 $\pm$ 0.59
[2000, 3000]	93.99 $\pm$ 0.18	93.89 $\pm$ 0.15	93.67 $\pm$ 0.16	92.64 $\pm$ 0.21	91.52 $\pm$ 0.49
[1000, 2000]	93.95 $\pm$ 0.17	93.96 $\pm$ 0.16	93.78 $\pm$ 0.16	92.91 $\pm$ 0.21	91.06 $\pm$ 0.56

*Table D.1: Relative error on the  $D^+$  cross-section in each kinematic bin due to the finite size of the Monte Carlo sample. Relative error on the  $D^+$  cross-section in each kinematic bin due to the statistical uncertainty.*

$p_T$ [MeV/c]	$y$				
	[2, 2.5]	[2.5, 3]	[3, 3.5]	[3.5, 4]	[4, 4.5]
[0, 1000]		9.17	5.92	6.94	
[1000, 2000]	3.28	1.09	0.90	1.12	2.46
[2000, 3000]	1.47	0.64	0.60	0.77	1.58
[3000, 4000]	1.29	0.69	0.70	0.92	1.85
[4000, 5000]	1.41	0.89	0.94	1.25	2.84
[5000, 6000]	1.70	1.18	1.29	1.79	4.92
[6000, 7000]	2.09	1.58	1.76	2.71	9.58
[7000, 8000]	2.59	2.06	2.41	3.92	
[8000, 9000]	3.21	2.74	3.34	6.20	
[9000, 10000]	4.10	3.59	4.36	10.10	

## 1090 D Systematics tables

1091 This section presents the systematic uncertainty tables for all modes other than  $D^0 \rightarrow$   
 1092  $K^-\pi^+$ . The systematic uncertainties themselves, and the respective  $D^0 \rightarrow K^-\pi^+$   
 1093 tables, are discussed and given in Section 7.

### 1094 D.1 Statistical uncertainty

Table D.2: Relative error on the  $D_s^+$  cross-section in each kinematic bin due to the statistical uncertainty.

$p_T$ [MeV/c]	$y$				
	[2, 2.5]	[2.5, 3]	[3, 3.5]	[3.5, 4]	[4, 4.5]
[1000, 2000]	15.24	6.00	6.22	9.11	
[2000, 3000]	5.29	2.75	2.92	4.35	10.81
[3000, 4000]	4.68	2.84	3.17	4.24	9.33
[4000, 5000]	5.02	3.49	3.92	5.50	12.22
[5000, 6000]	6.38	4.90	4.92	7.53	19.67
[6000, 7000]	7.63	6.20	7.34	11.04	
[7000, 8000]	8.96	8.06	9.56	14.30	
[8000, 9000]	13.57	11.23	13.06		
[9000, 10000]	14.89	13.21	17.08		

Table D.3: Relative error on the  $D^{*+}$  cross-section in each kinematic bin due to the statistical uncertainty.

$p_T$ [MeV/c]	$y$				
	[2, 2.5]	[2.5, 3]	[3, 3.5]	[3.5, 4]	[4, 4.5]
[1000, 2000]		4.52	2.28	2.82	5.91
[2000, 3000]	9.86	2.33	1.65	2.30	4.79
[3000, 4000]	4.89	2.01	1.78	2.60	6.16
[4000, 5000]	4.43	2.26	2.25	3.21	11.15
[5000, 6000]	4.75	2.92	3.16	4.79	2.99
[6000, 7000]	5.39	3.65	4.25	7.18	
[7000, 8000]	6.77	4.79	5.62	11.64	
[8000, 9000]	8.56	6.19	7.50	17.42	
[9000, 10000]	9.56	8.06	9.23		

*Table D.4: Relative error on the  $D^+$  cross-section in each kinematic bin due to the finite size of the Monte Carlo sample.*

$p_T$ [MeV/c]	$y$				
	[2, 2.5]	[2.5, 3]	[3, 3.5]	[3.5, 4]	[4, 4.5]
[0, 1000]		13.76	7.92	8.65	16.07
[1000, 2000]	6.32	1.82	1.41	1.65	3.23
[2000, 3000]	2.71	1.02	0.88	1.05	1.97
[3000, 4000]	2.23	1.01	0.93	1.13	2.10
[4000, 5000]	2.38	1.21	1.18	1.47	2.96
[5000, 6000]	2.66	1.55	1.55	2.03	5.14
[6000, 7000]	3.26	2.02	2.05	3.02	9.31
[7000, 8000]	4.02	2.63	2.81	4.47	
[8000, 9000]	5.38	3.44	3.69	6.86	
[9000, 10000]	6.48	4.19	4.77	10.11	

<sup>1095</sup> **D.2 Finite Monte Carlo sample size**

<sup>1096</sup> See Section 7.1 for discussion.

Table D.5: Relative error on the  $D_s^+$  cross-section in each kinematic bin due to the finite size of the Monte Carlo sample.

$p_T$ [MeV/c]	$y$				
	[2, 2.5]	[2.5, 3]	[3, 3.5]	[3.5, 4]	[4, 4.5]
[1000, 2000]	13.12	5.40	5.28	6.88	
[2000, 3000]	5.70	2.53	2.51	3.32	6.57
[3000, 4000]	4.51	2.46	2.41	3.20	6.14
[4000, 5000]	4.85	2.90	3.02	3.70	7.73
[5000, 6000]	5.56	3.57	3.75	4.85	
[6000, 7000]	7.06	4.69	5.05	6.77	
[7000, 8000]	8.53	5.89	6.89	9.79	
[8000, 9000]	10.21	7.93	8.30		
[9000, 10000]	14.17	11.35	11.10		

Table D.6: Relative error on the  $D^{*+}$  cross-section in each kinematic bin due to the finite size of the Monte Carlo sample.

$p_T$ [MeV/c]	$y$				
	[2, 2.5]	[2.5, 3]	[3, 3.5]	[3.5, 4]	[4, 4.5]
[1000, 2000]		4.13	1.81	2.17	4.07
[2000, 3000]	9.49	1.98	1.29	1.56	2.96
[3000, 4000]	4.85	1.61	1.31	1.65	3.52
[4000, 5000]	4.11	1.71	1.56	2.09	5.48
[5000, 6000]	4.31	2.06	2.07	2.72	10.35
[6000, 7000]	4.82	2.57	2.67	4.41	
[7000, 8000]	6.05	3.38	3.66	7.25	
[8000, 9000]	6.94	4.18	4.66	10.23	
[9000, 10000]	8.23	5.39	6.97		

*Table D.7: Relative error on the  $D^+$  cross-section in each kinematic bin due to the finite size of the PID calibration sample.*

$p_T$ [MeV/c]	$y$				
	[2, 2.5]	[2.5, 3]	[3, 3.5]	[3.5, 4]	[4, 4.5]
[0, 1000]		0.54	0.54	0.66	1.10
[1000, 2000]	0.51	0.51	0.46	0.48	0.65
[2000, 3000]	0.44	0.33	0.25	0.30	0.55
[3000, 4000]	0.36	0.20	0.15	0.23	0.65
[4000, 5000]	0.29	0.14	0.12	0.24	0.79
[5000, 6000]	0.24	0.11	0.13	0.31	1.03
[6000, 7000]	0.20	0.10	0.17	0.40	1.13
[7000, 8000]	0.19	0.11	0.21	0.50	
[8000, 9000]	0.19	0.15	0.28	0.60	
[9000, 10000]	0.21	0.26	0.39	0.80	

### D.3 PID calibration

1097 See Section 7.4 for discussion.

1098 See Section 7.4 for discussion.

*Table D.8: Relative error on the  $D_s^+ \rightarrow \phi\pi^+$  cross-section in each kinematic bin due to the finite size of the PID calibration sample.*

$p_T$ [MeV/c]	$y$				
	[2, 2.5]	[2.5, 3]	[3, 3.5]	[3.5, 4]	[4, 4.5]
[1000, 2000]	0.99	1.26	0.77	0.84	
[2000, 3000]	0.86	0.66	0.38	0.46	0.91
[3000, 4000]	0.70	0.37	0.21	0.37	0.95
[4000, 5000]	0.56	0.24	0.14	0.33	1.08
[5000, 6000]	0.37	0.17	0.12	0.34	
[6000, 7000]	0.34	0.13	0.15	0.47	
[7000, 8000]	0.24	0.14	0.20	0.86	
[8000, 9000]	0.26	0.15	0.33		
[9000, 10000]	0.22	0.23	0.41		

*Table D.9: Relative error on the  $D^{*+}$  cross-section in each kinematic bin due to the finite size of the PID calibration sample.*

$p_T$ [MeV/c]	$y$				
	[2, 2.5]	[2.5, 3]	[3, 3.5]	[3.5, 4]	[4, 4.5]
[1000, 2000]		0.27	0.20	0.27	0.61
[2000, 3000]	0.25	0.15	0.14	0.22	0.70
[3000, 4000]	0.20	0.12	0.17	0.22	0.89
[4000, 5000]	0.15	0.08	0.14	0.31	1.51
[5000, 6000]	0.12	0.10	0.15	0.58	1.52
[6000, 7000]	0.11	0.11	0.29	0.57	
[7000, 8000]	0.19	0.21	0.41	0.74	
[8000, 9000]	0.18	0.32	0.49	0.94	
[9000, 10000]	0.36	0.52	0.74		

*Table D.10: Relative error on the  $D^+$  cross-section in each kinematic bin due to the choice of PID calibration binning.*

$p_T$ [MeV/c]	$y$				
	[2, 2.5]	[2.5, 3]	[3, 3.5]	[3.5, 4]	[4, 4.5]
[0, 1000]		0.28	1.55	0.78	4.76
[1000, 2000]	10.28	1.21	1.51	0.59	4.05
[2000, 3000]	5.93	0.61	0.73	0.56	2.56
[3000, 4000]	3.51	0.20	0.53	0.51	2.98
[4000, 5000]	2.33	0.00	0.53	0.72	0.81
[5000, 6000]	1.08	0.05	0.59	0.66	3.78
[6000, 7000]	0.63	0.19	0.74	1.10	2.52
[7000, 8000]	0.38	0.28	0.31	2.62	
[8000, 9000]	0.08	0.62	0.25	5.74	
[9000, 10000]	0.18	1.10	4.03	9.43	

*Table D.11: Relative error on the  $D_s^+$  cross-section in each kinematic bin due to the choice of PID calibration binning.*

$p_T$ [MeV/c]	$y$				
	[2, 2.5]	[2.5, 3]	[3, 3.5]	[3.5, 4]	[4, 4.5]
[1000, 2000]	17.51	0.52	1.91	2.66	
[2000, 3000]	12.96	0.13	1.31	1.37	9.42
[3000, 4000]	6.58	0.11	0.32	0.81	3.57
[4000, 5000]	4.04	0.22	0.02	0.02	0.97
[5000, 6000]	2.27	0.42	0.00	1.55	
[6000, 7000]	1.74	0.01	0.82	4.46	
[7000, 8000]	0.57	0.19	0.78	9.83	
[8000, 9000]	0.23	0.14	2.60		
[9000, 10000]	0.09	0.62	3.22		

*Table D.12: Relative error on the  $D^{*+}$  cross-section in each kinematic bin due to the choice of PID calibration binning.*

$p_T$ [MeV/c]	$y$				
	[2, 2.5]	[2.5, 3]	[3, 3.5]	[3.5, 4]	[4, 4.5]
[1000, 2000]		0.27	0.39	1.02	0.26
[2000, 3000]	5.80	0.19	0.29	1.00	7.68
[3000, 4000]	1.54	0.16	0.61	0.40	1.17
[4000, 5000]	0.45	0.01	0.43	4.27	15.53
[5000, 6000]	0.15	0.46	0.99	0.86	4.86
[6000, 7000]	0.09	0.30	0.59	2.70	
[7000, 8000]	1.20	0.90	1.96	2.72	
[8000, 9000]	0.03	1.08	2.95	21.48	
[9000, 10000]	0.58	0.81	8.09		

*Table D.13: Relative error on the  $D^+$  cross-section in each kinematic bin due to the finite sample size and hadronic interaction uncertainty on the tracking efficiency correction measurement.*

$p_T$ [MeV/c]	$y$				
	[2, 2.5]	[2.5, 3]	[3, 3.5]	[3.5, 4]	[4, 4.5]
[0, 1000]		7.33	7.17	6.09	
[1000, 2000]	6.94	6.72	6.24	5.55	5.20
[2000, 3000]	6.72	5.85	5.45	5.19	5.01
[3000, 4000]	6.36	5.25	5.07	4.91	4.85
[4000, 5000]	5.88	4.99	4.90	4.81	4.73
[5000, 6000]	5.31	4.84	4.76	4.73	4.74
[6000, 7000]	5.22	4.79	4.72	4.70	4.73
[7000, 8000]	5.04	4.72	4.67	4.66	
[8000, 9000]	4.93	4.71	4.68	4.69	
[9000, 10000]	4.81	4.67	4.62	4.71	

## D.4 Tracking efficiency correction

1099 See Section 7.6 for discussion.

1100 See Section 7.6 for discussion.

*Table D.14:* Relative error on the  $D_s^+$  cross-section in each kinematic bin due to the finite sample size and hadronic interaction uncertainty on the tracking efficiency correction measurement.

$p_T$ [MeV/c]	$y$				
	[2, 2.5]	[2.5, 3]	[3, 3.5]	[3.5, 4]	[4, 4.5]
[1000, 2000]	6.81	6.75	6.58	5.10	
[2000, 3000]	6.64	5.75	5.15	4.60	4.41
[3000, 4000]	6.41	5.00	4.65	4.41	4.40
[4000, 5000]	5.91	4.70	4.41	4.38	4.38
[5000, 6000]	5.27	4.53	4.38	4.38	4.42
[6000, 7000]	4.94	4.44	4.36	4.36	
[7000, 8000]	4.78	4.38	4.35	4.38	
[8000, 9000]	4.65	4.37	4.34		
[9000, 10000]	4.55	4.35	4.36		

*Table D.15:* Relative error on the  $D^{*+}$  cross-section in each kinematic bin due to the finite sample size and hadronic interaction uncertainty on the tracking efficiency correction measurement.

$p_T$ [MeV/c]	$y$				
	[2, 2.5]	[2.5, 3]	[3, 3.5]	[3.5, 4]	[4, 4.5]
[1000, 2000]		6.57	7.06	7.05	6.94
[2000, 3000]	6.00	5.57	6.79	6.92	6.47
[3000, 4000]	5.66	5.21	6.40	6.78	5.65
[4000, 5000]	5.43	5.16	6.11	6.52	5.04
[5000, 6000]	5.26	5.12	5.86	6.01	4.86
[6000, 7000]	5.27	5.10	5.68	5.31	
[7000, 8000]	5.26	5.07	5.48	5.01	
[8000, 9000]	5.20	5.02	5.22	4.83	
[9000, 10000]	5.17	5.01	5.01		

*Table D.16: Relative error on the  $D^+$  cross-section in each kinematic bin due to the arbitrary choice of fit model.*

$p_T$ [MeV/c]	$y$				
	[2, 2.5]	[2.5, 3]	[3, 3.5]	[3.5, 4]	[4, 4.5]
[0, 1000]		1.63	0.49	0.83	
[1000, 2000]	0.09	0.27	0.27	0.34	0.88
[2000, 3000]	0.12	0.23	0.59	1.07	1.73
[3000, 4000]	0.17	0.36	0.81	1.49	1.63
[4000, 5000]	0.48	0.70	1.17	1.32	1.78
[5000, 6000]	0.48	1.04	1.09	1.75	1.21
[6000, 7000]	0.64	1.21	1.71	1.79	1.10
[7000, 8000]	1.34	1.22	1.48	1.52	
[8000, 9000]	1.03	1.61	1.51	1.13	
[9000, 10000]	1.06	1.63	1.14	3.34	

<sub>1101</sub> **D.5 Fit model**

<sub>1102</sub> See Section 7.8 for discussion.

Table D.17: Relative error on the  $D_s^+$  cross-section in each kinematic bin due to the arbitrary choice of fit model.

$p_T$ [MeV/c]	$y$				
	[2, 2.5]	[2.5, 3]	[3, 3.5]	[3.5, 4]	[4, 4.5]
[1000, 2000]	0.19	0.27	0.31	2.23	
[2000, 3000]	0.38	0.18	0.19	1.32	2.82
[3000, 4000]	0.10	0.33	0.52	0.89	1.08
[4000, 5000]	0.43	0.30	0.84	0.73	0.58
[5000, 6000]	0.60	0.46	0.78	0.91	0.42
[6000, 7000]	0.24	0.35	0.90	0.93	
[7000, 8000]	0.68	0.53	0.82	0.92	
[8000, 9000]	0.79	0.57	1.10		
[9000, 10000]	2.01	0.72	1.14		

Table D.18: Relative error on the  $D^{*+}$  cross-section in each kinematic bin due to the arbitrary choice of fit model.

$p_T$ [MeV/c]	$y$				
	[2, 2.5]	[2.5, 3]	[3, 3.5]	[3.5, 4]	[4, 4.5]
[1000, 2000]		0.15	0.36	0.57	0.98
[2000, 3000]	0.03	0.14	0.31	0.59	0.64
[3000, 4000]	0.17	0.31	0.55	0.73	0.55
[4000, 5000]	0.35	0.37	0.56	0.55	0.12
[5000, 6000]	0.29	0.48	0.60	0.33	0.00
[6000, 7000]	0.17	0.55	0.27	0.62	
[7000, 8000]	0.19	0.37	0.39	0.47	
[8000, 9000]	0.14	0.56	0.53	0.15	
[9000, 10000]	0.38	0.29	0.35		

## 1103 E MC and data comparison after full selection

1104 This section presents the comparison plots between Monte Carlo simulation and data.  
1105 As basically all of the selection applied in this analysis is implemented in the HLT2  
1106 lines, a comparison can only be made between fully selected distributions.

1107 Therefore, the data is corrected using the PID efficiencies as described in Section 4.7  
1108 and the Monte Carlo simulation is weighted using the tracking correction factors as  
1109 discussed in Section 4.2.1. In both corrections, only the central value of the correction  
1110 is applied, ignoring the statistical and systematic uncertainties on these two quantities.  
1111 Hence, a disagreement between Monte Carlo and data distributions can be caused by  
1112 inefficiencies in the correction.

1113 The signal contribution in data is obtained using the sWeights extracted from  
1114 the  $\ln \chi^2_{\text{IP}}$  fit. In the following, integrated distributions across all  $p_T$ - $y$  bins are  
1115 shown. In order to suppress expected differences this measurement is not sensitive to,  
1116 namely mismodelling of the charm meson kinematics,  $p_T$  and  $y$  of the charm meson  
1117 is reweighted. This reweighting uses the same  $p_T$ - $y$  binning scheme as is used in  
1118 the measurement. Distributions for the most important selection variables are given  
1119 in E.1–E.4

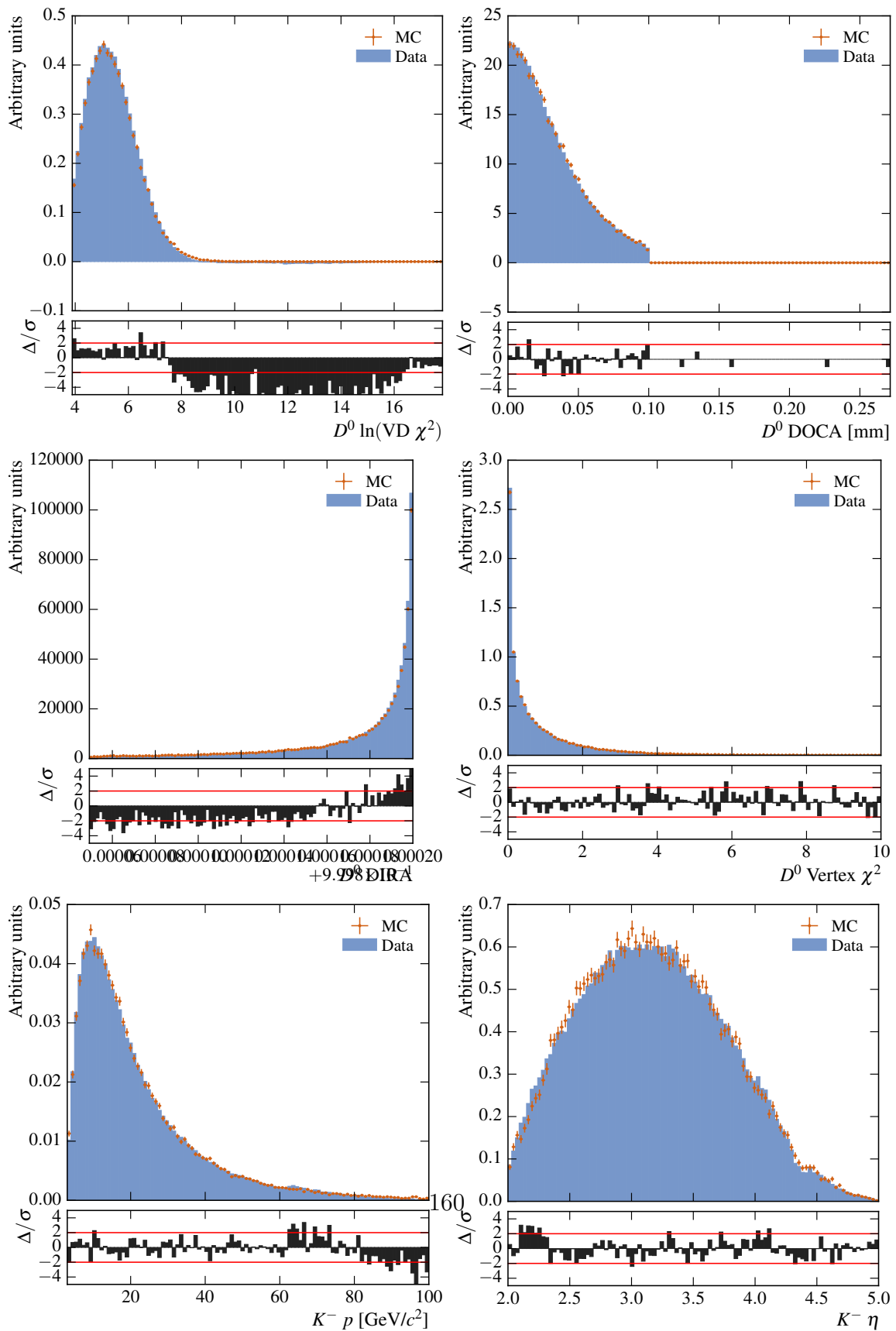


Figure E.1: MC/data comparison plots for  $D^0 \rightarrow K^- \pi^+$ .

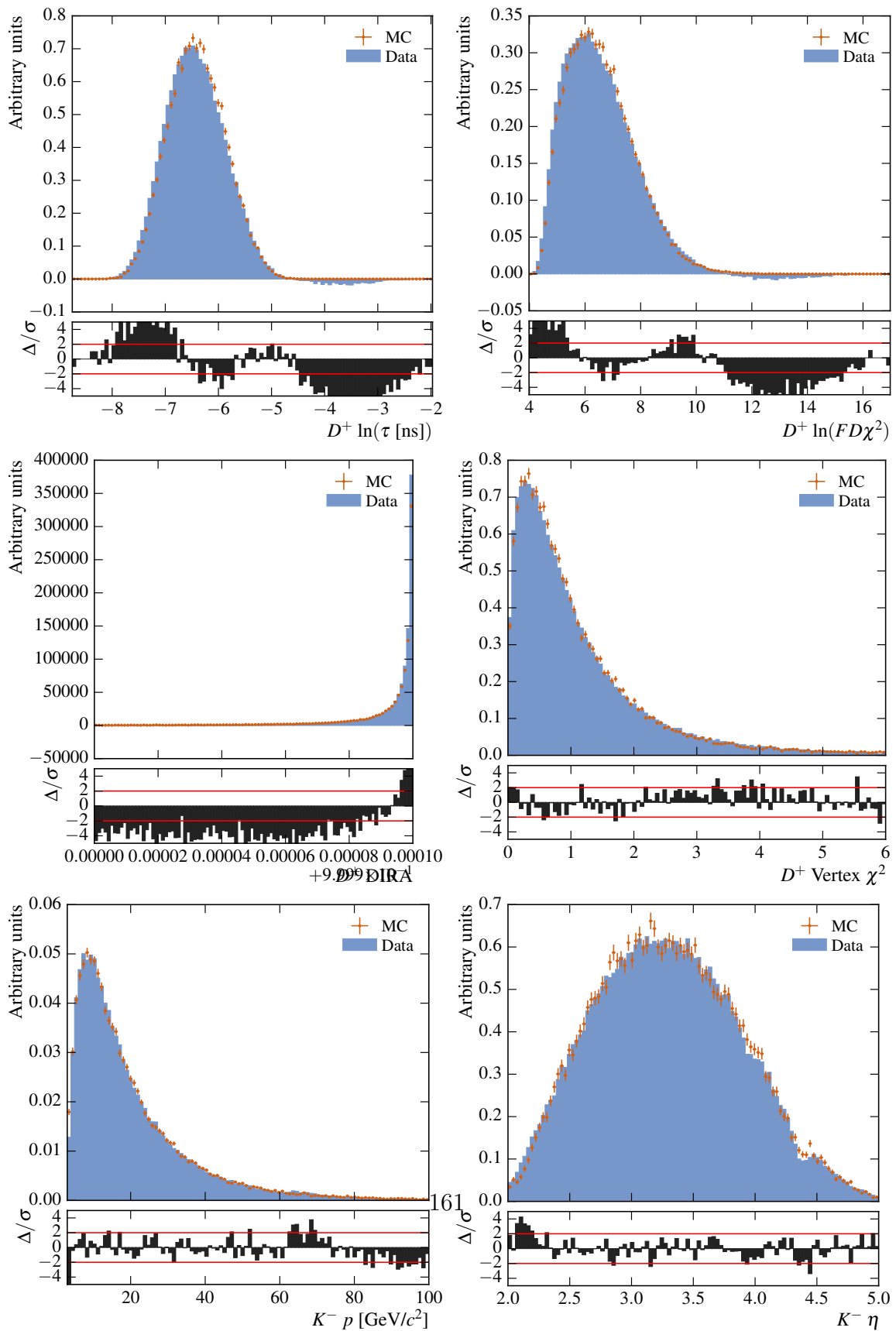


Figure E.2: MC/data comparison plots for  $D^+ \rightarrow K^- \pi^+ \pi^+$ .

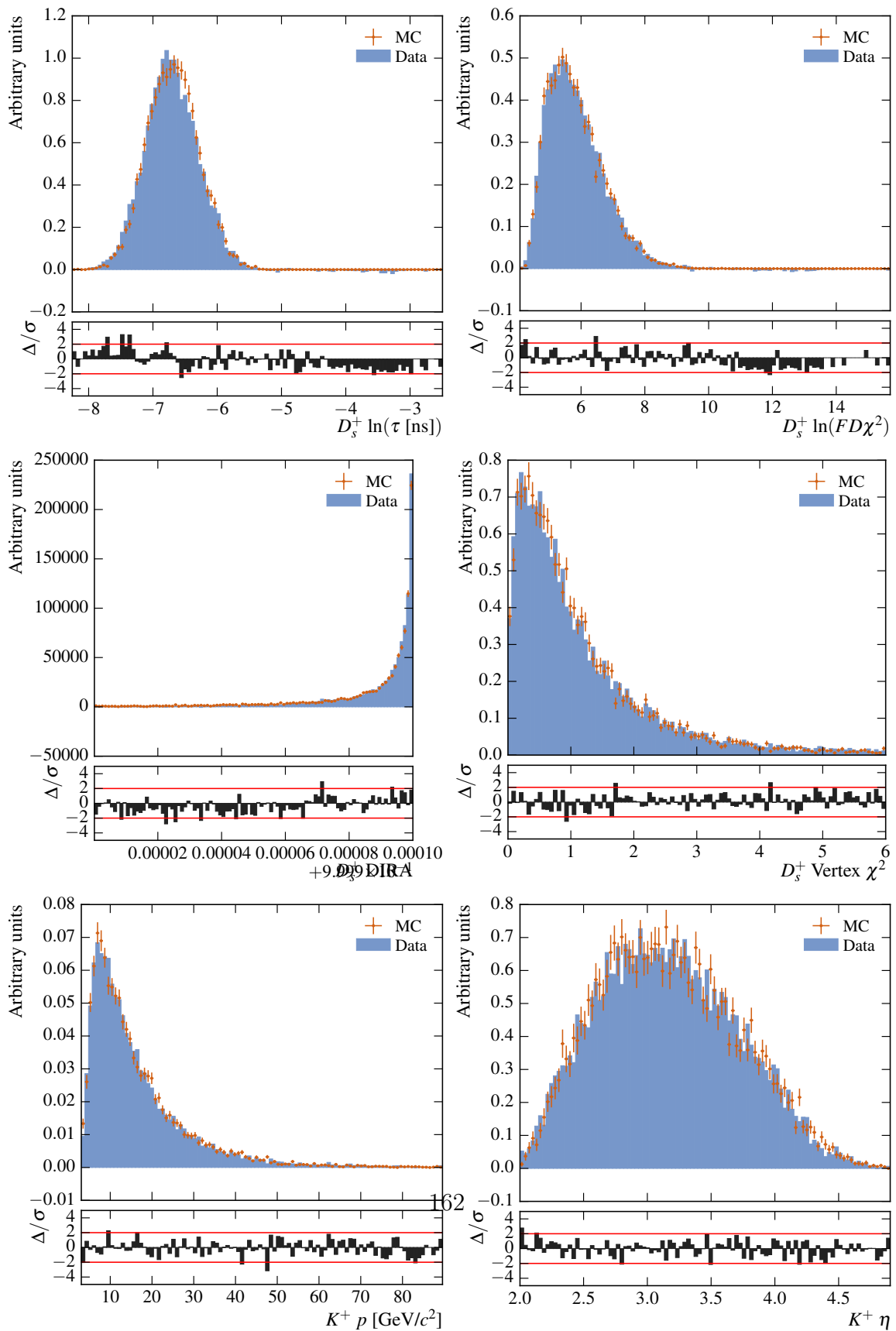


Figure E.3: MC/data comparison plots for  $D_s^+ \rightarrow \phi\pi^+$ .

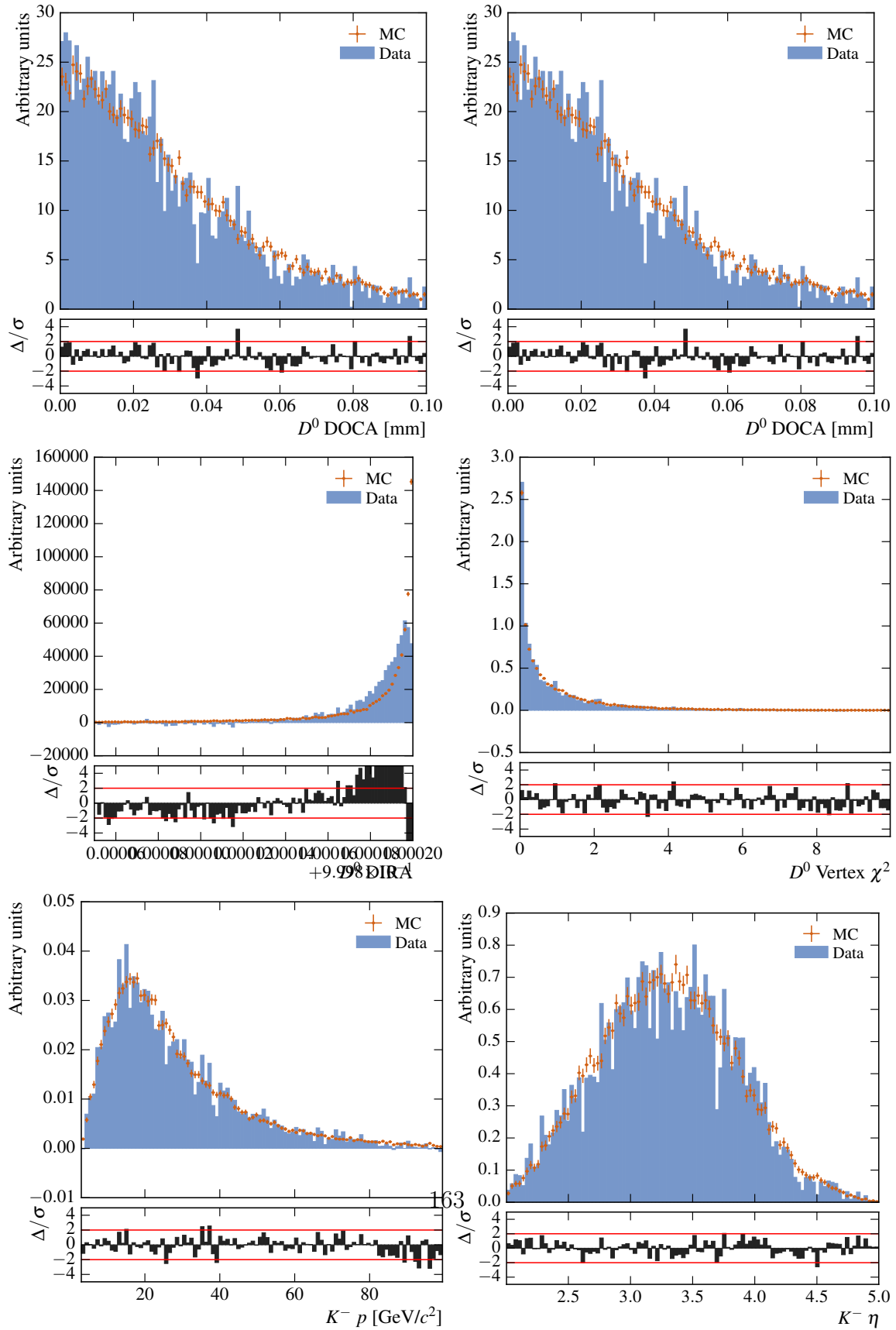


Figure E.4: MC/data comparison plots for  $D^{*+} \rightarrow D^0\pi^+$  with  $D^0 \rightarrow K^-\pi^+$ .

## References

- [1] R. Gauld, J. Rojo, L. Rottoli, and J. Talbert, *Charm production in the forward region: constraints on the small- $x$  gluon and backgrounds for neutrino astronomy*, [arXiv:1506.0802](https://arxiv.org/abs/1506.0802).
- [2] M. Cacciari, M. L. Mangano, and P. Nason, *Gluon PDF constraints from the ratio of forward heavy quark production at the LHC at  $\sqrt{s} = 7$  and 13 TeV*, [arXiv:1507.0619](https://arxiv.org/abs/1507.0619).
- [3] A. Bhattacharya *et al.*, *Perturbative charm production and the prompt atmospheric neutrino flux in light of RHIC and LHC*, [arXiv:1502.0107](https://arxiv.org/abs/1502.0107).
- [4] O. Zenaiev *et al.*, *Impact of heavy-flavour production cross sections measured by the LHCb experiment on parton distribution functions at low  $x$* , [arXiv:1503.0458](https://arxiv.org/abs/1503.0458).
- [5] LHCb collaboration, R. Aaij *et al.*, *Prompt charm production in pp collisions at  $\sqrt{s} = 7$  TeV*, [Nucl. Phys. \*\*B871\*\* \(2013\) 1](https://doi.org/10.1016/j.nuclphys.2013.01.001) LHCb-PAPER-2012-041, CERN-PH-EP-2013-009, [arXiv:1302.2864](https://arxiv.org/abs/1302.2864).
- [6] LHCb collaboration, R. Aaij *et al.*, *Measurements of prompt charm production cross-sections in pp collisions at  $\sqrt{s} = 13$  TeV*, [arXiv:1510.0170](https://arxiv.org/abs/1510.0170) LHCb-PAPER-2015-041, CERN-PH-EP-2015-272, [arXiv:1510.0170](https://arxiv.org/abs/1510.0170), to appear in JHEP.
- [7] C. Burr *et al.*, *Prompt charm production in pp collisions at  $\sqrt{s} = 13$  TeV in 2015 data*, .
- [8] ISO, *Quantities and units — Part 11: Mathematical signs and symbols for use in the physical sciences and technology*, ISO 31-11:1992, International Organization for Standardization, Geneva, Switzerland, 1992.
- [9] B. Kniehl, G. Kramer, I. Schienbein, and H. Spiesberger, *Inclusive charmed-meson production at the CERN LHC*, [Eur. Phys. J. \*\*C72\*\* \(2012\) 2082](https://doi.org/10.1007/s00367-012-1082-0), [arXiv:1202.0439](https://arxiv.org/abs/1202.0439).
- [10] T. Bauer *et al.*, *Prompt charm production in pp collisions at  $\sqrt{s} = 7$  TeV in 2010 data*, .
- [11] CLEO Collaboration, J. P. Alexander *et al.*, *Absolute measurement of hadronic branching fractions of the  $D_s^+$  meson*, [Phys. Rev. Lett. \*\*100\*\* \(2008\) 161804](https://doi.org/10.1103/PhysRevLett.100.161804).

- 1150 [12] LHCb collaboration, R. Aaij *et al.*, *Measurement of the track reconstruction*  
1151 *efficiency at LHCb*, JINST **10** (2015) P02007, [arXiv:1408.1251](https://arxiv.org/abs/1408.1251).
- 1152 [13] M. Pivk and F. R. Le Diberder, *Plots: A statistical tool to unfold data distribu-*  
1153 *tions*, Nuclear Instruments and Methods in Physics Research A **555** (2005) 356,  
1154 [arXiv:physics/0402083](https://arxiv.org/abs/physics/0402083).
- 1155 [14] Particle Data Group, K. A. Olive *et al.*, *Review of particle physics*, Chin. Phys.  
1156 **C38** (2014) 090001.
- 1157 [15] Particle Data Group, C. Amsler *et al.*, *Review of Particle Physics*, Phys. Lett.  
1158 **B667** (2008) 1.
- 1159 [16] L. Lyons, D. Gibaut, and P. Clifford, *How to combine correlated estimates of a*  
1160 *single physical quantity*, Nuclear Instruments and Methods in Physics Research  
1161 Section A **270** (1988), no. 1 110 .
- 1162 [17] Particle Data Group, K. Olive *et al.*, *Review of Particle Physics*, Chin. Phys.  
1163 **C38** (2014) 090001.